

# TREND-3

## Radiation Environments of Astronomy Missions and LEO Missions

### Final Report

ESTEC Contracts<sup>1</sup> No. 10725/94/NL/JG(SC) and No. 11711/95/NL/JG(SC) WO-3

#### Authors

##### **BIRA/IASB**

- J. Lemaire (Project Manager)
- D. Heynderickx, M. Kruglanski

##### **MSSL**

- A.D. Johnstone (MSSL Coordinator)
- D.J. Rodgers, S. Szita, G. Jones

##### **MPAe**

- E. Keppler (MPAe Coordinator)
- R. Friedel, G. Loidl

**August 1998**

<sup>1</sup>ESA Technical Management: E.J. Daly (WMA)



## APPENDIX 4

## ESA STUDY CONTRACT REPORT

No ESA Study Contract Report will be accepted unless this sheet is inserted at the beginning of each volume of the Report.

<b>ESA CONTRACT NO:</b> 10725/94/NL/JG, WO-3 to 11711/95/NL/JG	<b>SUBJECT:</b> Radiation Environments of Astronomy Missions and LEO Missions		<b>NAME OF CONTRACTOR:</b> BIRA/IASB, MSSL, MPAe
<b>* ESA CR( ) No:</b>	<b>* STAR CODE</b>	<b>No. of Volumes: 1</b> <b>This is Volume No: 1</b>	<b>CONTRACTOR'S REFERENCE</b>

**ABSTRACT:**

The contract work presented in this Final Report is a follow-up of the TREND-2 study (ESA/ESTEC TRP Contract No. 9828/92/NL/FM).

A number of new radiation belt models have been developed based on data from the following satellite experiments: AZUR/EI-88, SAMPEX/PET, UARS/PEM, CRRES/MEA, and ISEE/WIM. For each experiment, the mission and instrument characteristics and the data base formats have been described in detail in the Technical Notes of the project, and are summarised in this Final Report. The data binning procedures and the formats and limitations of the new models are described as well. The models have been intercompared where applicable, and have been compared to the standard NASA models AP-8 and AE-8. All new models have been implemented in the software package UNIRAD.

Besides the models developed in the framework of TREND-3, the ESA-SEE1 (Vampola 1996) model and the CRRESPRO (Meffert & Gussenhoven 1994) and CRRESELE (Brautigam & Bell 1995) models have also been adapted to and integrated in UNIRAD.

A large effort has been devoted to the development of a comprehensive Fortran subroutine library, called UNILIB, with the following functionalities: calculation of magnetic coordinates (e.g.  $B$ ,  $L$ ) and adiabatic invariants, coordinate transformations, field line and drift shell tracing, and averages of the atmospheric and ionospheric density over drift shells. The library is extensively documented on the World-Wide Web.

An extensive study has been made of the anisotropy of the low altitude trapped proton flux. After a review of the literature, one of the most commonly used models has been implemented in UNIRAD, together with an improved version. In addition, a method has been developed to render the anisotropy effects in terms of a natural coordinate system attached to the magnetic field. The method has been validated with the SAMPEX/PET data base.

Appropriate analytical functions have been found to fit the pitch angle distributions measured by CRRES/MEA. Finally, a new, corrected, Meteosat-3/SEM-2 data base has been produced.

The work described in this report was done under ESA contract. Responsibility for the contents resides in the author or organisation that prepared it.

Names of authors: J. Lemaire, D. Heynderickx, A.D. Johnstone, E. Keppler, M. Kruglanski, D.J. Rodgers, G. Jones, S. Szita, R. Friedel, G. Loidl

<b>** NAME OF ESA STUDY MANAGER</b> E.J. Daly DIV: WMA                      DIRECTORATE	<b>** ESA BUDGET HEADING</b>	
---	------------------------------	--

\* Sections to be completed by ESA

\*\* Information to be provided by ESA Study Manager



# Contents

<b>List of symbols</b>	<b>xix</b>
<b>List of acronyms</b>	<b>xxi</b>
<b>Preface</b>	<b>xxv</b>
Work performed by BIRA/IASB . . . . .	xxv
Work performed by MSSL . . . . .	xxvi
Work performed by MPAe . . . . .	xxvii
<b>Acknowledgments</b>	<b>xxix</b>
<b>1 General overview and results</b>	<b>1</b>
1.1 Improvements of UNIRAD . . . . .	1
1.1.1 New trapped particle models . . . . .	3
1.1.2 Directional flux modules . . . . .	3
1.1.3 UNILIB Library . . . . .	3
1.2 Anisotropy of trapped proton fluxes . . . . .	4
1.2.1 Conversion of omnidirectional to unidirectional fluxes . . . . .	4
1.2.2 Generalised anisotropy model . . . . .	4
1.3 AZUR/EI-88 Data base and radiation belt model . . . . .	5
1.4 SAMPEX/PET Data base and radiation belt model . . . . .	5
1.5 UARS/PEM Data base and radiation belt model . . . . .	5
1.6 Comparisons of the new trapped proton models . . . . .	6
1.7 ISEE/WAPS Data base and radiation belt model . . . . .	6
1.8 CRRES/MEA Data base and radiation belt model . . . . .	7
1.9 Radiation losses and particle injection studies . . . . .	7
1.10 Meteosat/SEM-2 Data base . . . . .	8

<b>2</b>	<b>UNIRAD Improvements and subroutine library</b>	<b>11</b>
2.1	Implementation of new trapped particle models in UNIRAD . . . . .	11
2.1.1	The UNIRAD program suite . . . . .	11
2.1.2	The TREP program . . . . .	13
2.1.3	New trapped particle models . . . . .	14
2.1.4	The ESA-SEE1 model . . . . .	15
2.1.5	The CRRESPRO and CRRESELE models . . . . .	15
2.1.5.1	The CRRESPRO model . . . . .	16
2.1.5.1.1	The PROTEL instrument . . . . .	16
2.1.5.1.2	Proton flux models . . . . .	17
2.1.5.2	The CRRESELE model . . . . .	18
2.1.5.2.1	The HEEF instrument . . . . .	18
2.1.5.2.2	Electron flux models . . . . .	19
2.1.6	Structure of the model data files . . . . .	19
2.1.7	Interpolation in flux maps . . . . .	20
2.1.8	Conversion to omnidirectional fluxes . . . . .	21
2.1.9	Modifications to TREP . . . . .	22
2.2	The UNIRAD library . . . . .	23
2.2.1	Portability . . . . .	23
2.2.2	Sources . . . . .	23
2.2.3	Functionality of the library . . . . .	24
2.2.4	Conventions used in the UNIRAD library . . . . .	24
2.2.4.1	Units . . . . .	24
2.2.4.2	Coordinate systems . . . . .	25
2.2.4.3	Component identifiers . . . . .	25
2.2.4.3.1	Error trapping . . . . .	26
2.2.5	Library documentation . . . . .	26
2.2.6	Installation and usage . . . . .	26
2.2.6.1	Initialization . . . . .	27
2.2.6.2	Main subroutines . . . . .	27
2.2.7	Models included in the library . . . . .	28
2.2.7.1	Magnetic field models . . . . .	28
2.2.7.2	Atmospheric models . . . . .	29
2.2.7.3	Collisional cross section models . . . . .	30
2.2.8	Magnetic drift shell . . . . .	30
2.2.8.1	Field line tracing . . . . .	30

2.2.8.2	Drift shell tracing . . . . .	31
2.2.9	Content of the library . . . . .	34
<b>3</b>	<b>Proton anisotropy</b>	<b>35</b>
3.1	Introduction . . . . .	35
3.2	Conventional trapped proton anisotropy models . . . . .	36
3.2.1	Notations . . . . .	36
3.2.1.1	Unidirectional flux . . . . .	38
3.2.2	Pitch-angle distribution . . . . .	38
3.2.2.1	Heckman-Nakano pitch-angle distribution . . . . .	39
3.2.2.2	Badhwar-Konradi pitch-angle distribution . . . . .	40
3.2.2.3	Comparison between Heckman-Nakano and Badhwar-Konradi distributions . . . . .	41
3.2.3	Lenchek-Singer East-West asymmetry model . . . . .	42
3.2.4	Combination of the angular distributions . . . . .	43
3.2.4.1	Global normalisation . . . . .	44
3.2.4.2	Separate normalisation . . . . .	44
3.2.4.3	Liouville's theorem . . . . .	45
3.2.5	Armstrong and Watts models . . . . .	46
3.2.6	BK-MIN and BK-MAX models . . . . .	49
3.3	Generalised anisotropy model . . . . .	50
3.3.1	First order expansion of the perpendicular flux . . . . .	50
3.3.2	Natural coordinate system . . . . .	51
3.3.3	Evaluation of $\Delta L$ . . . . .	52
3.3.4	Application to flux measurements . . . . .	55
3.3.4.1	Variation of $L_{GC}$ . . . . .	58
3.3.4.2	Flux scale height . . . . .	59
3.3.4.3	East-West asymmetry . . . . .	60
3.4	Intercomparison of the anisotropy models . . . . .	61
3.4.1	Angular distribution predicted by VF1-MIN and BK-MIN models . . .	61
3.4.1.1	Angular distribution at 450 km altitude . . . . .	64
3.4.1.2	Angular distribution at 1,500 km altitude . . . . .	65
3.4.2	Comparison with the semi-empirical model . . . . .	65
3.5	ANISO software overview . . . . .	69
3.5.1	Attitude interface file . . . . .	70
3.5.1.1	Changes implemented in the SAPRE program . . . . .	71

3.5.2	ANISO program . . . . .	71
3.5.2.1	Program check . . . . .	74
3.5.3	ANISOPOS . . . . .	76
3.5.3.1	Example . . . . .	77
<b>4</b>	<b>The AZUR/EI-88 data base and radiation belt model</b>	<b>79</b>
4.1	The AZUR mission . . . . .	79
4.1.1	Mission goals . . . . .	79
4.1.2	The EI-88/1 and EI-88/2 proton telescopes . . . . .	82
4.1.2.1	Measurement principle . . . . .	82
4.1.2.2	Detector layout and energy range . . . . .	84
4.2	The EI-88 data base . . . . .	87
4.2.1	Retrieval of the data sets . . . . .	88
4.2.2	Cleaning of the data sets . . . . .	92
4.2.2.1	Rejection criteria . . . . .	92
4.3	Model construction . . . . .	95
4.3.1	Effective areas of the EI-88 detectors . . . . .	96
4.3.2	Selection of bin sizes . . . . .	97
4.3.3	Correction for telescope field of view . . . . .	97
4.3.4	Final flux map . . . . .	104
4.3.5	Comparison to AP-8 . . . . .	104
<b>5</b>	<b>The SAMPEX/PET data base and radiation belt model</b>	<b>109</b>
5.1	The SAMPEX mission . . . . .	109
5.1.1	Spacecraft configuration . . . . .	109
5.1.2	Attitude control . . . . .	111
5.2	The Proton/Electron Telescope (PET) . . . . .	113
5.2.1	Detailed description of the PET telescope . . . . .	114
5.2.2	Analysis modes . . . . .	114
5.2.3	Calibrations . . . . .	116
5.3	The SAMPEX/PET data base . . . . .	117
5.3.1	PTLVxxxxx.DAT . . . . .	117
5.3.2	PKTSxxxxx.DAT . . . . .	117
5.3.3	SCEWxxxxx.DAT . . . . .	118
5.3.4	Generation of a new ephemeris data set . . . . .	119
5.4	Model construction . . . . .	120



5.4.1	Data binning . . . . .	120
5.4.2	Correction for telescope field of view . . . . .	120
5.4.3	Final flux map . . . . .	122
5.4.4	Comparison to AP-8 . . . . .	122
<b>6</b>	<b>The UARS/PEM data base and radiation belt model</b>	<b>127</b>
6.1	Mission and detector description . . . . .	127
6.1.1	The UARS mission . . . . .	127
6.1.2	Particle Environment Monitor . . . . .	128
6.1.3	The HEPS instrument . . . . .	130
6.2	Data processing . . . . .	132
6.2.1	Geometric factor correction . . . . .	133
6.2.2	Data binning . . . . .	134
6.2.2.1	Flux at the reference points . . . . .	137
6.2.2.2	Processing algorithm . . . . .	137
6.3	Proton PEM/UARS model . . . . .	139
6.3.1	Model coverage . . . . .	139
6.3.2	Detector field of view . . . . .	143
6.3.3	Corrected flux . . . . .	148
6.3.4	Proton flux model . . . . .	149
<b>7</b>	<b>Intercomparisons of the proton models</b>	<b>159</b>
7.1	Comparisons of the models for a LEO mission . . . . .	159
7.2	Comparisons of the models for a GTO mission . . . . .	161
7.3	Conclusions . . . . .	174
<b>8</b>	<b>The ISEE data base and radiation belt model</b>	<b>177</b>
8.1	The ISEE mission and instruments . . . . .	178
8.1.1	The ISEE-1/WIM instrument . . . . .	182
8.1.1.1	WAPS . . . . .	182
8.1.1.2	Scan platform . . . . .	182
8.1.2	The ISEE-2/KED instrument . . . . .	183
8.1.2.1	WAPS . . . . .	184
8.1.2.2	NAPS . . . . .	184
8.1.2.3	Temperature control and detector noise . . . . .	184
8.1.2.4	Instrument electronics . . . . .	184
8.1.2.5	Operational modes . . . . .	185

8.1.2.5.1	Mode A . . . . .	186
8.1.2.5.2	Mode B . . . . .	186
8.2	The ISEE raw data base . . . . .	186
8.2.1	Telemetry raw data . . . . .	187
8.2.2	Master Science File production . . . . .	187
8.3	The ISEE final data base . . . . .	188
8.3.1	Final data processing . . . . .	188
8.3.2	Format of the final data base . . . . .	190
8.3.2.1	Data base frame for ISEE-1 . . . . .	190
8.3.2.2	Data base frame for ISEE-2 . . . . .	190
8.3.2.3	Magnetic field model for ISEE-2 data . . . . .	190
8.4	Flux maps . . . . .	195
<b>9</b>	<b>The CRRES/MEA data base and radiation belt model</b>	<b>199</b>
9.1	Introduction . . . . .	199
9.2	Creation of an improved database . . . . .	199
9.2.1	Vampola's foldover correction . . . . .	201
9.2.2	Changes to resolution and format . . . . .	202
9.3	Data analysis . . . . .	202
9.3.1	Characteristics of the radiation belts . . . . .	202
9.3.2	Time lag correlation analysis . . . . .	202
9.3.2.1	Energy correlation . . . . .	207
9.3.2.2	Pitch angle correlation . . . . .	208
9.3.2.3	$L$ Correlation . . . . .	208
9.4	An $A_{p15}$ dependent electron model based on MEA data . . . . .	209
9.5	The ECM97 model . . . . .	211
9.5.1	Statistical variation . . . . .	211
9.5.2	Contamination . . . . .	213
9.5.3	$(L, \alpha_0)$ Binning . . . . .	213
9.5.4	Model Format . . . . .	217
9.5.5	Comparison with AE-8 . . . . .	217
9.5.6	Model Characteristics . . . . .	217
9.5.7	Outstanding problems . . . . .	217
9.6	Feasibility of a statistical model . . . . .	220

<b>10 Radiation losses and particle injection studies</b>	<b>223</b>
10.1 Introduction . . . . .	223
10.2 Theoretical background . . . . .	224
10.3 Relation to the work of Vampola (1996) . . . . .	225
10.4 Pitch angle distributions in the outer electron belt . . . . .	233
10.5 Fitting a Bessel function to the distribution outside the loss cone . . . . .	236
10.6 Fitting a Bessel function to the distribution inside the loss cone . . . . .	238
10.7 Estimated loss rates . . . . .	241
10.8 Conclusions . . . . .	243
<b>11 The Meteosat/SEM-2 data base</b>	<b>245</b>
11.1 The new data base . . . . .	245
11.2 Effect of Data Correction on TREND-2 Results . . . . .	245
11.2.1 Overview of the Error Correction . . . . .	245
11.2.2 Comparison of ‘Before’ and ‘After’ data . . . . .	251
11.2.3 Conclusions . . . . .	252
<b>References</b>	<b>253</b>
<b>A Correction procedure for finite telescope opening angles</b>	<b>259</b>
A.1 Conversion to fluxes . . . . .	259
A.1.1 General formulation . . . . .	259
A.1.2 Single element telescope . . . . .	261
A.1.3 Multi-element telescope . . . . .	262
A.2 Geometric factor correction . . . . .	262



# List of Figures

1.1	Description of Work Packages and associated deliverables . . . . .	2
2.1	Flow diagram of UNIRAD . . . . .	12
3.1	Representation of the coordinate system used in trapped proton anisotropy theory . . . . .	37
3.2	Comparison of the Heckman-Nakano and Badhwar-Konradi pitch angle distributions . . . . .	42
3.3	Comparison between different scale heights . . . . .	47
3.4	Representation of three consecutive magnetic drift shells . . . . .	51
3.5	Representation of a helicoidal trajectory . . . . .	53
3.6	$(B, L)$ Diagram of the SAMPEX/PET 86–120 MeV proton countrate . . . . .	55
3.7	Representation of the magnetic drift shell $L = 1.24$ , $B_m = 0.2$ . . . . .	56
3.8	Geocentric altitude of the southern mirror points of the drift shell ( $L = 1.24$ , $B_m = 0.2$ ) . . . . .	57
3.9	The variation $\Delta L$ of the shell parameter as a function of the azimuthal angle $\beta$ . . . . .	58
3.10	The SAMPEX 86–120 MeV proton countrate as a function of the shell parameter $L$ . . . . .	59
3.11	The SAMPEX 86–120 MeV proton countrate as a function of $L_{GC}$ . . . . .	60
3.12	The SAMPEX 86–120 MeV proton countrate as a function of the azimuthal angle $\beta$ . . . . .	61
3.13	VF1MIN predicted anisotropy of trapped proton differential flux at 60°W, 35°S and altitude 450 km . . . . .	62
3.14	BK-MIN predicted anisotropy of trapped proton differential flux at 60°W, 35°S and altitude 450 km . . . . .	62
3.15	Same as Fig. 3.13 but for an altitude of 1500 km based on the VF1MIN model. . . . .	63
3.16	Same as Fig. 3.14 but for an altitude of 1500 km based on the BK-MIN model. . . . .	63
3.17	Representation of the coordinate system used to compare different proton anisotropy models . . . . .	66

3.18	Dependence of the directional 100-MeV proton flux on the polar and azimuthal direction at the position (394.3 km, 25.7°S, 51.0°W) . . . . .	67
3.19	Dependence of the directional 100-MeV proton flux on the polar and azimuthal direction at the position (720.8 km, 7.9°S, 15.0°W) . . . . .	68
3.20	Flow diagram of UNIRAD . . . . .	70
3.21	Relative difference between the orbit-averaged omnidirectional integral spectrum produced respectively by ANISO and by TREP . . . . .	75
3.22	Angular distribution of trapped proton integral flux at 60°W, 35°S and altitude 450 km for 30, 40 and 50 MeV proton energies as obtained from the VF1MIN model . . . . .	78
4.1	Cross section of the AZUR satellite . . . . .	80
4.2	Representation of the orbital attitude of the AZUR satellite . . . . .	81
4.3	Cross section of the EI-88 instrument . . . . .	83
4.4	Cross section of the EI-88 sensors . . . . .	85
4.5	Energy deposited in the EI-88 detectors as a function of incident particle energy	86
4.6	Sample of the raw EI-88/1 channel 4 count rates in data file TAPE4.DAT . .	93
4.7	Sample of the EI-88/1 channel 4 count rates in data file TAPE4.DAT after running the cleaning programme . . . . .	94
4.8	Measured effective area for the EI-88 detectors [from Achtermann et al. (1970)]	96
4.9	Cumulative distribution of AZUR EI-88/1 measurements in $\alpha_0$ bins . . . . .	98
4.10	$(L, \alpha_0)$ Map of the number of measurements for channel 1 . . . . .	98
4.11	Uncorrected, predicted, and corrected flux averages for EI-88/1 channel 1 . .	100
4.12	Same as Fig. 4.11, for channel 6 and $L = 1.2$ . . . . .	100
4.13	Same as Fig. 4.11, for channel 1 and $L = 1.4$ . . . . .	101
4.14	Same as Fig. 4.13, for channel 6 and $L = 1.4$ . . . . .	101
4.15	Same as Fig. 4.13, for channel 1 and $L = 2.0$ . . . . .	102
4.16	Same as Fig. 4.13, for channel 6 and $L = 2.0$ . . . . .	102
4.17	Comparison of the equatorial pitch angles subtended by the EI-88/1 and EI-88/2 detectors . . . . .	103
4.18	$(L, \alpha_0)$ Map of the PAB97 model and AP-8 MAX for channel 1 . . . . .	105
4.19	$(L, \alpha_0)$ Map of the ratio of AP-8 MAX to the PAB97 model for channel 1 . . .	105
4.20	$(L, \alpha_0)$ Map of the PAB97 model and AP-8 MAX for channel 6 . . . . .	106
4.21	$(L, \alpha_0)$ Map of the ratio of AP-8 MAX to the PAB97 model for channel 6 . . .	106
4.22	World map of the PAB97 $>50$ MeV proton flux at 500 km . . . . .	107
4.23	World map of the AP-8 MAX $>50$ MeV proton flux at 500 km . . . . .	107
5.1	Mechanical design of the SAMPEX spacecraft and physical layout . . . . .	110

5.2	Pointing strategy for the SAMPEX spacecraft in two illustrative orbit planes . . . . .	111
5.3	Schematic of the PET telescope . . . . .	113
5.4	Effective areas of the SAMPEX/PET sensors . . . . .	122
5.5	$(L, \alpha_0)$ Map of the PSB97 model and AP-8 MIN for channel 1 . . . . .	123
5.6	$(L, \alpha_0)$ Map of the PSB97 model and AP-8 MIN for channel 5 . . . . .	123
5.7	$(L, \alpha_0)$ Map of the PSB97 model and AP-8 MIN for channel 9 . . . . .	124
5.8	$(L, \alpha_0)$ Map of the PSB97 model and AP-8 MIN for channel 13 . . . . .	124
5.9	World map of the PSB97 $>50$ MeV proton flux at 500 km . . . . .	125
5.10	World map of the AP-8 MIN $>50$ MeV proton flux at 500 km . . . . .	125
6.1	Line drawing of the UARS observatory showing the placement of the various instruments . . . . .	128
6.2	Diagram of the HEPS1 and HEPS2 telescopes . . . . .	131
6.3	UARS/PEM data coverage . . . . .	136
6.4	Flow chart of IDL procedures to produce the '.bin', '.cor' and '.res' files . . . . .	138
6.5	Iso-contours of $L$ at 585 km . . . . .	140
6.6	Iso-contours of the magnetic field intensity at 585 km . . . . .	140
6.7	Local pitch angle of the HEPS1/T1 telescope with azimuth angle $\mathcal{A} + 180^\circ$ (ascending leg) . . . . .	142
6.8	Local pitch angle of the HEPS1/T1 telescope with azimuth angle $180^\circ - \mathcal{A}$ (descending leg) . . . . .	142
6.9	Iso-contours of the equatorial pitch angle when $\alpha = 90^\circ$ at 585 km . . . . .	143
6.10	Raw $E \approx 100$ MeV proton flux at $1.295 < L < 1.305$ measured by the HEPS1/T2, HEPS1/T1, HEPS2/T2 and HEPS2/T1 telescopes as a function of the equatorial pitch angle for October to December 1991 . . . . .	144
6.11	Distribution of the local pitch angle of the HEPS1/T2, HEPS1/T1, HEPS2/T2 and HEPS2/T1 telescopes as a function of $\alpha_0$ at $1.295 < L < 1.305$ for October to December 1991 . . . . .	144
6.12	First simulation of the reponse of detector HEPS2/T1 . . . . .	146
6.13	Second simulation of the reponse of detector HEPS2/T1 . . . . .	146
6.14	Simulation of detector measurements as a function of $\alpha_0$ at different local pitch angles . . . . .	148
6.15	UARS/HEPS Differential flux as a function of the equatorial pitch angle for 17.2–24.4 MeV protons . . . . .	149
6.16	UARS/HEPS Differential flux as a function of the equatorial pitch angle for 31.7–42.1 MeV protons . . . . .	150
6.17	UARS/HEPS Differential flux as a function of the equatorial pitch angle for 94.0–122.5 MeV protons . . . . .	150

6.18	UARS/HEPS Differential proton flux spectra at $L = 1.2$ . . . . .	151
6.19	UARS/HEPS Differential proton flux spectra at $L = 1.3$ . . . . .	151
6.20	UARS/HEPS Differential proton flux spectra at $L = 1.4$ . . . . .	152
6.21	UARS/HEPS Differential proton flux as a function of $L$ at $\alpha_0 = 73^\circ$ . . . . .	152
6.22	UARS/HEPS Differential proton flux as a function of $L$ at $\alpha_0 = 41^\circ$ . . . . .	153
6.23	$(L, \alpha_0)$ map of the integral perpendicular proton flux at $E > 5.6$ MeV. . . . .	154
6.24	$(L, \alpha_0)$ map of the integral perpendicular proton flux at $E > 10.4$ MeV. . . . .	155
6.25	$(L, \alpha_0)$ map of the integral perpendicular proton flux at $E > 31.8$ MeV. . . . .	155
6.26	$(L, \alpha_0)$ map of the integral perpendicular proton flux at $E > 71.4$ MeV. . . . .	156
6.27	$(L, \alpha_0)$ map of the integral perpendicular proton flux at $E > 94.0$ MeV. . . . .	156
6.28	$(L, \alpha_0)$ map of the integral perpendicular proton flux at $E > 145.8$ MeV. . . . .	157
6.29	$(L, \alpha_0)$ map of the integral perpendicular proton flux at $E > 160.9$ MeV. . . . .	157
7.1	World map of the PAB97 directional proton flux above 30 MeV for the LEO orbit described in the text . . . . .	160
7.2	World map of the PUB97 directional proton flux above 30 MeV for the LEO orbit described in the text . . . . .	160
7.3	World map of the PSB97 directional proton flux above 30 MeV for the LEO orbit described in the text . . . . .	161
7.4	World map of the AP-8 MAX directional proton flux above 30 MeV for the LEO orbit described in the text . . . . .	162
7.5	World map of the AP-8 MIN directional proton flux above 30 MeV for the LEO orbit described in the text . . . . .	162
7.6	Integral PAB97 trapped proton fluxes above 30 MeV for the LEO orbit described in the text . . . . .	163
7.7	Integral PUB97 trapped proton fluxes above 30 MeV for the LEO orbit described in the text . . . . .	164
7.8	Integral PSB97 trapped proton fluxes above 30 MeV for the LEO orbit described in the text . . . . .	165
7.9	Integral AP-8 MAX trapped proton fluxes above 30 MeV for the LEO orbit described in the text . . . . .	166
7.10	Integral AP-8 MIN trapped proton fluxes above 30 MeV for the LEO orbit described in the text . . . . .	167
7.11	PAB97 Integral and differential trapped proton spectrum for the LEO orbit described in the text . . . . .	168
7.12	PUB97 Integral and differential trapped proton spectrum for the LEO orbit described in the text . . . . .	169



7.13	PSB97 Integral and differential trapped proton spectrum for the LEO orbit described in the text . . . . .	170
7.14	AP-8 MAX Integral and differential trapped proton spectrum for the LEO orbit described in the text . . . . .	171
7.15	AP-8 MIN Integral and differential trapped proton spectrum for the LEO orbit described in the text . . . . .	172
7.16	World map of the PAB97 directional proton flux above 30 MeV for the GTO orbit described in the text . . . . .	173
7.17	World map of the PUB97 directional proton flux above 30 MeV for the GTO orbit described in the text . . . . .	173
7.18	World map of the PSB97 directional proton flux above 30 MeV for the GTO orbit described in the text . . . . .	174
7.19	World map of the AP-8 MAX directional proton flux above 30 MeV for the GTO orbit described in the text . . . . .	175
7.20	World map of the AP-8 MIN directional proton flux above 30 MeV for the GTO orbit described in the text . . . . .	175
8.1	Plot of the ISEE orbits . . . . .	177
8.2	Cross section through the WAPS and the NAPS magnetic spectrometers . . .	179
8.3	ISEE orbits during one year . . . . .	180
8.4	ISEE Ion and electron fluxes vs. time on day 251/1978 . . . . .	181
8.5	Total magnetic field $B_T$ and components $B_X$ , $B_Y$ , $B_Z$ vs. time on day 251/1978	181
8.6	ISEE Master Science File production scheme . . . . .	188
8.7	ISEE Example of four original dynamic energy spectra and the averaged spectrum . . . . .	189
8.8	ISEE Electron flux map for all energies obtained with all data from 1977 day 307 up to 1987 day 61 . . . . .	196
8.9	ISEE Electron flux map for all energies obtained with the data from 1977 day 307 up to 1982 day 47 that contain spectrum information . . . . .	196
8.10	ISEE Electron flux map for energy range 17.5–28.0 keV obtained with the data from 1977 day 307 up to 1982 day 47 that contain spectrum information . . .	197
8.11	ISEE Electron flux map for energy range 28.0–37.6 keV obtained with the data from 1977 day 307 up to 1982 day 47 that contain spectrum information . . .	197
9.1	MEA Fluxes before and after the foldover correction in the three lowest energy channels, plotted against pitch angle . . . . .	200
9.2	Equatorially mirroring flux as a function of $L$ at 153 keV . . . . .	203
9.3	Equatorially mirroring flux as a function of $L$ at 976 keV . . . . .	203

9.4	Time delayed correlation coefficients for fluxes at $L = 4.0\text{--}4.5$ comparing 153 keV and 510 keV, 153 keV and 976 keV, and 153 keV and 1470 keV . . .	204
9.5	Time delayed correlation coefficients for fluxes at $L = 5.0\text{--}5.5$ comparing 153 keV and 510 keV, 153 keV and 976 keV, and 153 keV and 1470 keV . . .	204
9.6	Time delayed correlation coefficients for fluxes at $L = 3.0\text{--}3.5$ comparing 153 keV and 510 keV, 153 keV and 976 keV, and 153 keV and 1470 keV . . .	205
9.7	Time delayed correlation coefficients for fluxes at $L = 3.0\text{--}3.5$ comparing 510 keV and 976 keV, and 510 keV and 1470 keV . . . . .	205
9.8	Correlation coefficient between $80^\circ\text{--}90^\circ$ fluxes and $0^\circ\text{--}10^\circ$ fluxes . . . . .	206
9.9	Correlation coefficient between $80^\circ\text{--}90^\circ$ fluxes and the ratio of fluxes at $0^\circ\text{--}10^\circ$ and $80^\circ\text{--}90^\circ$ . . . . .	206
9.10	Correlation coefficient between 976 keV, $80^\circ\text{--}90^\circ$ fluxes at $L = 4$ and $L = 6$ .	207
9.11	510 keV Flux versus $L$ for 7 ranges of $A_{p15}$ . . . . .	210
9.12	1470 keV Flux versus $L$ for 7 ranges of $A_{p15}$ . . . . .	210
9.13	Greyscale plot of 510 keV standard deviation binned in $(L, \alpha_0)$ space . . . . .	212
9.14	Greyscale plot of 510 keV standard deviation binned in $(L, \alpha_0)$ space . . . . .	212
9.15	Fluxes in $0^\circ\text{--}10^\circ$ equatorial pitch angle bin for energies 153, 510, 976 and 1470 keV . . . . .	214
9.16	Back-calculated counts in $0^\circ\text{--}10^\circ$ equatorial pitch angle bin for energies 153, 510, 976 and 1470 keV . . . . .	214
9.17	Loss-cone fluxes at $L = 4$ over a 2-month period . . . . .	215
9.18	3 MeV Proton flux over the same 2-month period as in Fig. 9.17 . . . . .	215
9.19	Total 1 MeV electron flux over the same 2-month period as in Fig. 9.17 . . . . .	216
9.20	Greyscale plot of 976 keV mean flux binned in $(L, \alpha_0)$ space. . . . .	216
9.21	1 MeV Electron flux along the noon equator . . . . .	218
9.22	1 MeV Electron flux along the midnight equator . . . . .	218
9.23	Contour plot of log flux in a noon-midnight cut through the magnetosphere, for $K_p = 0$ . . . . .	219
9.24	Contour plot of log flux in a noon-midnight cut through the magnetosphere, for $K_p = 7$ . . . . .	219
9.25	976 keV Electron fluxes at $L = 6.5\text{--}6.7$ summed over 1 minute . . . . .	221
9.26	976 keV Electron fluxes at $L = 6.5\text{--}6.7$ summed over 8 minutes . . . . .	221
9.27	976 keV Electron fluxes at $L = 6.5\text{--}6.7$ summed over 1 orbit . . . . .	222
9.28	Dependence of median, and $10^{\text{th}}$ and $90^{\text{th}}$ percentiles on time bin . . . . .	222
10.1	A comparison between a Bessel function and a sine function fitted between the same two points, at $90^\circ$ and at $45^\circ$ . . . . .	226

10.2	The relation between the parameter $n$ from Vampola's (1996) fits and the Bessel function fit from this work . . . . .	226
10.3	Pitch angle distributions for $K_p = 0$ to $1^+$ , for $L = 2.5$ and $L = 3.3$ . . . . .	227
10.4	Pitch angle distributions for $K_p = 0$ to $1^+$ , for $L = 4.1$ and $L = 4.9$ . . . . .	228
10.5	Pitch angle distributions for $K_p = 0$ to $1^+$ , for $L = 5.7$ and $L = 6.5$ . . . . .	229
10.6	Pitch angle distributions for $K_p = 6$ to $7^+$ , for $L = 2.5$ and $L = 3.3$ . . . . .	230
10.7	Pitch angle distributions for $K_p = 6$ to $7^+$ , for $L = 4.1$ and $L = 4.9$ . . . . .	231
10.8	Pitch angle distributions for $K_p = 6$ to $7^+$ , for $L = 5.7$ and $L = 6.5$ . . . . .	232
10.9	The electron intensity at $90^\circ$ pitch angle obtained by fitting a Bessel function to the complete distribution as a function of $L$ , for low $K_p$ values . . . . .	233
10.10	The electron intensity at $90^\circ$ pitch angle obtained by fitting a Bessel function to the complete distribution as a function of $L$ , for high $K_p$ values . . . . .	234
10.11	The electron intensity at $90^\circ$ pitch angle measured by the CRRES/MEA detector, as a function of $L$ , for low $K_p$ values . . . . .	235
10.12	The electron intensity at $90^\circ$ pitch angle measured by the CRRES/MEA detector, as a function of $L$ , for high $K_p$ values . . . . .	235
10.13	The scattering angle derived from the Bessel function fit at five energies over the entire $L$ range for low $K_p$ values . . . . .	236
10.14	The scattering angle derived from the Bessel function fit at five energies over the entire $L$ range for high $K_p$ values . . . . .	237
10.15	The intensity in the field aligned direction obtained from the Bessel function fit inside the loss cone at five energies over the entire $L$ range for low $K_p$ values	238
10.16	The intensity in the field aligned direction obtained from the Bessel function fit inside the loss cone at five energies over the entire $L$ range for high $K_p$ values	239
10.17	The scattering angle inside the loss cone obtained from the Bessel function fit at five energies over the entire $L$ range for low $K_p$ values . . . . .	240
10.18	The scattering angle inside the loss cone obtained from the Bessel function fit at five energies over the entire $L$ range for high $K_p$ values . . . . .	241
10.19	The decay time calculated for low $K_p$ values . . . . .	242
10.20	The decay time calculated for high $K_p$ values . . . . .	242
11.1	E5-E4 flux, before and after data set corrections . . . . .	248
11.2	Anisotropy index, before and after data set corrections . . . . .	248
11.3	E5-E4 flux statistical plot, before data set corrections . . . . .	249
11.4	E5-E4 flux statistical plot, after data set corrections . . . . .	249
11.5	Anisotropy index statistical plot, before data set corrections . . . . .	250
11.6	Anisotropy index statistical plot, after data set corrections . . . . .	250



# List of Tables

2.1	List of the new flux models implemented in TREP . . . . .	15
2.2	Integration parameters (MeV) for integral omnidirectional PROTEL flux [from Meffert & Gussenhoven (1994)] . . . . .	17
2.3	Channel energies (MeV) for CRRES/HEEF [from Brautigam & Bell (1995)] . .	18
2.4	Summary of CRRES $A_{p15}$ model separation and statistics [from Brautigam & Bell (1995)] . . . . .	19
2.5	New or modified NAMELIST parameters for TREP . . . . .	22
2.6	Physical units used in the UNIRAD library . . . . .	25
2.7	URLs Of the main pages of the UNIRAD library documentation . . . . .	26
2.8	Subroutines implemented in the UNIRAD library . . . . .	32
2.8	(continued) . . . . .	33
2.8	(continued) . . . . .	34
3.1	Values of the parameters relative to BK-MIN and BK-MAX . . . . .	49
3.2	Magnetic coordinates $(B, L)$ , magnetic dip angle $I$ , parameter $\sigma$ and scale height $H^{\min}$ for two points of observation . . . . .	64
3.3	Record structure of the interface file . . . . .	71
3.4	ANISO Namelist parameters . . . . .	72
3.5	Format of the file PROJECT.TRD . . . . .	73
3.6	Format of the file PROJECT.SPD . . . . .	74
3.7	Interactive menu options of ANISOPOS . . . . .	76
3.8	ANISOPOS namelist parameters . . . . .	77
4.1	Orbital elements of the AZUR satellite . . . . .	82
4.2	Detector and absorber characteristics of the EI-88 instruments . . . . .	87
4.3	Energy channels of the EI-88 instruments for protons and $\alpha$ particles . . . . .	87
4.4	Record structure of the AZUR tape identification files . . . . .	88
4.5	Content of the AZUR tape pass header records . . . . .	88
4.6	Content of the AZUR tape data records . . . . .	89

4.6	(continued)	90
4.6	(continued)	91
4.7	Geometric factors and surface areas of the EI-88 sensors [from Häusler (1972)]	96
4.8	$(E, L, \alpha_0)$ Bin limits for the PAB97 model grid	99
5.1	SAMPEX Scientific Instruments	112
5.2	PET Detector, ADC, and discriminator characteristics	114
5.3	PET Response	115
5.4	SAMPEX/PET Data set file description	116
5.5	PET Channel characteristics	118
5.6	Description of the EPH structure	119
5.7	$(E, L, \alpha_0)$ Bin limits for the PET model grid	121
6.1	List of the UARS experiments	129
6.2	List of the PEM instruments	129
6.3	Characteristics of the HEPS detectors	130
6.4	Differential number flux uncertainties for protons from 5 to 150 MeV	132
6.5	Proton energy (MeV) channels of the EP1 and EP2 sensors of the HEPS detectors	133
6.6	Bin limits $(L, \alpha_0)$	135
8.1	Contents of the ISEE-1 file headers	191
8.2	Electron flux channels in the ISEE-1 data frames (in keV)	192
8.3	Record structure of the ISEE-2 final data base frames	193
8.3	(Continued)	194
8.4	Values of the one-byte quality flag in the ISEE-2 data files	194
9.1	Definitions of the parameters in the new MEA data base	201
9.2	$A_{p15}$ Ranges used for the new MEA model	209
11.1	Record structure of the Meteosat/SEM-2 archived data set record	246
11.1	(Continued)	247

# List of symbols

$A$	Detector surface area
$\alpha$	Pitch angle
$\alpha_0$	Equatorial pitch angle
$\beta$	Azimuthal angle defined in the local mirror plane
$B$	Geomagnetic field intensity
$\mathbf{B}$	Geomagnetic field vector
$B_m$	Mirror point geomagnetic field intensity
$B_0$	Equatorial geomagnetic field intensity
$B_c$	Geomagnetic field intensity at the atmospheric cutoff
$C$	Counting rate
$E$	Particle energy
$\epsilon$	Detector efficiency
$F_{10.7}$	Solar radio flux at 10.7 cm
$G$	Geometric factor ( $\text{cm}^2\text{sr}$ )
$\Gamma$	Telescope gathering power
$h$	Effective detector area
$j$	Differential particle flux
$J$	Integral particle flux
$L$	McIlwain's (1961) parameter ( $R_E$ )
$\lambda$	Wavelength ( $\text{\AA}$ )

$\omega$  Solid angle (sr)

$\phi$  Geocentric longitude or azimuth angle

$\varphi$  Angle introduced by Daly & Evans (1993)

$\mathbf{r}$  Position vector

$R$  Telescope directional response function

$S$  Total area

$d\sigma$  Element of surface area

$t$  Time

$T$  Total observation time

$\theta$  Polar angle

$Z$  Atomic number



# List of acronyms

<b>ADC</b>	Analog to Digital Converter
<b>ACS</b>	Attitude Control System
<b>ACE</b>	Attitude Control Electronics
<b>ASCII</b>	American Standard Code for Information Interchange
<b>BIRA</b>	Belgisch Instituut voor Ruimte-Aëronomie
<b>BFO</b>	Blood Forming Organs
<b>CCN</b>	Contract Change Notice
<b>CDF</b>	Common Data Format
<b>CIRA</b>	COSPAR International Reference Atmosphere
<b>COSPAR</b>	COMmittee for SPace Research
<b>CRRES</b>	Combined Release and Radiation Effects Satellite
<b>DEC</b>	Digital Equipment Corporation
<b>DGRF</b>	Definitive Geomagnetic Reference Field
<b>ESA</b>	European Space Agency
<b>ESTEC</b>	European Space and TEchnology Centre
<b>FOV</b>	Field Of View
<b>FTP</b>	File Transfer Protocol
<b>GEI</b>	GEocentric Inertial
<b>GEO</b>	GEostationary Orbit
<b>GSFC</b>	Goddard Space Flight Center

**GTO** Geostationary Transfer Orbit

**HETC** High Energy Transport Code

**HILT** Heavy Ion Large Telescope

**HTML** Hierarchical Text Mark-up Language

**HTTP** HyperText Transfer Protocol

**IASB** Institut d'Aéronomie Spatiale de Belgique

**IDL** Interactive Data Language

**IDFS** Instrument Data File Set

**IGRF** International Geomagnetic Reference Field

**IMF** Interplanetary Magnetic Field

**IRI** International Reference Ionosphere

**ISEE** International Sun Earth Explorer

**JPL** Jet Propulsion Laboratory

**LDEF** Long Duration Exposure Facility

**LEICA** Low Energy Ion Composition Analyzer

**LEO** Low Earth Orbit

**MAST** MAss Spectrometer Telescope

**MEA** Medium Electrons A

**MEPE** Medium Energy Particle Experiment

**MPAe** Max Planck Institut für Aeronomie

**MS-DOS** MicroSoft Disk Operating System

**MSIS** Mass-Spectrometer-Incoherent-Scatter

**MSSL** Mullard Space Science Laboratory

**NAPS** Narrow Angle Particle Spectrometer

**NASA** National Aeronautics and Space Administration

**NSSDC** National Space Science Data Center

**NOAA** National Oceanic and Atmospheric Administration

**PC** Personal Computer

**PEM** Particle Environment Monitor

**PET** Proton/Electron Telescope

**PI** Principal Investigator

**PLGD** Phillips Laboratory Gheophysics Directorate

**PS** PostScript

**PSI** Paul Scherrer Institute

**REM** Radiation Environment Monitor

**SAA** South Atlantic Anomaly

**SAMPEX** Solar, Anomalous, and Magnetospheric Particle EXplorer

**SDDAS** Southwest Data Display and Analysis System

**SEM** Space Environment Monitor

**SMEX** SMall EXplorer

**SPENVIS** SPace ENVironment Information System

**SwRI** Southwest Research Institute

**TN** Technical Note

**TREND** Trapped Radiation ENvironment Development

**UARS** Upper Atmosphere Research Satellite

**URL** Uniform Resource Locator

**VAX** Virtual Address eXtension

**VMS** Virtual Memory System

**WAPS** Wide Angle Spectrometer

**WIM** Williams Mother

**WO** Work Order

**WP** Work Package

**WWW** World Wide Web



# Preface

This final report contains the main results obtained by the TREND-3 team during the study “Radiation Environments of Astronomy Missions and LEO Missions”. The TREND (Trapped Radiation ENvironment Development) study was initiated by E.J. Daly and funded by ESA under two earlier contracts. The present study started on 1 Feb, 1994, under ESA Contract No. 10725/94/NL/JG(SC), and was extended as WO-3 to ESA Contract No. 11711/95/NL/JG(SC). The duration of the project was 41 months.

Three institutes from three ESA member states participated in this project:

- BIRA/IASB, the Belgisch Instituut voor Ruimte-Aëronomie/Institut d’Aéronomie Spatiale, Brussels, Belgium (the prime contractor);
- MSSL, the Mullard Space Science Laboratory, Dorking, UK;
- MPAe, the Max Planck Institut für Aeronomie, Katlenburg-Lindau, Germany.

In the sections below, the work performed by each team is summarised and grouped by Work Package (WP). The resulting Technical Notes (TN) are listed as well.

Seven progress meetings have been held at BIRA/IASB, MSSL, and MPAe, and a mid-term review was held at ESTEC. The Final Presentation was given at ESTEC on 15 Sep 1998. The databases, software and models have been installed at ESTEC/WMA.

In October 1995, the BIRA/IASB TREND team has organised an international workshop in Brussels, where results of TREND-2 and TREND-3 were presented to an audience of 60 researchers in the field of radiation belt physics. The workshop proceedings have been edited by J.F. Lemaire, D. Heynderickx, and D.N. Baker, and have been published by the American Geophysical Union as Geophysical Monograph 97. This volume, entitled *Radiation Belts. Models and Standards*, has received the 1996 Honorable Mention for Geography & Earth Sciences from the Association of American Publishers, Inc. Part of the expenses for the compilation of this monograph have been charged to the present TREND contract as external services.

## Work performed by BIRA/IASB

J.F. Lemaire is the overall project manager and coordinator for the BIRA/IASB team, which further consisted of D. Heynderickx (werkleider), M. Kruglanski (post doctoral research assistant),

V. Pierrard (post graduate student), M. Echim (graduate student from the Institute of Gravitation and Space Sciences, Bucharest; he visited for six months at BIRA/IASB, on the support of TREND), J.-M. Vandenberghe (graduate student), and L. Fedullo (software engineer).

D. Heynderickx was responsible for the analysis of the AZUR and SAMPEX data, and for building the data bases and empirical models resulting from these satellite observations. He has also upgraded the UNIRAD package, including the extension of the trapped particle models with the various models developed in this study, and with the ESA-SEE1, CRRESPRO, and CRRESELE models. He was in charge of WP 2.1 (Flight Data Comparisons), WP 2.2R (SAMPEX Proton Model), and WP 3.1R (UNIRAD Revisited), is the principal author of the UNIRAD user manual, has contributed to TN 5 and TN 10, and coordinated the production of this final report.

M. Kruglanski was responsible for WP 2.2 (Generalised Anisotropy Model), WP 2.1R (Improvement of ANISO Program), and WP 3.2R (UNIRAD Library). He has visited South West Research Institute, San Antonio, to get acquainted with the UARS/PEM data set and software, and to implement them at BIRA/IASB. He has written the UNILIB software library and its documentation. He is the principal author of TN 6, TN 6(2), and has contributed to TN 5, TN 10, and the UNIRAD manual.

V. Pierrard has performed a statistical analysis of the count rates and livetimes of the SAMPEX/PET detector, and has written a report. J.-M. Vandenberghe has assisted in the development of the UNILIB library and in the production of its documentation. M. Echim has assisted in the building of the UARS/PEM database and model. L. Fedullo has installed and maintained the DEC/Alpha stations and personal computers which were used at BIRA/IASB for this study.

## Work performed by MSSL

A.D. Johnstone was the coordinator for Mullard Space Science Laboratory, Dorking. His team consisted of D.J. Rodgers (research assistant), S. Szita (research assistant), and G. Jones (research assistant). They were mainly concerned with the analysis of electron flux measurements made by the SEM-2 on METEOSAT and by the MEA instrument on CRRES. These observations were used to produce databases and models for the energetic electron environment.

MSSL Was in charge of WP 1.2 (Analysis of CRRES/MEA Data), WP 1.3 (Model Unification), and WP 1.3R (Creation of ISEE Electron Model). This work is described in their TN 2. They also improved the MEA electron model as part of WP 1.2R, which is documented in TN 2. The CRRES/MEA and ISEE models have been implemented in the UNIRAD software suite.

In TN 9 they describe how they updated and corrected the METEOSAT/SEM-2 data base and model that was developed in the TREND-2 project. This work constituted WP 4.2R.

In TN 8 they determined appropriate functions to fit the pitch angle distributions measured by the MEA detector on CRRES.

## **Work performed by MP Ae**

E. Keppler was the coordinator of the team working at Max Planck Institut für Aeronomie, Katlenburg-Lindau. He was assisted by, firstly, R. Friedel (research assistant), and later by G. Loidl (research assistant). They produced a database of the electron flux measurements made by the WIM instruments on the ISEE-1 and ISEE-2 satellites. The MP Ae team was responsible for WP 1.1 (ISEE Data Analysis) and WP 1.1R (Merging of ISEE Particle and Magnetic Field Observations), and produced TN 1.





# Acknowledgments

During the TREND-3 modelling effort the ESA Technical Manager E.J. Daly has closely followed the progress of the data analysis and model development. His experience and advice have been very stimulating and greatly appreciated by all TREND team members. We also benefited from H. Evans' useful suggestions and comments.

The AZUR radiation belt model for trapped protons could never have been developed without the cooperation of D. Hovestadt, Max Planck Institut für Extraterrestrische Physik, Garching, who was the PI of the EI-88 directional detectors. He provided D. Heynderickx with the necessary documentation for the analysis of the AZUR data and granted permission to use the data set. We wish to acknowledge also the Director of NSSDC, J. King, who has unearthed this historical data set from the archives of the NSSDC, at GSFC, Greenbelt.

We wish to address our special thanks to J.B. Blake, Aerospace Corporation, Los Angeles, and R.A. Mewaldt, CALTECH, Pasadena, for offering the TREND project manager the opportunity to use the proton flux measurements of the Proton/Electron Telescope (PET) obtained onboard of the SAMPEX satellite, in order to build a new trapped proton environment model. R.A. Mewaldt and J.B. Blake are PI's for this comprehensive experiment. We thank also M.D. Looper, research assistant at Aerospace Corporation for implementing the unique PET dataset during two visits at BIRA/IASB, and for many long and fruitful discussions.

The TREND team at BIRA/IASB has also been given access to the PEM proton flux measurements obtained onboard of the UARS satellite. We are very grateful to J.D. Winningham and J.R. Sharber, South West Research Institute, San Antonio, PI and Co-I of PEM, for allowing M. Kruglanski to visit SwRI, and to use the PEM observations to build a database for trapped energetic protons. The TREND project manager also thanks the SwRI personnel, especially R.A. Frahm, for allowing us to retrieve and partly process these data on their computer facilities. This database has been used by M. Kruglanski, with the assistance of M.M. Echim (visiting BIRA/IASB from the Institute of Gravitation and Space Sciences, Bucharest), to build the UARS/PEM proton environment model described in this final report.

We thank also S. Chabrilat, post-graduate student at BIRA/IASB, who improved the computer code of the MSISE-90 atmospheric model. His help in implementing this atmospheric model in the UNILIB library is appreciated.

E. Keppler and his team at Max Planck Institut für Aeronomie, Katlenburg-Lindau, wish to acknowledge T.A. Fritz, Center for Space Physics, Boston University, for transferring the ISEE electron data to Germany. We wish also to acknowledge C.T. Russell for providing his magnetic

field observations, which have been incorporated in the ISEE database.

We wish to thank A.L. Vampola, Torrance, CA, for his cooperation with the TREND team working at MSSL. He provided the electron flux measurements obtained with his MEA instrument that flew onboard CRRES. The radiation belt model based on these data has been implemented in UNIRAD. We also thank A.L. Vampola for providing copies of the ESA-SEE1 model and documentation, and for his assistance in the implementation of the model in UNIRAD.

We thank E.G. Mullen, D.H. Brautigam, and M.S. Gussenhoven of Phillips Laboratory for providing us with copies of the CRRESPRO and CRRESELE models and for giving their permission to include them in UNIRAD. Their assistance is greatly appreciated, as well as many discussions which proved invaluable in the correct interpretation of the models.

T. Cayton (LANL) is acknowledged for providing the detectors used in the SEM-2 instrument on METEOSAT-3. The data of this detector have been used by MSSL to build the METEOSAT/SEM-2 energetic electron environment model described in this final report.

Finally, we acknowledge P. Simon, Director of BIRA/IASB, and his predecessor, Baron M. Ackerman, who gave full support to the TREND study and who have facilitated its realisation. The logistic and administrative personnel of BIRA/IASB is also generally acknowledged for its efficient help and good collaboration. We are grateful to J.-M. Vandenberghe for scanning in plots and drawings, and to A.H. Glover for carefully proof reading the manuscript.

J.F. Lemaire,

Project Manager

# Chapter 1

## General overview and results

In this chapter, we present an overview of the results obtained during this study and the development of new tools and models for the radiation belt environment. The main results and output produced during this ESA/ESTEC contract are presented following the order of the chapters in this final report.

The present study is the follow-up of the TREND-2 study (ESA/ESTEC TRP Contract No. 9828/92/NL/FM), the final report of which was issued in February 1995 (copies are available from E.J. Daly at ESTEC/WMA, Keplerlaan 1, PO Box 299, 2200 AG Noordwijk, The Netherlands, or from J. Lemaire, BIRA/IASB, Ringlaan 3, 1180 Brussel, Belgium). This final report contains an introductory description of the radiation belts and the physical processes in the magnetosphere. Other review papers can be found in AGU Monograph **97**, *Radiation Belts: Models and Standards*, eds. J.F. Lemaire, D. Heynderickx, and D.N. Baker (1996).

Figure 1.1 lists the WP numbers and content, the initials of the contributors and their institutes, the type, format, and identification number of the deliverables associated with each WP, and their status in October 1997 and in March 1998, when the TREND-3 project was terminated.

### 1.1 Improvements of UNIRAD

The UNIRAD software package is used by ESA to evaluate fluxes and fluences of energetic particles for space missions, as well as mission doses and damage equivalent fluences. A number of improvements of this package has already been made by BIRA/IASB during the TREND (1989–1992) and TREND-2 (1993–1995) studies. In the course of the present TREND-3 study, BIRA/IASB has added further features:

- new trapped particle models;
- two new modules to derive directional fluxes from omnidirectional models;
- a Fortran library of routines related to magnetic coordinates;

WP	Content	Authors	Institutes	Type of document	Format	Delivery date	Status Oct. 97	Status March 98
1.1.1.1R	Analysis of ISEE Data	EK;RF;GL	MPAe	TN1	LATEX	Jun 97	6hc delivered	Done
1.2: 1.2R	Improved MEA-3 MSSL model	DR; SS	MSSL	TN2	LATEX	March 96	2hc delivered	Done
1.3	Model unification MEA3-ISEE		MSSL	TN3			Not available	Not done
1.4	Analysis of Hipparcos			TN4			Cancelled	Cancelled
2.1: 2.1R; 2.2R	Flight Data Comparisons	DH; MK	BIRA-IASB	TN5(1;2;3)	LATEX	June 97	partly done	Done
2.2	Trapped proton anisotropy at low altitudes	MK;JL	BIRA-IASB	TN6	LATEX	April 66	6hc delivered @ ESTEC	Done
2.3R	Improved trapped proton anisotropy description	MK; DH	BIRA-IASB	TN 6(2)	LATEX	nov-97	6hc delivered @ ESTEC	Done
2.3	Secondary particle production		BIRA-IASB	TN7			Cancelled	Cancelled
4.1R	Radiation loss injection study	DR	MSSL	TN8	Mac Vers.	nov-97	Preliminary draft	Done
4.2R	METEOSAT-3 analysis: corrections & new DB	DR; SS	MSSL	TN9	LATEX	Jul 97	available; 1hc	Done
3.2R	UNIRAD Improvements and subroutine Library	DH; MK	BIRA-IASB	TN10	LATEX	nov-97	available; 1hc	Done
1.1.1.1R	ISEE DB frame binned flux frame and software description	EK;RF;GL	MPAe	DDD	LATEX	Jun 97	available; 6hc delivered	Done
1.1.1.1R	ISEE DB frame binned flux frame and software	EK;RF;GL	MPAe	SW; DB	LATEX	Jun 97	available; delivered	Done
1.2: 1.3R	Description document for users of MasterScience File : ISEE-2	AJ; GJ	MSSL	DDD	typed	Dec 96	available; 1hc	Done
1.2: 1.3R	ISEE-2 electron RB model	AJ; GJ	MSSL	SW; DB	fortran	nov-97	Not available yet	Done
1.2: 1.2R	MEASMSSL model software documents	DR; SS	MSSL	SRD; ADD; DDD	LATEX	Aug 96	available; 2hc delivered	Done
	UNIRAD v 3.0 Trapped Radiation Software	DH; MK; JL	BIRA-IASB	User manual	LATEX	nov-96	available; 2hc delivered	Done
	UNILIB subroutines documentation	MK; JM	BIRA-IASB	User manual	html	Jul 97	available	Done
	UNILIB subroutines PSS-05	MK	BIRA-IASB	URD; SRD	LATEX	Jul 97	available	Done
	UNILIB subroutines	MK	BIRA-IASB	SW	fortran	Jul 97	available; on WWW	Done
	UNIRAD package	DH; MK	BIRA-IASB	SW	fortran; IDL	nov-96	available; to customers	Done
	proton AZUR model / PAB	DH	BIRA-IASB	SW;DB	fortran; IDL	Jul 97	available	Done
	proton SAMPEX model / PSB	DH	BIRA-IASB	SW;DB	fortran; IDL	Jul 97	available	Done
	proton UARS model / PUB	MK; ME		SW;DB	fortran	Jul 97	available	Done
	electron MEA3 / EMM	AD; DR; GL	MSSL	SW;DB	fortran	nov-97	available	Done
	electron ISEE / EIM	AD; DR; GL	MSSL	SW;DB	fortran	nov-97	available	Done
	ESA-SEE1 neural Network model implementation	DH	BIRA-IASB	SW;DB	fortran	Jul 97	available	Done
	electron METEOSAT-P2 / EMsM	AD; DR; GL	MSSL	SW;DB	fortran	mars-98	not available	Done
	Radiation Environment of Astronomy and LEO Missions	All	BIRA-IASB MSSL MPAe	FR	LATEX	nov-97	not available	Done

**Figure 1.1.** WP numbers and content, initials of the contributors and their institutes, type, format, and identification number of the deliverables associated with each WP, and their status in October 1997 and in March 1998

- improvement of the functionality of the package, including added graphical capabilities.

### 1.1.1 New trapped particle models

The new trapped particle models are based on data from the AZUR, SAMPEX, UARS, CRRES, and ISEE missions (Table 2.1 contains a list of the new models). The coordinate systems and final format used for these new models are different from those of the NASA models AP-8 and AE-8 (Vette 1991b). In particular, the equatorial pitch angle  $\alpha_0$  has been used instead of  $B/B_0$  to construct the new flux maps. Consequently, a new interpolation routine (MODINT) was written for the new flux maps to replace the TRARA routine that is used with AP-8 and AE-8. The AP-8 and AE-8 models are still in UNIRAD, and their implementation has not been changed. The new trapped particle models are described in Chapters 4, 5, 6, 7, 8, and 9.

In a parallel study (ESA/ESTEC/WMA/P.O.15135), A.L. Vampola (1996) has developed a new trapped electron model from the CRRES/MEA data, using a neural network. The resulting model, called ESA-SEE1, is meant to be a replacement of AE-8 MIN, and has been implemented in UNIRAD in the present study. The new model is in the same format as the AE-8 model.

### 1.1.2 Directional flux modules

Another improvement of the UNIRAD package is the addition of two modules to derive directional proton fluxes from an omnidirectional model (see Sect. 1.2). The direction or field of view for which the unidirectional flux is wanted, can be specified in a frame of reference attached to the orbiting satellite.

### 1.1.3 UNILIB Library

A third enhancement of the UNIRAD software suite consists of the building of a structured, modular, user friendly, and well documented library of subroutines which provides the following functionalities:

- coordinate transformations between the most used coordinate systems;
- magnetic field line tracing, including the location of mirror points, foot points, and equatorial crossing;
- magnetic drift shell tracing;
- averaging of atmospheric parameters (densities and temperatures) over drift shells;
- evaluation of the magnetic flux for a drift shell, and the third adiabatic invariant.

The subroutines making up the library were written in Fortran. The library is available on the World Wide Web (WWW) (<http://www.magnet.oma.be/unilib/home.htm>), together with comprehensive documentation in HTML format, a set of examples, and a list of frequently asked questions. The library is described in Chapter 2 of this Final Report and in Technical Note 10.

## 1.2 Anisotropy of trapped proton fluxes

The widely used NASA AP-8 models provide omnidirectional proton fluxes for a wide range of energies over the whole region of the trapped proton belts. At low altitudes, the gyroradius of protons with energies above 50 MeV is comparable with the scale height of their flux with respect to altitude. For  $L \leq 2$ , the proton flux scale height is determined by the thermospheric density scale height, which varies between 50 and 100 km depending on the level of solar activity. The resulting steep proton flux gradient causes an asymmetry in the flux registered by spacecraft, both in pitch angle and in azimuth. The azimuthal asymmetry is traditionally called the East-West asymmetry. Physical models of the East-West asymmetry presented in the literature are reviewed in Technical Note 6 and in Chapter 3 of this Final Report.

### 1.2.1 Conversion of omnidirectional to unidirectional fluxes

The most commonly used model of the proton flux asymmetry has been upgraded and implemented in UNIRAD, in the form of two modules: ANISO and ANISOPOS.

Both modules use an existing model of the azimuthal asymmetry, and offer a choice of two models of the pitch angle distribution. From the omnidirectional flux obtained with the TREP module, they derive the unidirectional proton flux for a set of directions specified by the user in a reference frame attached to an orbiting, non-spinning satellite (ANISO) or for a user defined point in space (ANISOPOS). ANISO Also provides the unidirectional fluence over a spacecraft orbit.

The implementation of these new modules are described in Technical Note 6 and in Chapter 3 of this Final Report.

### 1.2.2 Generalised anisotropy model

In Part 2 of Technical Note 6, a new method is presented to describe the azimuthal asymmetry of the low altitude trapped proton flux. Instead of deriving unidirectional fluxes from given omnidirectional fluxes, this approach starts out from the new unidirectional flux models developed in this study (see Sects. 1.3–1.5). The new method uses a natural coordinate system attached to the magnetic field distribution to provide the full angular dependence of the trapped proton flux. As it is constructed from unidirectional flux maps, the influence of the atmosphere on the flux distribution is implicitly taken into account. The new method has been shown to be more consistent than the methods reviewed in Part 1 of Technical Note 6.

### 1.3 AZUR/EI-88 Data base and radiation belt model

The AZUR satellite which operated in a low Earth orbit for six months in 1969 and 1970, had on board two energetic particle telescopes, one orientated perpendicular to the magnetic field, and one at an angle of  $45^\circ$  with the magnetic field vector. These detectors measured proton fluxes in six energy channels ranging from 1.5 to 104 MeV. About three months of data have been archived at NSSDC

A copy of the data set was obtained from NSSDC and installed at BIRA/IASB. The count rates have been corrected for the telescope opening angle with the method described in Appendix A. The corrected fluxes were binned into an  $(E, L, \alpha_0)$  map, which was implemented in UNIRAD. The new flux map (called PAB97) was compared to AP-8 MAX, from which it appears that AP-8 MAX overestimates the low energy proton flux for  $L \leq 2$ . The instrument characteristics, the processing of the data, and the building of the new model are summarised in Chapter 4 of this Final Report and described in detail in Technical Note 5.

### 1.4 SAMPEX/PET Data base and radiation belt model

The SAMPEX spacecraft was launched in 1992 into a low Earth orbit and is still operational. Its instrument complement includes an energetic particle telescope, which observes (besides electrons and high  $Z$  ions) protons in the energy range 18.5–500 MeV. The proton data have been made available to BIRA/IASB by R.H. Mewaldt, CALTECH, and J.B. Blake, Aerospace Corporation, for the purpose of building a new directional trapped proton model.

The countrates for one year of data (1994–1995) have been corrected for the telescope opening angle with the method described in Appendix A. The corrected fluxes were binned into an  $(E, L, \alpha_0)$  map, which was implemented in UNIRAD. The new flux map (called PSB97) was compared to AP-8 MIN, from which it appears that AP-8 MIN overestimates the proton flux for  $L \leq 2$ . The instrument characteristics, the processing of the data, and the building of the new model are summarised in Chapter 5 of this Final Report and described in detail in Technical Note 5.

### 1.5 UARS/PEM Data base and radiation belt model

The low Earth orbiting UARS spacecraft is equipped with a series of instruments designed to study the upper atmosphere. One set of instruments consists of four energetic particle telescopes, with different orientations to the zenith direction. These instruments measure proton count rates in the energy range 0.5–150 MeV. The PEM proton data have been made available to BIRA/IASB by SwRI for the purpose of building a new directional trapped proton model.

The count rates for one year of data (1991–1992) from one of the telescopes have been corrected for the telescope opening angle with the method described in Appendix A (the detailed angular response function of the telescope has not been made available in time by the instrument

builders, so that a best guess for this function had to be used). The corrected fluxes were binned into an  $(E, L, \alpha_0)$  map, which was implemented in UNIRAD. The new flux map (called PUB97) was compared to AP-8 MAX, from which significant differences are evident, especially in the energy range 70–100 MeV (the data should however, be re-examined when the actual angular response function of the instruments becomes available from the instrument builders). The instrument characteristics, the processing of the data, and the building of the new model are summarised in Chapter 6 of this Final Report and described in detail in Technical Note 5.

## 1.6 Comparisons of the new trapped proton models

In Chapter 7, we intercompare the flux maps obtained from the AZUR, SAMPEX and UARS data. The AP-8 directional fluxes are added to the comparisons to put the results into perspective. The usage of the models derived from the new flux maps, i.e. their implementation in TREP, is described in Technical Note 10 and in Chapter 2 of this Final Report.

As the new trapped proton models are based on data from low altitude satellites, their use is limited to predictions for low altitude missions. The new models, as well as the AP-8 models, have been applied to a typical MIR or Space Station orbit. The model limitations have been demonstrated on a GTO orbit. All model calculations were made with the UNIRAD programme suite.

## 1.7 ISEE/WAPS Data base and radiation belt model

The ISEE 1&2 electron measurements were made with the WIM instruments, which are described in detail in Technical Note 1, and briefly in Chapter 8 of this Final Report. The data from these instruments have been retrieved and stored in a new data base. The magnetic field components measured during the ISEE missions (Russell 1987) have been included in the data base, as well as the model magnetic field components obtained with the BLXTRA software. The calculated direction of the magnetic field was used to determine the pitch angles for the individual flux measurements of ISEE 2. A quality flag was added to the data base for each data frame, indicating the relative difference between the observed and calculated magnetic field intensity. The comparison of measured and model magnetic field components is illustrated in a series of plots and histograms in Technical Note 1.

The electron fluxes have been binned in  $(E, L, \alpha_0)$  coordinates to produce a new trapped electron model, in the format described in Chapter 2. The ISEE data base and electron belt model cover more than ten years of data, nearly one solar cycle.



## 1.8 CRRES/MEA Data base and radiation belt model

The CRRES/MEA electron data set has been described and analysed in the TREND-2 study. It appeared, for a number of reasons, that the data had to be re-analysed after applying an additional correction to depressed count rates in the inner radiation belt caused by instrument saturation. At the same time, the time resolution of the data base was doubled to increase the equatorial pitch angle resolution and to expand the data coverage.

The new MEA data base is thus an improvement over the data base produced in TREND-2. The radiation belt model based on the new data base is also significantly improved. With the new data base, different time lag correlation analysis has been performed. These analyses showed that a time delay of about 1.5 days is observed between the increases of the fluxes at 500 keV and those of the 150 keV electrons. The comparison of energies 970 keV and 150 keV gives a longer time lag of 3 days at  $L=4.0-4.5$ . For 1470 keV and 150 keV the delay is almost 5 days. These results are confirmed by observations from other missions and are in agreement with the predictions of the recirculation model. Interesting correlations have also been found in the pitch angle distributions of the electrons at  $L > 5$ . It was also noted that there is good agreement between the position and height of the peak between the MEA data and the CRRES/HEEF results presented by Brautigam et al. (1992).

The updated MEA model, called ECM97, is organised in  $(E, L, \alpha_0)$  coordinates which have been proven to best organise the data. The standard deviation of the flux in the bins has been calculated and plotted. The new data base has a lower standard deviation than the TREND-2 data base throughout the outer radiation belt, and across almost all of the inner belt. However, standard deviations remain high in the slot region and in the loss cone. This is not unexpected since these regions have low fluxes and are highly variable.

The new electron belt model has been incorporated in the UNIRAD software package. It has been compared to the AE-8 model, details on which can be found in Technical Note 2 and in Chapter 9.

## 1.9 Radiation losses and particle injection studies

The equatorial pitch angle distributions of radiation belt electrons obtained from the data of the CRRES/MEA instrument are solutions of a time dependent Fokker-Planck equation which has been solved first by Roberts (1969), and extended by the MSSL team as part of this study.

For equatorial pitch angles within the loss cone, the solution can be decomposed in a series of normal modes characterised by decay time constants. The normal mode corresponding to the longest time constant can be expressed in terms of the zero order Bessel function of the first kind. The MSSL team has used the CRRES/MEA averaged pitch angle distributions at different energies, at different  $L$  values, and for two different geomagnetic activity levels, to fit the free parameters of the lowest order normal mode solution. This resulted in analytical fits of the observed pitch angle distribution for pitch angles between  $90^\circ$  and the  $L$  dependent loss cone angle. These fits are found to be more suited than the commonly used  $\sin^n \alpha$  functions.

The free fit parameters are the flux intensity  $j(\mu_0 = 0)$  at pitch angle  $90^\circ$ , and  $\mu_{sc}$ , the cosine of the scattering angle characterizing the slope of the pitch angle distribution for  $\mu_0 = \cos \alpha_0$  increasing monotonically from 0 to  $\cos \alpha_{0c}$ , where  $\alpha_{0c}$  is the atmospheric loss cone angle. The value of  $\mu_{sc}$  is determined experimentally from the ratio of the averaged measured flux  $j(\mu_0 = 0)$  at  $90^\circ$  pitch angle to the averaged measured flux  $j(\mu_{0c})$  at the edge of the loss cone. The fitted values for  $j(\mu_0 = 0)$  and of  $\mu_{sc}$  depend on  $L$  as well as on the energy of the trapped electrons. This is a first step in the process of searching parametrised (analytical) models for the equatorial pitch angle distribution as a function of  $L$  and  $E$ .

The same fitting procedure has been used by the MSSL team to fit the pitch angle distribution inside the loss cone. In this case, the lowest normal mode solution of the Fokker-Planck equation is the alternate Bessel function  $I_0(x)$  which has the properties that it is equal to 1 at  $x = 0$  and increases monotonically as  $x$  increases. Using  $j(\mu_0 = 1)$ , the average flux intensity measured at zero pitch angle, and  $j(\mu_{0c})$ , the flux at the edge of the loss cone, the two free parameters  $j(\mu_0 = 1)$  and  $\alpha_{sc}$ , the mean scattering angle, can be determined. These parameters depend on  $L$  and  $E$ .

The electron precipitation flux integrated over the loss cone can be calculated once the two fit parameters are known. In this way, the MSSL team has been able to infer the characteristic decay times of electrons of different energies for different values of  $L$ , and for different values of the geomagnetic activity index  $K_p$ . The calculated decay times range from 10 seconds to 3 hours, with the smallest values for the lowest  $K_p$  range and smaller  $L$  values. These decay times are much smaller than those which are determined from direct measurements of the decay times which are normally in the range of 5 to 10 days (McIlwain 1996). The probable reasons for this discrepancy is that in our study the flux in the loss cone is overestimated by the measurements of the MEA detector.

The details of this study are given in Technical Note 8. A summary is presented in Chapter 10 of this Final Report.

## 1.10 Meteosat/SEM-2 Data base

A comprehensive study of the magnetospheric electron flux (40–300 keV) at geosynchronous orbit was performed during the TREND-2 study, based on observations made by the Space Environment Monitor (SEM-2) onboard Meteosat.

Since the completion of the TREND-2 study, a number of problems have been identified with respect to the Meteosat/SEM onboard data and postprocessing. These problems became apparent in the unnatural clustering of the polar-azimuthal data around certain preferred flux values, and in regular spikes seen in some elements of the polar arrays.

During the present study, the SEM-2 data set was re-examined with the aim of producing a new data base. The comparison of the old and new data bases is presented in Technical Note 9 and in Chapter 11 of this Final Report.

Although the various errors could have significant effects on individual data points, most of the TREND-2 results rely on statistical analyses where the effect of including a few erroneous

points in a large sample would have been small. The sample plots of ‘before’ and ‘after’ data presented in Technical Note 9 show that the statistical models produced in the TREND-2 study are not significantly modified when the error corrections are applied. Therefore, the conclusions drawn from the old data base concerning local time dependence and overall flux range have not been changed significantly. This conclusion holds for all the local time dependence models, for the Fourier and wavelet analyses, for the correlation analysis showing the time lags between different energy flux variations, and the models of flux probability versus mission duration.

The text of a paper by Rodgers (1991), based on the old Meteosat/SEM data base, has been updated for the new data base. The new text, which covers 18 months of Meteosat-3 anomalies and SEM-2 data, is reproduced in Technical Note 9.



# Chapter 2

## UNIRAD Improvements and subroutine library

In this chapter we describe a series of improvements to the UNIRAD package performed by the TREND team at BIRA/IASB. Two types of improvements have been made:

1. the addition of new flux maps from five satellite data sets: AZUR/EI-88, SAMPEX/PET, UARS/PEM, CRRES/MEA, and ISEE/WAPS, and the addition of the ESA-SEE1, CRRESPRO, and CRRESELE models;
2. the development of a library of subroutines.

### 2.1 Implementation of new trapped particle models in UNIRAD

The first series of improvements of UNIRAD has been the implementation of new radiation belt models that have been developed during this study (detailed descriptions of the development of the new models can be found in Technical Notes 1, 2, and 5 of this study). In addition, the ESA-SEE1 model developed by A. Vampola (1996) on the basis of a neural network study of the CRRES/MEA data, has been implemented. Finally, the CRRESPRO (Meffert & Gussenhoven 1994) and CRRESELE (Brautigam & Bell 1995) models, developed by Phillips Laboratory Geophysics Directorate (PLGD), have also been adapted to and integrated in UNIRAD.

Table 2.1 contains a list of the new radiation belt models, the data sets they were constructed from, and the Technical Note number in which they are described in detail.

#### 2.1.1 The UNIRAD program suite

The UNIRAD suite of programs provides information about the radiation environment in an arbitrary Earth orbit, predicting satellite exposures to particle fluxes, the resulting radiation dose,

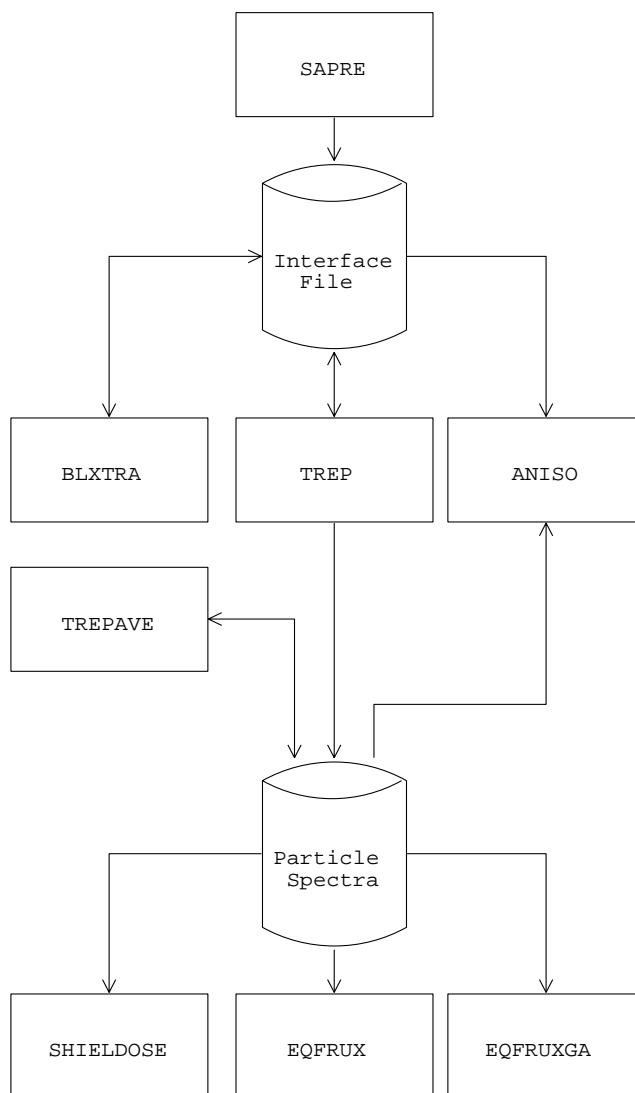


**Figure 2.1.** Flow diagram of UNIRAD

and the resulting damage-equivalent fluences for solar cell degradation calculations (Heynderickx et al. 1996d).

From the orbit parameters, the system will generate a detailed trajectory, magnetic coordinates, integral and differential proton and electron fluences, doses for three shield geometries in four detector materials, and solar cell degradation information, in both printed and graphical form.

The UNIRAD package consists of the following programs:

- **SAPRE**: orbit generator which produces a data file used by the next two programs in the package;

- BLXTRA: calculates the geomagnetic coordinates  $(B, L)$  from the geographic coordinates generated by SAPRE;
- TREP: determines the radiation flux for the geographic coordinates generated by SAPRE from the NASA trapped radiation models AP-8 and AE-8 and determines the solar proton flux over the mission. It produces a data file with the energy spectra of trapped protons and electrons and of solar protons;
- TREPPOS: calculates the trapped radiation flux for pairs of  $(B, L)$  or  $(B/B_0, L)$  coordinates interactively input by the user. It produces a data file with the energy spectra of trapped protons and electrons;
- TREPAVE: averages the spectra generated by TREP or TREPPOS for different orbits;
- ANISO: transforms the trapped proton omnidirectional integral flux produced by TREP into unidirectional integral and differential fluxes, taking into account pitch angle and azimuthal dependence. The user can define a set of look directions with respect to a satellite reference frame. The resulting fluxes are averaged over the orbit.
- ANISOPOS: provides the angular distribution (i.e. pitch angle and azimuthal dependence) of the unidirectional integral or differential flux at a given geographic location.
- SHIELDOSE: reads the energy spectra resulting from TREP, TREPAVE, or TREPPOS and converts them to radiation dose-depth curves for different detector materials and simple shielding geometries;
- EQFRUX: determines 1 MeV electron damage equivalent fluences from the TREP spectra to evaluate degradation of Si solar cells;
- EQFRUXGA: idem as EQFRUX, but for GaAs solar cells;
- UNIRAD.PRO: a set of IDL routines to produce graphical output.

The flow diagram of UNIRAD is shown in Fig. 2.1.

### 2.1.2 The TREP program

TREP Calculates orbital radiation environment fluxes for a spacecraft trajectory generated by SAPRE. It estimates fluxes of trapped particles in function of  $(B, L)$  coordinates, and computes solar proton event probabilities to estimate solar proton fluences. The output consists of:

1. the time dependent fluxes of trapped protons, solar protons, and trapped electrons;
2. trajectory-averaged spectra for trapped protons and electrons;
3. solar flare fluence spectra, taking into account geomagnetic shielding.

TREP accesses the NASA trapped particle models AP-8 (Sawyer & Vette 1976) and AE-8 (Vette 1991a) at each orbital point contained in the common interface file produced by SAPRE. The NASA trapped radiation models AP-8 and AE-8 are distributed as tables of omnidirectional fluxes in function of particle energy  $E$  and  $(B/B_0, L)$ , where

$$B_0 = \frac{0.311653}{L^3}. \quad (2.1)$$

The NASA models AP-8 and AE-8 are static models built with data obtained in the sixties and seventies. There are two sets of models: AP-8 MAX and AE-8 MAX for solar maximum conditions, and AP-8 MIN and AE-8 MIN for solar minimum conditions. Since these models were built with specific magnetic field models, the same magnetic field models should be used to calculate the  $(B/B_0, L)$  values that serve as input to AP-8 and AE-8. The appropriate magnetic field models are: Jensen & Cain (1962) for AE-8 MIN, AP-8 MIN, and AE-8 MAX, and GSFC 12/66 (Cain et al. 1967) updated to epoch 1970 for AP-8 MAX (Heynderickx et al. 1996ab). Two coordinate pairs  $(B, L)$  are written to the common interface file `PROJECT.INT`, corresponding to the field models used with the proton and electron model, respectively.

The position of the SAA in the old magnetic field models to be used with AP-8 and AE-8 is different from its actual position due to the secular variation on the geomagnetic field (Fraser-Smith 1987). This has important effects on the prediction of trapped particle fluxes for low altitude orbits. Therefore, a correction has been built into TREP: when the NAMELIST parameter SAAROT is set to 1 (the default value), a correction term  $\Delta\phi(t)$  is added to the geodetic longitude before the calculation of  $(B, L)$  (the actual value of the longitude on the interface file is not changed):

$$\Delta\phi(t) = 0.3^\circ (t - \text{EPOCH}). \quad (2.2)$$

where  $t$  is the orbit epoch as written in the header of the common interface, and EPOCH is the epoch of the geomagnetic field model. This correction is also made for the new trapped particle models. The new models were constructed with the IGRF magnetic field model for the epoch of the observations and external magnetic field models for the models that extend beyond the inner radiation belt.

### 2.1.3 New trapped particle models

Several new proton and electron models have been developed during the TREND-3 study. They are listed in Table 2.1, with their epoch and number of submodels. The models are described in the references given in Table 2.1. The ESA-SEE1 model developed by Vampola (1996) has been implemented as well as the CRRESPRO (Meffert & Gussenhoven 1994) and CRRESELE (Brautigam & Bell 1995) models developed by Phillips Laboratory.

The naming convention for the new models is as follows:

1. the first character of the name indicates whether it is a proton (P) or an electron (E) model;



**Table 2.1.** List of the new flux models implemented in TREP.  $N$  Is the number of submodels.

Name	Particle	Satellite	Instrument	Epoch	$N$	Reference
PAB97	Protons	AZUR	EI-88	1970	1	Technical Note 5
PSB97	Protons	SAMPEX	PET	1995	1	Technical Note 5
PUB97	Protons	UARS	PEM	1992	1	Technical Note 5
PCP94	Protons	CRRES	PROTEL	1991	2	Meffert & Gussenhoven (1994)
ECS96	Electrons	CRRES	MEA	1991	1	Vampola (1996)
ECM97	Electrons	CRRES	MEA	1991	5	Technical Note 2
EIM97	Electrons	ISEE	WAPS	1979	5	Technical Note 1
ECP95	Electrons	CRRES	HEEF	1991	8	Brautigam & Bell (1995)

2. the second character identifies the spacecraft which collected the data ('A' stands for AZUR, 'S' for SAMPEX, 'U' for UARS, 'C' for CRRES, and 'I' for ISEE);
3. the third character identifies the institute where the model was developed ('B' stands for BIRA/IASB, 'M' for MSSL or MPA, 'P' for PLGD, and 'S' for SEE);
4. the last two characters form the year in which the model was developed (not the epoch of the model!).

#### 2.1.4 The ESA-SEE1 model

The ESA-SEE1 model developed by Vampola (1996) is meant to be a replacement of AE-8 MIN, and therefore has the same structure as the NASA model. The model data file `ESA-SEE1.DAT` provided by Vampola (1996) is not in the same `BLOCK DATA` format as the version of the NASA models used in TREP. The program `VAMPOLA.FOR` was developed to rewrite the `ESA-SEE1.DAT` file in the format used by TREP. The resulting `BLOCK DATA` file `ECS96BD.FOR` is linked to TREP, and makes use of the `TRARAP` subroutine developed by Daly & Evans (1993) to interpolate in the flux map.

#### 2.1.5 The CRRESPRO and CRRESELE models

The CRRESPRO and CRRESELE software packages developed by Phillips Laboratory determine omnidirectional energetic proton and electron fluences for user-defined orbits. The flux models used in these software packages are based on measurements made with the PROTEL (Violet et al. 1993) and HEEF (Hunerwadel et al. 1987) instruments onboard the Combined Release and Radiation Effects Satellite (CRRES), which flew from 25 July 1990 to 12 October

1991 during solar maximum. CRRES was in a geosynchronous transfer orbit with an inclination of  $18^\circ$ , a perigee of 350 km, and an apogee of 33 000 km. It traversed the radiation belts twice per orbit with a period of  $9^h 52^m$ .

Both flux models are provided in a series of binary files containing omnidirectional differential flux maps in  $(L, B/B_0)$  space. In order to implement these flux maps in TREP, we first converted the binary files to ASCII format. Then, new flux map files were created for omnidirectional integral fluxes, which were obtained by integrating the differential fluxes in accordance with the guidelines of Meffert & Gussenhoven (1994) and Brautigam & Bell (1995). Finally, the new flux maps were converted into BLOCK DATA format using the procedure outlined in Sect. 2.1.6.

The conversion from differential flux  $j$  to integral flux  $J$  is defined as:

$$J(> E_i) = \int_{E_i}^{\infty} j(E) dE, \quad (2.3)$$

where  $E_i$  is the lower energy boundary of channel  $i$ . The integration is approximated by a summation:

$$J(> E_i) = \sum_{k=i}^N j(E_k) \Delta E_k, \quad (2.4)$$

with  $\Delta E_k$  the width of channel  $k$  and  $N$  the number of channels. The summation for channel  $i$  begins at the lower boundary of that channel and ends at the upper boundary of the highest energy channel.

### 2.1.5.1 The CRRESPRO model

**2.1.5.1.1 The PROTEL instrument** The CRRESPRO flux models are based on in situ flux measurements made by the PROton TELEscope (PROTEL) onboard CRRES. PROTEL Had two detector heads which together measured protons from 1 to 100 MeV in 24 energy steps, giving a complete spectrum every 1.024 s. The angular resolution of the detector low (high) energy head was  $\pm 10^\circ \times \pm 10^\circ$  ( $\pm 12^\circ \times \pm 17^\circ$ ). A full description of PROTEL is available in Violet et al. (1993) and Lynch et al. (1989).

The PROTEL detectors comprised detector stacks and a logic system that required single or double coincidence to verify that the proper energy particle is counted. In addition, both active and passive shielding were used around much of the detector stack. The detectors were extensively calibrated prior to launch. During calibration, it was found that energetic protons ( $> 60$  MeV) incident over a large angular angle with respect to the detector axis could degrade sufficiently in the shielding, pass through the necessary angle in the detector stack, and be counted. This contamination was found to be significant enough for very hard spectra, such as occurs for  $L$  values between 1.1 and 1.7, to require correction. A correction scheme was devised based on the assumption of an empty atmospheric loss cone (Gussenhoven et al. 1993).

One channel (15.2 MeV) had significantly lower sensitivity than the other channels and one channel was an overlap channel at 8.5 MeV. To avoid both redundancy and the appearance of

**Table 2.2.** Integration parameters (MeV) for integral omnidirectional PROTEL flux [from Meffert & Gussenhoven (1994)]

Channel	$E_{lo}$	$E_{mid}$	$E_{hi}$	$\Delta E$
1	1.1	1.5	1.9	0.8
2	1.9	2.1	2.3	0.4
3	2.3	2.5	2.7	0.4
4	2.7	2.9	3.1	0.4
5	3.1	4.3	5.5	2.4
6	5.5	5.7	5.9	0.4
7	5.9	6.8	7.7	1.8
8	7.7	8.5	9.3	1.6
9	9.3	9.7	10.1	0.8
10	10.1	10.7	11.3	1.2
11	11.3	13.2	15.1	3.8
12	15.1	19.4	23.7	8.6
13	23.7	26.3	28.9	5.2
14	28.9	30.9	32.9	4.0
15	32.9	36.3	40.2	7.3
16	40.2	41.1	43.2	3.0
17	43.2	47.0	50.8	7.6
18	50.8	55.0	59.2	8.4
19	59.2	65.7	72.2	13.0
20	72.2	81.3	90.4	18.2

discontinuities in differential and integral spectra at certain  $L$  values, the 8.5 MeV and 15.2 MeV channels were not used.

**2.1.5.1.2 Proton flux models** In March 1991, a magnetic storm caused a reconfiguration of the inner magnetosphere, resulting in, among other features, the formation of a second proton belt over a certain energy range. Because of this change, two CRRES models were created. The “quiet” model uses data from July 1990 to March 1991, and the “active” model uses data from March 1991 to October 1991. Note that the terms “quiet” and “active” have no correspondence to quiet and active as determined by the index  $K_p$ . The channel characteristics of the PROTEL integral flux maps are given in Table 2.2.

The CRRES PRO models are in the form of omnidirectional differential flux maps organised in  $(E, L, B/B_0)$  coordinates. The bin widths of the  $L$  range are  $0.05 R_E$ , while for  $B/B_0$  the bin limits are chosen such that they cover approximately  $\pm 68^\circ$  magnetic latitude in a dipole field with steps of  $2^\circ$ .

The CRRES PRO models have been implemented in UNIRAD as one model, called PCP94,

**Table 2.3.** Channel energies (MeV) for CRRES/HEEF [from Brautigam & Bell (1995)]

Channel	$E_{lo}$	$E_{mid}$	$E_{hi}$	$\Delta E$
0	0.50	0.65	0.80	0.30
0.a	0.80	0.825	0.85	0.05
1	0.85	0.95	1.05	0.20
1.a	1.05	1.15	1.25	0.20
2	1.25	1.60	1.70	0.45
3	1.70	2.00	2.10	0.40
4	2.10	2.35	2.50	0.40
5	2.50	2.75	2.90	0.40
6	2.90	3.15	3.30	0.40
7	3.30	3.75	4.10	0.80
8	4.10	4.55	4.95	0.85
9	4.95	5.75	6.60	1.65

containing 2 submodels.

### 2.1.5.2 The CRRESELE model

**2.1.5.2.1 The HEEF instrument** The flux models used by CRRESELE are based on in situ flux measurements made by the High Energy Electron Fluxmeter (HEEF) onboard CRRES (Brautigam & Bell 1995). HEEF Was designed to measure the flux of 1–10 MeV electrons in 10 differential number flux channels and to return a complete spectrum every 0.512 s. The telescope consists of a well collimated stack of three particle detection elements, the top two being solid state detectors, and the third a bismuth germanate (BGO) crystal. A passive beryllium shield is placed at the entrance of the telescope to stop lower energy ( $<0.3$  MeV) electrons. A plastic scintillator surrounds the BGO crystal to veto particles that penetrate it from the sides and would otherwise trigger accidental counts.

As the result of extensive post-launch analysis of the actual flight and test data of the HEEF replica, the spectrum energies were revised. The lowest energy differential channel was omitted because of the large uncertainty in its geometric factor, and the highest energy differential channel was omitted because its counting efficiency was so low that it rendered little statistically meaningful data for modelling purposes. The final set of energy channels is listed in Table 2.3.

To facilitate the determination of the integral flux, the fictitious channels 0.a and 1.a have been introduced to fill the gaps in the energy spectrum between channels 0 and 1 and between channels 1 and 2, respectively. The omnidirectional flux at these two fictitious channels is determined by interpolating between the adjacent channels in each case. This procedure is followed to provide a stepwise continuous spectrum, which can then be summed over a discrete set of energies to give the integral omnidirectional flux.

**Table 2.4.** Summary of CRRES  $A_{p15}$  model separation and statistics [from Brautigam & Bell (1995)]

Model Nr.	$A_{p15}$ Range	Average $A_{p15}$	Days/model	% of total
0	5.0–7.5	6.8	13	3.2
1	7.5–10.0	8.7	83	20.7
2	10.0–15.0	12.5	69	17.1
3	15.0–20.0	17.1	82	20.6
4	20.0–25.0	22.4	72	17.7
5	25.0–55.0	35.7	83	20.7

**2.1.5.2.2 Electron flux models** The potential problem of energetic proton contamination of HEEF in the inner zone has not been addressed in the construction of the CRRESELE model. The slot region, populated by the temporary third electron belt during the second half of the CRRES mission, would require special treatment in comparison to the outer belt. Therefore, the CRRESELE models are developed for the outer zone electron belts only, and are limited to the interval  $2.5 \leq L \leq 6.8$ .

The CRRESELE models are in the form of omnidirectional differential flux maps organised in  $(E, L, B/B_0)$  coordinates. The bin widths of the  $L$  range are  $0.05 R_E$ , while for  $B/B_0$  the bin limits are chosen such that they cover approximately  $\pm 68^\circ$  magnetic latitude in a dipole field with steps of  $2^\circ$ .

Eight models are available. Six of these models are parametrized by geomagnetic activity, i.e. in terms of the  $A_{p15}$  index which is defined as the average of the preceding 15 daily values of  $A_p$ . Six ranges of  $A_{p15}$  were defined, for each of which a full electron model was constructed. The statistics of the six  $A_{p15}$  ranges are given in Table 2.4. Two additional models, independent of  $A_{p15}$ , are available as well. For model 6, the entire data base was averaged, providing a mission average model. Model 7 was constructed from the maximum flux found at each  $L$  bin of the daily averaged data base.

The CRRESELE models have been implemented in UNIRAD as one model, called ECP95, containing 8 submodels.

## 2.1.6 Structure of the model data files

For all the models listed in Table 2.1, except the ESA-SEE1 model, a new model format and a set of interpolation routines were developed. The flux maps are stored in data files, one for each model, which are transformed into BLOCK DATA files by the program MODTOBD.FOR. The format of the data files is common to all models. The number of submodels in Table 2.1 refers to the number of flux maps in a model corresponding to, for instance, different geomagnetic conditions. For each submodel, the internal and external magnetic field parameters have to be specified.

The flux maps are given on a three-dimensional rectangular grid in  $E$ ,  $L$ , and a third coordinate  $x$  which is either  $B$ ,  $B/B_0$ , or the equatorial pitch angle  $\alpha_0$ . The third coordinate is identified in the third record of the flux map data file as 1, 2, or 3, corresponding to the above coordinates. The directionality of the flux map is given by a flag: 0 for unidirectional, 1 for omnidirectional. The fluxes are considered to be integral fluxes.

### 2.1.7 Interpolation in flux maps

The interpolation in the flux maps is performed tri-linearly in  $(E, L, x)$  space over the parallelepiped containing the point for which the flux  $f(E, L, x)$  is required. The vertices of this parallelepiped are  $(E_1, L_1, x_1)$ ,  $(E_1, L_1, x_2)$ ,  $(E_1, L_2, x_1)$ ,  $(E_1, L_2, x_2)$ ,  $(E_2, L_1, x_1)$ ,  $(E_2, L_1, x_2)$ ,  $(E_2, L_2, x_1)$ , and  $(E_2, L_2, x_2)$ , where  $E \in [E_1, E_2]$ ,  $L \in [L_1, L_2]$ , and  $x \in [x_1, x_2]$ . The interpolation function has the form:

$$\begin{aligned} f(E, L, x) = & (1-p)(1-q)(1-r)f(E_1, L_1, x_1) + (1-p)(1-q)r f(E_1, L_1, x_2) \\ & + (1-p)q(1-r)f(E_1, L_2, x_1) + (1-p)qr f(E_1, L_2, x_2) \\ & + p(1-q)(1-r)f(E_2, L_1, x_1) + p(1-q)r f(E_2, L_1, x_2) \\ & + pq(1-r)f(E_2, L_2, x_1) + pqr f(E_2, L_2, x_2), \end{aligned} \quad (2.5)$$

with

$$\left. \begin{aligned} p &= \frac{E - E_1}{E_2 - E_1} \\ q &= \frac{L - L_1}{L_2 - L_1} \\ r &= \frac{x - x_1}{x_2 - x_1} \end{aligned} \right\}. \quad (2.6)$$

Interpolation of the flux maps between grid values is handled by the subroutine MODINT, which is contained in the program file MODINT.FOR. This subroutine takes as input the number of grid bins in each dimension, the grid limits and reference values, a vector containing the flux values over the grid, and a vector of energies (and its length) plus a pair of  $L$  and third coordinate for which the flux is required. The subroutine returns a vector of fluxes of the same size as the vector of input energies.

The flux maps can cover regions where no measurements were available when building the map. The corresponding value in these bins has to be set to  $-1$ . The interpolation program MODINT uses the value  $-1$  as a flag: if a value of  $-1$  is encountered during interpolation, the procedure is stopped and a flux value of  $-1$  is returned. In turn, TREP interprets a flux value of  $-1$  as a sign that the geographic point in question is outside the region covered by the model map, and will issue a warning. The same warning is issued when the geographic point or the energy is completely outside of the model map.

MODINT Can be called directly by TREP, or by the routine that converts unidirectional to omnidirectional fluxes.

### 2.1.8 Conversion to omnidirectional fluxes

The omnidirectional flux  $J$  at a given location  $P$  and energy  $E$  can be expressed in terms of the unidirectional flux  $j$  as:

$$J(E) = \int_0^{2\pi} \int_0^\pi j[E, L(\alpha), \alpha, \phi] \sin \alpha d\alpha d\phi \quad (2.7)$$

(Roederer, 1970). Using the relation between the local pitch angle  $\alpha$ , the local magnetic field strength  $B$ , and the equatorial pitch angle  $\alpha_0$ :

$$\frac{\sin^2 \alpha}{B} = \frac{\sin^2 \alpha_0}{B_0}, \quad (2.8)$$

and assuming that the dependence of the flux on  $\alpha$  is symmetric around  $\pi/2$ , Eq. (2.7) can be rewritten as:

$$J(E) = 2 \frac{B}{B_0} \int_0^{2\pi} \int_{\mu_0}^1 \frac{j_0[E, L(\alpha_0), \alpha_0, \phi] \cos \alpha_0}{\sqrt{1 - \frac{B}{B_0} (1 - \cos^2 \alpha_0)}} d \cos \alpha_0 d\phi, \quad (2.9)$$

with

$$\mu_0 = \sqrt{1 - \frac{B_0}{B}}. \quad (2.10)$$

The subroutine UNIOMN, contained in MODINT.FOR, uses Eq. (2.9) to derive omnidirectional fluxes from a unidirectional flux map parametrised in terms of  $E$ ,  $L$ , and  $\alpha_0$ , and which does not depend on  $\phi$  (the azimuthal dependence of the flux will be implemented later). The integration is carried out using the trapezoid method, so that

$$\begin{aligned} J(E) = & 2\pi \frac{B}{B_0} \sum_{i=1}^n \left\{ j_{0,i} \left[ 1 - \frac{B}{B_0} (1 - \cos^2 \alpha_{0,i}) \right]^{-1/2} + j_{0,i+1} \left[ 1 - \frac{B}{B_0} (1 - \cos^2 \alpha_{0,i+1}) \right]^{-1/2} \right\} \\ & \times (\cos \alpha_{0,i+1} - \cos \alpha_{0,i}) \\ & + 2\pi \frac{B}{B_0} \left\{ j_{0,n} \left[ 1 - \frac{B}{B_0} (1 - \cos^2 \alpha_{0,n}) \right]^{-1/2} + j_{0,n+1} \left[ 1 - \frac{B}{B_0} (1 - \cos^2 \alpha_0) \right]^{-1/2} \right\} \\ & \times (\cos \alpha_0 - \cos \alpha_{0,n}), \end{aligned} \quad (2.11)$$

where  $j_{0,i}$  represents the flux map entry  $j_0[E, L(\alpha_{0,i}), \alpha_{0,i}]$ , and  $n$  is the index of the  $\alpha_0$  grid value preceding  $\alpha_0$ .

The integration in Eq. (2.9) can be rewritten in terms of  $B$  or  $B_0$  to accomodate the flux maps organised in these coordinates. This extension to UNIOMN will be added later.

**Table 2.5.** New or modified NAMELIST parameters for TREP

Parameter	Data Type	Default	Function
TRPMOD	INTEGER	1	Proton model selection: 1: AP-8 2: PAB97 3: PSB97 4: PUB97 5: PCP94
TREMOD	INTEGER	1	Electron model selection: 1: AE-8 2: ECS96 3: LANL 4: ECM97 5: EIM97 6: ECP95
IMODP	INTEGER	1	Index of proton submodel
IMODE	INTEGER	1	Index of electron submodel
OMNIP	INTEGER	1	Flag for conversion to omnidirectional proton fluxes
OMNIE	INTEGER	1	Flag for conversion to omnidirectional electron fluxes

### 2.1.9 Modifications to TREP

In order to add the new flux models, the TREP program had to be modified in several ways:

1. addition of models in the same format as the NASA models AP-8 and AE-8;
2. addition of models in a different format, including the development of new interpolation routines;
3. addition of a routine for converting unidirectional fluxes to omnidirectional fluxes;
4. modification and extension of the TREP NAMELIST parameters to accomodate the preceding modifications.

The addition of new models has been described in Sects. 2.1.6 and 2.1.7, and flux conversion in Sect. 2.1.8, respectively. The NAMELIST parameters added or modified are listed in Table 2.5. The new version of TREP has been used to produce the spectra used in Part IV of Technical Note 5 and in Chapter 7 of this Final Report.



## 2.2 The UNIRAD library

The development of the UNIRAD library was the task of WP 3.2R of the TREND-3 project. The main objectives of the WP are to improve the software used to build radiation belt models and to predict the radiation experienced by spacecraft in orbit around the Earth. To this effect, other coordinates than  $(B, L)$  have been investigated to organise trapped particle fluxes, especially at low altitude. The UNIRAD library provides tools to evaluate these new coordinates, which are related to interactions of particles with the environment, such as the atmospheric constituents encountered or the energy loss experienced by the trapped particles. The software library therefore implements tools to compute the geomagnetic field, to trace magnetic field lines and drift shells, to determine the minimum altitude of mirror points and to evaluate physical quantities averaged along a drift trajectory.

### 2.2.1 Portability

The library has been developed on a DEC/AXP platform under the operating system OpenVMS. The modules of the library have been written conformly to standard FORTRAN 77, extended by the use of STRUCTURE and RECORD statements. These statements greatly increase the user friendliness of the library and are generally supported by all FORTRAN 77 compilers.

Machine specific code has been avoided so that the library can be ported on VAX, AXP, HP, Sun, and PC platforms, under different operating systems. Under the operating systems VAX/VMS and OpenVMS/AXP, the library is callable directly from IDL routines, to allow graphical representation and data analysis.

### 2.2.2 Sources

The UNIRAD library has been partially derived from the UNIRAD software [programme BLXTRA, see Heynderickx et al. (1996d)] and from the code developed by Hassitt (1965) at the University of California (San Diego) provided to BIRA/IASB by C.E. McIlwain. The UNIRAD library subroutines which evaluate the geomagnetic field intensity and McIlwain's (1961) parameter  $L$  are those developed earlier at BIRA/IASB for BLXTRA under the first TREND project.

The Hassitt code calculates averages of the atmospheric density over a drift shell. In this code, the Jensen and Cain (1962) magnetic field model and the atmosphere model of Anderson & Francis (1964) are used, respectively, to trace the drift shell and to evaluate the atmospheric number densities. Hassitt (1965) deduced the averaged atmospheric density over a drift shell by weighting the atmospheric number densities with proton cross sections for charge exchange, ionisation and excitation. The Hassitt code has been extended during the course of the TREND-2 project to incorporate additional magnetic field models and the latest atmosphere and ionosphere models (Heynderickx et al. 1995, 1996c). M. Kruglanski, who was responsible for WP 3.2R, has developed a new version of this drift shell program which differs significantly

from that of Hassitt. Both codes have been tested for a number of case studies and give comparable results.

### 2.2.3 Functionality of the library

A main goal of the UNIRAD library is to evaluate the effects of the interaction of trapped protons with the atmosphere. These effects are usually described through effective scale heights. Different scale heights are obtained from the averages of different physical quantities over one complete longitudinal drift period of the trapped particles. The different physical quantities are, for instance:

- the amount of atmospheric material encountered by the particle;
- the number of charge-exchange collisions;
- the number of ionisation or excitation interactions;
- the energy lost by the trapped particle;
- the pitch angle deviation experienced by the trapped particle.

These quantities are generally expressed per unit of time.

Another key goal of the library is to provide subroutines to compute specific coordinates for the geomagnetically trapped particles, for instance:

- the magnetic field intensity  $B_m$  at the mirror points;
- the equatorial pitch angle  $\alpha_0$ ;
- the McIlwain (1961) parameter  $L$ ;
- the second and third adiabatic invariants  $J$  and  $\Phi$  ;
- the intersections of the magnetic field line with the Earth's surface.

### 2.2.4 Conventions used in the UNIRAD library

#### 2.2.4.1 Units

The SI units are used in the UNIRAD library except for the quantities listed in Table 2.6. Angles are given in degrees.

**Table 2.6.** Physical units used in the UNIRAD library

Quantity	Unit	Relation to SI
energy	MeV	$1.602177 \times 10^{-13} \text{ J}$
date	day	86400 s
dipole geomagnetic moment	Gauss $R_E^3$	$2.58621 \times 10^{16} \text{ T m}^3$
distance	km	$10^3 \text{ m}$
Earth radius	$R_E$	6,371,200 m
mass	amu	$1.66054 \times 10^{-27} \text{ kg}$
mass thickness	$\text{g cm}^{-2}$	$10 \text{ kg m}^{-2}$
mass density	$\text{g cm}^{-3}$	$10^3 \text{ kg m}^{-3}$
number density	$\text{cm}^{-3}$	$10^6 \text{ m}^{-3}$
magnetic flux density	Gauss	$10^{-4} \text{ T}$
cross section	mbarn	$10^{-31} \text{ m}^2$

### 2.2.4.2 Coordinate systems

Geographic positions are generally given in the Geocentric Equatorial (GEO) coordinate system in the form of longitude, colatitude and radial distance from the centre of the Earth. The vector attached to a geographic position is given by its spherical components (e.g.  $V_\rho$ ,  $V_\theta$ ,  $V_\phi$ , where the subscripts  $\rho$ ,  $\theta$  and  $\phi$  indicate the radial distance, the colatitude and the longitude in GEO, respectively). The spherical components of a vector are related to its cartesian components by the transformation

$$\begin{bmatrix} V_\rho \\ V_\theta \\ V_\phi \end{bmatrix} = \begin{bmatrix} \sin \theta \cos \phi & \sin \theta \sin \phi & \cos \theta \\ \cos \theta \cos \phi & \cos \theta \sin \phi & -\sin \theta \\ -\sin \phi & \cos \phi & 0 \end{bmatrix} \begin{bmatrix} V_x \\ V_y \\ V_z \end{bmatrix}. \quad (2.12)$$

One should note that the GEO spherical components and the Geocentric Inertial (GEI) spherical components of any vector are identical.

The library includes several subroutines to convert GEO coordinates to other coordinate systems, and inversely.

### 2.2.4.3 Component identifiers

Each component has a unique identifier in the UNIRAD library.

The FORTRAN COMMON BLOCK components of the library are identified by the two characters UC followed by three digits. The FORTRAN subroutine components of the library are identified by two characters, related to the functionality of the component, followed by three digits. The characters UL, UF, UD, UM, UA, and UT correspond to geomagnetic labels, field line tracing, drift shell tracing, magnetic models, atmospheric models, and general tools, respectively. Each component of the library is uniquely defined by its 3-digit code.

**Table 2.7.** URLs Of the main pages of the UNIRAD library documentation, relative to the root locator `http://www.magnet.oma.be/home/unilib/`

URL	Content
<code>home.htm</code>	Home page of the library
<code>toc.htm</code>	List of the library components
<code>faq.htm</code>	Frequently asked questions
<code>index.htm</code>	Set of links to other pages ordered by keywords
<code>structure.htm</code>	Description of the FORTRAN structures used by the library

For the variables used in the library, the first character of the identifier indicates the type of the variable. The correspondences between the first character of the identifier and the FORTRAN type of the field are: A–H, P–Y for REAL\*8; I, J, K and N for INTEGER\*4; L for CHARACTER\*( \*); M for structure record; and Z for EXTERNAL.

**2.2.4.3.1 Error trapping** When an error occurs in a subroutine of the library, the error diagnostic is returned by way of a negative integer value of the form `-dddii`. The first three digits (`ddd`) are set to the three digits of the name of the subroutine where the error occurs. The last two digits (`ii`) are used to differentiate between errors inside a same subroutine.

## 2.2.5 Library documentation

The documentation of the UNIRAD library is provided in the form of HTML pages. The documentation contains a list of Frequently Asked Questions, a list of all the components of the library, and a detailed description of each component. Some examples are provided as well. The Universal Resource Locators (URLs) of the main pages of the documentation are listed in Table 2.7.

## 2.2.6 Installation and usage

The UNIRAD library contains two items:

1. an object library file (`unilib.lib`, `unilib.olb`, or `libunilib.a`, depending on the operating system);
2. an include file (`structure.h`).

The object library file is intended to be used by the linker. It includes the object code of all the subroutines contained in the UNIRAD library. The include file contains the definition of all the structures defined in the library. The include file can be called in user source code by the

statement `INCLUDE 'STRUCTURE.H'`. Both files can be downloaded from the HTML page <http://www.magnet.oma.be/home/unilib/hreg.htm>.

The functionality of the library has to be accessed with the help of a FORTRAN programme or an IDL routine. Note that except under the operating systems VAX/VMS and OpenVMS/AXP, additional C codes have to be produced to interface the library with the IDL software.

### 2.2.6.1 Initialization

Before most of the library subroutines can be used, the different COMMON BLOCKs of the UNIRAD library have to be initialized. The following initialisation subroutines are provided inside the library :

- UT990: to initialize the different COMMON BLOCKs of the UNIRAD library;
- UM510: to select a geomagnetic field model;
- UM520: to select an external magnetic field model;
- UA610: to select an atmospheric, ionospheric and/or plasmaspheric model.

### 2.2.6.2 Main subroutines

The subroutines of the UNIRAD library can be divided into three sets:

1. the main subroutines;
2. the internal subroutines;
3. the miscellaneous subroutines.

The internal subroutines are subroutines called by other subroutines of the library and as such, are not directly accessed by the user. The main subroutines are top-level subroutines, they include:

- UL220: to evaluate  $B_m$ ,  $L$ ,  $K = I\sqrt{B_m}$  for a set of field line segments passing through a given position where  $I$  is the a line integral called the integral invariant function (McIlwain 1961);
- UD310: to trace a magnetic drift shell;
- UD320: to average physical quantities over a drift shell;
- UD330: to evaluate the third invariant;
- UF420: to trace a magnetic field line segment passing through a given position;

- UM530: to evaluate the magnetic field vector;
- UA630: to evaluate the atmospheric number and mass densities;
- UA636: to evaluate the atmospheric number or mass densities weighted by cross sections;
- UT980: to print the library error messages.

The miscellaneous subroutines are subroutines called by other subroutines of the library but that users can also use directly (e.g. UM539, UT540, UT541, UT550).

The HTML pages relative to the main subroutines are a good starting point to learn about the UNIRAD library. Another starting point to understand the philosophy of the library are the examples provided in the HTML documentation.

## **2.2.7 Models included in the library**

### **2.2.7.1 Magnetic field models**

The library includes some internal and external magnetic field models. The set of internal magnetic field models is composed of:

1. the International Geomagnetic Reference Field (IGRF) model;
2. the Jensen & Cain (1962) model;
3. the GSFC12/66 model (Cain et al., 1967);
4. a simple centred tilted dipole magnetic field.

The IGRF model is the empirical representation of the Earth's magnetic field recommended for scientific use by the International Association of Geomagnetism and Aeronomy (IAGA). The Jensen & Cain (1962) model and the GSFC12/66 model (Cain et al. 1967) are included in the library since they have been used to produce the NASA trapped radiation belt models AP-8 and AE-8 (Heynderickx et al. 1996ab). The simple dipole magnetic field model is deduced from a truncation to the second order of the expansion of the IGRF geomagnetic field models.

Eight external magnetic field models are included in the library:

1. Mead & Fairfield (1975) model;
2. Tsyganenko (1987) short model;
3. Tsyganenko (1987) long model;
4. Tsyganenko (1989) model;
5. Olson & Pfitzer (1977) quiet model;

6. Olson & Pfitzer (Olson et al. 1988) dynamic model;
7. model T96 (Tsyganenko & Stern, 1996);
8. Ostapenko-Maltsev (1997) model.

The Mead & Fairfield (1975) and Tsyganenko (1987, 1989) magnetic field models depend on levels of magnetic disturbance parameterized by  $K_p$ . The Tsyganenko (1989) model is tilt dependent and was primarily developed as a tail model. The Olson & Pfitzer (1977) model is an average model fit to quiet conditions without parameter. The dynamic model (Olson et al. 1988) is a scalable model depending upon the activity level but without a tilt dependence. The scale factors are determined by the activity index  $D_{st}$  and the standoff distance of the magnetopause determined by the solar wind density and velocity. The model T96 (Tsyganenko & Stern 1996) depends on the solar wind pressure and the  $B_Z$  and  $B_Y$  components of the interplanetary magnetic field. The Ostapenko-Maltsev (1997) model was obtained by a least-square fit of fourth order polynomials to 14,000 vector field measurements from the data base of Fairfield et al. (1994). The model depends on the  $D_{st}$  and  $K_p$  indices, as well as on the solar wind dynamic pressure and the  $z$  component of the interplanetary magnetic field.

The different magnetic field models are accessible through subroutines UM510, UM520 and UM530.

### 2.2.7.2 Atmospheric models

Some atmospheric models as well as ionospheric and plasmaspheric extensions are accessible from the library. The library includes:

1. the neutral atmosphere empirical model MSISE-90 (Hedin 1991), improved by Chabrillat (1995);
2. the Anderson and Francis (1964) atmosphere and ionosphere model;
3. the international reference ionosphere IRI-90 (Bilitza 1990);
4. a plasmaspheric extension of IRI-90 (Carpenter & Anderson 1992);
5. a simple atmospheric model based on a table of Allen (1985);
6. the atmospheric model used by Pfitzer (1990).

The MSISE-90 atmospheric model is a very comprehensive reference model for the upper atmosphere based on measurements from several rockets, satellites and incoherent scatter radars. It is extended to the middle and lower atmosphere on the base of a tabulation of zonal average temperature and pressure. The IRI-90 ionospheric model is a reference model for the ionospheric densities and temperatures. Although outdated and obsolete, the Anderson and Francis (1964) model is included in the library since it had been originally used by Hassitt (1965). The last two models are simplified models which provide only the total atmospheric mass density.

The atmospheric models, the ionospheric model and its plasmaspheric extension are accessible through the use of the subroutines UA610 and UA630.

### 2.2.7.3 Collisional cross section models

Two models to evaluate the cross sections for collisions between protons and atmospheric particles are included in the library:

1. the Hassitt (1965) cross sections;
2. a collection of cross sections compiled by Pierrard (1994).

The Hassitt model is included for historical reason and includes cross sections from unreferenced origin. Pierrard's (1994) compilation includes cross sections of charge exchange, ionisation, excitation and nuclear collision from several sources. Both models are accessible through the use of the subroutines UA636 and UA637.

## 2.2.8 Magnetic drift shell

The tracing of magnetic drift shells is the central part of the UNIRAD library: when a drift shell is traced with the help of the library, more than twenty subroutines of the library are used. The tracing of is drift shell is mainly controlled by the subroutines UD310, UF410 and UF420. The algorithm is separated in two parts, the magnetic field line tracing and the drift shell tracing.

### 2.2.8.1 Field line tracing

A segment of a magnetic field line is described as a set of elementary segments. Each segments is characterized by its GEO location, arc length, radius of curvature,... (see the definition of the FORTRAN structure `/zseg/`). The field line segments are traced by the subroutine UF420 and its dependencies. The algorithm has been derived from Pfitzer's (1991) one and is still based on Gill's (1951) 4-order Runge-Kutta integration method. The input arguments of the subroutine UF420 are the GEO coordinates of a point on the magnetic field line, a set of mirror-point magnetic field intensities and, eventually, an altitude. The subroutine traces the segment of the magnetic field line that includes all the pair of mirror points and eventually the points of the magnetic field line that reaches the altitude provided as input. Note that the resulting field segment does not necessarily include the starting point.

When the subroutine UF420 is called, it checks first that the starting point is located inside the most external boundary conditions (the boundary conditions are defined by the mirror-point magnetic field intensities and the given altitude). If this is not the case, the field line is traced in the direction of decreasing field intensity until a boundary condition is reached. The field line segment is then firstly traced in the increasing field intensity direction until all the boundary conditions have been reached. Afterwards, this first part of the field line segment is reversed and the rest of the field line segment is traced in the opposite direction. Each time when a



boundary condition is overstepped, the field line tracing is suspended and the exact location on the field line corresponding to the boundary condition is calculated by an iterative search. Such an iterative search is also applied when an extremum of the magnetic field intensity is overreached.

Note that the integral invariant function  $I$  is not evaluated during the field line tracing, but that the intermediate  $B$  value of the Runge-Kutta integration step are stored in order to calculate the value of  $I$  afterwards (see subroutine UL230).

### 2.2.8.2 Drift shell tracing

Magnetic drift shells are defined by their mirror-point magnetic field intensity  $B_m$  and McIlwain shell parameter  $L$ : the drift shell  $(B_m, L)$  consists of a family of magnetic field line segments

- which are bounded by the magnetic field intensity  $B_m$ , and,
- the integral invariant function  $I$  which corresponds to the requested  $L$  value.

Drift shells can be traced by subroutine UD310. The input arguments of the subroutine are  $B_m$ ,  $L$  and the number  $n$  of field line segments to be traced. As output the subroutine returns the set of field line segments such that the longitudes of the points with the lowest magnetic field intensity along each field line segment are equidistant. The subroutine UD310 calls the subroutine UF410,  $n$  times, to find and trace the different field line segments.

The arguments of the subroutine UF410 are  $B_m$ ,  $L$ , a longitude and an altitude range. When the subroutine is entered, it seeks first a magnetic field line for which the point  $P_{\min}$  with the lowest magnetic field intensity has the requested longitude and lies in the given altitude range. If the magnetic field intensity at  $P_{\min}$  is greater than  $B_m$ , the lower limit of the altitude range is set to the altitude of the current  $P_{\min}$  and the programme seeks for an other magnetic field line.

When a field line which satisfied all conditions on  $P_{\min}$  is obtained, the  $I$  value of the field line segment (delimited by the magnetic field intensity  $B_m$ ) is evaluated and compared to the expected value. According to the value obtained for the integral invariant function, the altitude range of the point  $P_{\min}$  is adapted:

- when the invariant function is larger than the requested  $I$ , the upper limit of the altitude range is set to the altitude of the current  $P_{\min}$ ;
- when the invariant function is lower than the requested  $I$ , the lower limit of the altitude range is set to the altitude of the current  $P_{\min}$ .

Afterwards, a new magnetic field line is sought again.

This iterative process is repeated until the integral invariant function is found to be equal to the expected  $I$  within a tolerance specified in the common block UC190. During the iterations, the programme is aborted when

1. the number of iterations exceeds 20;

**Table 2.8.** Subroutines implemented in the UNIRAD library

Name	Usage
UL220	get information on a magnetic field line segment
UL230	evaluate the integral invariant coordinate $I$
UL240	evaluate the Hilton's function
UL242	inverse the Hilton function
UL245	equatorial pitch angle
UD310	trace a magnetic drift shell
UD315	search the mirror point with the lowest altitude
UD316	search the equatorial point with the lowest magnetic field intensity
UD319	transfer a field line segment from common block UC170 to UC130
UD320	evaluate a double time integral over a drift shell
UD321	evaluate a time integral over a magnetic field line
UD327	search an extremum
UD328	evaluate the second derivative of $B$
UD329	interpolate between two or three points
UD330	evaluate the third invariant
UD331	evaluate the magnetic flux through a spherical cap
UD332	evaluate the magnetic flux through a spherical pie
UF410	search the geographic position of a magnetic field line
UF411	search a local magnetic equator
UF415	rebuild the labels of the field line
UF420	trace a magnetic field line segment passing through a given position
UF421	initialize and close a field line segment
UF422	follow a field line until a boundary condition is reached
UF423	Runge Kutta step
UF424	search the lowest $B$ value
UF425	evaluate the curvature of the field lines
UF426	interpolating an extremum of $B$
UF427	interpolating a value of $B$
UF428	interpolating an altitude
UF429	transpose a field line segment
UM510	select a geomagnetic field model
UM511	set the Jensen & Cain model coefficients
UM512	set the GSFC 12/66 model coefficients
UM513	set the DGRF/IGRF model coefficients
UM515	perform a Schmidt normalisation
UM517	transform from Schmidt to Kluge normalisation
UM520	select an external magnetic field model
UM521	ground disturbances from $K_p$
UM522	position of the Sun

**Table 2.8.** (continued)

---

UM523	GEO to GSM transformation
UM524	GEO to SM transformation
UM530	evaluate the magnetic field vector
UM531	geomagnetic field
UM532	external magnetic field
UM533	distance to the magnetopause
UM535	geocentric to geodetic transformation
UM536	geodetic to geocentric transformation
UM537	Kluge evaluation of the geomagnetic field
UM539	evaluate the magnetic field
UT540	compute modified Julian Day from date
UT541	convert spherical coordinates to cartesian coordinates
UT542	convert spherical vector components to cartesian components
UT545	compute date from modified Julian Day
UT546	convert cartesian coordinates to spherical coordinates
UT547	convert cartesian vector components to spherical components
UT550	select a coordinate transformation
UT551	initialize an Euler rotation matrix
UT552	initialize a quaternion rotation matrix
UT555	coordinate conversion
UT556	vector conversion
UA610	select an atmospheric, ionospheric and/or plasmaspheric model
UA612	provide a list of atmospheric constituents
UA630	evaluate the density numbers and mass densities
UA631	Anderson and Francis atmosphere
UA632	MSISE-90 atmosphere
UA633	IRI-90 ionosphere
UA634	compute mass density from number density
UA635	evaluate the Debye length
UA636	evaluate a weighted atmospheric mass
UA637	proton cross sections
UA638	Hassitt proton cross sections
UA639	equatorial electron density
UT980	print the error messages
UT981	search information on a subroutine
UT982	print the link between two subroutines
UT985	transfer a field line of the drift shell to IDL
UT986	pass general variables to IDL
UT990	initialize the UNIRAD library
UT991	print the magnetic field line

---

**Table 2.8.** (continued)

UT992	print the magnetic drift shell
UT993	store a magnetic field drift shell
UT998	evaluate the magnetic field vector and the normal to the field line
UT999	radius of curvature in a dipolar magnetic field

2. the upper and lower limits of the altitude range become equal;
3. an unrecoverable error occurs during the field line tracing.

In that case, the subroutine UF410 returns with a specific error diagnostic.

The subroutine UD310 succeeds only when all the magnetic field line segments of the drift shell have been successfully traced.

### 2.2.9 Content of the library

The complete set of subroutines implemented in the library is listed in Table 2.8. The user documentation for the UNIRAD library has been written in the HyperText Mark-up Language (HTML) and has not been reproduced in this Final Report. The documentation consists of:

- Frequently Asked Questions (FAQs) and their answers, available at:  
<http://www.magnet.oma.be/home/unilib/faq.htm>
- a set of pages with a detailed description of the subroutines making up the library, one HTML page per subroutine. These HTML pages are made up of the following sections: Name, Synopsis, Arguments, Description, Dependencies, See Also, and Examples. The pages can be accessed directly from a Table of Contents (TOC) page. In addition, links are provided between related pages. The URL of the TOC page is  
<http://www.magnet.oma.be/home/unilib/toc.htm>.

# Chapter 3

## Proton anisotropy

### 3.1 Introduction

At the inner edge of the radiation belts, the trapped proton fluxes are highly anisotropic due to the interaction of the particles with the Earth's atmosphere. An important part of the flux anisotropy consists of a steep pitch-angle distribution related to the atmospheric loss cone. An additional azimuthal anisotropy appears for the high-energy trapped proton fluxes. This anisotropy is observable when the scale length of the proton radiation fluxes is comparable to or shorter than the size of the proton gyration radius. The azimuthal anisotropy results in an East-West asymmetry effect where the fluxes of protons coming—for a given position—from the East are higher than the fluxes of proton coming from the West.

One purpose of modelling this flux anisotropy is to deduce angular dependent proton flux spectra from standard omnidirectional flux data bases which were, until recently, the only ones available. Such a model has been developed analytically by Watts et al. (1989) which combines the Heckman and Nakano (1969) pitch-angle distribution with the Lenchek and Singer (1962) East-West asymmetry factor. The Watts et al. (1989) model has been used by the *Science Applications International Corporation* (SAIC) to evaluated radiation shielding for manned spacecraft (Armstrong et al. 1990; Appleby et al. 1992) and to analyse data from the LDEF satellite (Armstrong et al. 1992ab).

In the software tools ANISO and ANISOPOS developed in the framework of this study, the model of Watts et al. (1989) and an alternative version based on the Badhwar and Konradi (1990) pitch-angle distribution have been implemented. The purpose of both programmes is to provide angular dependent proton flux spectra starting from the standard omnidirectional flux model AP-8.

Since unidirectional trapped proton flux data bases are now available, our second objective is to build directional models of the radiation belt directly from these data bases. To this end, a generalised anisotropy model for the LEO radiation environment is introduced.

The Lenchek and Singer (1962) East-West asymmetry factor, the Heckman and Nakano (1969) pitch-angle distribution, and consequently the anisotropy model of Watts et al. (1989),

are based on the assumption that, at low altitude, the energetic proton flux is directly controlled by the density distribution of the Earth's atmosphere over a particle drift shell (Yoshida et al. 1960; Haerendel 1962). The anisotropy model of Watts et al. (1989) depends explicitly on the local value of the magnetic dip angle and of the atmospheric scale height. A trapped radiation belt model based on this type of description of the anisotropy will probably poorly satisfy the constraints imposed on the angular flux distribution by Liouville's theorem (Roederer 1970; Hess 1968), which links the unidirectional particle fluxes observed at two different geographic position located on a same magnetic drift shell. Such a link introduces a compulsive constraint on all models depending on local values.

In order to obtain a more general description of the trapped proton anisotropy, we introduce an alternative approach based only on the use of a coordinate system attached to the magnetic field lines. It results in a model which does not include parameters depending explicitly on the geographic location where the model is evaluated. This kind of approach is not original. It corresponds to the use of action variables, i.e. the adiabatic invariants  $\mu$ ,  $J$  and  $\Phi$  (Schulz and Lanzerotti 1974).

This study has been fully reported in Technical Note 6 and Technical Note 6 Part II, which are outputs of WP.2.2 and WP.2.3R.

## 3.2 Conventional trapped proton anisotropy models

After defining the notations used in the following paragraphs, the pitch-angle distribution models and the effect of the finite gyroradius length will be reviewed. Afterwards, their combination will be analysed and improvements will be proposed. Special attention will be drawn to the atmospheric scale height determination and to the Armstrong et al. (1990) models VF1MIN and VF1MAX. A trapped proton anisotropy model based on the Badhwar & Konradi (1990) pitch angle distribution will also be investigated.

### 3.2.1 Notations

In this section, we will introduce geometric planes and direction vectors defined at the point of observation. These planes and vectors and their relative orientation are shown in Fig. 3.1. In this figure, the point of observation is located at the origin of the coordinate system. The local horizontal plane is represented, as well as the local vertical plane which contains the magnetic field line passing through the point of observation, and the plane perpendicular to the magnetic field line (mirror plane). The vector  $\bar{D}$  represents an arbitrary direction which could be the look or viewing direction of a detector.

In a spherical geocentric coordinate system, the position of observation is characterized by the vector  $R \bar{1}_R$  where  $R$  is the distance from the Earth's centre ( $\bar{1}_R$  is the unit vector in the zenith direction). The altitude is given by  $h = R - R_E$ ,  $R_E$  being the Earth's radius. At this location, the geomagnetic field vector is denoted by  $B \bar{1}_B$ . In the northern hemisphere,

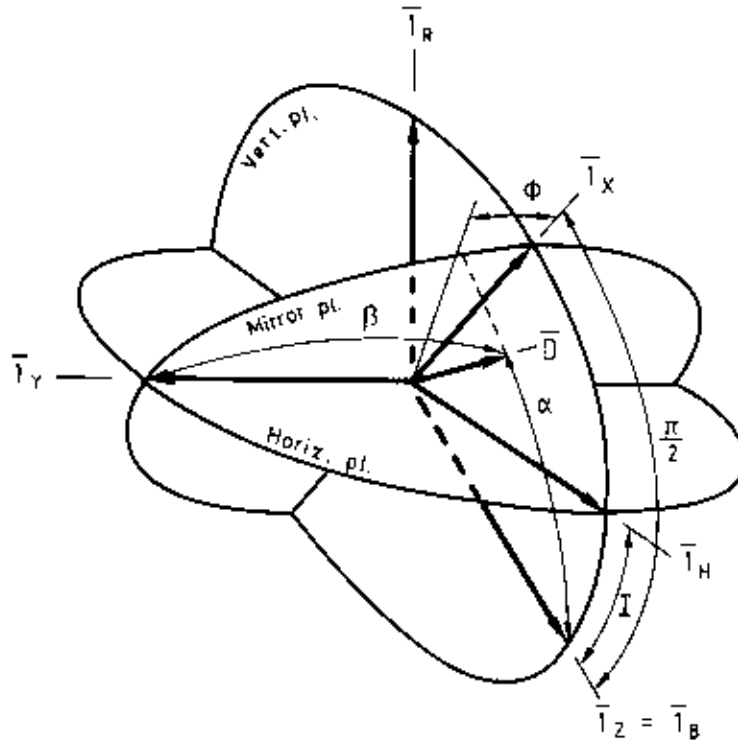


**Figure 3.1.** Representation of the coordinate system used in trapped proton anisotropy theory (see text)

the magnetic field vector points down to the Earth while in the southern hemisphere, it points upward away from the Earth.

A useful coordinate system is introduced with the  $z$ -axis along the magnetic field ( $\bar{I}_z = \bar{I}_B$ ), the  $y$ -axis along the magnetic East direction ( $\bar{I}_y \propto \bar{I}_B \times \bar{I}_R$ ) and the  $x$ -axis perpendicular to the magnetic vector in the vertical plane [ $\bar{I}_x \propto (\bar{I}_B \times \bar{I}_R) \times \bar{I}_B$ ]. The magnetic dip angle  $I$ , i.e. the angle between the magnetic field and the horizontal plane, is defined by  $\cos I = \bar{I}_H \cdot \bar{I}_B$ , where  $\bar{I}_H = \bar{I}_R \times \bar{I}_y$  is the intersection of the horizontal plane and the vertical plane.

In a dipole magnetic field, the position of observation is also characterized by McIlwain's (1961) magnetic shell parameter  $L$ , the magnetic latitude  $\lambda$  and the magnetic longitude  $\varphi$ . The magnetic dip angle is related to  $\lambda$  by

$$2 \tan \lambda = \tan I. \quad (3.1)$$

A vector  $\bar{D}$  is specified in the coordinate system  $(\bar{I}_x, \bar{I}_y, \bar{I}_z)$  by a polar angle  $\alpha$  and an azimuthal angle  $\phi$ . An angle  $\beta$  is also introduced which measures the deviation from the magnetic East direction ( $\cos \beta = \bar{D} \cdot \bar{I}_y = \sin \alpha \sin \phi$ ).

The gyroradius of a charged particle with velocity parallel to  $\bar{D}$ , a charge  $q$ , a mass  $m_0$  and kinetic energy  $E$ , is given by:

$$r_g = \frac{r_{gm}}{\sin \alpha} = \tilde{r}_g \sin \alpha \quad (3.2)$$

(Hess 1968, Walt 1994), where  $r_{\text{gm}}$  is the gyroradius at the mirror point of the particle, and where

$$\tilde{r}_{\text{g}} = \frac{p}{qB} = \frac{\sqrt{E^2 + 2m_0c^2E}}{qcB} \quad (3.3)$$

is the gyroradius of a particle mirroring at the position of observation where the magnetic field intensity is equal to  $B$ , and  $p$  is the relativistic momentum of the particle.

On the field line passing through the position of observation, the magnetic dip angle, the magnetic field intensity and the altitude of the mirror point are respectively  $I_{\text{m}}$ ,  $B_{\text{m}}$  and  $h_{\text{m}}$ . For particles close to their mirror points at the position of observation<sup>1</sup>, it is convenient to introduce the deviation from a 90° pitch-angle:  $\theta = \pi/2 - \alpha$ .

### 3.2.1.1 Unidirectional flux

The integral unidirectional flux  $J$  is defined as

$$J(E, \bar{D}) = \int_E^\infty j(E', \bar{D}) dE'. \quad (3.4)$$

where  $j(E, \bar{D})$  is the unidirectional and differential flux of protons of energy  $E$  in the direction  $\bar{D}$ . Without loosing generality the differential flux can be expressed as

$$j(E, \bar{D}) = j_0(E) \left[ \frac{1}{C} f(E, \theta) g(E, \theta, \phi) \right] \quad (3.5)$$

where  $j_0(E)$  is the omnidirectional differential flux defined by

$$j_0(E) = \int_{4\pi} j(E, \bar{D}) d\Omega \quad (3.6)$$

and the second factor represents the angular dependence of the directional flux. The functions  $f$  and  $g$  are related respectively to the pitch-angle distribution and the azimuthal distribution with respect to the East-West direction. Note that  $f$  does not represent a phase-space distribution but represents a particle flux distribution.  $C$  is a normalisation factor.

### 3.2.2 Pitch-angle distribution

The pitch-angle distribution  $f(\theta) d\theta$  gives the flux of particles observed for pitch-angles between  $\pi/2 - \theta - d\theta$  and  $\pi/2 - \theta$ . The distributions of Heckman & Nakano (1969) and Badhwar & Konradi (1990) are reviewed and compared.

---

<sup>1</sup>When a particle is not close to its mirror point, it travels further along the field line down into the atmosphere and will be absorbed.



### 3.2.2.1 Heckman-Nakano pitch-angle distribution

The theoretical approach proposed by Heckman and Nakano (1969) assumes that the flux along a magnetic field line is inversely proportional to the atmospheric density at the mirror point location. This assumption is based on observations of the Explorer I satellite. In a large range of the Explorer I measurements, the radiation flux increases exponentially with the altitude (Yoshida et al. 1960). Considering as a first approximation that the atmospheric density varies as  $\rho \propto \exp(-h/H)$ , these observations support the assumption that the radiation flux is inversely proportional to the atmospheric density. This assumption was widely adopted [e.g. Haerendel (1962), Lenchek & Singer (1962)].

Heckman and Nakano (1969) expressed the angular distribution  $f(\theta) d\theta$  as the product of the probability  $P_1$  that the particle has a pitch-angle between  $\theta$  and  $\theta + d\theta$  and the probability  $P_2$  that the particle is observed in a field line segment  $\Delta x$ . The probability  $P_1$  is given by

$$P_1(\theta, \theta + d\theta) \propto \frac{1}{\rho(h_m)} d\ell, \quad (3.7)$$

where the pitch-angle range  $[\theta, \theta + d\theta]$  corresponds to a range  $[\ell, \ell + d\ell]$  of the mirror-point locations along the field line. The distance  $\ell$  and the mirror-point altitude are approximatively related by  $h_m = h - \ell \sin I$ .

The second probability  $P_2$  takes into account the time  $\Delta x/v_{\parallel}$  spent by the particle in the segment  $\Delta x$  (where  $v_{\parallel}$  is the particle velocity along the field line) and  $\tau_b$  the bounce period of the particle:

$$P_2 \propto \frac{\Delta x}{v_{\parallel}} \frac{1}{\tau_b} \propto \sin^{-1} \theta. \quad (3.8)$$

Heckman and Nakano (1969) used a dipole field to obtain the relation between  $d\ell$  and  $d\theta$ :

$$d\ell = \frac{4}{3} R \left[ \cos I (2 + \cos^2 I_m) \tan I_m \right]^{-1} \tan \theta d\theta. \quad (3.9)$$

In a small-angle approximation,  $\tan \theta = \theta$ ,  $\sin \theta = \theta$ ,  $I = I_m$ , the integration of Eq. (3.9) gives

$$\ell = \frac{2}{3} R \left[ (2 + \cos^2 I) \sin I \right]^{-1} \theta^2. \quad (3.10)$$

In an exponential atmosphere, the pitch-angle distribution  $f_{\text{HN}}(\theta) d\theta = P_1 P_2$  is given by

$$f_{\text{HN}}(\theta) d\theta \propto \frac{d\theta}{\exp(-h_m/H)} \propto \exp\left(\frac{-\theta^2}{2\sigma^2}\right) d\theta \quad (3.11)$$

where the square of the standard deviation is defined by

$$\sigma^2 = \frac{3}{4} \frac{H}{R} (2 + \cos^2 I) \quad (3.12)$$

and  $H$  is the atmospheric scale height. The Heckman-Nakano expression for the pitch-angle distribution has the advantage to be easy to use, but on the other hand,  $f_{\text{HN}}(\theta)$  is only valid for

small values of  $\theta$ , and it doesn't take into account the non-dipolar terms of the geomagnetic field.

Equation (3.12) shows that the Heckman-Nakano pitch-angle distribution does not depend on the atmospheric density but depends on the density gradient, i.e. the density scale height. When the atmospheric scale height is small, the pitch-angle distribution becomes narrow when approaching  $\theta = 0$ . When the atmospheric scale height is larger, the pitch-angle distribution will spread and the small-angle approximation may no longer be valid. Note also that there is no true loss cone in the Heckman-Nakano formulation of the pitch-angle distribution.

### 3.2.2.2 Badhwar-Konradi pitch-angle distribution

Empirical pitch-angle distributions have been proposed (e.g. Valot & Engelmann 1973, Badhwar & Konradi 1990) and are characterised by the use of a loss cone angle  $\alpha_L$ . The Badhwar-Konradi distribution is given by

$$f_{BK}(\theta) = \begin{cases} \xi \exp(-b\xi) & |\theta| < \pi/2 - \alpha_L \\ 0 & |\theta| > \pi/2 - \alpha_L \end{cases} \quad (3.13)$$

where  $\xi = (\cos \theta - \sin \alpha_L)/\sqrt{B}$  and  $b$  is a shape parameter. The two parameters,  $\alpha_L$  and  $b$ , have to be fitted to experimental unidirectional flux measurements. The Badhwar-Konradi distribution is an empirical fit function: it is not based on physical grounds, e.g. a pitch-angle diffusion theory. However, it gives an excellent fit for the AP-8 MIN omnidirectional fluxes, as well as for the measurements of Fischer et al. (1977).

When particles are inside the loss cone ( $|\theta| > \pi/2 - \alpha_L$ ), they are precipitating into the atmosphere; these particles do not contribute to the flux intensity of trapped ions: there are no particles inside the loss cone. The parameter  $b$  controls the shape of the distribution defined by Eq. (3.13) for small values of  $\theta$ .

The Badhwar-Konradi pitch-angle distribution does not depend explicitly on either the atmospheric density  $\rho$  or the atmospheric scale height  $H$ . This distribution is connected to  $\rho$  and  $H$  through the loss cone  $\alpha_L$  and the empirical shape parameter  $b$  which have to be determined on a case by case basis to fit the experimental datasets.

The loss cone  $\alpha_L$  can be related to the atmospheric cut-off field intensity  $B_c$  which is the highest magnetic field intensity  $B_m$  for which the drift shell ( $B_m, L_m$ ) is populated by stably trapped particles.  $B_c$  is a function of  $L_m$  and is directly related to  $\alpha_L$  by

$$\sin \alpha_L = \sqrt{\frac{B_m}{B_c}}. \quad (3.14)$$

The magnetic cut-off  $B_c$  and the loss cone angle  $\alpha_{L0}$ , obtained from

$$\sin \alpha_{L0} = (B_c/B_0)^{-1/2}, \quad (3.15)$$

are different for different magnetic field and atmospheric models. The parameters  $B_c$  and  $\alpha_L$ , and their dependence on  $L_m$  must be re-evaluated for each new dataset, and are specific to the epoch of the magnetic field model used.

### 3.2.2.3 Comparison between Heckman-Nakano and Badhwar-Konradi distributions

The Heckman-Nakano and the Badhwar-Konradi expressions correspond to two different approaches:

- Badhwar and Konradi (1990) propose an empirical fit function applied to an experimental trapped particle dataset (e.g. AP-8 MIN), while Heckman and Nakano's (1969) approach is a theoretical one which depends on a model of the atmospheric scale height and on an assumption linking the atmospheric density to the radiation flux.
- The parameter  $\sigma$  of the pitch-angle distribution  $f_{\text{HN}}(\theta)$  is defined locally in geographic coordinates, while the  $f_{\text{BK}}(\theta)$  parameters  $\alpha_L$  and  $b$  only depend on  $E$  and  $L_m$ , as a consequence of Liouville's theorem (see Sect. 3.2.4.3).

The Badhwar-Konradi parameters  $\alpha_L$  and  $b$  [Eq. (3.13)] have been obtained from a fitting procedure (Heynderickx & Lemaire 1993) of an unidirectional version of the AP-8 MIN model where the value of  $L$  is determined using the Jensen and Cain (1962) geomagnetic field model and the energy is set to  $E = 20 \text{ MeV}$  (the parameters  $\alpha_L$  and  $b$  vary slightly with energy).

To evaluate the Heckman-Nakano parameter  $\sigma$  [Eq. (3.12)], the atmospheric density scale height given by

$$H = 33.4 \text{ km} \times \exp \left( \frac{R - 6371.2 \text{ km}}{383 \text{ km}} \right) \quad (3.16)$$

is used. Equation (3.16) corresponds to the atmospheric scale height used by Colborn et al. (1990) when applying the Watts et al. (1989) model for solar minimum.

In Fig. 3.2, the pitch-angle distributions  $f_{\text{HN}}$  and  $f_{\text{BK}}$  are compared at two geographic locations: (394.3 km, 25.7°S, 51.0°W) and (720.8 km, 7.9°S, 15.0°W), i.e. two mirror points on the same drift shell defined by  $L = 1.24$  and  $B_m = 0.2$ . At 394.3 and 720.8 km altitude, the atmospheric scale height of Eq. (3.16) is equal to 93.5 and 219.3 km, respectively. For the purpose of comparison, the parameters  $b$  and  $\alpha_{0c}$  of the Badhwar & Konradi (1990) function have been fitted to the SAMPEX countrates presented later in Sect. 3.3.4 (see Fig. 3.11). For both distributions, the unidirectional flux has been normalized to 1 at  $\alpha = 90^\circ$ .

The Badhwar-Konradi pitch-angle distribution is steeper than the Heckman-Nakano distribution: beyond the local pitch-angle  $\alpha_L$ ,  $f_{\text{BK}}(\alpha) = 0$ , whereas  $f_{\text{HN}}(\alpha)$  does not vanish within the loss cone. Remember, however, that for pitch-angles faraway from  $90^\circ$ , Heckman and Nakano's small-angle approximation is no more valid.

Since the Badhwar & Konradi (1990) function depends only on  $E$  and  $L$ , the  $f_{\text{BK}}$  pitch-angle distribution is identical at both locations. On the other hand, the variation of the ratio  $H/R$  from  $1/72$  to  $1/32$  between the two locations implies an important change of the Heckman & Nakano (1969) pitch-angle distribution. According to Liouville's theorem (see Sect. 3.2.4.3) the pitch-angle distributions at the mirror point must be the same as at any mirror point on the same drift shell, including the lowest-altitude mirror point. Therefore, models based on the  $f_{\text{HN}}$  function have to be restricted to a region of space where the ratio  $H/R$  does not vary.

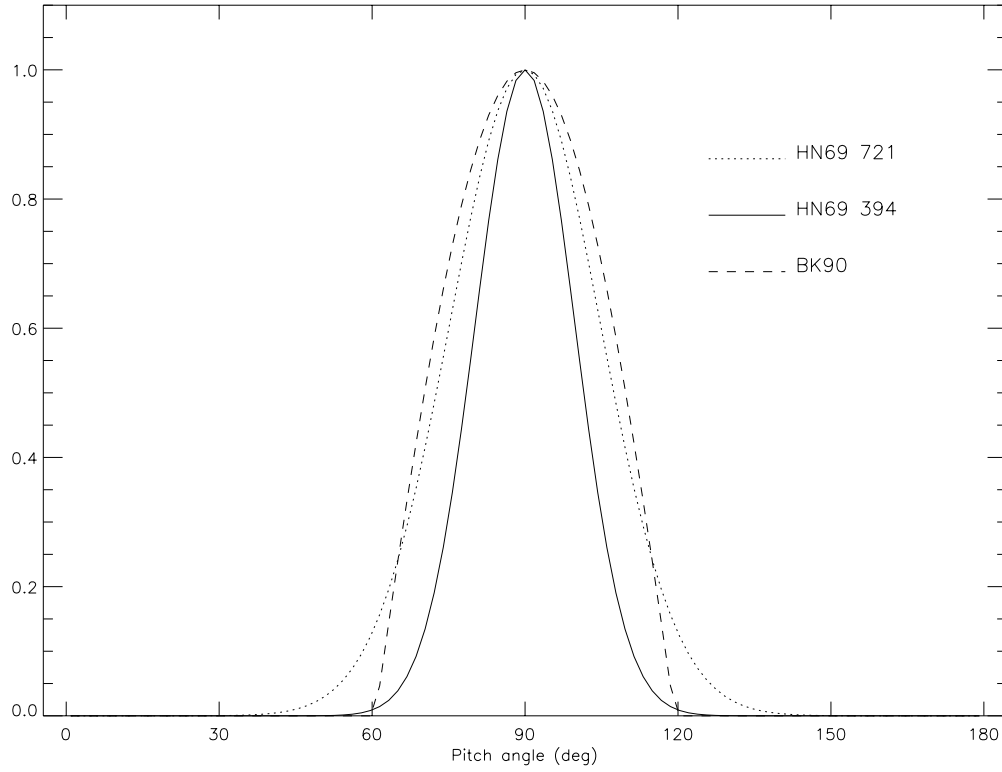


**Figure 3.2.** Comparison of the Heckman & Nakano (1969) and Badhwar & Konradi (1990) pitch angle distributions at  $L = 1.24$  and  $B_m = 0.2$ . The dotted and solid lines correspond to the Heckman & Nakano (1969) distribution evaluated at an altitude of 720.8 and 394.3 km, respectively. The dashed line corresponds to the Badhwar & Konradi (1990) distribution, whatever the altitude. Note that the normalisation is such that  $f(\pi/2) = 1$ .

In conclusion, Heckman-Nakano's and Badhwar-Konradi's pitch-angle distributions produce qualitatively similar results. However, the Heckman and Nakano (1969) results deviate from the expected result at higher altitude. The Badhwar and Konradi approximation is adiabatically invariant, since it depends only on the  $(B, L)$  coordinate system which are adiabatic invariants in a static magnetic field; this guarantees a satisfactory pitch-angle distribution at all altitudes.

### 3.2.3 Lenchek-Singer East-West asymmetry model

The Lenchek & Singer (1962) model is the first and, to our knowledge, the only one, describing the azimuthal distribution of the trapped particle fluxes at low altitude where East-West effects become important.

As depicted by Lenchek and Singer (1962), for a given point of observation, protons coming from the West have their guiding centres above the point of observation, while those coming from the East have their guiding centres below this point. Therefore, during their drift, protons

coming from the West will experience averaged atmospheric densities smaller than those with the same pitch angle but coming from the East. This East-West asymmetry is observable when the gyroradii of the trapped protons become comparable with the atmospheric scale heights,  $H$ .

For a proton at an altitude  $h$  with a velocity in the direction  $\bar{D}$  (e.g. the axis of the detector), the altitude of the local guiding centre is given by  $h + r_g \cos I \cos \beta$ . Let  $h_m$  be its mirror point altitude in the guiding centre approximation, i.e. on the field line passing through the point of observation. When the gyroradius is not small compared to the atmospheric scale height, its mirror point altitude will be given by  $h_m + r_{gm} \cos I_m \cos \beta_m$ . Assuming that the atmospheric density decreases exponentially with a scale height  $H$  and that the flux is inversely proportional to the atmospheric density at the mirror point (see Sect. 3.2.2.1), the omnidirectional flux at  $h$  and  $h_m$  has to be corrected by a factor proportional to

$$\frac{\exp\left(-\frac{h_m}{H}\right)}{\exp\left(-\frac{h_m + r_{gm} \cos I_m \cos \beta_m}{H}\right)} = \exp\left(\frac{r_{gm} \cos I_m \cos \beta_m}{H}\right). \quad (3.17)$$

Note that this correction depends on the local magnetic field configuration in the neighbourhood of the mirror point. Therefore, the correction factor may be different for all mirror points of a given drift shell ( $B_m, L_m$ ).

In order to avoid field line tracing, the correction factor may be approximated by

$$g_{LS}(\theta, \phi) = \exp\left(\frac{\tilde{r}_g \cos I \sin \alpha \sin \phi}{H}\right) \quad (3.18)$$

when the pitch-angle is near  $90^\circ$ ,  $I_m \simeq I$ ,  $\beta_m \simeq \beta$ ,  $r_{gm} \simeq \tilde{r}_g$ , where  $\tilde{r}_g$ , the gyroradius of particles mirroring at the point of observation, is given by Eq. (3.3). Expression (3.18) has the advantage to be easy to use and to outline the dependence on the pitch-angle  $\alpha$  and on the azimuthal direction  $\phi$ .

Of course, when the gyroradius of a trapped ion becomes larger than the density scale height this first order approximation should become questionable. But so far no other alternative and more general theory has been proposed.

### 3.2.4 Combination of the angular distributions

In the previous sections, models for the pitch-angle and azimuthal distributions have been reviewed. In order to obtain the total angular distribution of the proton or heavier ion fluxes the pitch-angle distribution and the East-West asymmetry distribution must be combined and renormalized.

Let  $f(E, \theta)$  be the pitch-angle distribution and  $g(E, \theta, \phi)$  the distribution with respect to the East-West direction where  $\theta = \pi/2 - \alpha$  is the complement of the pitch-angle, and  $\phi$  is the azimuthal angle. The differential unidirectional flux then becomes

$$j = j_0(E) \frac{1}{C} f(E, \theta) g(E, \theta, \phi), \quad (3.19)$$

where  $j_0$  is the omnidirectional trapped proton flux and  $C$  is a normalisation factor. Note that this decomposition of the unidirectional flux is not restrictive. The factor  $C$  and the functions  $f$  and  $g$  have to be determined so that the omnidirectional flux computed from Eq. (3.19) is equal to  $j_0(E)$ , i.e.

$$\int_0^\pi \int_0^{2\pi} j \, d\phi \, d\cos \alpha = j_0(E). \quad (3.20)$$

There are different methods to satisfy this normalisation condition. Each method leads to a different expression of the unidirectional flux  $j$ , but each expression will provide the same omnidirectional flux  $j_0$ . Below, we restrict our description to the two most commonly used methods.

### 3.2.4.1 Global normalisation

The first method of normalisation is to define the factor  $C$  in Eq. (3.19) as

$$C = \int_0^\pi \int_0^{2\pi} f(E, \frac{\pi}{2} - \alpha) g(E, \frac{\pi}{2} - \alpha, \phi) \, d\phi \, d\cos \alpha. \quad (3.21)$$

In this case, the factor  $C$  is a constant, i.e. it depends neither on  $\alpha$  nor on  $\phi$ . For instance, when  $g_{\text{LS}}$  is used to describe the East-West asymmetry distribution, the integration over  $\phi$  is analytical and the factor  $C$  is given by Kern (1989):

$$C_G = 2\pi \int_0^\pi f(E, \frac{\pi}{2} - \alpha) I_0 \left( \frac{\tilde{r}_g \cos I \sin \alpha}{H} \right) d\cos \alpha, \quad (3.22)$$

where  $I_0$  is the zero order modified Bessel function (Abramowitz and Stegun, 1964).

### 3.2.4.2 Separate normalisation

A second method of normalisation consists of normalizing separately the two functions  $f$  and  $g$ :

$$C_f = \int_0^\pi f(\frac{\pi}{2} - \alpha) \, d\cos \alpha \quad (3.23)$$

and

$$C_g = \int_0^{2\pi} g(\frac{\pi}{2} - \alpha, \phi) \, d\phi. \quad (3.24)$$

In this case, the total normalisation factor is given by

$$C = C_f C_g. \quad (3.25)$$

Note that the total normalisation factor  $C$  now depends on the angle  $\alpha$ . For instance, when  $g_{\text{LS}}$  is used to describe the East-West asymmetry, the factor  $C$  will be given by

$$C_S = 2\pi I_0 \left( \frac{\tilde{r}_g \cos I \sin \alpha}{H} \right) \int_0^\pi f(\frac{\pi}{2} - \alpha) \, d\cos \alpha. \quad (3.26)$$

Obviously, the expressions (3.22) and (3.26) are different. These two expressions will lead to two different expressions for the unidirectional flux, but both will provide the same omnidirectional flux  $j_0(E)$ .

Therefore, a trapped proton anisotropy model is determined by a selection of an omnidirectional flux  $j_0$ , a pitch-angle distribution  $f$ , an azimuthal distribution  $g$ , and by the choice of the normalisation method: Eqs. (3.22) or (3.26).

### 3.2.4.3 Liouville's theorem

As explained previously [see Eq. (3.19)], to create an anisotropy model, a pitch-angle distribution as well as a East-West asymmetry angular distribution must be selected or determined experimentally. Until a more comprehensive physical model is available, different criteria (e.g. the ease of use, the accuracy, etc.) will be used to select the appropriate distributions. In this section, we will study the constraint on the angular distribution functions  $f$  and  $g$  resulting from the application of the Liouville's theorem. This constraint affects the parameters on which the angular distributions depend.

In a stationary geomagnetic field and when magnetic field lines are electric equipotentials, the magnetic field intensity  $B_m$  at the mirror point and the McIlwain (1961) parameter  $L_m$  fully characterize a drift shell of trapped particles, i.e. the whole shell of guiding center field lines. Consider now unidirectional particle fluxes observed at two different locations  $\bar{r}$  and  $\bar{q}$  on a same drift shell. In the absence of Coulomb or wave-particle interactions, according to Liouville's theorem for trapped particles (Roederer 1970, Hess 1968), the fluxes are related by

$$\int_0^{2\pi} \frac{j(\bar{r}, \alpha_r, \phi_r)}{E} d\phi_r = \int_0^{2\pi} \frac{j(\bar{q}, \alpha_q, \phi_q)}{E} d\phi_q. \quad (3.27)$$

In a stationary magnetic field, when the flux is assumed to be gyrotropic, Expression (3.27) reduces to  $j(\bar{r}, \alpha_r) = j(\bar{q}, \alpha_q)$ . The pitch-angles are determined by the conservation of the first adiabatic invariant, i.e. the magnetic moment:

$$\frac{\sin^2 \alpha_r}{B(\bar{r})} = \frac{\sin^2 \alpha_q}{B(\bar{q})}. \quad (3.28)$$

At two points where the magnetic field intensities are equal,  $\alpha_r = \alpha_q$  and

$$f(\bar{r}, \theta) \int_0^{2\pi} g(\bar{r}, \theta, \phi_r) d\phi_r = f(\bar{q}, \theta) \int_0^{2\pi} g(\bar{q}, \theta, \phi_q) d\phi_q. \quad (3.29)$$

This relation is the basic constraint on the angular flux distribution imposed by Liouville's theorem.

When the flux is gyrotropic (i.e. independent of  $\phi$ ), the constraint (3.29) shows that the pitch-angle distribution observed at conjugate points [i.e. with the same  $(B, L)$  coordinates] must be equal. This condition is satisfied by a pitch-angle distribution like  $f_{BK}$  given by Eq. (3.13), where the controlling parameters  $\alpha_L$  and  $b$  depend on  $E$  and  $L_m$ . On the other hand, the pitch-angle distribution  $f_{HN}$  does not satisfied Condition (3.29), since the controlling parameters  $h, H$

and  $I$  of this pitch-angle distribution are evaluated at the point of observation. One way to meet Condition (3.29) with the Heckman-Nakano pitch-angle distribution would be to use effective parameters depending on coordinates such as  $B_m$  or  $L_m$ , which both are adiabatic invariants in a static magnetic field. For instance, an effective scale height  $H_{\rho'}$  may be defined as the scale height of the averaged atmospheric density over a drift shell.

When the azimuthal distribution due to the East-West effect is important, due to Constraint (3.29), the functions  $f$  and  $g$  are not independent from one another. A common practice is to simply meet separately the two following conditions:

$$f(\bar{r}, \theta) = f(\bar{q}, \theta) \quad (3.30)$$

and

$$\int_0^{2\pi} g(\bar{r}, \theta, \phi_r) d\phi_r = \int_0^{2\pi} g(\bar{q}, \theta, \phi_q) d\phi_q. \quad (3.31)$$

For instance, to satisfy Condition (3.31) with the Lenchek-Singer distribution [see Eq. (3.18)], one has to use an effective atmospheric scale height averaged over the whole drift shell. Furthermore, one has to use either a separate normalisation [see Sect. 3.2.4.2], or to restrict the application of the model to a simple centered dipole magnetic field.

In short, Liouville's theorem, which links particle flux observed at different locations on a drift shell, imposes a drastic condition [Eq. (3.29)] to the experimental or theoretical angular distribution for trapped proton directional flux models. When the separate normalisation [Eqs. (3.23) and (3.24)] is used, this criterion is reduced to Eq. (3.30). Therefore, parameters like  $(B_m, L_m, \alpha_L, H_{\rho'}, h_{\tilde{m}}, \dots)$  averaged over drift shells have to be preferred to local parameters like  $h, H, I$  to determine pitch angle distributions.

### 3.2.5 Armstrong and Watts models

Armstrong et al. (1990) applied the model for angular distribution developed by Watts et al. (1989) for the AP-8 MIN and MAX model to evaluate differential energy spectra of trapped proton unidirectional fluxes at low altitude. The assumptions on which this model is based have been discussed in another section. The energy spectra presented by these authors were averaged over circular orbits with a  $28.5^\circ$  inclination and an altitude ranging from 300 to 500 km. To analyse the radiation environment of the Space Station, Armstrong et al. (1990) converted the energy spectra to Si and Blood Forming Organs (BFO) doses using Burrell's (1964) one-dimension proton transport code. To compare their prediction with data from the Long Duration Exposure Facility (LDEF), Armstrong et al. (1992b) also developed a three-dimensional transport calculation based on the High-Energy Transport Code (HETC) code (Armstrong & Chandler 1972). The comparison showed that AP-8 underestimates the LDEF data by about a factor of 2 and that the Watts et al. (1989) model produces weaker anisotropies than those observed. This latter discrepancy can be attributed to the inappropriate atmospheric scale height used in Armstrong et al.'s (1990) calculation.

In this section, we describe the trapped proton anisotropy models labelled VF1MIN and VF1MAX by Colborn et al. (1990). VF1 stands for Vector Fluxes, version 1. The VF1MIN



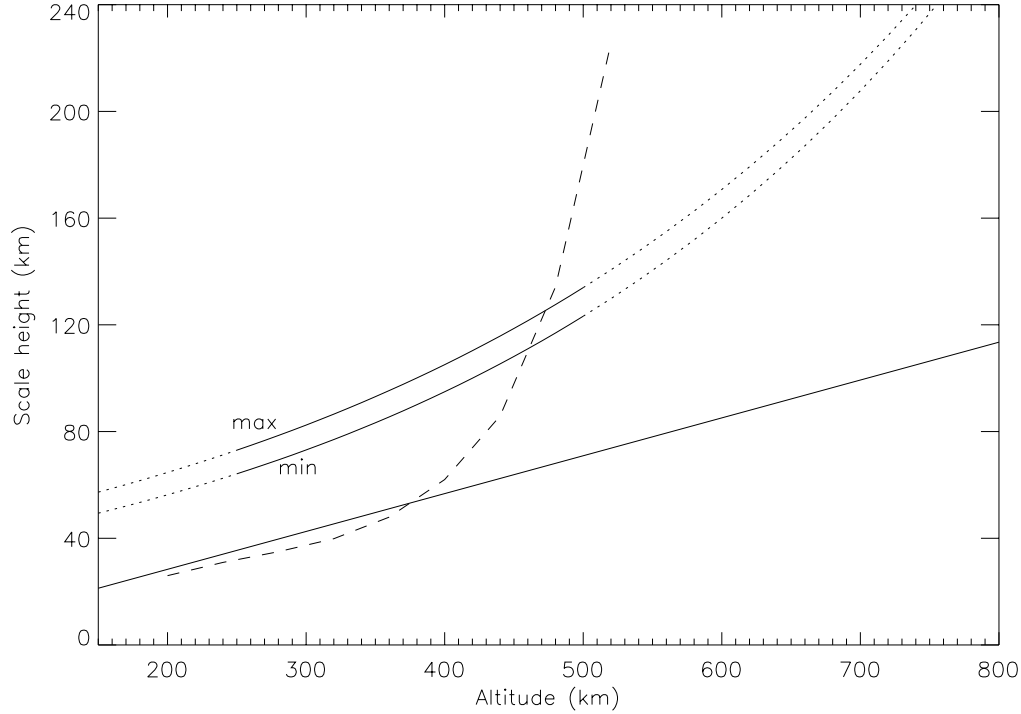


**Figure 3.3.** Comparison between different scale heights. The dotted-partly-solid lines represent effective scale heights  $H^{\min}$  and  $H^{\max}$  used by Armstrong et al. (1990) and given in Eqs. (3.32) and (3.33). The solid line is the scale height obtained from Allen's (1985) atmosphere model. The dashed line correspond to the stopping-power scale height as a function of  $h_{\tilde{m}}$  (Heckman & Brady 1966).

and VF1MAX models correspond to solar minimum and solar maximum. In these models, conversion factor, to transform omnidirectional flux into unidirectional flux, is given by

$$W_{VF}(E, \alpha, \phi) = \frac{\exp\left(-\frac{(\pi/2 - \alpha)^2}{2\sigma^2}\right)}{\sin \alpha \sqrt{2\pi}\sigma \operatorname{erf}\left(\frac{\pi}{\sqrt{8}\sigma}\right)} \frac{\exp\left(\frac{r_g \cos I \sin \phi}{H}\right)}{2\pi I_0(r_g \cos I/H)} \quad (3.32)$$

where  $I_0$  is the modified Bessel function. Note that Eq. (3.32) is deduced from a separated normalisation where  $f_{HN}$  is normalized with respect to  $\alpha$  instead of  $\cos \alpha$ . The omnidirectional spectra  $j_0(E)$  at solar minimum and solar maximum are taken from the AP-8 MIN and MAX models respectively. Colborn et al. (1990) have used the atmospheric scale height  $H$  obtained from the Johnson and Smith (1985) atmospheric model:  $H$  is an increasing function of the altitude which has been approximated for solar minimum and maximum by

$$H^{\min} = 33.4\text{km} \times \exp\left(\frac{h}{383\text{km}}\right), \quad (3.33)$$

$$H^{\max} = 39.8\text{km} \times \exp\left(\frac{h}{412\text{km}}\right). \quad (3.34)$$

Expressions (3.33) and (3.34) are assumed to be valid in an altitude range between 250 and 500 km. In this study, we have reconstructed the models VF1MIN and VF1MAX from Eqs. (3.32)–(3.34) where the modified Bessel function is evaluated by the expansion series

$$C_{gW} = 2\pi \sum_{k=0}^{\infty} \frac{1}{k!^2} \left( \frac{r_g \cos I \sin \alpha}{2H} \right)^{2k} \quad (3.35)$$

which converges rapidly (Evans & Daly 1989).

In Fig. 3.3, Colborn et al. (1990) scale heights are compared to the atmospheric scale height  $H(h)$  based on Allen's (1985) table of atmospheric densities and Heckman & Brady's (1966) effective scale height  $H_{\Delta E}$  based on the energy loss by a particle along its trajectory. The atmospheric scale height  $H(h)$  (full solid line) and Colborn et al. (1990) effective scale heights  $H^{\min}$  and  $H^{\max}$  (dotted-partly-solid lines) are functions of the altitude  $h$ . The Heckman & Brady (1966) effective scale height  $H_{\Delta E}$  (dashed line) has been determined for a set of drift shells  $(B_m, L_m)$  where  $L_m$  is fixed at 1.38 and where  $B_m$  varies from 0.2043 to 0.2355 gauss. The effective energy loss scale height  $H_{\Delta E}$  is a function of the lowest mirror point altitude  $h_m$ .

The shapes of the Colborn et al. (1990) scale heights are similar for solar minimum and solar maximum. The difference between  $H^{\min}$  and  $H^{\max}$  does not exceed 11 km in the altitude range 250–500 km. In that altitude range,  $H^{\min}$  and  $H^{\max}$  are about 45 km larger than Allen's (1985) atmospheric scale height. Additional atmospheric models can, of course, also be used to determine this latter local density scale height. It can be seen that the altitude distribution of the effective scale height  $H_{\Delta E}$  is quite different from all others. Below 350 km,  $H_{\Delta E}$  is almost equal to the local atmospheric scale height of Allen's (1985) model. At these altitudes, the main constituents of the atmosphere are  $N_2$ ,  $O_2$ , and  $O$  which have almost the same ratio  $A/Z$ . Therefore the rate of energy loss is proportional to the atmospheric density. Above 350 km, Heckman and Brady's (1966) effective scale height increases very sharply, indeed the abundance of He and H is increasing about this height. Consequently, the ionization energy losses are no longer proportional to the total atmospheric density.

Note that  $H_{\Delta E}$  is a function of  $B_m$  and  $L_m$ ; it is not a function of the altitude of the point of observation. For instance, when an observer is located at different positions corresponding to  $B_m = 0.2230$  gauss and  $L_m = 1.38$ , the altitude of his actual position may vary from 326 to 1,670 km but the effective scale height  $H_{\Delta E}$  will be constant and equal to 41 km. In contrast, according to Expr. (3.34), at 326 km the scale height  $H^{\max}$  will be about 88 km while at 1,670 km it will be larger than 2,000 km!

Since Armstrong et al. (1990) restrict their model to the altitude range between 250 and 500 km, trapped protons are only observed in the South Atlantic Anomaly, where the mirror points are the lowest ones. When the observer is not near the position of a lowest mirror point, the drift shell generally hits the Earth's surface in the vicinity of the South Atlantic Anomaly. Therefore, when the Armstrong et al. (1990) model is supposed to become inadequate, the radiation flux of protons is negligible. However, their model provides reasonable values of the scale height of pitch-angles close to  $90^\circ$ , i.e. where the directional proton flux is maximum.

**Table 3.1.** Values of the parameters relative to BK-MIN and BK-MAX trapped proton flux anisotropy models

Model	$H$	$p_1$	$p_2$	$p_3$	$p_4$
BK-MIN	100.0	-0.032392	0.039836	0.13164	-8.8674
BK-MAX	100.0	-0.031690	0.039119	0.09294	-6.1651

### 3.2.6 BK-MIN and BK-MAX models

We define also two very simple models based on the Badhwar and Konradi (1990) pitch-angle distribution. The models will be called BK-MIN and BK-MAX, respectively for solar minimum and solar maximum conditions.

In these models, the anisotropy conversion factor to transform omnidirectional flux into unidirectional flux, is deduced from Eqs. (3.13) and (3.18) with a separate normalisation (see Sect. 3.2.4.2). When  $\alpha_L < \alpha < \pi - \alpha_L$ , it is given by

$$W_{\text{BK}}(E, \alpha, \phi) = \frac{\xi(\alpha) \exp(-b\xi(\alpha))}{2 \int_{\alpha_L}^{\pi/2} \sin \alpha' \xi(\alpha') d\alpha'} \frac{\exp\left(\frac{r_g \cos I \sin \phi}{H}\right)}{2\pi I_0(r_g \cos I/H)}, \quad (3.36)$$

where  $\xi(\alpha) = (\sin \alpha - \sin \alpha_L)/\sqrt{B}$ . When  $\alpha \leq \alpha_L$ , the conversion factor is given by  $W_{\text{BK}}(E, \alpha, \phi) = 0$ . The integral in Eq. (3.36) is evaluated numerically by a Gauss-Legendre quadrature. The loss-cone angle  $\alpha_L$  is related to the equatorial loss-cone angle  $\alpha_{L0}$  by the conservation of the magnetic moment [see Eq. (3.28)]:

$$\sin \alpha_L = \sqrt{\frac{B}{B_0}} \sin \alpha_{L0} \quad (3.37)$$

When, at the location of observation,  $B$  is greater than  $B_0/\sin^2 \alpha_{L0}$ , the trapped protons are absorbed by the atmosphere and the proton flux is set equal to zero.

The equatorial loss-cone pitch angle  $\alpha_{L0}$ , the slope parameter  $b$  and scale height  $H$  are functions of the drift shell parameter  $L$ . For the sake of simplicity,  $H$  is set to a constant value and the parameters  $\alpha_{L0}$  and  $b$  are defined as functions of  $L$ .

The parameters  $\alpha_{L0}$  and  $b$  are obtained from the fit of the distribution  $f_{\text{BK}}$  to the AP-8 unidirectional fluxes of 20 MeV trapped protons. The parameters are closely approximated by the expressions:

$$\alpha_{L0}^{-1} = p_1 + p_2 L \quad (3.38)$$

and

$$b^{-1} = p_3 + p_4 \ln L, \quad (3.39)$$

where  $\alpha_{L0}$  is expressed in degrees and  $b$  in gauss<sup>1/2</sup>. The values of the scale heights and of the different parameters  $p_1$ ,  $p_2$ ,  $p_3$  and  $p_4$  are given in Table 3.1 for solar minimum and maximum conditions. The parameters  $p_1$ ,  $p_2$ ,  $p_3$  and  $p_4$  were evaluated for 20 MeV protons; their values vary slightly with the proton energy.

### 3.3 Generalised anisotropy model

For a point of observation located at the inner edge of the radiation belts, the observed flux of energetic trapped protons is known to depend on the look direction, even for a fixed pitch angle (Watts et al. 1989). This effect is known as the East-West asymmetry (Heckman & Nakano 1963). For instance, aboard the SAMPEX spacecraft, the countrate associated to 86–120 MeV protons and observed at  $L \approx 1.15$  and  $B_m \approx 0.197$  Gauss varies by a factor of 6 between the periods when the detector is looking to the East and the periods when it is looking to the West (Looper et al., 1997). This East-West effect is explained by the fact that protons viewed with the same pitch angle but in different azimuthal directions have their guiding centres on different magnetic field lines and thus belong to different drift shells, where the fluxes are rather different from each other. Consequently, to take into account that the guiding centres of the observed protons no longer correspond to the point of observation, the  $L$  value  $L_{GC}$  associated with the guiding centre should be used instead of the  $L$  value associated with the point of observation. This approach means that the flux maps have to be organized in  $(E, B_m, L_{GC})$ .

#### 3.3.1 First order expansion of the perpendicular flux

The shell parameter  $L_{GC}$  associated to a guiding centre depends on the look direction and also on the particle energy through the Larmor radius

$$r_g = \frac{p}{qB} \sin \alpha \quad (3.40)$$

where  $p$  and  $q$  are the momentum<sup>2</sup> and charge of the proton, respectively, and  $B$ , the local magnetic field intensity. Therefore, when building and using a model of the form  $f(E, B_m, L_{GC})$ ,  $L_{GC}$  has to be evaluated for every look direction and for each energy covered by the instrument. As the computation of  $L$  involves an integration along a field line segment, building and using such models is very demanding of CPU time.

To avoid the evaluation of  $L_{GC}$  when using the  $j_{\perp}(E, B_m, L_{GC})$  map, an alternative approach which uses an expansion to first order in  $L$  of the perpendicular flux is applied instead. With this approximation, the flux can be written as

$$\begin{aligned} f_p(E, \alpha, \beta) &= j_{\perp}(E, B_m, L_{GC}) \\ &= j_{\perp}(E, B_m, L) + \Delta L \times \left. \frac{\partial j_{\perp}}{\partial L} \right|_{E, B_m} + O^{(2)}(\Delta L) \end{aligned} \quad (3.41)$$

where  $\Delta L \equiv L_{GC} - L$ . The  $L_{GC}$  evaluation problem is now reduced to evaluating  $\Delta L$ , for which we propose an analytical expression in the next section. As shown below,  $\Delta L$  is in close relationship with the distance between the point of observation P and the drift shell of the observed protons. For example, when P is located in the magnetic equatorial plane of a centred dipole field,  $\Delta L$  is equal to the distance between the drift shell and P.

---

<sup>2</sup>The particle momentum and energy are related by  $p^2 c^2 = E^2 + 2m_0 c^2 E$  where  $c$  is the speed of light and  $m_0$  the rest mass of the particle. For protons,  $m_0 = 1.6725 \cdot 10^{-27}$  kg.

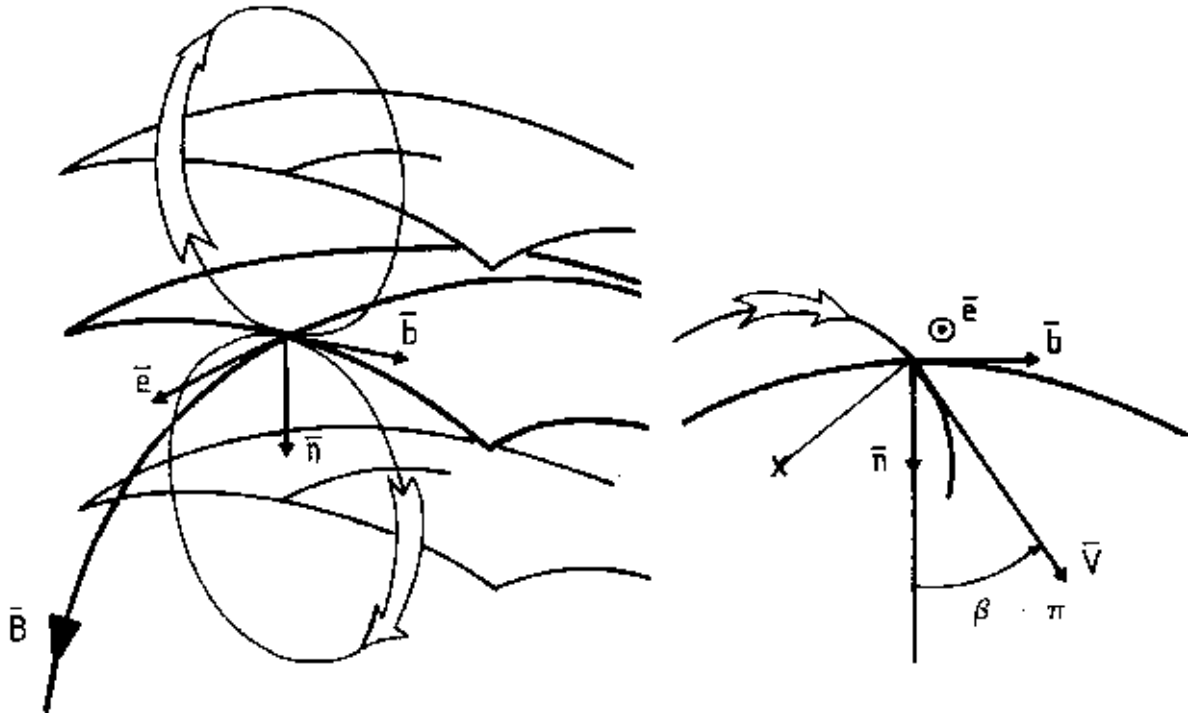


**Figure 3.4.** Left panel: representation of a magnetic field line segment and of three neighbouring magnetic drift shells separated by one gyroradius. The circles represent the proton gyration motions.  $\mathbf{e}$ ,  $\mathbf{n}$ , and  $\mathbf{b}$  are the vectors tangent, normal and bi-normal to the magnetic field line, respectively. Right panel: cut view in the plane  $(\mathbf{n}, \mathbf{b})$  perpendicular to the magnetic field.

### 3.3.2 Natural coordinate system

To evaluate  $\Delta L = L_{GC} - L$ , we will characterize the look direction by a pair of polar and azimuthal angles  $(\alpha, \beta)$  measured in a local coordinate system attached to the local magnetic field line. Since the drift velocity of the guiding centre of a particle is perpendicular to both the magnetic field vector  $\mathbf{B}$  and the perpendicular gradient  $\nabla_{\perp} B$  (Roederer 1970), a natural coordinate system is such that

- the origin coincides with the point P of observation;
- the  $z$ -axis points in the direction  $\mathbf{e}$  of the magnetic field vector;
- the  $x$ -axis points in the direction  $\mathbf{n}$  of the normal to the magnetic field line;
- the  $y$ -axis points in the direction  $\mathbf{b} = \mathbf{e} \times \mathbf{n}$  of the bi-normal to the magnetic field line.

The coordinate system  $(\mathbf{e}, \mathbf{n}, \mathbf{b})$  is represented in the left hand panel of Fig. 3.4 where a magnetic field line and three neighbouring drift shells are shown. The typical cyclotron motion of particles attached to upper and lower drift shells are displayed also. The figure illustrates that

particles coming from the right do not belong to the same drift shell as particles coming from the left. If a gradient of particle flux exists, the flux of particles observed from both directions will differ. The right hand panel of Fig. 3.4 is a cut view in the plane  $(\mathbf{n}, \mathbf{b})$  on which the azimuthal angle  $\beta - \pi$  is defined.

In the coordinate system  $(\mathbf{e}, \mathbf{n}, \mathbf{b})$ , the magnetic field line and the drift shell passing through the point of observation P are parallel to the axis  $\mathbf{e}$  and the plane  $(\mathbf{n}, \mathbf{b})$ , respectively. Consequently, when a proton is observed in the look direction  $(\alpha, \beta)$ , its pitch angle is equal to  $\pi - \alpha$ . Its gyration motion corresponds to a clockwise circular motion in the plane  $(\mathbf{n}, \mathbf{b})$  which is perpendicular to  $\mathbf{B}$ . Since the local guiding centre Q of the observed proton lies in both the plane  $(\mathbf{n}, \mathbf{b})$  and the plane perpendicular to the look direction, the direction of Q is given by  $(\pi/2, \beta + \pi/2)$ . The distance between the local guiding centre and P is the Larmor radius  $r_g$  given by Eq. (3.40).

In the following, we will assume that  $r_g$  remains much smaller than the scale length of the magnetic field. Since the scale length of the magnetic field is about a third of the geocentric distance, this assumption remains valid in a large energy range. With this assumption, the magnetic field does not change significantly from P to Q and we can assume that the coordinate systems  $(\mathbf{e}, \mathbf{n}, \mathbf{b})$  at these two locations are identical. The drift shell of a proton observed in the look direction  $(\alpha, \beta)$  then contains Q and is parallel to the plane  $(\mathbf{b}, \mathbf{e})$ . The distance from P to the drift shell is given by

$$d_P(\alpha, \beta) = r_g \cos(\beta + \pi/2) = -\frac{P}{qB} \sin \alpha \sin \beta. \quad (3.42)$$

One should note that protons viewed in the direction  $(\alpha, \pi - \beta)$  will belong to the same drift shell as protons viewed in the direction  $(\alpha, \beta)$  and that the proton fluxes in these two directions should be identical. In particular, when the azimuthal direction  $\beta$  is equal to 0 or  $\pi$ , the drift shell of the observed protons passes through the point of observation and  $\Delta L = 0$ .

### 3.3.3 Evaluation of $\Delta L$

To establish the relationship between  $\Delta L$  and the parameters such as  $\alpha$ ,  $\beta$ ,  $B$ ,  $L$ , and  $E$ , we will first connect  $\Delta L$  with these parameters at the local magnetic equator<sup>3</sup>. Then, the parameters at the local magnetic equator will be connected to the same parameters at the current point of observation.

Since  $L$  is defined in a centred magnetic dipole by the geocentric distance of the drift shell in the equatorial plane, we can assume that  $\Delta L$  is well approximated by the distance at the magnetic equator between the drift shell of the observed proton and the drift shell passing through the point of observation, i.e.

$$\Delta L \approx -d_{P_0}(\alpha_0, \beta_0), \quad (3.43)$$

---

<sup>3</sup>In a non-dipolar magnetic field, we define the local magnetic equator as the surface where the magnetic field intensity is minimum along magnetic field lines.

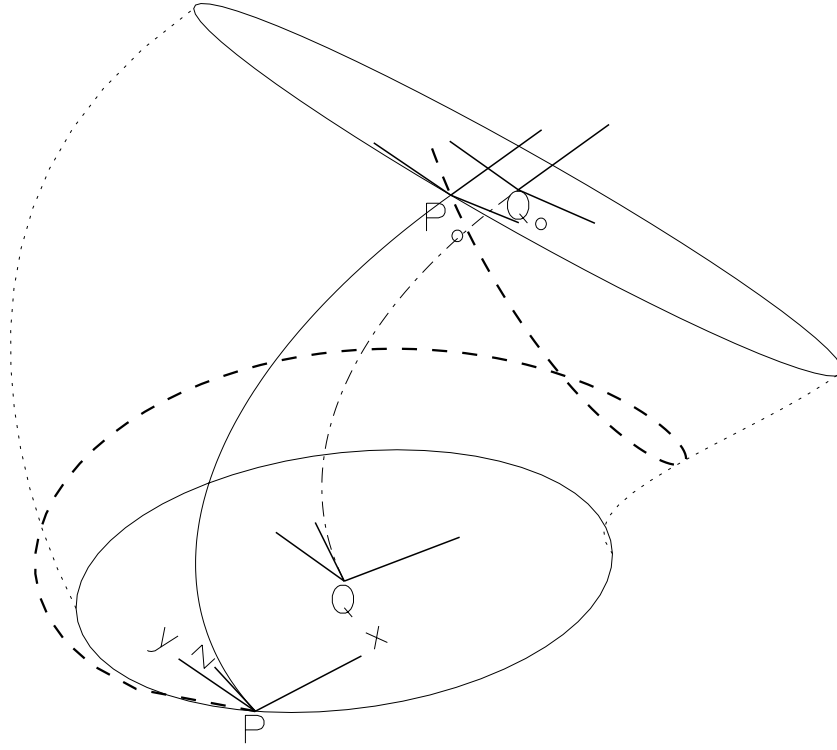


**Figure 3.5.** Representation of the helicoidal trajectory (dashed curve) of a particle around its guiding centre (dot-dash curve). When the particle passes through the point  $P$  ( $P_0$ ), its instantaneous guiding centre is located at  $Q$  ( $Q_0$ ). The two points  $P$  and  $P_0$  are located on the same magnetic field line (solid curve).

where  $(\alpha_0, \beta_0)$  is the look direction of protons belonging to the same drift shell as  $Q$  but viewed from a point  $P_0$  in the magnetic equatorial plane which belongs to the magnetic field line passing through  $P$ . The minus sign takes into account that the distance to the drift shell is measured along the  $\mathbf{n}$ -axis which points in the direction of decreasing  $L$ .

The previous statements are illustrated in Fig. 3.5 where the dashed curve represents the helicoidal trajectory of a proton passing through  $P$ . Its guiding centre is represented by the dot-dash curve and includes the point  $Q$ . The magnetic field line passing through  $P$  is represented by a solid curve. The axes of the coordinate system ( $\mathbf{e}$ ,  $\mathbf{n}$ ,  $\mathbf{b}$ ) are represented at both points  $P$  and  $Q$ . According to the conservation of the magnetic moment, after one, two, three, ... gyrations, the trajectory of the proton will cross again the magnetic field line passing through  $P$ . So, protons belonging to the guiding centre passing through  $Q$  can be always observed from the equatorial point  $P_0$  of the magnetic field line passing through  $P$ . For the sake of clarity, the helicoidal trajectory of Fig. 3.5 is passing through  $P_0$  after one gyration motion, which is generally not the case.

Protons belonging to the guiding centre passing through  $Q$  can be observed from both lo-

cations P and P<sub>0</sub> but with different look directions:  $(\alpha, \beta)$  and  $(\alpha_0, \beta_0)$ , respectively. The relationship between the polar angles  $\alpha$  and  $\alpha_0$  is directly given by the conservation of the first adiabatic invariant:

$$\frac{\sin^2 \alpha_0}{B_0} = \frac{\sin^2 \alpha}{B}, \quad (3.44)$$

where  $B_0$  is the magnetic field intensity at P<sub>0</sub>. On the contrary, the relationship between the azimuthal angles  $\beta$  and  $\beta_0$  is not easily established. Nevertheless, a simple relation is obtained for particular values of  $\beta$ :

1. When  $\beta = 0$  or  $\pi$ ,  $d_P(\alpha, \beta) = 0$ , i.e. the magnetic field line passing through P belongs to the drift shell of the observed proton. Consequently,  $d_{P_0}(\alpha_0, \beta_0) = 0$  and thus  $\beta_0 = 0$  or  $\pi$ .
2. When  $\beta = -\pi/2$ , the drift shell of the observed proton is the most inner observable one. Since, in the magnetic equatorial plane, the drift shell shall remain the innermost one,  $\beta_0 = -\pi/2$ .
3. When  $\beta = \pi/2$ , the drift shell is the outermost observable one and  $\beta_0 = \pi/2$ .

For these particular cases, we the simple relation

$$\beta_0 = \beta \quad (3.45)$$

holds. The simplicity of Equation (3.45) is due to the choice of the coordinate system, the **n**-axis of which is always perpendicular to the drift shells. With regard to the other approximations made previously, we assume that the validity of Equation (3.45) can be reasonably extended to the full range of the azimuthal angles.

From Equations (3.42)–(3.45), the variation of the shell parameter with the azimuthal angle  $\beta$  is approximativated by

$$\begin{aligned} \Delta L &= r_{g0} \sin \beta \\ &= \frac{p}{q\sqrt{B_0 B_m}} \sin \beta. \end{aligned} \quad (3.46)$$

The magnetic field intensities  $B_0$  and  $B_m$  are related to the local values by the relations

$$\begin{cases} B_m &= \frac{B}{\sin^2 \alpha} \\ B_0 &= \frac{M}{L^3} \end{cases} \quad (3.47)$$

where  $M = 0.311653 \text{ Gauss } R_E^{-3}$  is the magnetic moment used to compute the parameter  $L$  (McIlwain, 1961). In combination with Eq. (3.41), Eq. (3.46) provides a description of the unidirectional proton flux which includes the East-West asymmetry.

In this way, Eqs. (3.41) and (3.46) provide a new semi-empirical model for the description of the trapped proton anisotropy at low altitudes. In this model the dependence of the particle



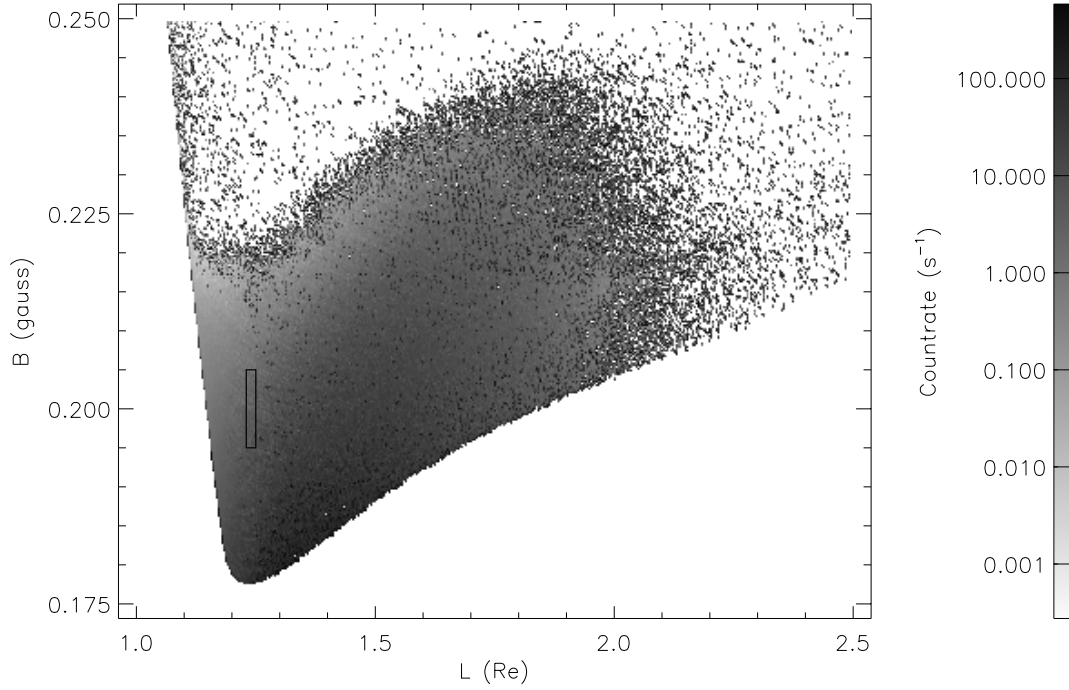


**Figure 3.6.**  $(B, L)$  diagram of the SAMPEX 86–120 MeV proton count rate. The rectangular box corresponds to the bin selected to test the new semi-empirical model.

flux on the azimuthal angle  $\beta$  is based on theoretical assumptions while the dependence on the pitch angle  $\alpha$  has to be obtained empirically from a data set of measurements. This new semi-empirical model allows a complete description of the trapped proton fluxes at any location in the whole magnetosphere. Equation (3.41) can be re-written to highlight the main parameters:

$$f_p(\alpha, \beta) = j_{\perp}(E, B_m, L) + \left( \frac{\sqrt{E^2 + 2m_0c^2E}}{qc \sqrt{MB_m L^{-3}}} \right) \sin \beta \times \left. \frac{\partial j_{\perp}}{\partial L} \right|_{E, B_m} \quad (3.48)$$

From Eq. (3.48), it clearly appears that the observed flux  $f_p(\alpha, \beta)$  is only a function of  $E$ ,  $B_m$ ,  $L$ , and  $\beta$ , where the perpendicular flux  $j_{\perp}(E, B_m, L)$  has to be determined from unidirectional measurements or models (e.g. the directional version of AP-8). One should note that the perpendicular flux model only depends on the particle energy  $E$  and drift shell labels  $(B_m, L)$ .

### 3.3.4 Application to flux measurements

To complete the semi-empirical model, measurements of the directional proton flux in the radiation belts have to be available in order to determine  $j_{\perp}$  and  $\partial j_{\perp} / \partial L$ . Three datasets of unidirectional proton fluxes in the SAA have been studied in TREND-3:

- AZUR/EI-88 with a field of view of  $\pm 21^\circ$ ;
- SAMPEX/PET with a field of view of  $\pm 30^\circ$ ;

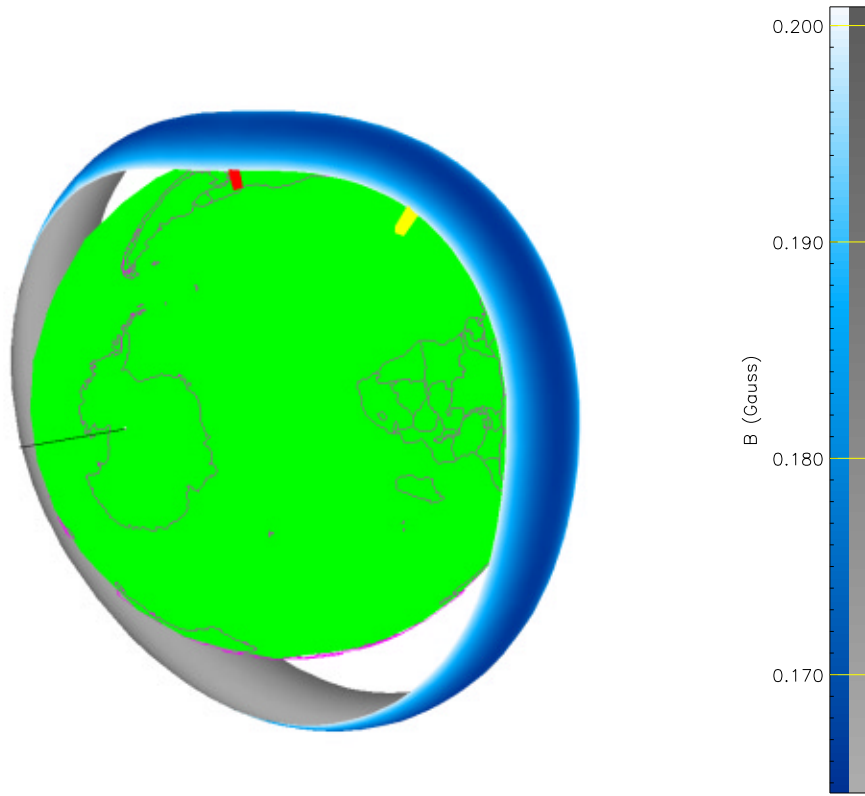


**Figure 3.7.** Representation of the magnetic drift shell  $L = 1.24$ ,  $B_m = 0.2$ . The two bars correspond to two mirror points in the southern hemisphere with a longitude of  $51^\circ\text{W}$  and  $15^\circ\text{W}$ , respectively. The IGRF 1995 magnetic field model has been used to trace the drift shell.

- UARS/HEPS with a field of view of  $\pm 15^\circ$ .

A detailed description of these satellite missions and their instruments can be found in Chapters 4, 5, and 6, respectively. Unfortunately, up to now, only the PET data can be used to test and evaluate the new model, since

- a lack in the AZUR documentation prevents the computation of the azimuthal angle from the ephemeris data;
- the 3-axis stabilised attitude of the UARS spacecraft reduces the variation of  $\beta$  to a very small angle range for a fixed value of  $B_m$  and  $L$ .

As a test case for the new semi-empirical model, we have selected from the SAMPEX/PET data a bin in  $(E, B_m, L)$  space for the period of time which extends from mid 1994 to mid 1995. The bin is specified by

$$\begin{aligned} 0.195 < B_m < 0.205, \\ 1.23 < L < 1.25, \\ 86.1 < E < 120.0. \end{aligned} \tag{3.49}$$

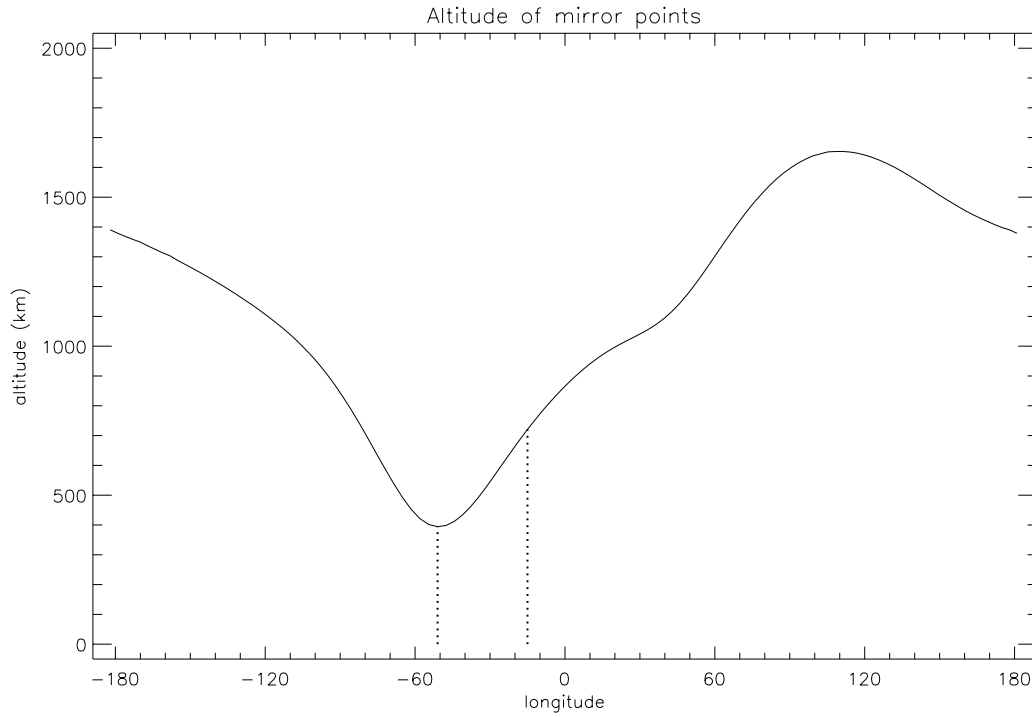


**Figure 3.8.** Geocentric altitude of the southern mirror points of the drift shell ( $L = 1.24$ ,  $B_m = 0.2$ ) as a function of the mirror point longitude. The dotted lines indicate the mirror point with the lowest altitude (at  $51^\circ$ W of longitude) and an other mirror point located at 336.5 km higher (at  $15^\circ$ W of longitude).

The IGRF 1995 magnetic field model is used to evaluate the  $B_m$  and  $L$  values. The energy range corresponds to the channel pen/p81 of the PET instrument (86–120 MeV). The Larmor radius at the mirror point corresponding to the central point of the bin specified by Eqs. (3.49) is equal to 77.2 km. The bin is represented on Fig. 3.6 where the countrates of the channel pen/p81 are shown as a function of  $B_m$  and  $L$ .

The magnetic drift shell ( $L = 1.24$ ,  $B_m = 0.2$ ) which corresponds to the central point of the selected SAMPEX data bin, is represented in a 3-D view in Fig. 3.7. The drift shell is clearly not axially symmetric and is mainly deformed near the SAA regio. The altitudes of the southern mirror points are shown on Fig. 3.8 as a function of the mirror point longitude. The lowest altitude on the shell is located at the mirror point 394.3 km,  $25.7^\circ$ S and  $51.0^\circ$ W. The location of this particular mirror point is indicated by the black bar in Fig. 3.7 and by a dotted line in Fig. 3.8. The variation of  $L_{GC}$  and the proton flux scale height are investigated below for this particular bin of data.

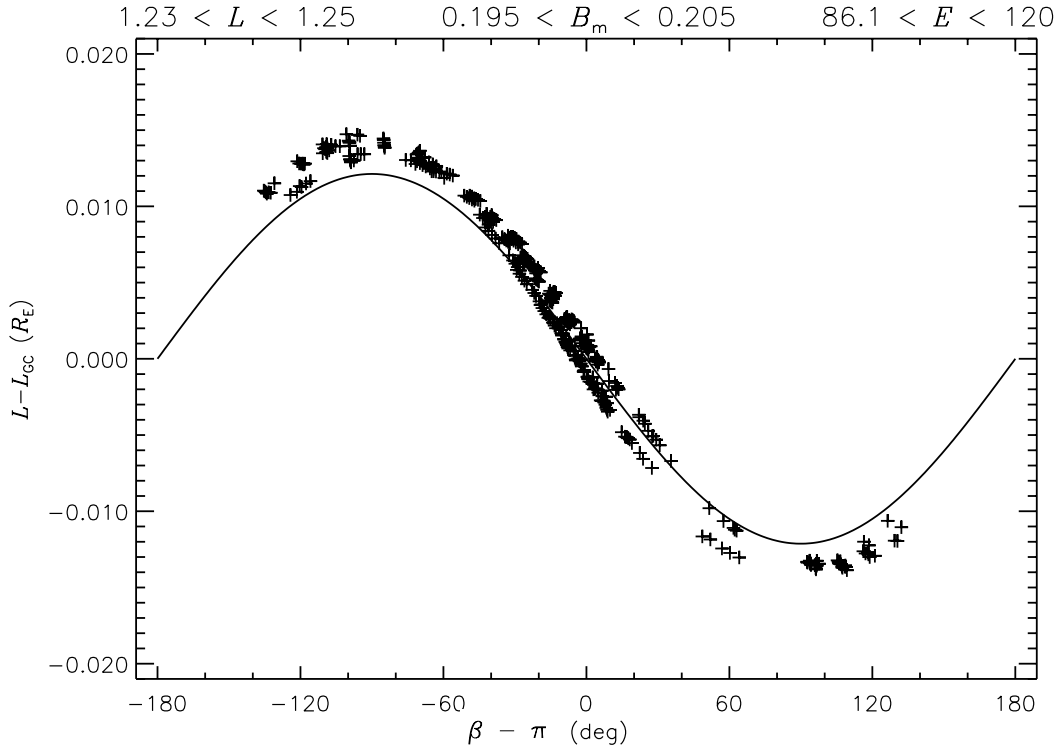


**Figure 3.9.** The variation  $\Delta L$  of the shell parameter obtained in Eq. (3.46) as a function of the azimuthal angle  $\beta$  (solid curve) is compared to the difference  $L - L_{GC}$  obtained from the SAMPEX ephemeris (+ symbols) in the coordinate bin defined in the text.

### 3.3.4.1 Variation of $L_{GC}$

Equation (3.46) predicts a variation of the shell parameter with respect to the azimuthal parameter given by

$$\Delta L = r_{gm} \sqrt{\frac{B_m}{B_0}} \sin \beta, \quad (3.50)$$

where  $r_{gm}$  and  $B_m$  are the gyroradius and magnetic field intensity at the mirror point. The validity of Eq. (3.46) or (3.50) depends only on the configuration of the magnetic field model. Instead of selecting, at random, geographic positions and look directions to evaluate the validity of these equations, we have used the SAMPEX ephemeris as a test case for the assumptions and approximations underlying Eq. (3.50).

For each point of the ephemeris in the bin defined by Eqs. (3.49), we have evaluated the shell parameter  $L$  as well as the value  $L_{GC}$  of the shell parameter at the guiding centre of 100 MeV protons. In Fig. 3.9, the difference  $L - L_{GC}$  is compared to the sinusoidal variation  $\Delta L$  predicted by Eq. (3.46) for  $B_m = 0.20$  and  $L = 1.24$ . The relatively good agreement between  $\Delta L$  and the ephemeris data validates the approximation in the determination of  $\Delta L$ . The residual scattering of the ephemeris data is attributed to the scatter of  $B_m$  and  $L$  in the bin.

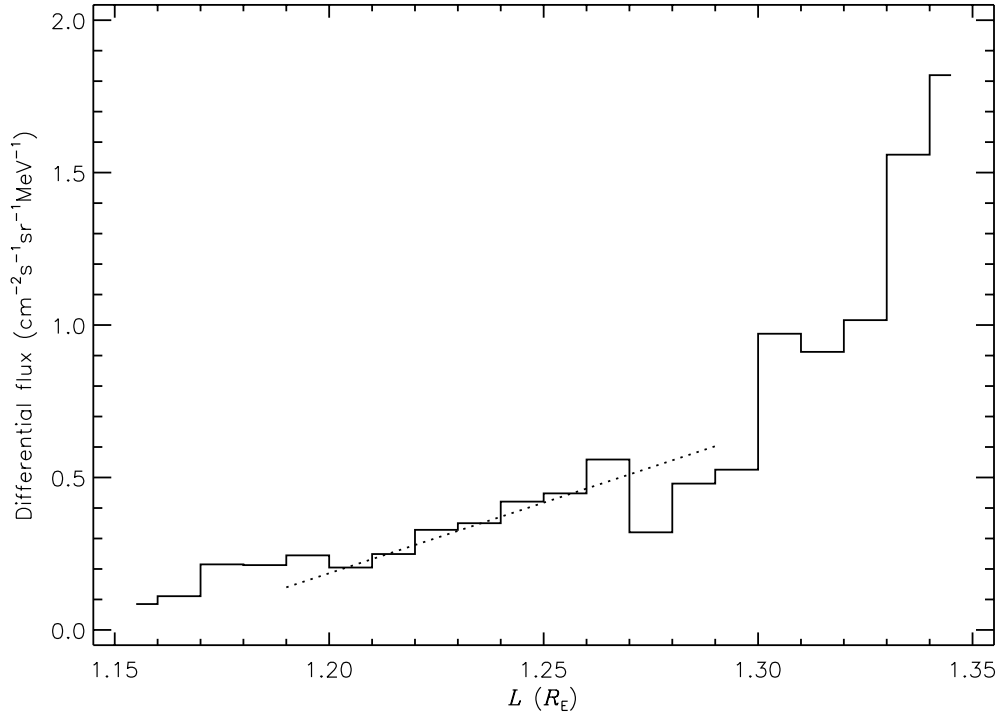


**Figure 3.10.** Dependence of the SAMPEX 86–120 MeV proton count rate on  $L$  for  $0.195 < B_m < 0.205$  and  $|\sin \beta| < 0.05$ . The dotted curve corresponds to a linear fit based on the data for which  $1.23 < L < 1.25$ .

### 3.3.4.2 Flux scale height

In order to apply the new semi-empirical model, the profile of the perpendicular flux with respect to  $L$  has to be determined. This profile will provide the two parameters of Eq. (3.41):  $j_\perp$  and its derivative with respect to  $L$ .

The profile of the perpendicular flux as a function of the shell parameter  $L$  has been obtained by selecting the PET data for which  $-0.05 < \sin \beta < 0.05$ ,  $0.195 < B_m < 0.205$  and  $1.15 < L < 1.35$ . The selection on  $\sin \beta$  retains those measurements with  $L_{GC}$  values close to  $L$ , so that  $j_\perp$  is well approximated by the mean of the selected fluxes, and that a linear fit can be used to determine  $\partial j_\perp / \partial L$ . Figure 3.10 shows the dependence on  $L$  of the proton count rate of the data points that meet the above conditions. Due to the small livetime of the PET measurements, and the corresponding poor statistics, the data in Fig. 3.10 have been binned in twenty  $L$  bins between  $L = 1.15$  and  $1.35$ . The problem relative to small livetimes is specific to the PET data and is discussed in detail in Technical Note 5, Part II.

Figure 3.11 shows a “zoom” of Fig. 3.10 around  $L = 1.24$ . The data points have again been binned in twenty  $L$  bins, now between  $L = 1.23$  and  $1.25$ . A linear fit of the binned flux of Fig. 3.11 is used to evaluate the flux at  $L = 1.24$  and the value of its derivative. The linear fit is

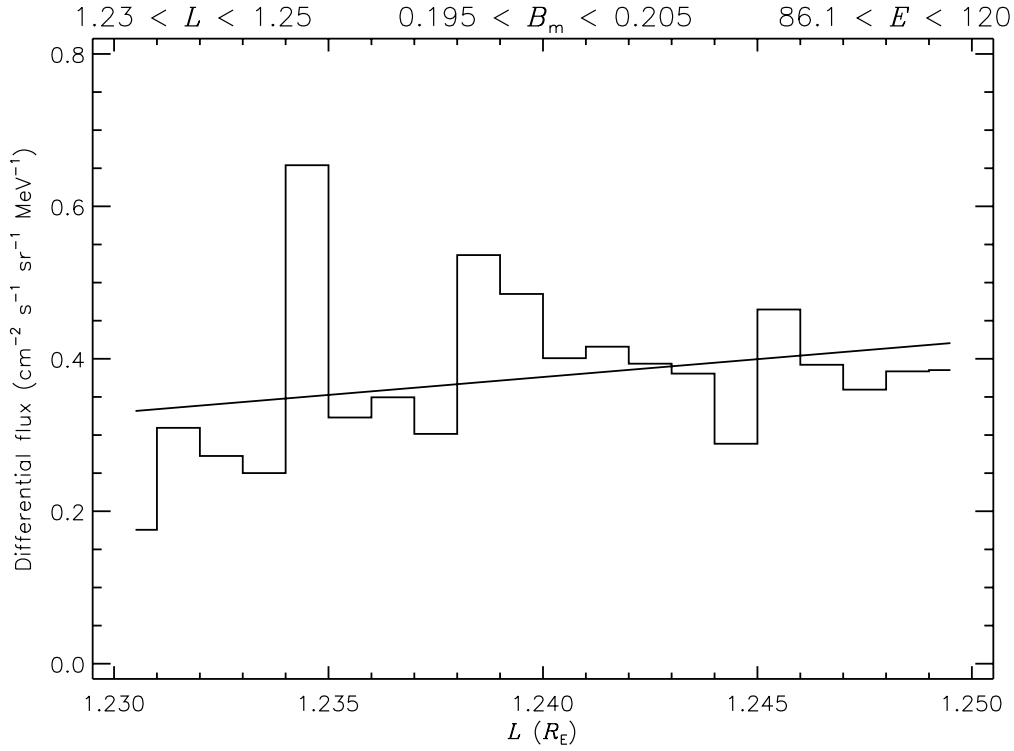


**Figure 3.11.** Dependence of the SAMPEX 86–120 MeV proton countrate on  $L$  for  $0.195 < B_m < 0.205$ ,  $1.23 < L < 1.25$  and  $|\sin \beta| < 0.05$ . The solid line corresponds to a linear fit.

given by

$$j_{\perp} = 0.375 \text{ cm}^{-2} \text{ s}^{-1} \text{ sr}^{-1} \text{ MeV}^{-1}, \quad \frac{\partial j_{\perp}}{\partial L} = 4.63 \text{ cm}^{-2} \text{ s}^{-1} \text{ sr}^{-1} \text{ MeV}^{-1} R_E^{-1}. \quad (3.51)$$

The linear fit is represented on Figs. 3.10 and 3.11 by a dotted line and a solid line, respectively. One should note the large scattering of the binned data around the linear fit. The scattering is related to the Poisson statistic behaviour of the PET measurements. Unfortunately this behaviour complicates the evaluation of the new semi-empirical model.

### 3.3.4.3 East-West asymmetry

For the bin defined by Eqs. (3.49), we have evaluated the dependence of the observed flux on the azimuthal angle  $\beta$ . In Fig. 3.12, the flux obtained with Eq. (3.41) is compared to the SAMPEX/PET measurements in the selected bin. As before, the data points have been binned, now in twenty  $\beta$  bins. Note that the bins around  $\beta = 0^\circ$  are empty.

Now that the dependence on  $L$  of the perpendicular flux is determined, Eq. (3.41) can be used to evaluate the East-West asymmetry effect. The East-West effect predicted by the new semi-empirical model is a sine curve, which is represented in Fig. 3.12 as a solid line. The main trend of the binned data is well rendered by the sine curve. Nevertheless the scatter

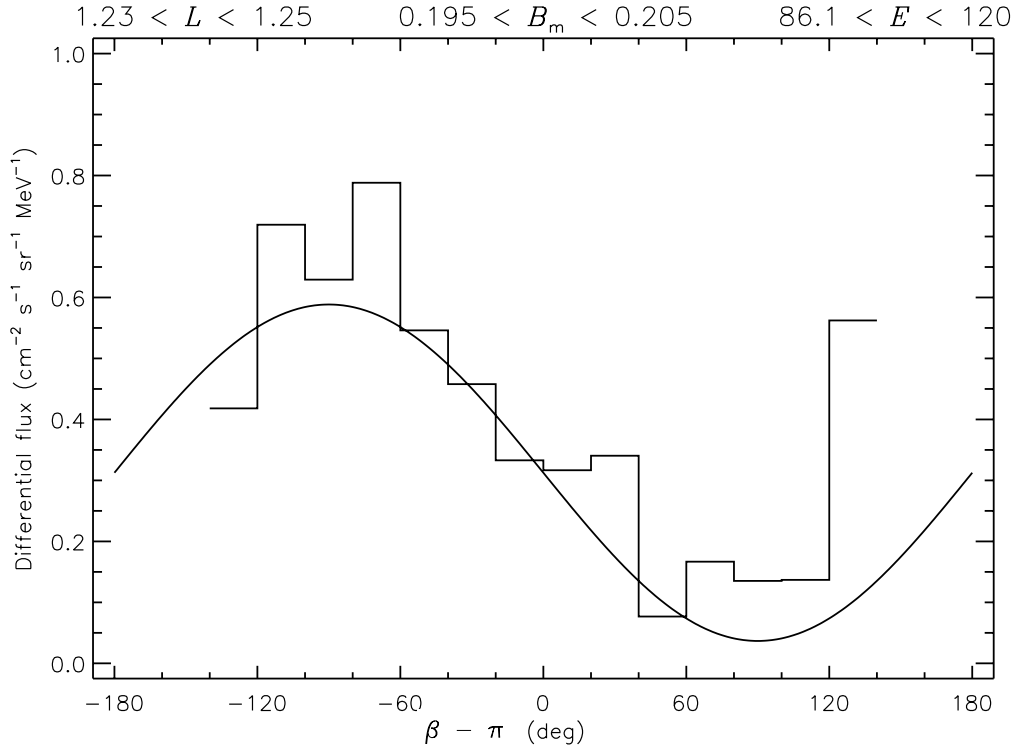


**Figure 3.12.** Dependence of the SAMPEX 86–120 MeV proton countrate on the azimuthal angle  $\beta$  for the points in the bin ( $0.195 < B_m < 0.205$ ,  $1.23 < L < 1.25$ ), i.e. the same points as Fig. 3.9. The solid curve corresponds to the linear fit of Fig. 3.11 where  $\Delta L$  is obtained from Eq. (3.46).

around the sine curve is large. Part of the scattering is due to the finite size of the bin in  $B$ ,  $L$ , and energy. Further uncertainties are introduced by the relatively large opening angle ( $60^\circ$ ) of the PET instrument which creates an uncertainty on the angles  $\alpha$  and  $\beta$ . Finally, the saturation problem of the PET (see Technical Note 5), resulting in low proton count rates, adds an inherent uncertainty factor. The combined data scatter prohibits a quantitative assessment of the model. Therefore, comparisons of the model to the directional dependence of PET data in other bins will probably not improve the validation. Moreover, even with one year of data, the coverage in  $\beta$  is not complete in all  $(B, L)$  bins.

## 3.4 Intercomparison of the anisotropy models

### 3.4.1 Angular distribution predicted by VF1-MIN and BK-MIN models

Two examples of angular distributions obtained with the VF1MIN and BK-MIN models are presented in Figs. 3.13–3.16, which correspond to the differential trapped proton flux predicted at two different points of observation  $\bar{p}$  and  $\bar{q}$  in the South Atlantic Anomaly. Both points are located at  $60^\circ\text{W}$  and  $35^\circ\text{S}$ , with altitudes of 450 km and 1,500 km, respectively.

Differential flux  $E = 20.0 \text{ MeV}$

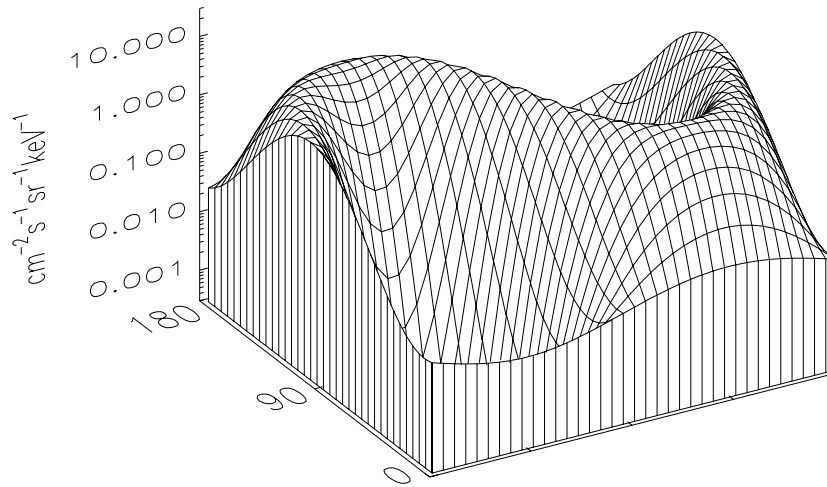


**Figure 3.13.** VF1MIN predicted anisotropy of trapped proton differential flux at  $60^\circ\text{W}$ ,  $35^\circ\text{S}$  and altitude 450 km. The proton energy is set to 20 MeV and the omnidirectional flux is fixed to  $12.5 \text{ cm}^{-2} \text{s}^{-1} \text{keV}^{-1}$ . The coordinate system is fixed relatively to the zenith direction ( $z$ -axis) and the local magnetic East direction.

Differential flux  $E = 20.0 \text{ MeV}$

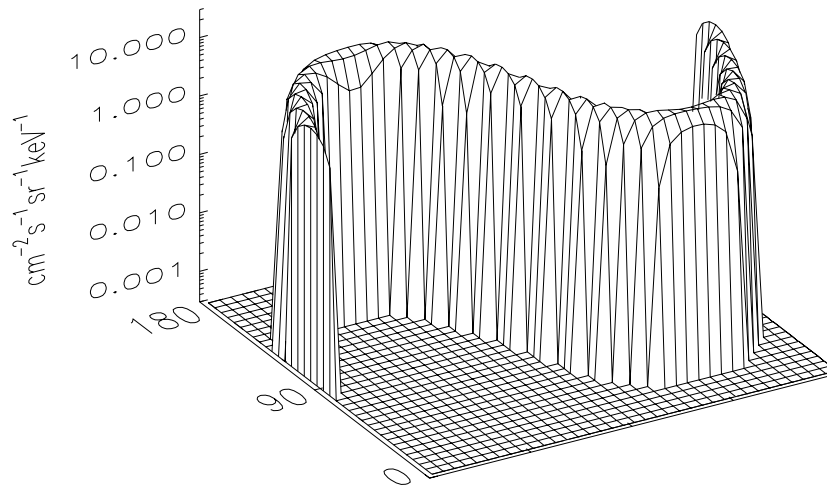


**Figure 3.14.** BK-MIN predicted anisotropy of trapped proton differential flux at  $60^\circ\text{W}$ ,  $35^\circ\text{S}$  and altitude 450 km. The proton energy is set to 20 MeV and the omnidirectional flux is  $12.5 \text{ cm}^{-2} \text{s}^{-1} \text{keV}^{-1}$ . The coordinate system is fixed relatively to the zenith direction ( $z$ -axis) and the East direction.



Differential flux  $E = 20.0$  MeV

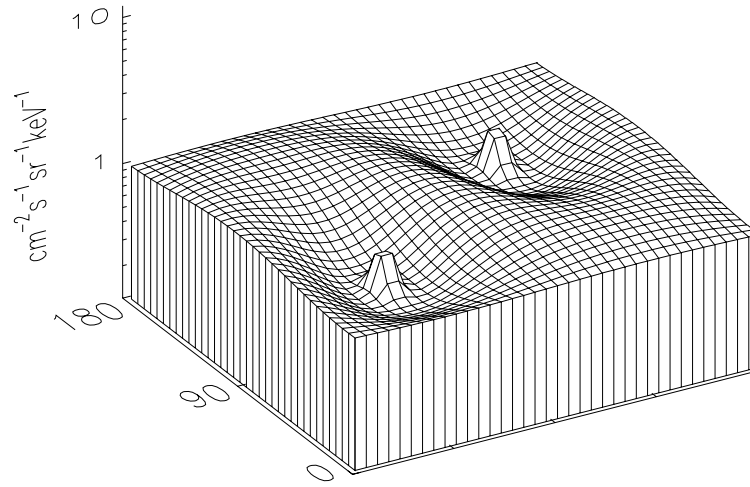


**Figure 3.15.** Same as Fig. 3.13 but for an altitude of 1500 km based on the VF1MIN model.

Differential flux  $E = 20.0$  MeV

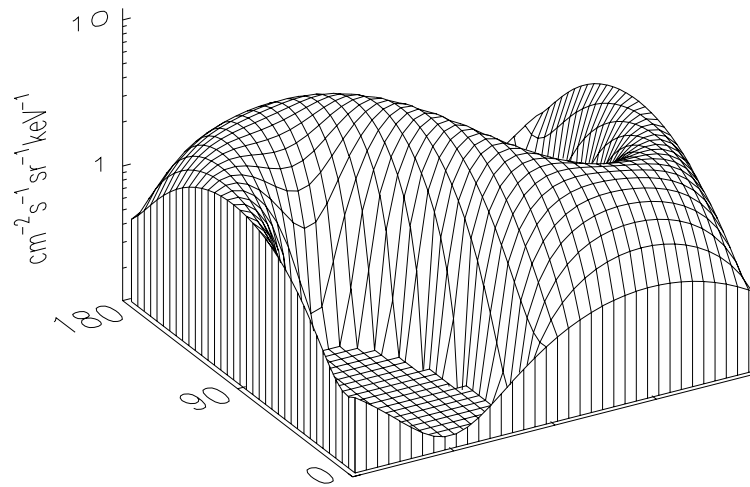


**Figure 3.16.** Same as Fig. 3.14 but for an altitude of 1500 km based on the BK-MIN model.

**Table 3.2.** Magnetic coordinates  $(B, L)$ , magnetic dip angle  $I$ , parameter  $\sigma$  and scale height  $H^{\min}$  for two points of observation. The  $(B, L)$  coordinates are obtained using the Jensen and Cain (1962) geomagnetic field model.

location	$B$ (gauss)	$L$	$I$ (deg)	$\sigma$ (deg)	$H^{\min}$ (km)	$\alpha_L$ (deg)
60°W, 35°S, 450 km	0.2210	1.28	33.6	10.3	108.1	79.5
60°W, 35°S, 1500 km	0.1551	1.47	35.2	37.4	1677.2	51.0

We use an orthogonal coordinate system defined as follows:

- the  $z$ -axis points to the zenith (corresponds to  $\bar{l}_R$  in Fig. 3.1);
- the  $y$ -axis is defined by the intersection of the mirror plane and the horizontal plane; it points in the eastward direction (corresponds to  $\bar{l}_y$  in Fig. 3.1);
- the  $x$ -axis is defined by the intersection between the mirror plane and the local vertical plane which contains the magnetic field line (corresponds to  $\bar{l}_H$  in Fig. 3.1).

We consider protons with energy  $E = 20$  MeV and an omnidirectional differential flux of  $12.5 \text{ cm}^{-2} \text{ s}^{-1} \text{ keV}^{-1}$ . The Jensen and Cain (1962) geomagnetic field model was used to obtain the  $(B, L)$  coordinates. The magnetic coordinates  $(B, L)$ , the magnetic dip angle  $I$ , the parameter  $\sigma$ , the scale height  $H^{\min}$  and the Badhwar & Konradi (1990) loss cone angle  $\alpha_L$  are given in Table 3.2.

#### 3.4.1.1 Angular distribution at 450 km altitude

The predicted angular distributions observed at the point  $\bar{p}$  corresponding to an altitude of 450 km are presented in Figs. 3.13 and 3.14, respectively, for the VF1MIN and BK-MIN models. The unidirectional differential fluxes are presented as a function of the polar and azimuthal angles. It can be seen that the angular variations of the unidirectional differential flux are quite different in Figs. 3.13 and 3.14. In Fig. 3.13, the angular distribution has two deep valleys centred respectively around the polar angles  $56^\circ$  and  $124^\circ$  and azimuthal angles  $90^\circ$  and  $270^\circ$ . These two directions correspond to the directions of the magnetic field line. The angular distribution found with the BK-MIN model, shown in Fig. 3.14, is much steeper than that corresponding to the VF1MIN model and looks like a sheer ridge. In other words, a narrower angular distribution is obtained with the BK-MIN model than with the VF1MIN model.

The pitch-angle distribution of the BK-MIN model is more sharply peaked than the one corresponding to the VF1MIN model. In the BK-MIN model, based on Badhwar and Konradi's (1990) approximation, the loss cone is defined explicitly in terms of the angle  $\alpha_L$ . At the point  $\bar{p}$ ,  $\alpha_L = 79.5^\circ$  and the unidirectional flux is confined to a cone of  $21^\circ$  opening angle. On the other hand, in the Heckman and Nakano (1969) description used in the VF1MIN model, the loss

cone is defined implicitly through the parameter<sup>4</sup>  $\sigma$ . At the point  $\bar{p}$ ,  $\sigma = 10.3^\circ$  which induces a smoother anisotropy than the Badhwar and Konradi (1990) pitch-angle distribution. At  $\alpha = 90^\circ$ , the differential flux predicted by the VF1MIN model is lower than that predicted by the BK-MIN model due to the normalisation with respect to the omnidirectional flux [see Sect. 3.2.4, Eq. (3.20)].

Since the parameter  $\alpha_L$  is obtained from a fit of the AP-8 MIN unidirectional flux database (see Sect. 3.2.2.3), the results obtained with the BK-MIN model are a better approximation for the AP-8 MIN trapped proton model than those obtained with the VF1MIN model.

### 3.4.1.2 Angular distribution at 1,500 km altitude

The angular distributions of the unidirectional differential flux predicted at the second point,  $\bar{q}$  (with altitude 1,500 km), are presented in Figs. 3.15 and 3.16, respectively, for the VF1MIN and BK-MIN models. The shape of the angular distribution for both models is quite different from that for altitude 450 km illustrated in Figs. 3.13 and 3.14.

The valleys in Fig. 3.15 are shallower than in Fig. 3.13 as a result of an increase of the parameter  $\sigma$  from  $10.3^\circ$  to  $37.4^\circ$ . However, unexpected peaks appear in the centre of both valleys at pitch-angles of  $0^\circ$  and  $180^\circ$ . They are caused by the singularity in the conversion factor  $W_{VF}$  of Eq. (3.32). Indeed, when  $\sin \alpha$  tends to zero, Expression (3.32) diverges. The singularity is a consequence of the particular normalisation method chosen by Watts et al. (1989) [see Eq. (3.32)]. This divergence should have appeared already at the lower altitude ( $\bar{p}$ ), i.e. in Fig. 3.13 where  $\sigma = 10.3^\circ$ . But in this case the value of the gaussian  $\exp[-(90^\circ - \alpha)^2/2\sigma^2]$  in Eq. (3.32) becomes very small when  $\alpha$  is near  $0^\circ$  or  $180^\circ$ , and consequently the divergence of  $W_{VF}$  is masked. In contrast, at  $\bar{q}$  where  $\sigma = 37.4^\circ$ , the value of the gaussian is much larger and the divergence of Eq. (3.32) is emphasized; therefore the two peaks clearly appear in the directions parallel and anti-parallel to the magnetic field direction.

At low altitude, where the parameter  $\sigma$  is small, this singularity does not appear. Therefore, when the altitude of observation exceeds 1,000 km, the VF1MIN and VF1MAX models should not be used.

In the BK-MIN model, the extension to a higher altitude does not cause any problems. The loss cone angle at the point  $\bar{q}$  is about  $51^\circ$  and the ridge seen in Fig. 3.14 flattens out in Fig. 3.16. In other words, the pitch-angle distribution and the East-West asymmetry become less anisotropic. However, the fact that two deep holes remain proves that at 1,500 km altitude the anisotropy of the trapped proton flux is still important.

### 3.4.2 Comparison with the semi-empirical model

In this section, we compare the new semi-empirical model described in Sect. 3.3 to the model of Watts et al. (1989) and to the BK-MIN model. For the sake of clarity, the omnidirectional

---

<sup>4</sup>The pitch-angle distribution is described with the help of a gaussian of which  $\sigma$  is the half-width parameter (see Sect. 3.2.2.1).

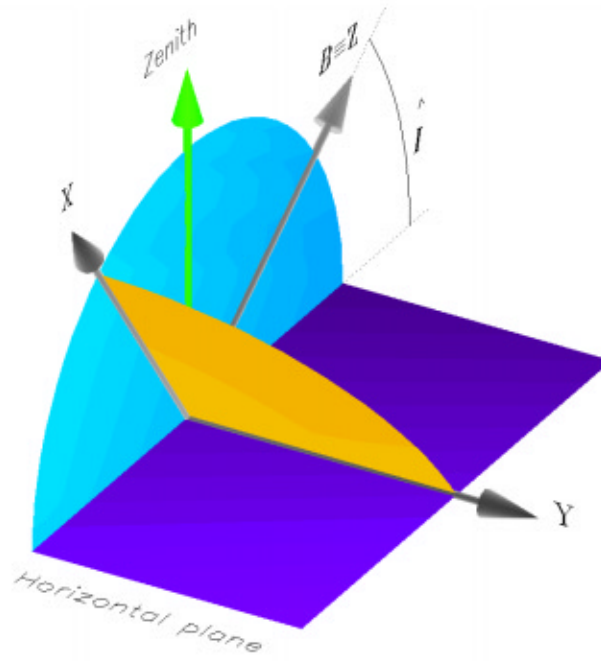


**Figure 3.17.** Representation of the coordinate system used to compare different proton anisotropy models

fluxes of the latter two models are normalized to unity, and the look directions are determined in a coordinate system such that

1. the  $Z$ -axis is parallel to the magnetic field vector;
2. the  $Y$ -axis lies in the local horizontal plane and points in the magnetic East direction;
3. the plane  $XZ$  contains the zenith direction, i.e. it is a local vertical plane;
4. the plane  $XY$  corresponds to the local mirror plane.

The coordinate system is represented in a 3-D view on Fig. 3.17. The representation in Fig. 3.17 includes the local horizontal plane, the local mirror plane and the local vertical plane which contains the magnetic field vector. Note that the coordinate system  $(Z, X, Y)$  differs from the coordinate system  $(e, n, b)$  [defined in Sect. 3.3.2] by a rotation about the  $Z$ -axis only, i.e. the azimuthal angle  $\phi$  differs from the angle  $\beta$  by an offset. The value of this offset depends on the magnetic field configuration, and thus on the geographic position.

The conversion factors  $W_{\text{HN-LS}}$ ,  $W_{\text{BK-LS}}$  and  $W_{\text{BK-beta}}$  of the three models, are compared at two geographic locations: (394.3 km, 25.7°S, 51.0°W) and (720.8 km, 7.9°S, 15.0°W), i.e. the two mirror points on the drift shell  $L = 1.24$ ,  $B_m = 0.2$ , shown in Fig. 3.7. Both points are highlighted on Figs. 3.7 and 3.8 and have been used already to compare the two pitch-angle distributions  $f_{\text{HN}}$  and  $f_{\text{HN}}$ .

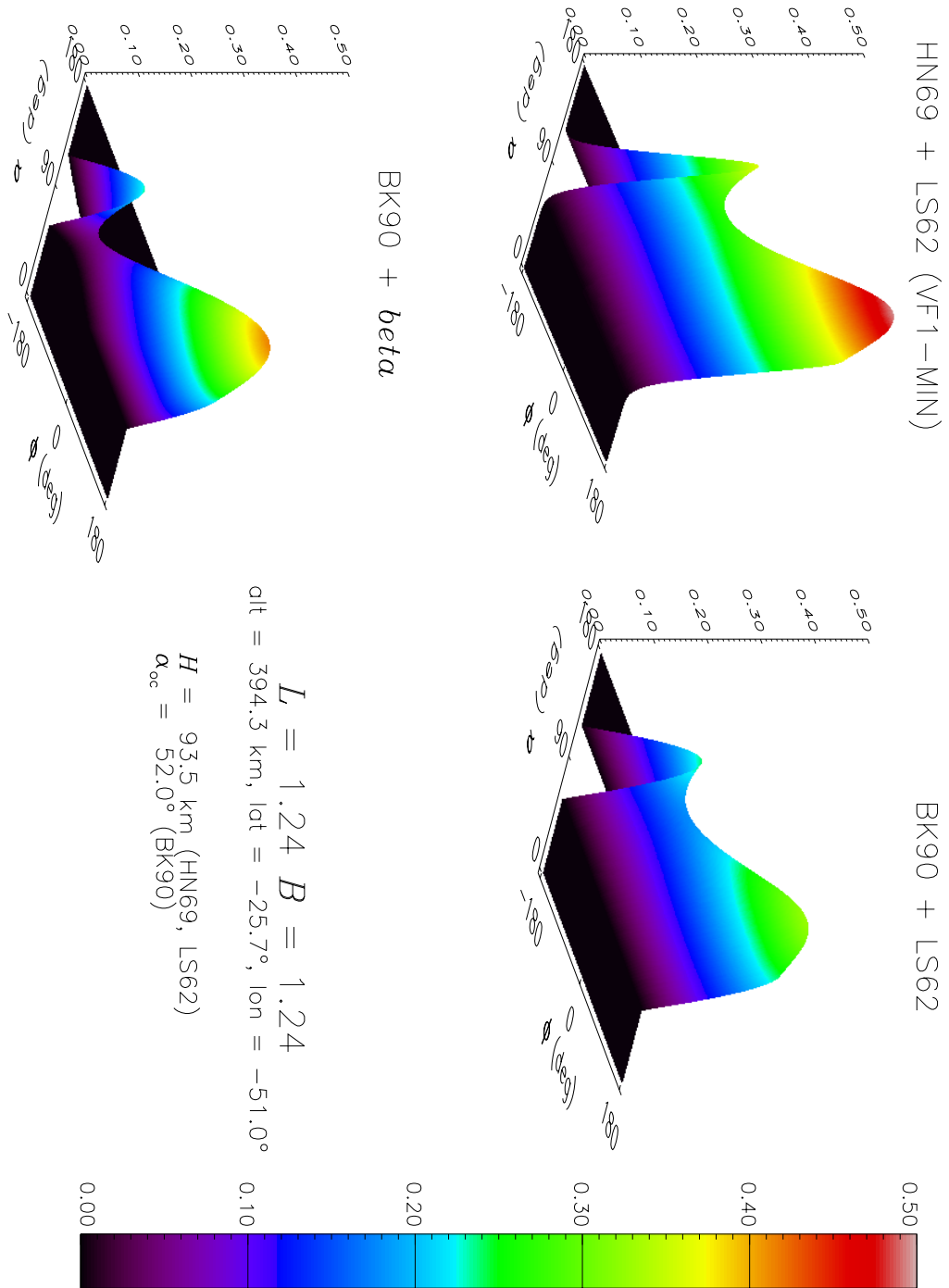


**Figure 3.18.** Dependence of the directional 100-MeV proton flux on the polar and azimuthal direction at the position (394.3 km, 25.7°S, 51.0°W)

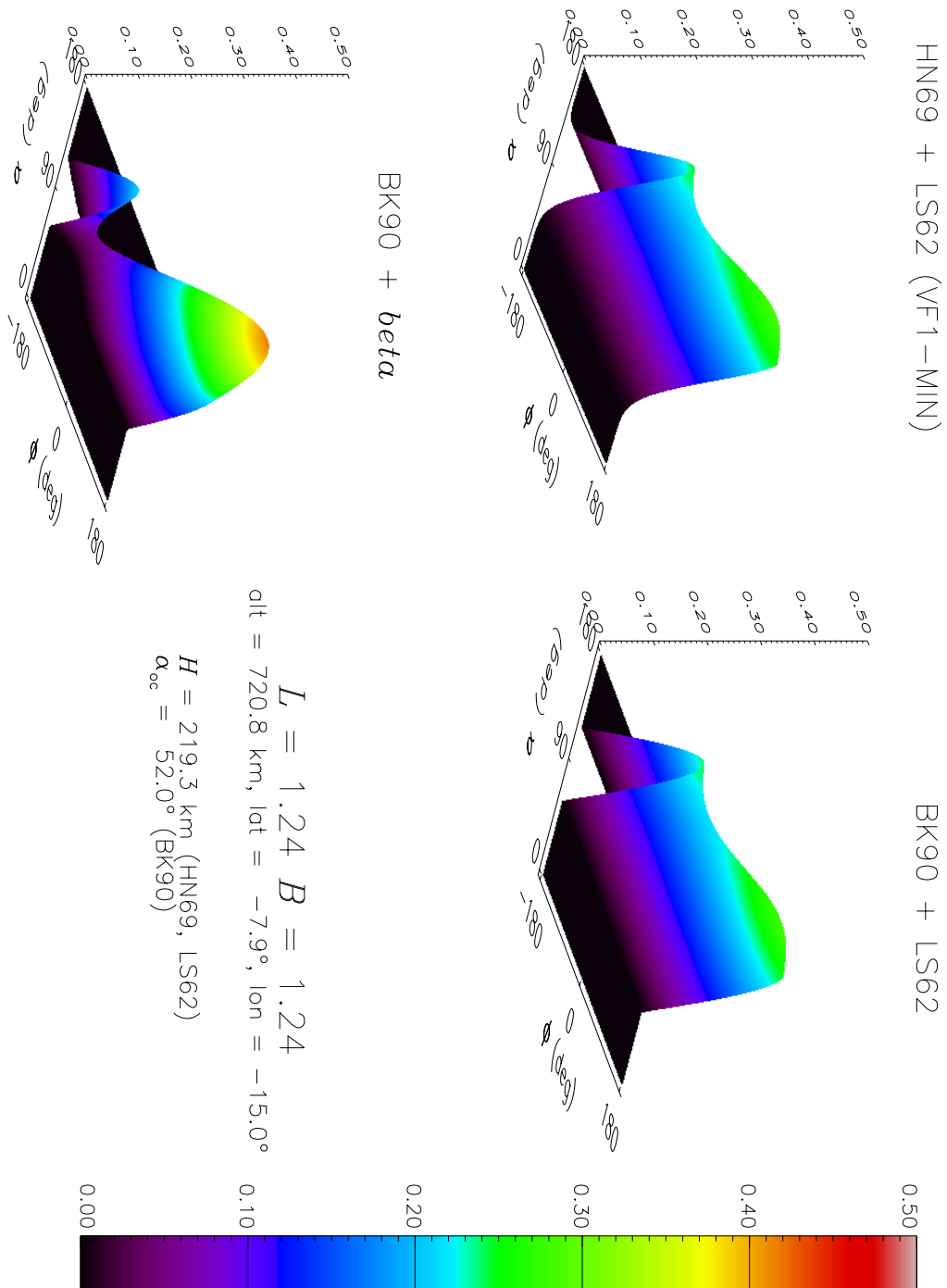


**Figure 3.19.** Dependence of the directional 100-MeV proton flux on the polar and azimuthal direction at the position (720.8 km, 7.9°S, 15.0°W)

In Figs. 3.18 and 3.19, the dependences of the flux on the polar and azimuthal angles ( $\alpha, \phi$ ) predicted by both models are compared at the two geographic locations for 100 MeV protons. Only the conversion factors  $W_{\text{HN-LS}}$ ,  $W_{\text{BK-LS}}$ , and  $W_{\text{BK-beta}}$  are represented on both figures. In Fig. 3.18, which corresponds to the lowest mirror point, the East-West asymmetry is apparent for the three models. One should note that the new semi-empirical model is more asymmetric than the two others.

In Fig. 3.19, the asymmetry is much reduced for the  $W_{\text{HN-LS}}$  and  $W_{\text{BK-LS}}$  functions. This reduction is due to the variation by a factor 7/3 of the atmospheric scale height between 394 and 721 km of altitude. On the other hand, the asymmetry of the new semi-empirical model remains unchanged. Between Fig. 3.18 and Fig. 3.19, the function  $W_{\text{BK-beta}}$  has not changed except by a small shift in the azimuthal angle due to a variation of the offset between the angles  $\beta$  and  $\phi$ .

### 3.5 ANISO software overview

The software package UNIRAD (Heynderickx et al. 1996d) is a suite of programs developed for ESA for evaluating the radiation fluences and doses experienced by a spacecraft along its orbit.

This section is devoted to the implementation of the trapped proton anisotropy models VF1-MIN, VF1-MAX, BK-MIN and BK-MAX in the UNIRAD package. This implementation consists mainly in a program called ANISO which allows to calculate the trapped proton unidirectional fluences observed for a given orbit and a given direction  $\bar{D}$  of the detector view angle, both are input parameters specified by the user.

The unidirectional fluences are obtained by the transformation of the omnidirectional differential flux into an unidirectional flux along the orbit. The unidirectional differential flux is then averaged over the whole orbit to provide an unidirectional fluence.

One should note that the ANISO software does not implemented the generalized anisotropy model presented in Section 3.3.

The implementation of ANISO does not modify the use of UNIRAD when the East-West anisotropy is bypassed. Part of the flow diagram of the new UNIRAD package is represented in Fig. 3.20. This diagram illustrates the interdependence between different program elements. The original set of UNIRAD programs has been grouped on the left hand part of the diagram. Except for PROJECT.SHP, the other output files are not shown. The right hand part of the diagram corresponds to the inputs and output of the ANISO program. The PROJECT.INT and PROJECT.MAT files contain the ephemeris and attitude of the satellite or view angles of the particle detectors. The magnetic field vector and the omnidirectional integral fluxes are provided to ANISO through the PROJECT.SPP file generated by TREP. The output file PROJECT.TRD contains the orbit averaged unidirectional integral and differential fluences. The structure of the file PROJECT.TRD is similar to that of the file PROJECT.TRI and is described in Table 3.5.

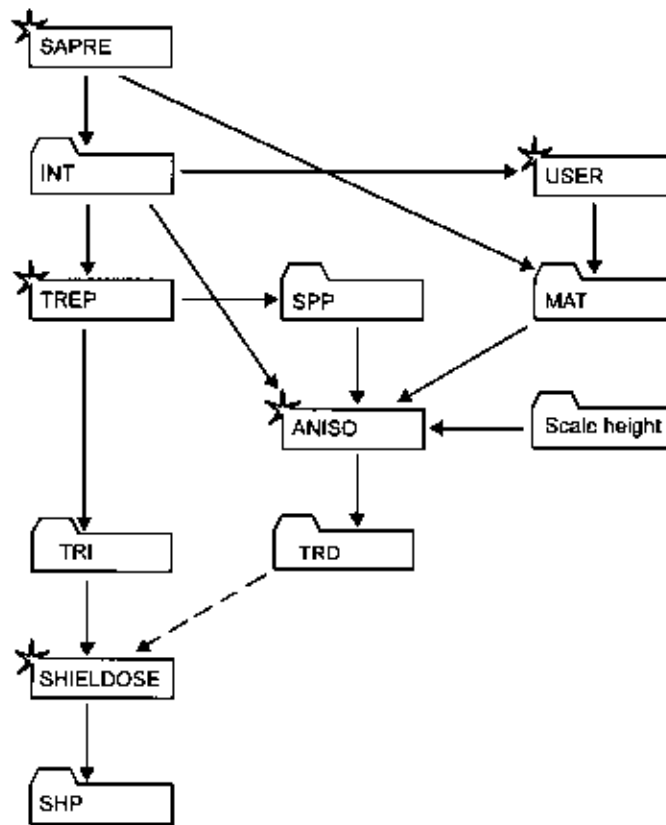


Figure 3.20. Flow diagram of UNIRAD

### 3.5.1 Attitude interface file

The attitude interface file **PROJECT.MAT** is an input of **ANISO** which contains the attitude of the satellite along its orbit. This file may be generated by **SAPRE** for the three cases listed in Sect. 3.5.1.1. For other cases, the file **PROJECT.MAT** must be produced by the user as an input.

The attitude interface file **PROJECT.MAT** is in Fortran unformatted format, with fixed record length of 80 bytes, in direct access. Each record corresponds to an orbital point in the common interface file (**PROJECT.INT**). The structure of the attitude interface file is given in Table 3.3. The rotation matrix is given by

$$[A(i, j)] = \begin{bmatrix} \bar{l}_R \cdot \bar{l}_x & \bar{l}_R \cdot \bar{l}_y & \bar{l}_R \cdot \bar{l}_z \\ \bar{l}_\theta \cdot \bar{l}_x & \bar{l}_\theta \cdot \bar{l}_y & \bar{l}_\theta \cdot \bar{l}_z \\ \bar{l}_\phi \cdot \bar{l}_x & \bar{l}_\phi \cdot \bar{l}_y & \bar{l}_\phi \cdot \bar{l}_z \end{bmatrix} \quad (3.52)$$

where  $(\bar{l}_x, \bar{l}_y, \bar{l}_z)$  is the coordinate system attached to the satellite and  $(\bar{l}_R, \bar{l}_\theta, \bar{l}_\phi)$  is the geocentric spherical coordinate system. The unit vector  $\bar{l}_R$  points to the zenith. The unit vectors  $\bar{l}_\theta$  and  $\bar{l}_\phi$  lie in the horizontal plane, pointing respectively to the geographic South and East directions.



**Table 3.3.** Record structure of the interface file `PROJECT.MAT` determining the attitude of particle detector or the view angle directions

Word	Data Type	Description
1–9	REAL*8	Rotation matrix describing the satellite attitude relative to the geographic spherical axis ( $\bar{I}_R, \bar{I}_\theta, \bar{I}_\phi$ ) at the current location of the satellite
10	REAL*8	Angle between the zenith direction and the satellite velocity vector (degrees)

### 3.5.1.1 Changes implemented in the SAPRE program

The SAPRE program has been modified to generate simple attitude interface files. This new feature is controlled by the new namelist parameter `IATTI` (INTEGER\*4). The default value is set to 0; in this case no attitude interface file is generated. When `IATTI` is set to a positive value, a `PROJECT.MAT` file is generated by SAPRE. The file contains the attitude of the satellite which corresponds to one of the 3 orientations of the satellite:

**IATTI =1** The  $z$ -axis of the satellite points to the zenith. The  $x$ -axis and  $y$ -axis are in the horizontal plane pointing respectively to the geographic North and West directions.

**IATTI =2** The  $z$ -axis is parallel to the velocity vector of the satellite. The  $x$ -axis lies in the orbital plane pointing away from the Earth. The  $y$ -axis is perpendicular to the orbital plane, pointing to the South.

**IATTI =3** The  $(\bar{I}_x, \bar{I}_y, \bar{I}_z)$  coordinate system is parallel to the geographic equatorial inertial coordinate system.

When different SAPRE namelists are present in the same file `PROJECT.NML`, `IATTI` has to be either equal to zero in every namelist, or always greater than zero. In other words, trajectories with and without ANISO calculations should not be mixed.

## 3.5.2 ANISO program

The ANISO program transforms trapped proton omnidirectional integral fluxes produced by TREP into orbit-averaged unidirectional integral and differential fluences. The program may also provide the unidirectional integral or differential fluxes along the orbit of the satellite. The transformation is based on the trapped proton anisotropy models described in Sect. 3.2.5 and 3.2.6. The ANISO program takes as input the namelist `ANISO` and reads the geodetic and  $(B, L)$  coordinates from the common interface file `PROJECT.INT`, the satellite attitude from the attitude interface file `PROJECT.MAT`, the magnetic field vector components and the full proton flux spectrum from the file `PROJECT.SPP`.

**Table 3.4.** ANISO Namelist parameters

Parameter	Type	Default	Function
JANIS	I*4	1	Anisotropy model identification number 1: VF1MIN model (Watts et al., 1990) 2: VF1MAX model (Watts et al., 1990) 3: BK-MIN model (Badhwar and Konradi, 1990) 4: BK-MAX model (Badhwar and Konradi, 1990)
NDIR	I*4	180	Number of look directions ( $12 \times 15$ )
DALPH	R*4(400)		Polar angle for each look direction in degrees. Default: $DALPH(j + 15 * i + 1) = 7.5 + 15i$ where $i$ varies from 0 to 11 and $j$ from 0 to 14.
DBETA	R*4(400)		Azimuthal angle for each look direction in degrees. Default: $DBETA(j + 15 * i + 1) = 24j$ where $i$ varies from 0 to 11 and $j$ from 0 to 14.
XOMEGA	R*4(400)	0	Solid angle (sr) for each look direction. When XOMEGA is set to zero, XALPH and XBETA are used as polar and azimuthal opening angle to compute the solid angle.
XALPH	R*4(400)	15	Polar opening angle, in degrees
XBETA	R*4(400)	24	Azimuthal opening angle, in degrees
IFULL	I*4	0	When IFULL is greater than zero, the spectrum file PROJECT.SPD is generated.

The namelist parameters controlling the program ANISO are listed in Table 3.4. The polar and azimuthal angles DALPH and DBETA are defined in the coordinate system  $(\bar{l}_x, \bar{l}_y, \bar{l}_z)$  attached to the satellite.

Please note that the trapped proton anisotropy models have to be used with the appropriate omnidirectional spectra. VF1MIN and BK-MIN make use of the model AP-8 for solar minimum<sup>5</sup> while VF1MAX and BK-MAX are defined for solar maximum<sup>6</sup>. ANISO produces a warning when the omnidirectional model and the anisotropy model are not consistent with each other.

The file PROJECT.TRD produced by ANISO contains the orbit-averaged integral and differential spectra of trapped protons for the different look directions defined by (DALPH =

<sup>5</sup>In the TREP namelist, the omnidirectional AP-8 MIN model is correctly selected by the settings: SOLACT = 'MIN', OMNI = 1 and ISPEC = 1. The  $(B, L)$  coordinates are then computed with the Jensen and Cain (1962) geomagnetic model.

<sup>6</sup>In the TREP namelist, the omnidirectional AP-8 MAX model is correctly selected by the settings: SOLACT = 'MAX', OMNI = 1 and ISPEC = 1. The  $(B, L)$  coordinates are then computed with the GSFC 12/66 (Cain et al., 1967) geomagnetic model updated to epoch 1970.

**Table 3.5.** Format of the file PROJECT.TRD. When more than one trajectory is specified, the whole structure is repeated.

Record	Format	Description
1	1X,A80	Project header
2	5H E-W ,A8	Omnidirectional trapped proton model header
3	1X,A32	Header of the internal geomagnetic field model
4	1X,A32	Header of the external geomagnetic field model
5	I3,3X,I3,3X, F8.1,12X,I3	Numbers of internal and external field models, epoch for internal magnetic field model and number of look directions
6	F6.1,2F8.1	Orbit inclination (deg), perigee height (km) and apogee height (km)
7	34X,E11.4, 4X, A6	Total orbit time (hrs) and anisotropy model header
8	2F10.5	Polar and azimuthal angle (degrees) of the first look direction
9	2F10.5, F20.6	Polar and azimuthal opening angle (degrees) and solid opening angle ( $100 = 4\pi$ sr)
10	I4,16X,2I4	Number of energies (NENERP) in trapped proton spectra, index of the look direction and number of look directions
11	3E11.4	Proton energy (MeV), integral ( $\text{cm}^{-2}\text{s}^{-1}$ ) and differential ( $\text{cm}^{-2}\text{s}^{-1}\text{keV}^{-1}$ ) flux
:		:
10+NENERP	3E11.4	Proton energy, integral and differential flux
11+NENERP		Blank line
12+NENERP		Blank line
13+NENERP		Blank line
14+NENERP		Same as lines 8–(13 + NENERP) for the second look direction
:		:

$\zeta, \text{DBETA} = \eta$ ). The format of the file is described in Table 3.5. For each look direction, the orbit-averaged trapped proton differential spectra is evaluated as

$$\bar{j}(E, \zeta, \eta) = \frac{\Delta\Omega}{\sum_{\bar{p}} \delta t(\bar{p})} \sum_{\bar{p}} W(E, \bar{p}, \zeta, \eta) \left( -\frac{dJ(E, \bar{p})}{dE} \right), \quad (3.53)$$

where the summation is taken over each orbital point,  $\delta t$  is the elapsed time between two successive orbit points,  $\Delta\Omega$  the opening solid angle (XOMEGA),  $J(E, \bar{p})$  is the TREP omnidirectional integral spectrum and  $W$  is the anisotropy correction factor [see Eqs. (3.32)] where the look direction  $(\zeta, \eta)$  is related to the correct proton velocity direction  $(\alpha, \phi)$ . The orbit-averaged

**Table 3.6.** Format of the file PROJECT.SPD. When more than one trajectory is specified, the whole structure is repeated.

Record	Format	Description
1	7X, I12, 12X, 3 I12	Number of look directions (NDIR) and starting date (year, month, day)
2	7X, <NDIR>F12.2	Polar angle (deg) for each direction (DALPH)
3	7X, <NDIR>F12.2	Azimuthal angle (deg) for each direction (DBETA)
4	7X, I12, 12X, 3F12.2	Number of energies (NENERP) and location $\bar{p}$ of the satellite (altitude, latitude and longitude)
5	F7.1, <NDIR>E12.4	Energy and conversion factor $W(E, \bar{p}, \zeta, \eta)$ for each direction
:	:	:
4+NENERP	F7.1, <NDIR>E12.4	Energy and conversion factor for each direction
5+NENERP		Same as lines 4–(4 + NENERP) for the second location
:		:
—		Blank line

integral spectra are computed as

$$\bar{J}(E, \zeta, \eta) = \int_E^\infty \bar{j}(E', \zeta, \eta) dE'. \quad (3.54)$$

When the namelist parameter IFULL is greater than zero, the file PROJECT.SPD is generated. This file contains the angular distribution of the trapped proton fluxes along the orbit. The format of this file is described in Table 3.6.

### 3.5.2.1 Program check

To test the ANISO we have calculate the right hand side of the following equality:

$$\bar{J}(E) = \sum_{\zeta, \eta} \bar{J}(E, \zeta, \eta) \quad (3.55)$$

and compared it to the orbit-averaged omnidirectional integral spectrum provided by TREP. In Fig. 3.21, the relative difference (in percentage) between the two spectra is presented as a function of the proton energy. It corresponds to fifteen consecutive orbits at 300 km perigee,

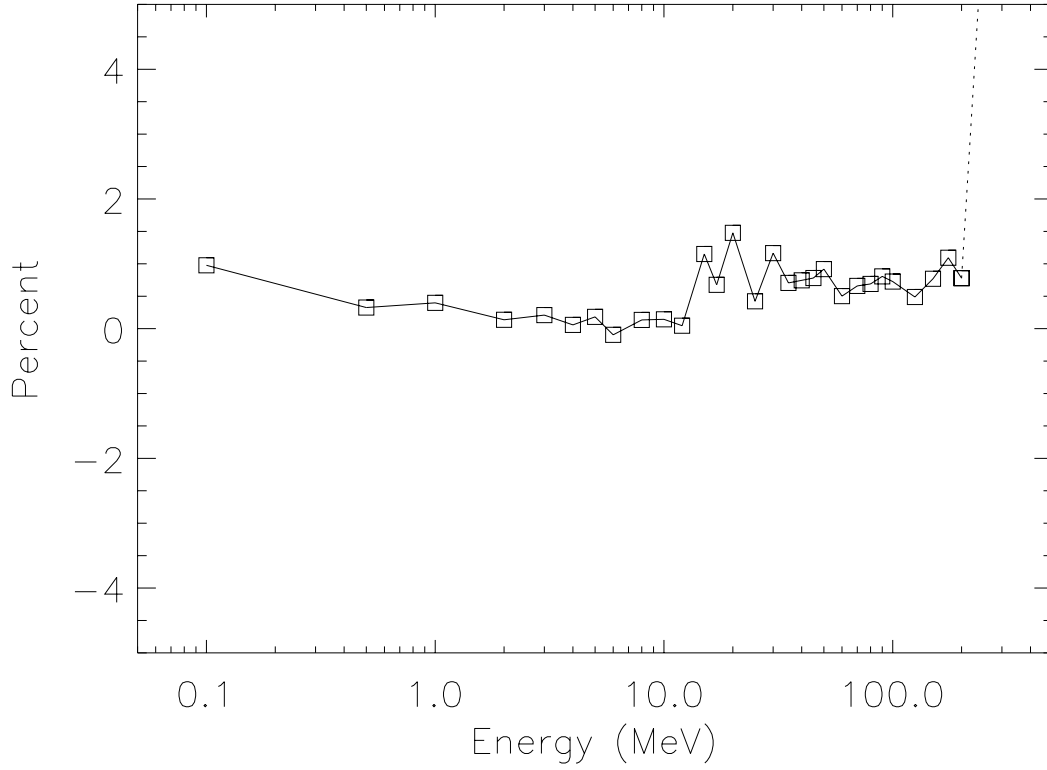


**Figure 3.21.** Relative difference between the orbit-averaged omnidirectional integral spectrum produced respectively by ANISO and by TREP. This average is evaluated over fifteen consecutive orbits at 300 km perigee, 2,000 km apogee and  $28.5^\circ$  inclination. The trapped proton models are AP-8 MIN and VF1MIN, respectively for TREP and ANISO.

2,000 km apogee and  $28.5^\circ$  inclination. The unidirectional flux is computed over the 180 default look directions. The omnidirectional integral spectrum provided by ANISO is almost identical to the TREP spectrum which is a test of validity of the numerical code. The very small differences are due to

1. the numerical differentiation of the TREP omnidirectional integral spectrum  $J(E, \bar{p})$ ,
2. the approximations in the normalisation of the anisotropy factor  $W(E, \bar{p}, \zeta, \eta)$ ,
3. the numerical integration of the orbit-averaged differential spectrum  $\bar{j}(E, \zeta, \eta)$ ,
4. the finite size of the opening solid angle  $\Delta\Omega$ .

In spite of all these sources of errors, the differences remain very small. This leads us to conclude that the ANISO program is functioning correctly.

**Table 3.7.** Interactive menu options of ANISOPOS

Code	Action
1	Modify the title
2	Change the geomagnetic field model:
21	– IGRF/DGRF
22	– Jensen and Cain (1962)
23	– GSFC 12/66
3	Modify the epoch of the geomagnetic field model
4	Change the trapped proton anisotropy model:
41	– VF1MIN
42	– VF1MAX
43	– BK-MIN
44	– BKMAX
5	Change the omnidirectional integral flux:
51	– Power law spectrum, defined by two energies and two flux values
52	– Exponentially decreasing spectrum, defined by two energies and two flux values
53	– PROJECT.TRI
6	Modify the lower energy of the spectrum
7	Modify the upper energy of the spectrum
8	Specify the geodetic altitude of the point of observation
9	Specify the geodetic latitude of the point of observation
10	Specify the geographic longitude of the point of observation
11	Evaluate the $(B, L)$ coordinates of the point of observation
0	Run the model
-1	Exit and print the results

### 3.5.3 ANISOPOS

As a byproduct of ANISO a standalone program called ANISOPOS has also been developed. This program evaluates the trapped proton flux anisotropy at a given single location. ANISOPOS works interactively and is self-explanatory.

The user has to supply a project name, a title, an internal geomagnetic field model [e.g. Jensen & Cain (1962)], and the geographical coordinates of a point of observation, and has to select an anisotropy model (e.g. BK-MIN or VF1MIN). The integral flux is generated either by a ASCII input file (PROJECT.TRI) or as a fit to a power law or to an exponential function. Here the user has to input two values of the particle energy corresponding to the range of energy over which the fit is performed and two value of the integral flux. ANISOPOS takes its input interactively from the keyboard. The different commands are given in Table 3.7.

ANISOPOS calculates the unidirectional differential and integral trapped proton fluxes and generates the output files PROJECT.TRD and PROJECT.TRI.

**Table 3.8.** ANISOPOS namelist parameters. This namelist is only used for non-interactive applications.

Parameter	Type	Default	Function
TITLE	A*56		Project header
GDALT	R*8	500	Geodetic altitude in km
GDLAT	R*8	-35°	Geodetic latitude in degrees
GDLON	R*8	300°	Geographic longitude in degrees
MODEL	I*4	0	Geomagnetic field model number, from 0 to 2
BLTIME	R*8	1995	Epoch for the geomagnetic field model IGRF
GSFCTIME	R*8	1970	Epoch for the geomagnetic field model GSFC 12/66
JANIS	I*4	1	Anisotropy model number
SPECTRUM	I*4	1	Omnidirectional integral flux number (1–3). The integral flux is defined by the file PROJECT.TRI when SPECTRUM = 3.
ENG01	R*8	1	When SPECTRUM is less than 3, energy of the lower limit of the spectrum, in MeV
FJ01	R*8	10 <sup>5</sup>	When SPECTRUM is less than 3, integral flux at ENG01
ENG10	R*8	10	When SPECTRUM is less than 3, energy of the upper limit of the spectrum, in MeV
FJ10	R*8	10 <sup>4</sup>	When SPECTRUM is less than 3, integral flux at ENG10

The file PROJECT.TRI contains the omnidirectional fluxes while PROJECT.TRD contains the matrix of unidirectional fluxes for a set of look angles.

For non-interactive applications, ANISOPOS takes its input from the namelist ANISOPOS of the file PROJECT.NML. The parameters of the namelist are listed in Table 3.8.

### 3.5.3.1 Example

A sample run of ANISOPOS is presented in Fig. 3.22. It corresponds to the angular distribution of trapped proton differential flux predicted by VF1MIN. The flux is evaluated at the 60°W, 35°S and altitude 450 km. The location and the trapped proton anisotropy model are the same as those used in Fig. 3.13. The omnidirectional flux is fixed to

$$J(E) = 10^4 \left( \frac{E}{10 \text{ MeV}} \right)^{-4} \text{ cm}^{-2} \text{ s}^{-1}. \quad (3.56)$$

Each panel of Fig. 3.22 is the polar plot of the angular distribution in a different plane. The radius of each curve is proportional to the directional flux intensity. The different curves correspond respectively to the integral flux for proton energies above  $E = 30, 40$  and  $50 \text{ MeV}$ .

The upper left panel corresponds to the local mirror plane, i.e. the plane which is perpendicular to the magnetic field direction. The horizontal axis corresponds to the intersection between the local mirror plane and the local horizontal plane. This intersection determines the local magnetic East and West directions. The upper left panel illustrates clearly the East-West effect.

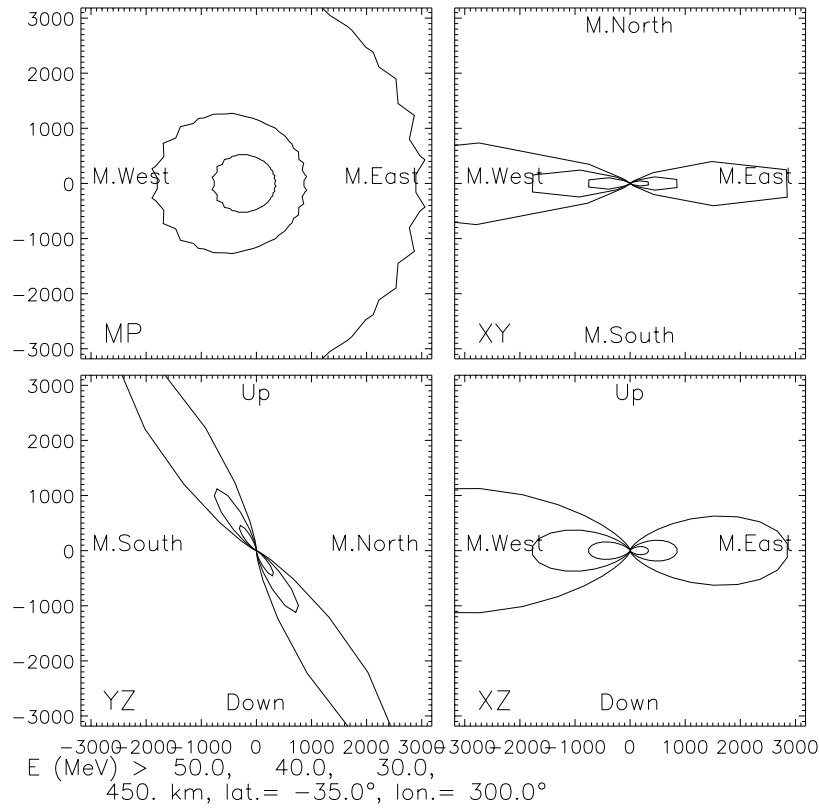


**Figure 3.22.** Angular distribution of trapped proton integral flux at  $60^\circ\text{W}$ ,  $35^\circ\text{S}$  and altitude 450 km for 30, 40 and 50 MeV proton energies as obtained from the VF1MIN model. The upper left panel corresponds to the local mirror plane. The other three panels correspond to cut view in the planes  $xy$ ,  $yz$  and  $xz$  of the satellite coordinate system in the horizontal plane. The  $z$ -axis points to the zenithal direction and the  $x$ -axis points to the East direction in the horizontal plane.

The upper right panel corresponds to a cut view in the local horizontal plane. The horizontal axis is the same as in the upper left panel. The vertical axis lies in the local horizontal plane and is perpendicular to the local magnetic East-West axis: it determines the local magnetic North and South direction. At the point of observation, the loss cone occupies a large fraction of the solid angle.

The lower left and lower right panels correspond to cut views in two vertical planes. At the point of observation, the magnetic field line is parallel to the plane of the lower left panel. The horizontal axis in this panel corresponds to the local magnetic North-South axis. The pitch-angle distribution is nicely illustrated in this panel.

The lower right panel corresponds to the plane perpendicular to the one of the lower left panel. Its horizontal axis corresponds to the magnetic East-West axis. These four panels provide to the user a reliable sketch of the trapped proton anisotropy at the point of observation.



# Chapter 4

## The AZUR/EI-88 data base and radiation belt model

One of the tasks of WP 2.1 and 2.1R (Flight Data Comparisons) was to re-examine the old AZUR data set in order to build a proton belt model. The low altitude part of the NASA AP-8 MAX model is based entirely on the AZUR data set (Vette 1991b).

### 4.1 The AZUR mission

The AZUR satellite was launched on November 8, 1969, into a  $102.9^\circ$  inclination, sun-synchronous polar orbit with apogee 3145 km and perigee 384 km. The last telemetry data were recorded on June 18, 1970. Unfortunately, the data gathered after March 5, 1970 have been lost.

A cross sectional view of the AZUR satellite is shown in Fig. 4.1. The satellite was magnetically stabilized, with one axis aligned along the magnetic field direction, as shown in Fig. 4.2. The full orbital parameters are given in Table 4.1. The AZUR satellite has international reference 1969-097A No. 4221.

The instrument complement included detectors to measure the directional and omnidirectional fluxes of protons and electrons. These instruments and the high quality of the resulting measurements made the AZUR mission particularly well suited for the study of the trapped radiation environment, despite the short duration of the mission. The energetic proton measurements, which were collected during the maximum of Solar Cycle 20, were the basis for the low altitude part of the NASA model AP-8 MAX (Sawyer & Vette 1976).

#### 4.1.1 Mission goals

The mission goals were the measurements of the following quantities:

1. directional proton intensities in several energy intervals between 0.25 and 100 MeV (two particle telescopes EI-88/1 and EI-88/2, PI D. Hovestadt);

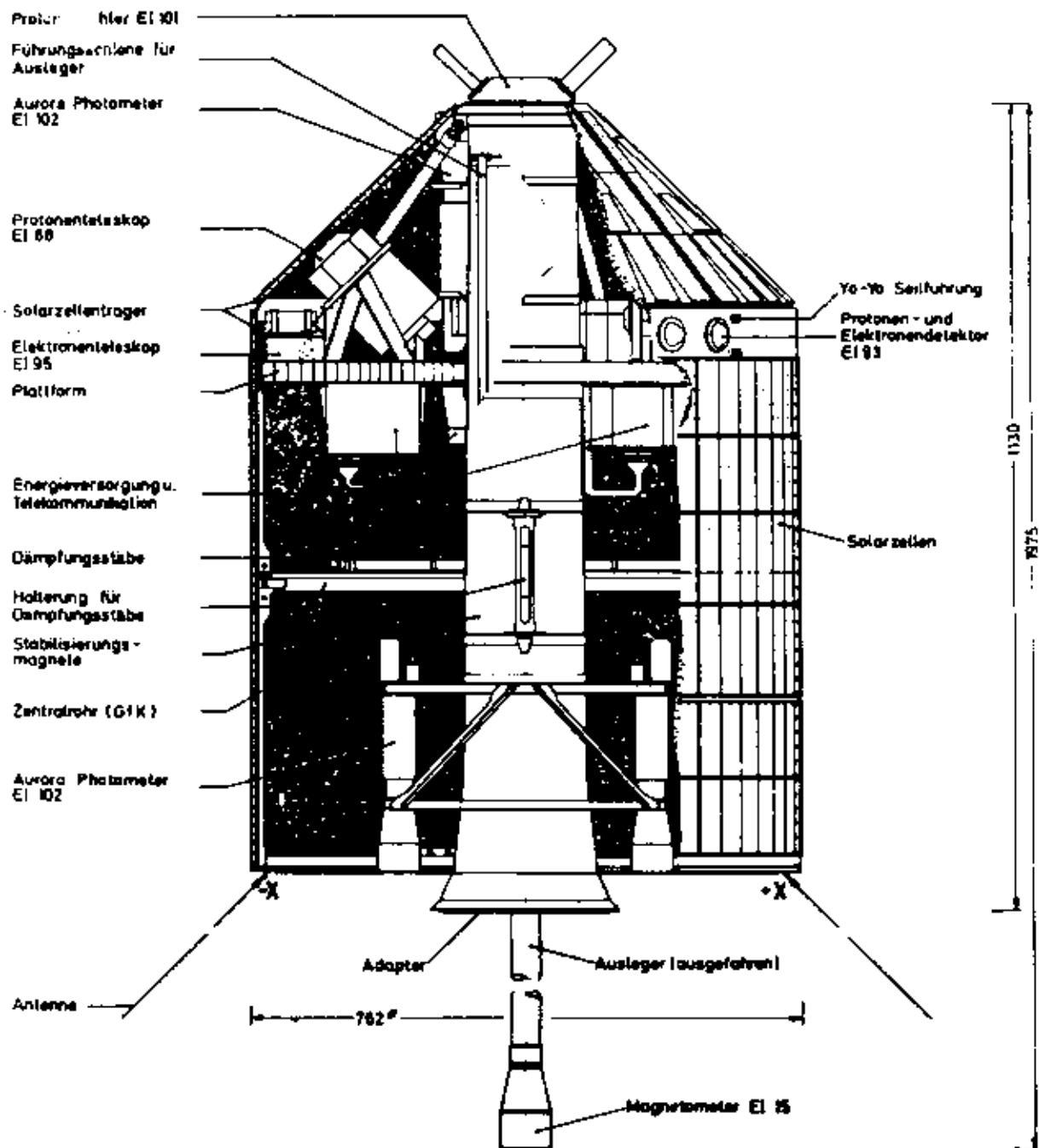


Figure 4.1. Cross section of the AZUR satellite

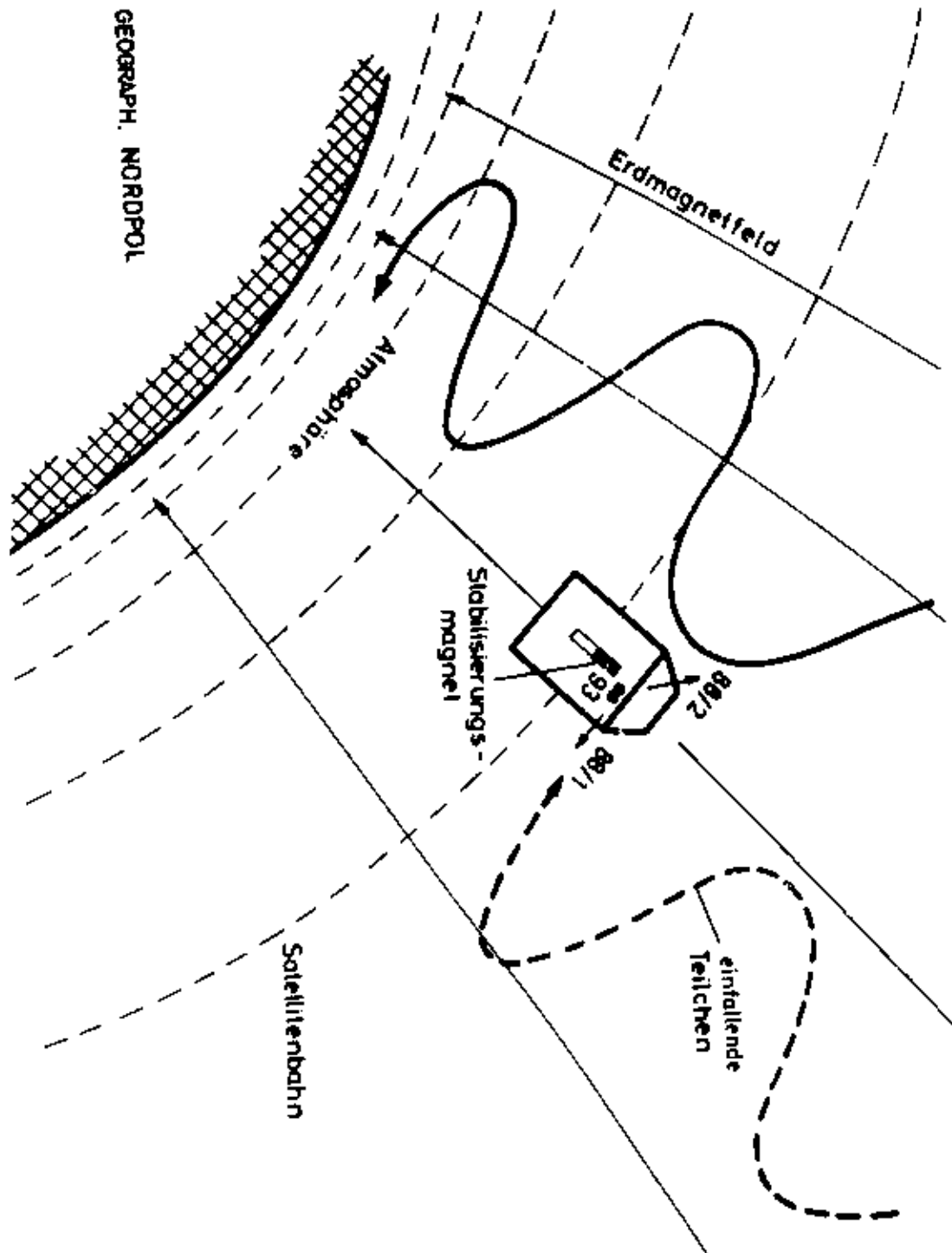


Figure 4.2. Representation of the orbital attitude of the AZUR satellite

**Table 4.1.** Orbital elements of the AZUR satellite

Orbital Element	Nominal Orbit	First Orbit
Semi-major axis (km)	8179.09	8142.80
Eccentricity	0.17337	0.16957
Inclination (deg)	102.671	102.975
Argument of perigee (deg)	161.801	161.906
Right ascension of ascending node (deg)	125.490	126.564
Period (m)	122.688	121.87603
Perigee height (km)	382.69	383.84
Apogee height (km)	3218.72	3145.43
Geocentric perigee latitude at injection (deg)	17.741 N	17.617 N
Precession of perigee (deg/day)	1.667	1.671
Precession of node line (deg/day)	0.96	

2. directional intensity of alpha particles in the energy range 6.5–19 MeV;
3. omnidirectional proton intensities in two energy ranges: 20–45 MeV and 40–80 MeV;
4. omnidirectional integral electron intensity above two thresholds: 1.5 and 4.0 MeV;
5. directional integral intensity of charged particles parallel, antiparallel and perpendicular to magnetic field lines, above 40 keV for electrons and 0.7 MeV for protons;
6. omnidirectional integral intensity of charged particles above two thresholds: 12 and 30 MeV for protons, 0.7 and 3.2 MeV for electrons;
7. optical emission by  $N_2^+$  ( $\lambda = 3914 \text{ \AA}$ ) and  $OI-N_2$  ( $\lambda = 2972 \text{ \AA}$ );
8. transverse hydromagnetic waves with amplitudes above  $5 \gamma$  (magnetometer EI-15, PI G. Musmann).

The payload consisted of seven instruments. Descriptions of each instrument package can be found in Achtermann et al. (1970). In this study, we only use the measurements made by the two directional proton telescopes (EI-88/1 and EI-88/2), which are described below, and the magnetometer data.

## 4.1.2 The EI-88/1 and EI-88/2 proton telescopes

### 4.1.2.1 Measurement principle

The EI-88 experiment measures the directional proton flux in the energy range 1.5–100 MeV. Figure 4.3 is a cross section of the instrument. The aperture opening is constructed with a

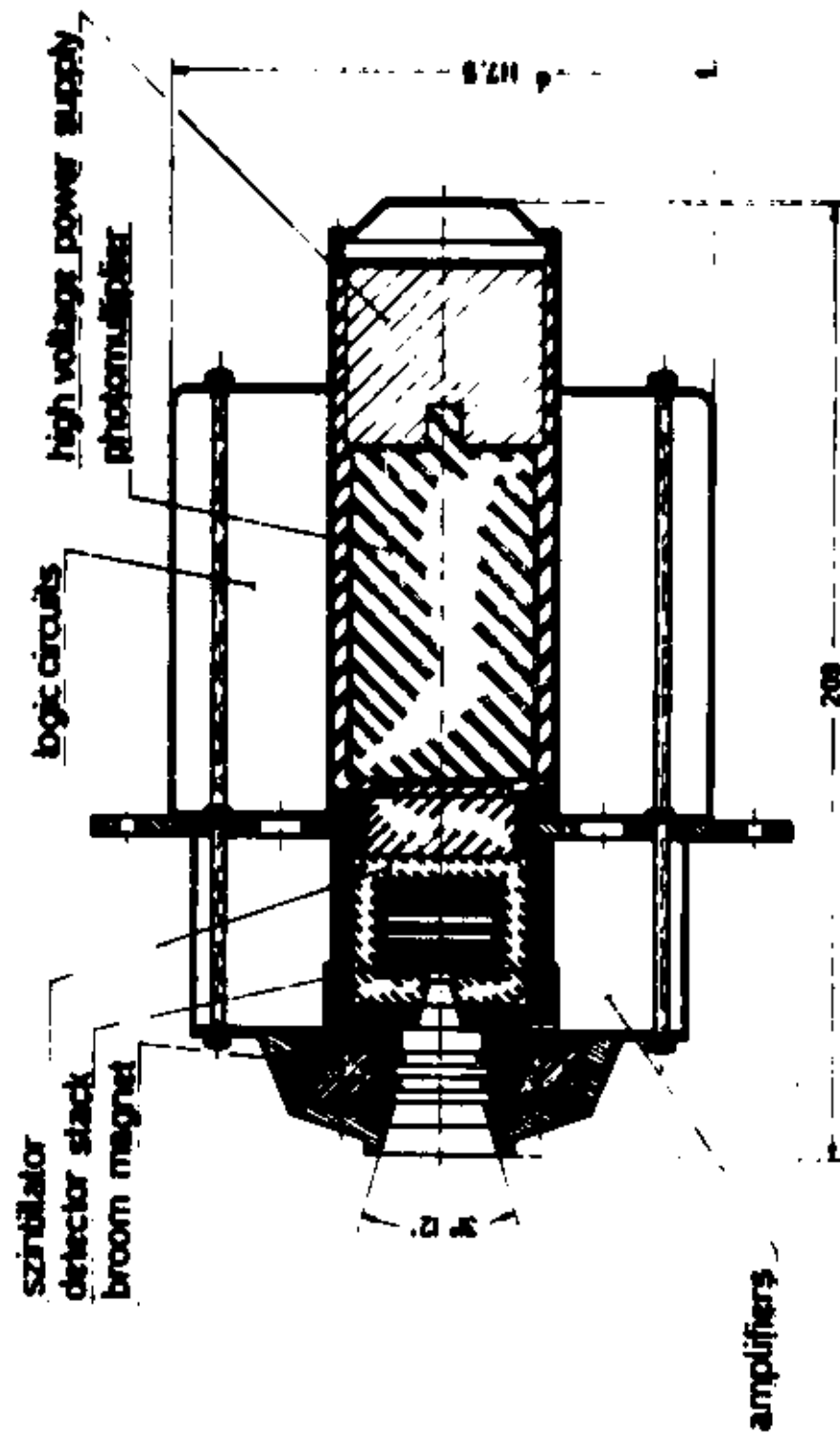


Figure 4.3. Cross section of the EI-88 instrument

number of Al and Ta collimators and is continued through a plastic scintillator surrounding the detectors and absorbers. The scintillator is connected to a photomultiplier by means of a plexiglass light conductor. The detectors respond to particle beams through the aperture opening. The energy dependent reach of the incident particles determines the number of detectors and absorbers they penetrate. Through the implementation of seven detectors and a treatment of the detector signal logic the total measurement range is divided into six energy ranges for protons and one channel for  $\alpha$  particles. The anticoincidence rates are referred to as channel 8.

The lower limit of the detector range is determined by the thickness of the Ni foil placed before the scintillator, the thickness of the first detector, and the electronic threshold of the second detector. The Ni foil with thickness  $1 \mu \sim 8.9 \times 10^{-4} \text{ g cm}^{-2}$  serves to shield the scintillator and the detectors from incoming light. The upper energy limit of the instrument is given by the absorption thickness of the combined detector cage up to the aft inner wall of the scintillator. In addition to its role as upper energy limit for particles coming in through the aperture, the scintillator also tags particles that penetrate from outside the aperture through the combined shielding. An anticoincidence switch between scintillator and detectors prohibits these particles to be measured. In order to limit the impulse rate of the scintillator and, correspondingly, the dead time of the instrument, the electronics are constructed around the scintillator and the photomultiplier to provide additional shielding.

The electronic thresholds of the semiconductor detectors (see Table 4.2) are chosen sufficiently high so that electrons penetrating the aperture without scattering do not produce a signal. This arrangement does not rule out electrons undergoing multiple scattering and pile-up effects. Therefore, the instruments are equipped with a sweeping magnet which ensures that the influence of electrons on the ion count rates is negligible (Achtermann et al. 1970).

#### 4.1.2.2 Detector layout and energy range

Figure 4.4 shows a cross section through the EI-88 sensors. The plastic scintillator surrounds an Al cage that contains the seven detectors and the three absorbers. The detector connectors are fed through holes in the scintillator and the closest Ta shield to the amplifiers, which are arranged around the detector cage. Figure 4.5 shows the energy deposited in the detectors as a function of the energy of the incident proton. The detector thresholds and switching logic yield the energy ranges for protons and  $\alpha$  particles listed in Table 4.3.

The detectors EI-88/1 and EI-88/2 are identical except for a small difference in aperture angle, and thus geometric factor. The angular response function of the telescopes is discussed in Sect. 4.3.1. The integration time for both instruments is fixed at 10 s. Due to the slow spin rate of the satellite, this rather long integration time does not compromise the quality of the directional measurements.

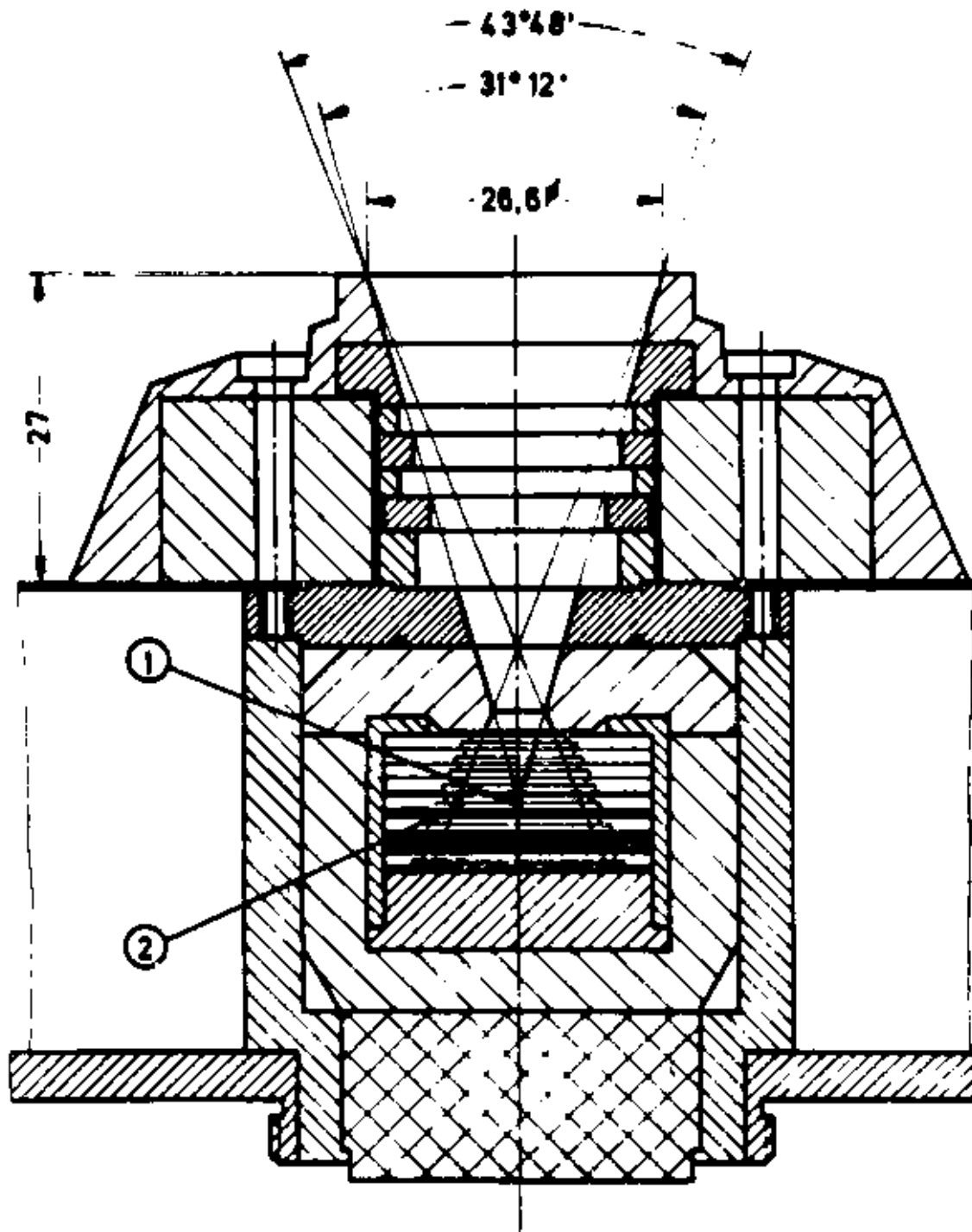


Figure 4.4. Cross section of the EI-88 sensors

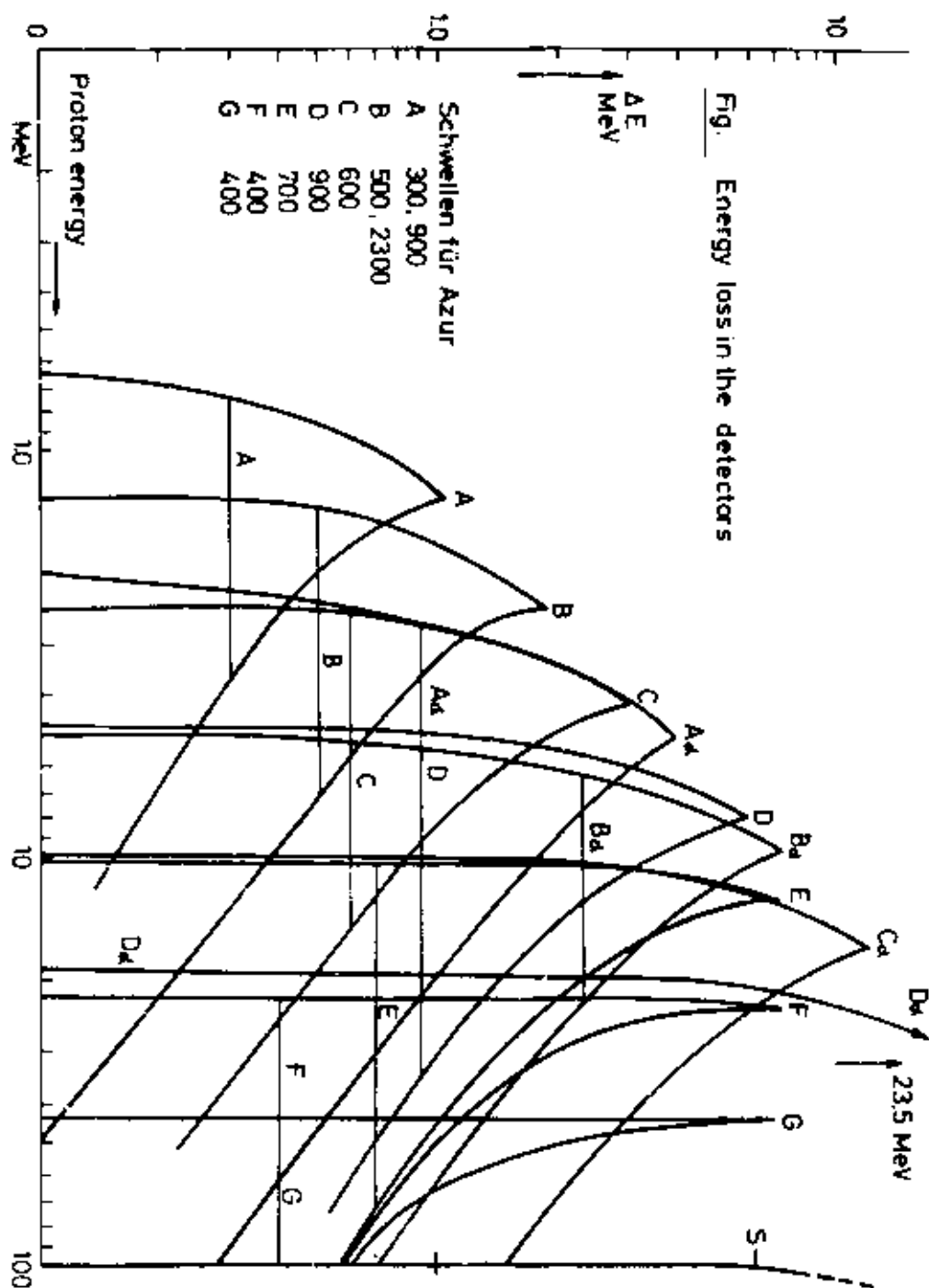


Figure 4.5. Energy deposited in the EI-88 detectors as a function of incident particle energy



**Table 4.2.** Detector and absorber characteristics of the EI-88 instruments

Detector	Absorber	Thickness ( $\mu$ )	Electronics threshold (keV)
A	Ni	1	
		20	300, 900
		50	500, 2300
B		100	600
C	Al	30	
		300	900
D	Al	200	
		400	700
E	Cu	565	
		30	
F	Al	400	400
		1750	
G	Ta	400	400
		7050	

**Table 4.3.** Energy channels of the EI-88 instruments for protons and  $\alpha$  particles

Channel	Logic	Particle	Energy range (MeV)
1	A B $\bar{C}$ $\bar{S}$	protons	1.5–2.7
2	A B $\bar{D}$ $\bar{S}$	$\alpha$	6.0–19.0
3	B C $\bar{D}$ $\bar{S}$	protons	2.7–5.2
4	C D $\bar{E}$ $\bar{S}$	protons	5.2–10.4
5	D E $\bar{F}$ $\bar{S}$	protons	10.4–22.0
6	E F $\bar{G}$ $\bar{S}$	protons	22.0–48.8
7	F G $\bar{S}$	protons	48.8–104.0
8	S	anticoincidence	

## 4.2 The EI-88 data base

In this section we describe the downloading of the data sets to a DEC Alpha workstation running OpenVMS. The data analysis is performed with a series of IDL programmes and one FORTRAN programme [to calculate  $(B, L)$  values]. The different steps in the analysis procedure are outlined and the format of the final data base is described.

**Table 4.4.** Record structure of the AZUR tape identification files

Word	Content
1	1
2	Satellite Id. Nr. 6909701
3	Experiment Id. Nr. 889293
4	Tape Nr.
5–81	Spares

**Table 4.5.** Content of the AZUR tape pass header records

Word Nr.	Content	Representation
1	Type of record	Integer
2	Year of begin of pass	Integer
3	Day of begin of pass	Integer
4	Second of begin of pass	Integer
5	Year of end of pass	Integer
6	Day of end of pass	Integer
7	Second of end of pass	Integer
8	Orbit number at begin of pass	Integer
9	First character of station name	Character
10	Second character of station name	Character
11	Third character of station name	Character
12	Fourth character of station name	Character
13	Fifth character of station name	Character
14	$K_p$	Float
15–81	Spare	

### 4.2.1 Retrieval of the data sets

The data were sent to BIRA/IASB by NSSDC in the form of two magnetic tapes. Originally, the data were sent to NSSDC by MPE on 14 tapes, each tape containing a data file and a tape identification file. NSSDC merged the data set to two tapes containing 28 binary files in total: 14 data files and 14 identification files. The tapes are 9 track, 800 bpi, unlabelled, with RECFM=VBS and BLKSIZE=9844. These two tapes were read at BIRA/IASB on an Apollo workstation and the 28 files were then transferred by binary FTP to the Alpha workstation.

The tapes were written by a CYBER machine. The internal representation of floating numbers on this architecture differs from the representation on the Alpha hardware. In addition, al-

**Table 4.6.** Content of the AZUR tape data records

Word Nr.	Content	Representation
1	Type of record (pass header or data)	Integer
2	Quality	Integer
3	Year	Integer
4	Day	Integer
5	UT (ms)	Integer
6	LT hour	Integer
7	LT min	Integer
8	MLT hour	Integer
9	MLT min	Integer
10	Orbit Nr.	Integer
11	Spare	
12	Geographic latitude (deg)	Float
13	Geographic longitude (deg)	Float
14	Geographic distance ( $R_E$ )	Float
15	Right ascension (deg)	Float
16	Declination (deg)	Float
17	Magnetic latitude (deg)	Float
18	Magnetic longitude (deg)	Float
19	$L$ ( $R_E$ )	Float
20	$B$ (gauss)	Float
21	$\Lambda$ (invariant latitude, deg)	Float
22	$R$ ( $R_E$ )	Float
23	Angle between satellite axis and $\mathbf{B}$ (deg)	Float
24	Azimuth with respect to $\mathbf{B}$ (deg)	Float
25	Aspect angle to sun (deg)	Float
26	Azimuth angle with respect to sun (deg)	Float
27	$\gamma_1$ Spin axis (geocentric, deg)	Float
28	$\gamma_2$ Spin axis (geocentric, deg)	Float
29	$\gamma_3$ Spin axis (geocentric, deg)	Float
30	$B_x$ Magnetic field vector component (geocentric, deg)	Float
31	$B_y$ Magnetic field vector component (geocentric, deg)	Float
32	$B_z$ Magnetic field vector component (geocentric, deg)	Float
33	Spare	
34	Spare	
35	Spare	
36	Station (abbreviation to one character)	Character

**Table 4.6.** (continued)

Word Nr.	Content	Representation
37	Orbit counter	Integer
38	Record counter	Integer
39	Corrected orbit counter	Integer
40	Corrected record counter	Integer
41	EI-88/1 Channel 1 counts plus 1	Integer
42	EI-88/1 Channel 2 counts plus 1	Integer
43	EI-88/1 Channel 3 counts plus 1	Integer
44	EI-88/1 Channel 4 counts plus 1	Integer
45	EI-88/1 Channel 5 counts plus 1	Integer
46	EI-88/1 Channel 6 counts plus 1	Integer
47	EI-88/1 Channel 7 counts plus 1	Integer
48	EI-88/1 Channel 8 counts plus 1	Integer
49	EI-88/2 Channel 1 counts plus 1	Integer
50	EI-88/2 Channel 2 counts plus 1	Integer
51	EI-88/2 Channel 3 counts plus 1	Integer
52	EI-88/2 Channel 4 counts plus 1	Integer
53	EI-88/2 Channel 5 counts plus 1	Integer
54	EI-88/2 Channel 6 counts plus 1	Integer
55	EI-88/2 Channel 7 counts plus 1	Integer
56	EI-88/2 Channel 8 counts plus 1	Integer
57	EI-93 Channel 1 counts plus 1	Integer
58	EI-93 Channel 2 counts plus 1	Integer
59	EI-93 Channel 3 counts plus 1	Integer
60	EI-93 Channel 4 counts plus 1	Integer
61	EI-92 Channel 1 counts plus 1	Integer
62	EI-92 Channel 2 counts plus 1	Integer
63	EI-92 Channel 3 counts plus 1	Integer
64	EI-92 Channel 4 counts plus 1	Integer
65	EI-92 Channel 5 counts plus 1	Integer
66	EI-92 Channel 6 counts plus 1	Integer
67	EI-88/1 Detector current	Integer
68	EI-88/1 Logic	Integer
69	EI-88/2 Detector current	Integer
70	EI-88/2 Logic	Integer
71	EI-93 Detector current	Integer
72	EI-92 Detector current	Integer
73	Light in EI-92	Integer



The modes of operation alternate in a fixed sequence of a period of 16 formats (10 s each): 14 formats designated with 0 are followed by 2 formats designated 1. The first format with a 1 and the first format with a 0 are a mixture of coincidence and single rates and can therefore not be used. For the final data base all formats with a 1 were rejected.

## 4.2.2 Cleaning of the data sets

The next step in the data processing is the “cleaning” of the ASCII data files `TAPEnn.DAT` generated by `TAPE.PRO`. This routine reads in a data file `TAPEnn.DAT`, rejects bad data records and produces an output file `CLEANnn.DAT`. The records of the ASCII files produced by the programme `CLEAN.PRO` do not contain all the words listed in Table 4.6, in particular the data for EI-93 and EI-92 (words 57–66), housekeeping data (words 67–81), and records 1, 11, 33–35, and 37–40 were not copied. The first line in each `CLEANnn.DAT` file consists of column headers.

The effect of the cleaning programme is shown in Figs. 4.6 and 4.7, which show the raw and cleaned count rates for a sample of channel 4 data in file `TAPE4.DAT`.

### 4.2.2.1 Rejection criteria

Not all the records in the data files are valid measurement records. Bad or contaminated records and housekeeping records were identified and not included in the final data files. Below, we describe the different rejection criteria.

**Calibration mode** Data records with the calibration mode flag (word 74) set to one can be safely rejected.

**Quality flag** Data records with quality flag (word 2) equal to two are of bad quality (or don't contain data) and can be safely rejected.

**Pitch angle not defined** A value  $-7.0$  for the angle between the satellite axis and **B** (word 23) indicates a problem with the magnetometer data. These data records are rejected.

**Mixed mode records** The modes of operation of EI-88 alternate in a fixed sequence of a period of 16 formats (10 s each): 14 formats designated with 0 are followed by 2 formats designated 1. The first format with a 1 and the first format with a 0 are a mixture of coincidence and single rates and can therefore not be used. The combined rejection criterion is that each record is rejected for which word 68 differs from word 68 in the previous record, or for which word 70 differs from word 68 in the previous record. The first record in every data file is rejected as well.

**Satellite conditions** The operational conditions of the satellite and instruments are recorded in the housekeeping records 67–81. Data records for which the actual values of the following parameters deviate too much from the average (over the whole data file, except for

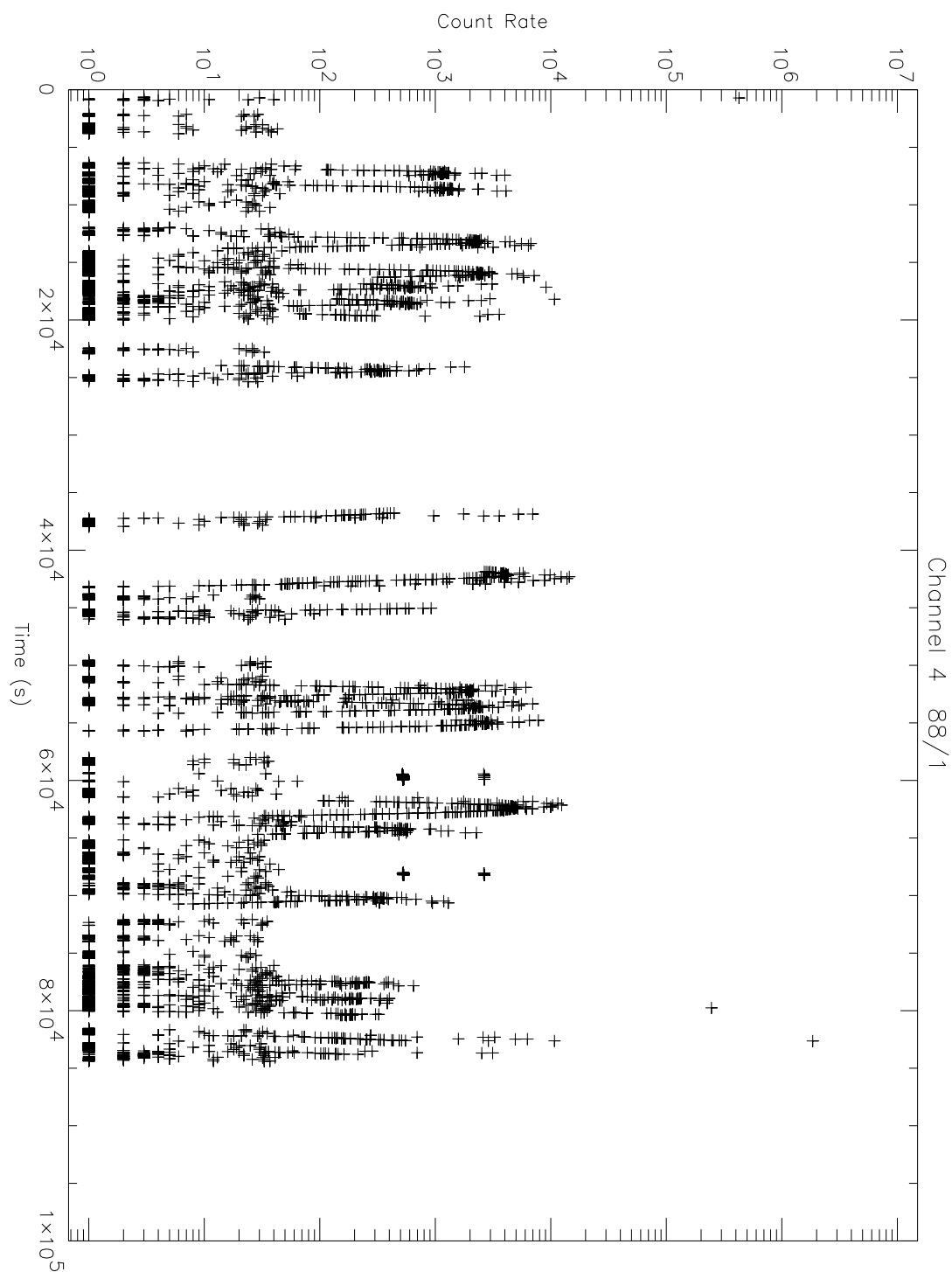


**Figure 4.6.** Sample of the raw EI-88/1 channel 4 count rates in data file TAPE4.DAT

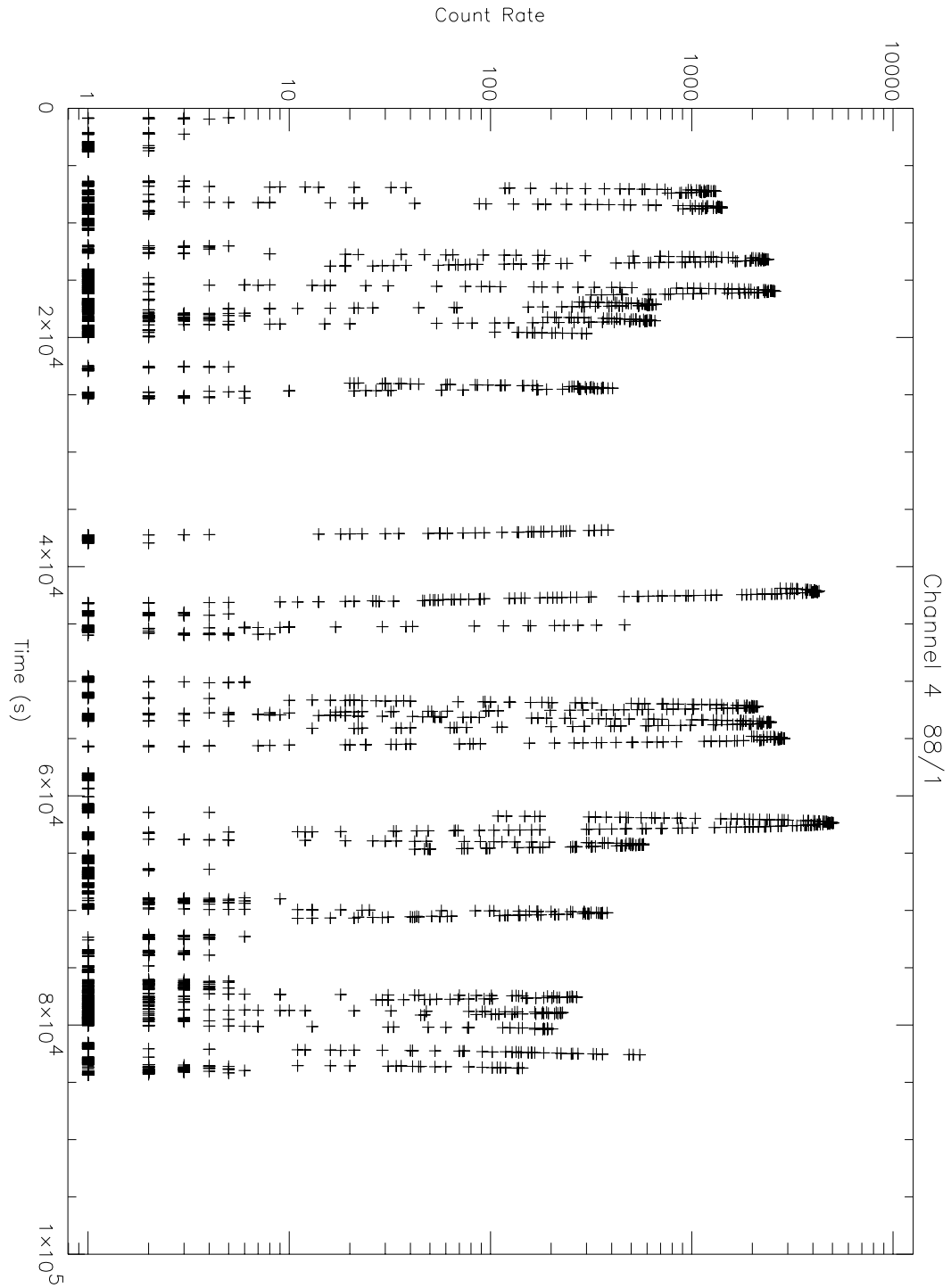


**Figure 4.7.** Sample of the EI-88/1 channel 4 count rates in data file TAPE4.DAT after running the cleaning programme



the records already flagged as suspect) value of the parameter are flagged, for each EI-88 detector separately: detector current, temperature, photomultiplier current, and 16 V voltage. If the record is flagged, the count rates for the corresponding detector are set to  $-1$ . On visual inspection of the time evolution of the individual data points, it was found that the record preceding a record with deviating conditions was very often erroneous as well. Therefore, the records preceding (while checking that there are no gaps in the telemetry) bad condition records are flagged as well.

**Deviation from neighbouring values** The above “cleaning” criteria are able to identify most of the measurements that are invalid because of instrumental or telemetric effects. However, after a detailed inspection of time plots and listings of the cleaned data, some spurious data were still found. We did not find a criterion to identify these deviating points unambiguously, and decided on another scheme to remove them: after applying all the above criteria, each count rate (for each channel and detector separately) is compared to the average of the preceding and succeeding count rate. If the middle count rate is more than a factor five (a value of five turned out to be a good compromise between not rejecting too many data points and not rejecting enough spurious points) above the average count rate, it is set to  $-1$ . On average, about a few dozen measurements per channel and per data file are rejected by this criterion.

**Abnormally high values** After applying the selection criteria described above, a small number of data points still deviate from the surrounding points (in contrast to “neighbouring points”, by “surrounding points” are meant points separated from a given point by at least two ten-second interval) when plotted as a function of time, in the sense that these suspect points have count rates in one or more detectors that are much higher (up to two orders of magnitude) than those of the neighbouring points. We inspected time plots of all the data, for each detector separately, and identified the remaining suspect data points by eye. Since there are only very few of these points (a few dozen over the whole data base) and they deviate clearly from the neighbouring points, we feel confident in eliminating them. Also, the averages and standard deviations of the data after removing these points improve substantially. “Removing a point” in this context means that the count rate of the specific detector channel is set to  $-1$ .

## 4.3 Model construction

In order to construct flux maps, count rates have to be converted to physical units (fluxes) and averaged over two-dimensional coordinate grids. The conversion to fluxes is an iterative process because of the finite aperture of the detectors, i.e. the true unidirectional flux has to be derived from the measured count rate in successive approximations, using the procedure outlined in Appendix A.

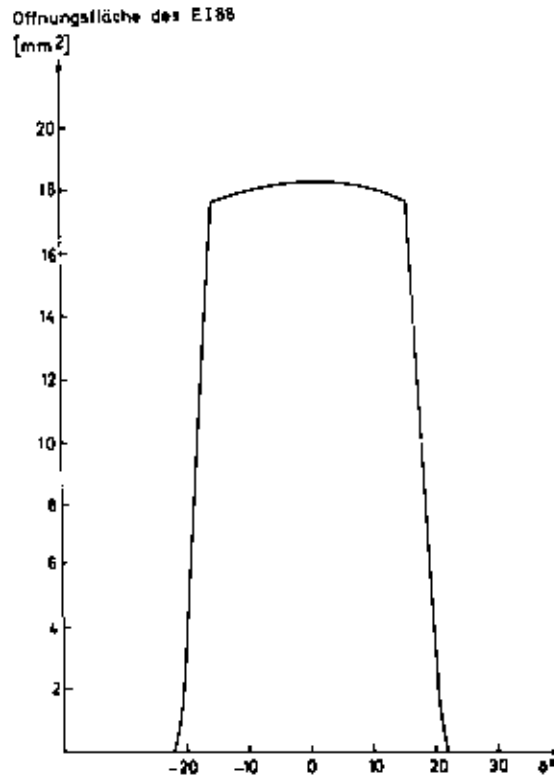


**Figure 4.8.** Measured effective area for the EI-88 detectors [from Achtermann et al. (1970)]

**Table 4.7.** Geometric factors and surface areas of the EI-88 sensors [from Häusler (1972)]

Channel	$G$ (cm <sup>2</sup> sr)	$A$ (cm <sup>2</sup> )	$G$ (cm <sup>2</sup> sr)	$A$ (cm <sup>2</sup> )
	<b>EI-88/1</b>		<b>EI-88/2</b>	
1–5	0.0580	0.1817	0.0595	0.1864
6	0.0612	0.1917	0.0628	0.1967
7	0.0772	0.2418	0.0792	0.2481

### 4.3.1 Effective areas of the EI-88 detectors

The cone shape of the EI-88 detector stacks (see Fig. 4.4) ensures that lower-lying sensors are not obscured by the sensors above them. Therefore, for an ideal detector of this type each sensor should have the same effective area. Plots of the effective areas for different particle energies are shown for the various sensors in Häusler (1972, Figs. 8–10). Figure 8 in Achtermann et al. (1970)—reproduced in Fig. 4.8—shows the analytically derived effective area function that only depends on the detector geometry, and thus is valid (in the ideal case) for each sensor. Figure 10 in Achtermann et al. (1970) shows the measured effective area for 8 MeV protons

in channel 4, which corresponds closely to the analytical effective area. From measurements in a particle beam the authors conclude that for the first five channels the effective area is not dependent on energy. However, particles with higher energies (from about 34 MeV on) can penetrate the edge of the telescope shielding and part of the scintillator, and thus cause an enlargement of the geometric factor for channels 6 and 7. Häusler (1972) lists the geometric factors for the respective channels (see Table 4.7). In the analysis of the AZUR data, an analytic representation of the effective area function shown in Fig. 4.8 was used.

### 4.3.2 Selection of bin sizes

After a comparative study of several coordinate grids, it was found that an  $(E, L, \alpha_0)$  grid is best suited for the data binning. As the equatorial pitch angle always ranges between  $0^\circ$  and  $90^\circ$ , the  $(L, \alpha_0)$  bins are rectangular regardless of the  $L$  range, which is not the case for other coordinate grids, such as  $(L, B)$ .

The bin limits were chosen so that the measurements are distributed as evenly as possible over the bins. Firstly, a set of  $L$  values was selected. The AZUR orbit is such that the magnetic equator is only covered for  $L \leq 1.6$ . For higher  $L$  values, the range of equatorial pitch angles “seen” by the satellite rapidly diminishes with increasing  $L$ . Beyond  $L = 3$ , the coverage is too small to be useful for a radiation belt model, so we limit the model to  $L = 3$ .

After selecting the bin limits of the  $L$  grid, the whole database was binned in an  $(L, \alpha_0)$  grid with equidistant spacing of the  $\alpha_0$  bin limits at  $3^\circ$ . Then, the number of measurements falling in each  $\alpha_0$  bin was summed over the  $L$  bins, to obtain the total number of measurements in each  $\alpha_0$  bin. The cumulative number of measurements is shown in Fig. 4.9 as  $\times$  symbols, and was fitted by a parabolic curve. Points on this curve which are equidistant in ordinate define a series of  $\alpha_0$  values. We have set the number of  $\alpha_0$  bins to 50, and derived the  $\alpha_0$  values corresponding to 50 equidistant intervals in cumulative number of measurements. The resulting values are the bin limits for a new  $\alpha_0$  grid, which is superimposed on Fig. 4.9, and listed in Table 4.8. In order to close the grid, the values  $0^\circ$  and  $90^\circ$  were added.

The database was then rebinned over the new  $(L, \alpha_0)$  grid. The distribution of the measurements in channel 1 over the  $(L, \alpha_0)$  map is shown in Fig. 4.10.

### 4.3.3 Correction for telescope field of view

The IDL programme MODEL.PRO reads in the flux averages created by BINNING.PRO and writes the final flux map AZUR90.DAT (we have only treated the EI-88/1 data). Since the AZUR data coverage in  $(L, \alpha_0)$  space is not uniform, MODEL.PRO extends the equatorial pitch angle dependence where necessary to the equator ( $\alpha_0 = 90^\circ$ ). The extension is achieved by fitting, for each  $E$  and  $L$  bin, the function

$$j(\alpha_0, B_0) = \begin{cases} K \left( \frac{\sin \alpha_0}{\sqrt{B_0}} - \frac{1}{\sqrt{B_c}} \right) \exp \left[ -\beta \left( \frac{\sin \alpha_0}{\sqrt{B_0}} - \frac{1}{\sqrt{B_c}} \right) \right] & \alpha_0 \geq \alpha_{0L} \\ 0 & \alpha_0 \leq \alpha_{0L} \end{cases} \quad (4.1)$$

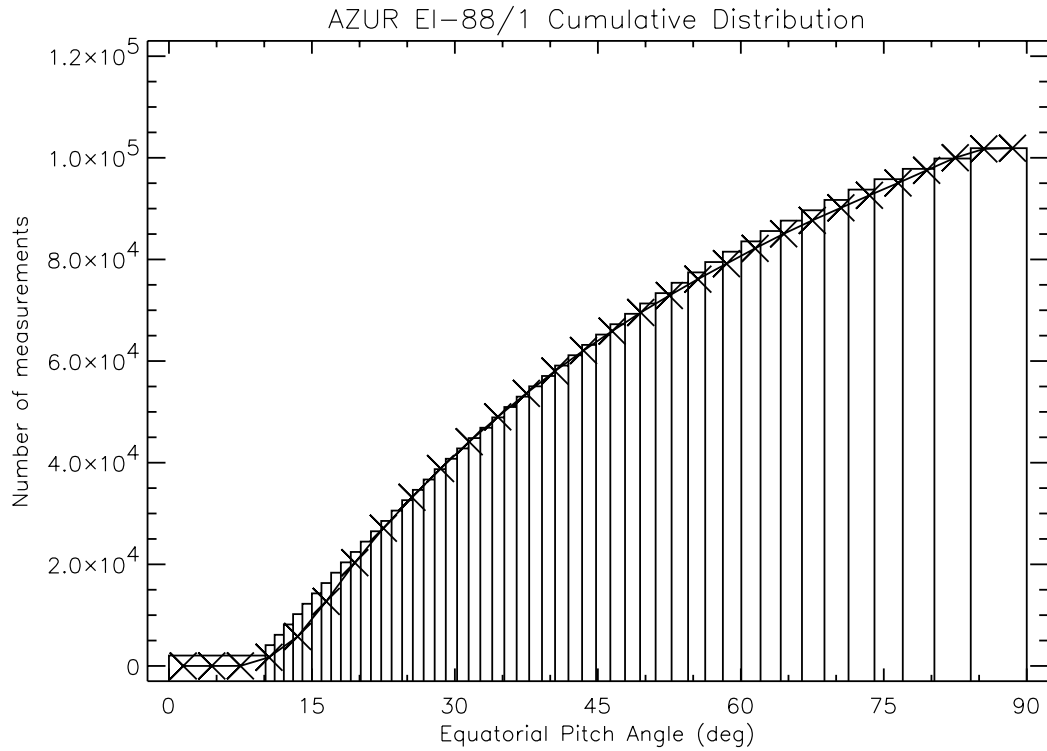


**Figure 4.9.** Cumulative distribution of AZUR EI-88/1 measurements in  $\alpha_0$  bins. The symbols  $\times$  represent evenly spaced bins of width  $3^\circ$ , while the final bins are represented in histogram style.

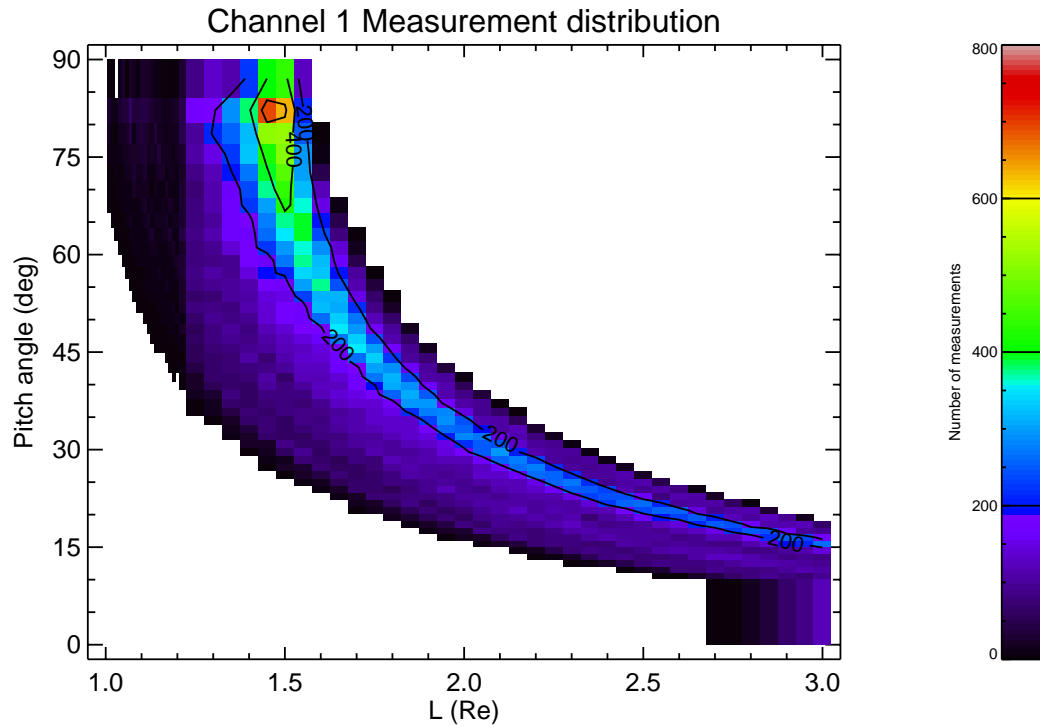


**Figure 4.10.**  $(L, \alpha_0)$  Map of the number of measurements for channel 1

**Table 4.8.**  $(E, L, \alpha_0)$  Bin limits for the PAB97 model grid

$E$ Limits (MeV)	$L$ Limits ( $R_E$ )	$\alpha_0$ Limits (deg)
1.5	1.005	0.0000
2.7	1.015	10.1397
5.2	1.025	11.0914
10.4	1.035	12.0522
22.0	1.045	13.0235
48.8	1.055	14.0045
104.0	1.065	14.9966
	1.075	15.9996
	1.085	17.0134
	1.095	18.0394
	1.105	19.0770
	1.115	20.1277
	1.125	21.1908
	1.135	22.2679
	1.145	23.3591
	1.155	24.4643
	1.165	25.5853
	1.175	26.7215
	1.185	27.8749
	1.195	29.0455
	1.205	30.2336
	1.225	31.4412
	1.275	32.6680
	1.325	33.9164
	1.375	35.1861
	1.425	36.4796
	1.475	37.7977
	1.525	39.1410
	1.575	40.5126
	1.625	41.9128
	1.675	43.3450
	1.725	44.8099
	1.775	46.3115
	1.825	47.8518
	1.875	49.4333
	1.925	51.0610
	1.975	52.7376
	2.025	54.4695
	2.075	56.2616
	2.125	58.1198
	2.175	60.0540
	2.225	62.0722
	2.275	64.1886
	2.375	66.4169
	2.425	68.7793
	2.475	71.3020
	2.525	74.0215
	2.575	76.9961
	2.625	80.3106
	2.675	84.1227
	2.725	90.0000
	2.775	
	2.825	
	2.875	
	2.925	
	2.975	
	3.025	

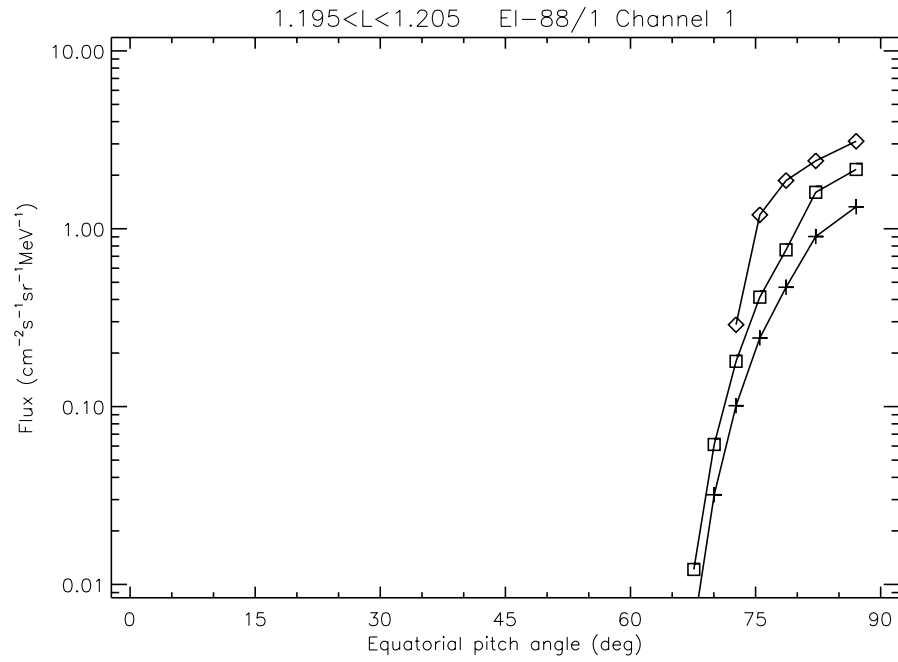


**Figure 4.11.** Uncorrected flux averages ( $\square$ ) for EI-88/1 channel 1,  $L = 1.2$ . The symbols  $+$  represent the flux predicted by means of Eq. (A.19), and the symbols  $\diamond$  are the corrected bin averages.

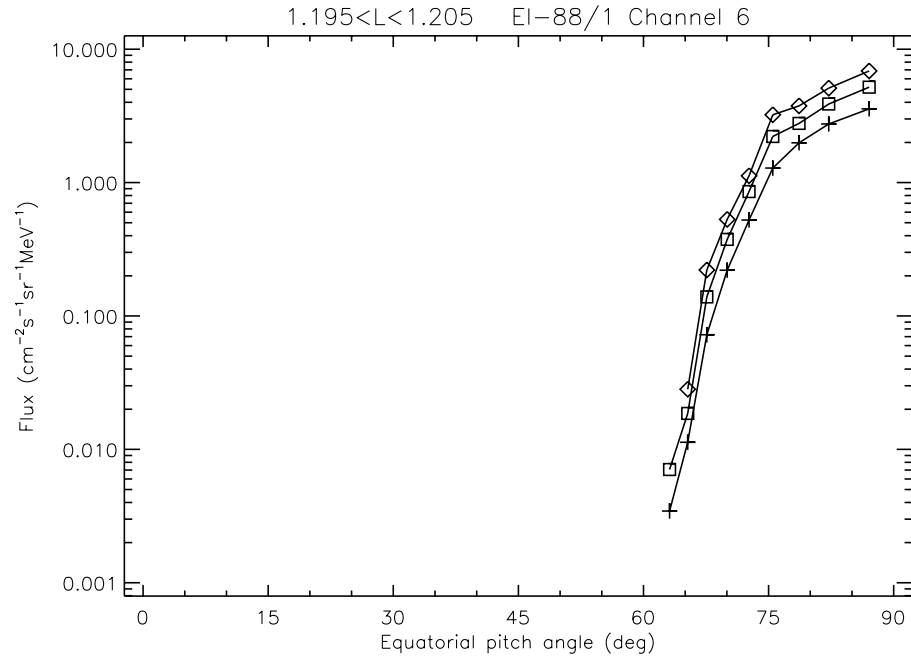


**Figure 4.12.** Same as Fig. 4.11, for channel 6 and  $L = 1.2$

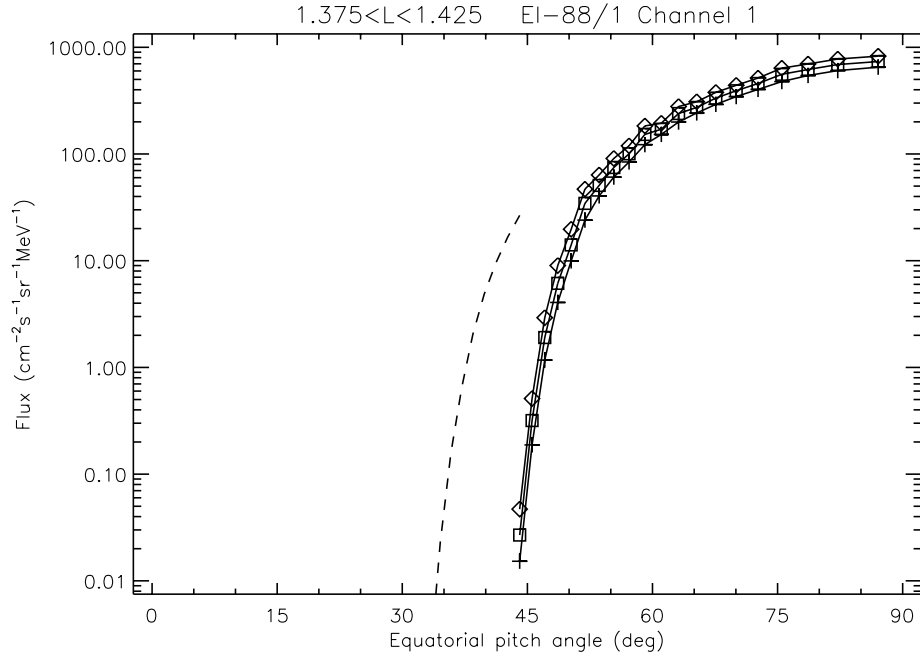


**Figure 4.13.** Uncorrected flux averages for EI-88/1 (perpendicular to the magnetic field) channel 1,  $L = 1.4$ . The symbols have the same meaning as in Fig. 4.11. The dashed line represents the flux predicted by means of Eq. (A.19) for detector EI-88/2 (at an angle of  $45^\circ$  to the magnetic field).

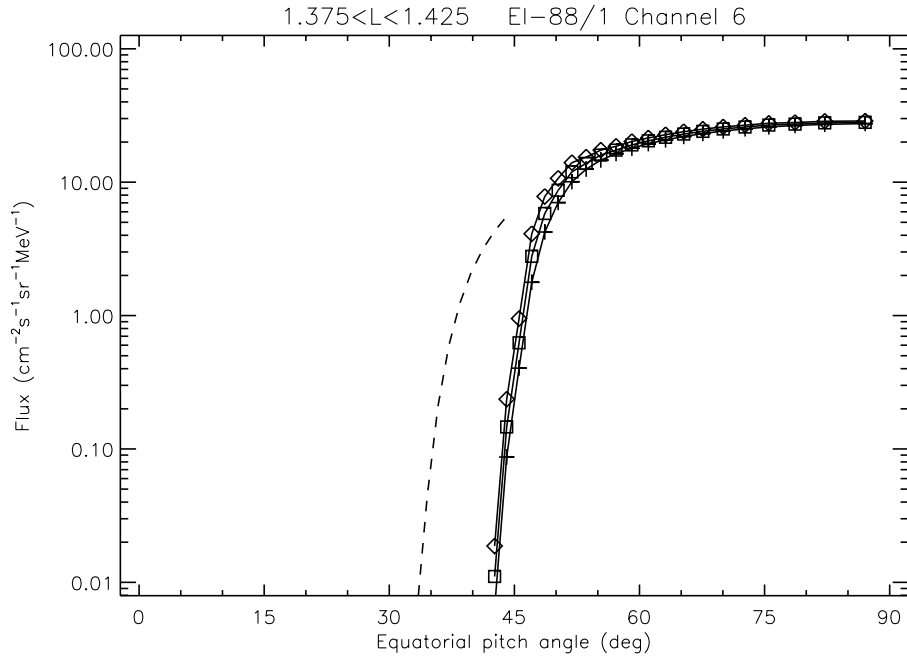


**Figure 4.14.** Same as Fig. 4.13, for channel 6 and  $L = 1.4$

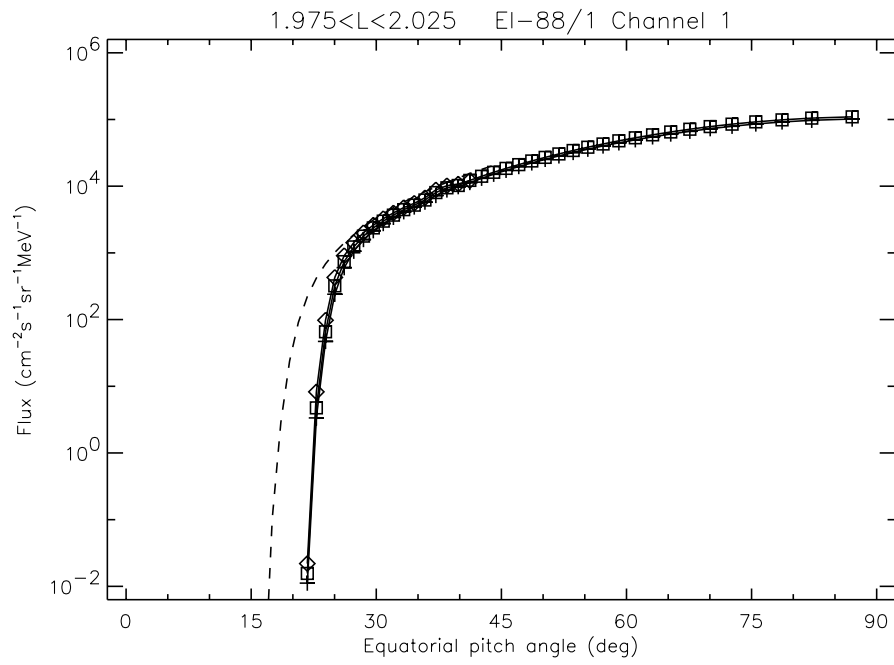


**Figure 4.15.** Same as Fig. 4.13, for channel 1 and  $L = 2.0$

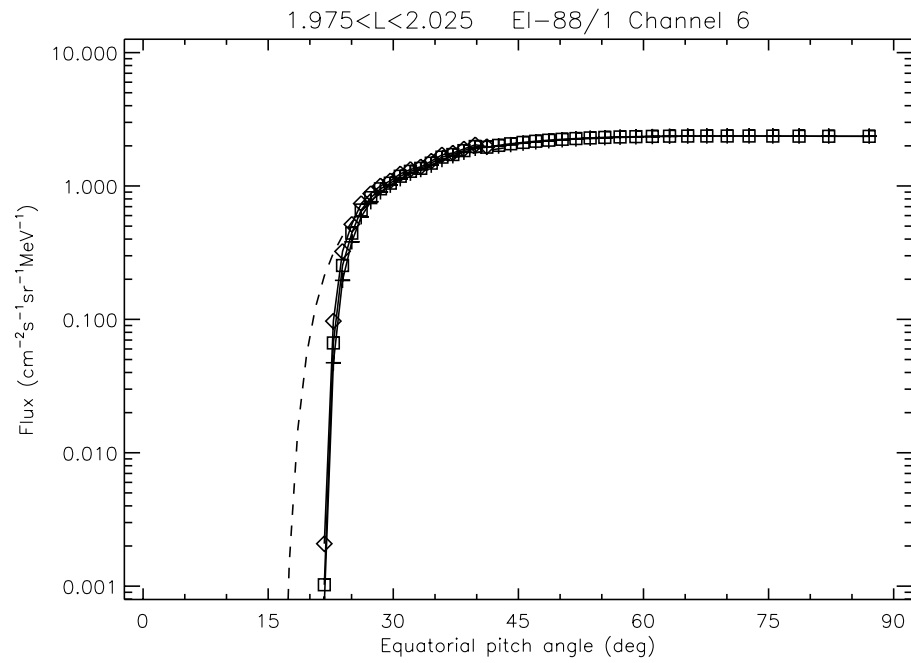


**Figure 4.16.** Same as Fig. 4.13, for channel 6 and  $L = 2.0$



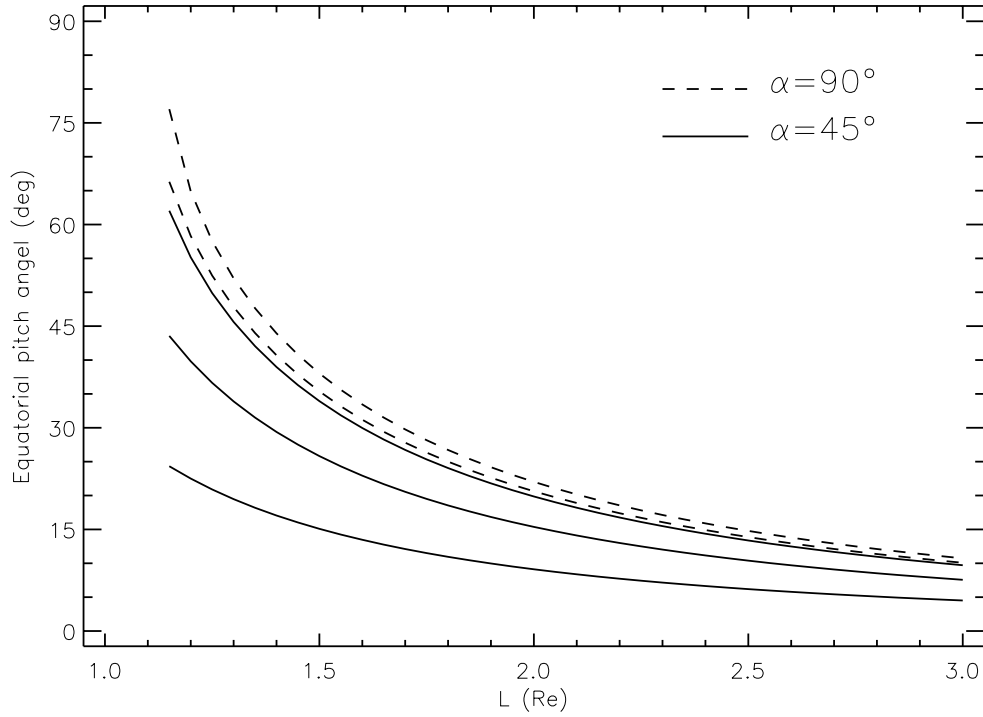


**Figure 4.17.** Comparison of the equatorial pitch angles subtended by the EI-88/1 and EI-88/2 detectors

(Badhwar & Konradi 1990, Heynderickx & Lemaire 1993) to the non-zero fluxes in the bin averages, and replacing zero flux values outside the loss cone with the values obtained with the fit function. When not enough bin averages are different from zero, the fit is replaced by the pitch angle dependence of AP-8 MAX, scaled to the flux value of the bin closest to the equator. The extension of the pitch angle coverage is necessary for the application of Eq. (A.19), as the integration in  $\alpha_0$  can extend beyond the equatorial pitch angle range covered by the measurements. MODEL.PRO Also has a feature to replace non-zero flux values with the fit function, which is necessary when a bin average clearly deviates from the surrounding points.

Figures 4.11–4.16 show the uncorrected average fluxes ( $\square$ ) as a function of  $\alpha_0$  for channels 1 and 6 for detector EI-88/1, for three values of  $L$ . Superimposed on the figures are the fluxes obtained by means of Eq. (A.19) (+), and the bin means obtained by averaging the fluxes after one iteration of the correction procedure outlined in Sect. A.2 ( $\diamond$ ).

The correction for the telescope opening angle clearly depends on the  $L$  value and on the energy channel. The correction is largest where the flux dependence on  $\alpha_0$  is steepest, i.e. for the smallest  $L$  values and the lowest energy channels.

The reason we have not included the EI-88/2 measurements in the model, is their limited coverage in  $(L, \alpha_0)$  space. In addition, these measurements can not be corrected with the method outlined in Sect. A.2. To illustrate this point, we have used Eq. (A.19) to calculate the flux seen by EI-88/2 for the cases represented in Figs. 4.11–4.16 and superimposed the resulting values in these figures as dashed lines. The fluxes as seen by EI-88/2 are shifted towards

the loss cone with respect to the real flux distribution (for  $L = 1.2$ , EI/88-2 does not see any flux at all). The correction procedure used for EI-88/1 would result in a correction factor equal to zero for almost all measurements. The difference between the integrated fluxes for the respective telescopes is caused by the different  $\alpha_0$  intervals covered by the two instruments, as shown in Fig. 4.17.

#### 4.3.4 Final flux map

The bin averages obtained after one iteration of the procedure outlined above are used to build the final flux map. The  $\alpha_0$  coverage of the final bin averages is not extended toward the equator. Instead, for  $(L, \alpha_0)$  bins not covered by the measurements, the flux is set to  $-1$ , so that the software using the model map can exclude the corresponding points. The resulting coverage in  $(L, \alpha_0)$  space is illustrated in Figs. 4.18 and 4.20 for the lowest and highest energy channels. The fitting procedure described in Sect. 4.3.3 is applied, however, to correct bin averages that clearly deviate from the pitch angle dependence defined by the other bins (the number of corrections is very small).

The final flux map is then transformed into a BLOCK DATA file by means of the programme MODTOBD.FOR. This programme also transforms differential into integral fluxes. The implementation of the new AZUR model (called PAB97) in UNIRAD is described in Technical Note 10.

#### 4.3.5 Comparison to AP-8

Figures 4.18 and 4.20 show two flux maps of the PAB97 model in  $(L, \alpha_0)$  space, together with the directional AP-8 MAX maps for the same grid values. Figures 4.19 and 4.21 show the ratios of the AP-8 MAX values to the PAB97 model values. It can be seen that for the lowest  $L$  values the PAB97 fluxes are smaller than the corresponding AP-8 MAX fluxes by a factor of about two. For higher  $L$  values, the agreement between the two models is satisfactory.

Another way of comparing the PAB97 model to AP-8 consists of drawing world maps of fluxes at fixed altitude. Figures 4.22 and 4.23 show the distributions of the PAB97 and AP-8 MAX proton flux  $> 50$  MeV at an altitude of 500 km, respectively. Again, the PAB97 flux is lower than the AP-8 MAX flux.

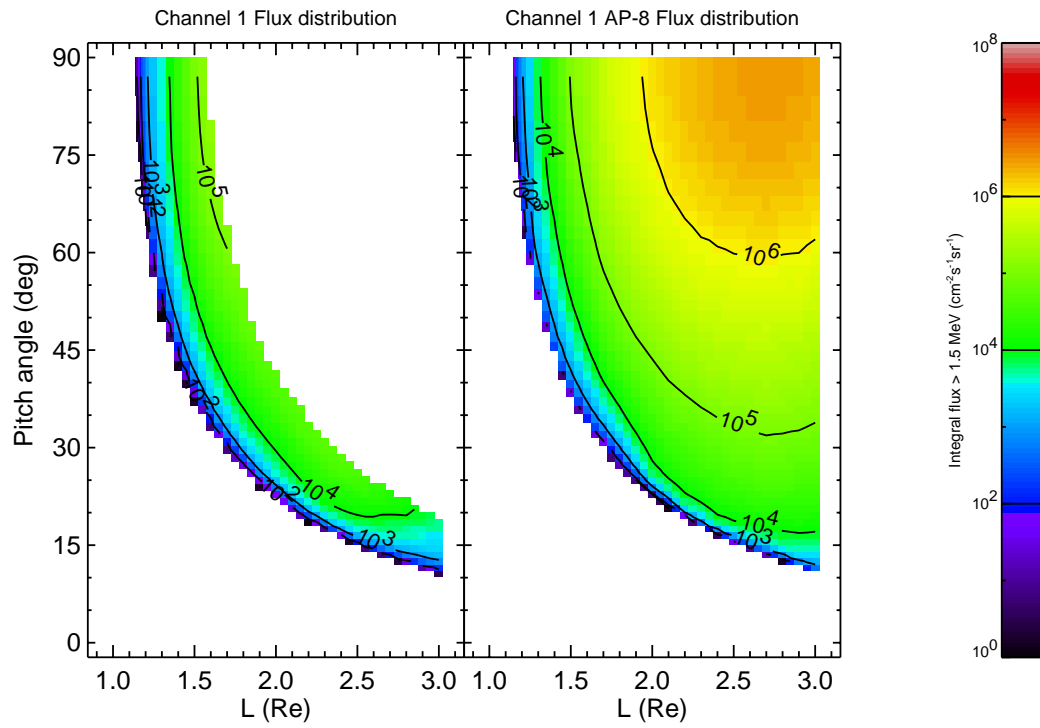


**Figure 4.18.**  $(L, \alpha_0)$  Map of the PAB97 model and AP-8 MAX for channel 1

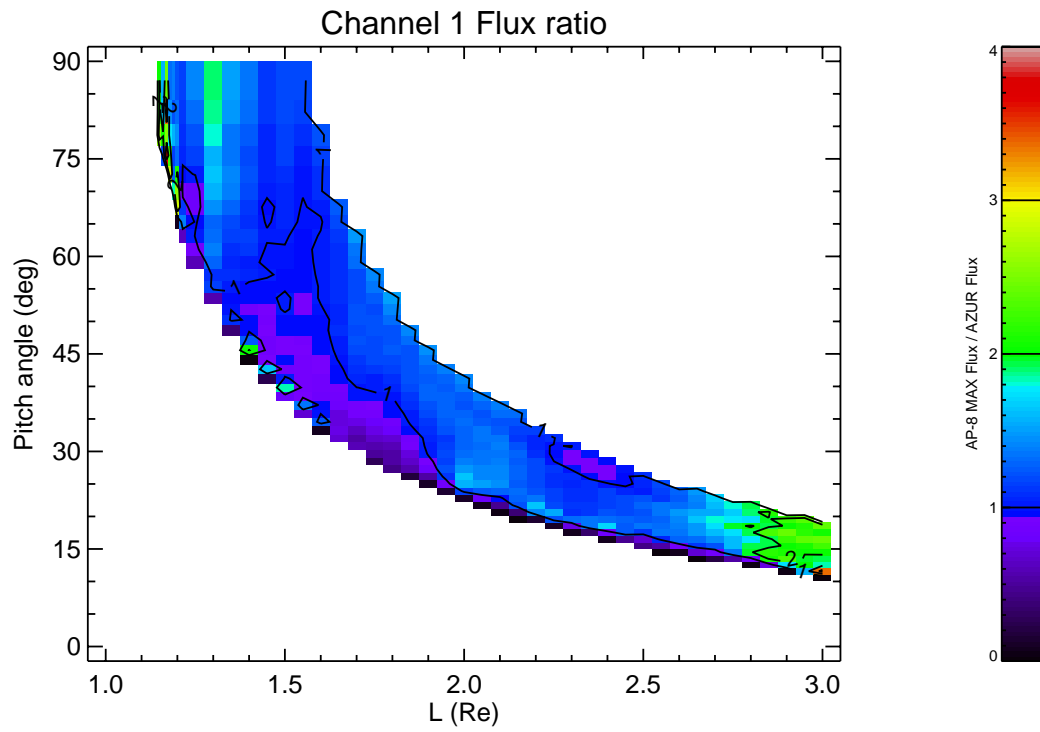


**Figure 4.19.**  $(L, \alpha_0)$  Map of the ratio of AP-8 MAX to the PAB97 model for channel 1

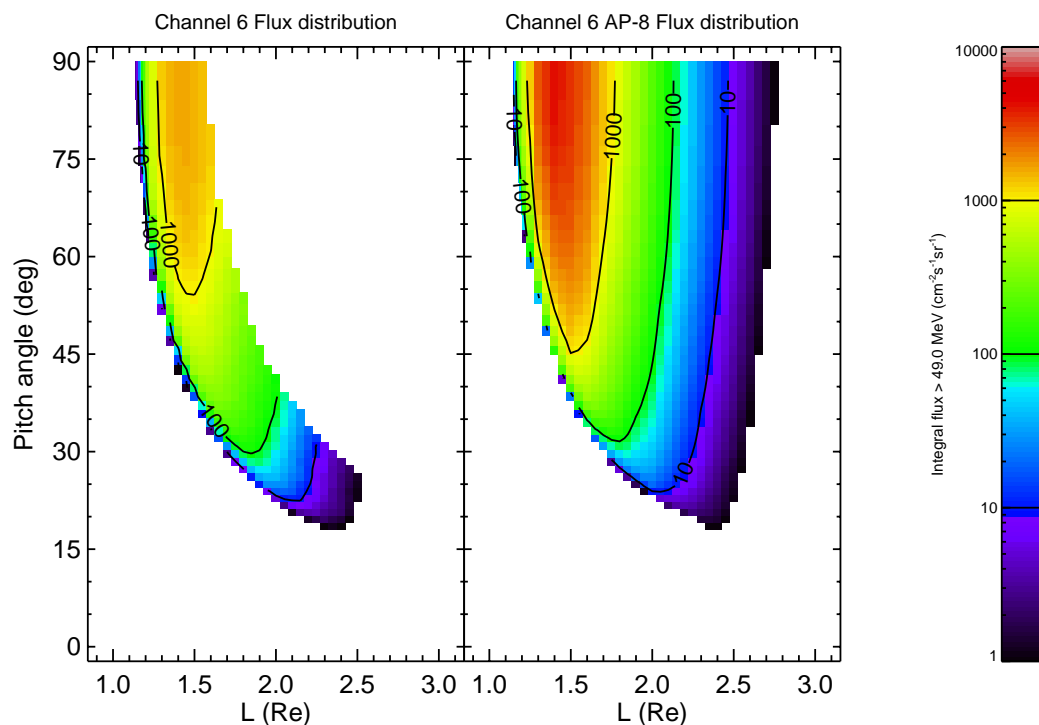


**Figure 4.20.**  $(L, \alpha_0)$  Map of the PAB97 model and AP-8 MAX for channel 6

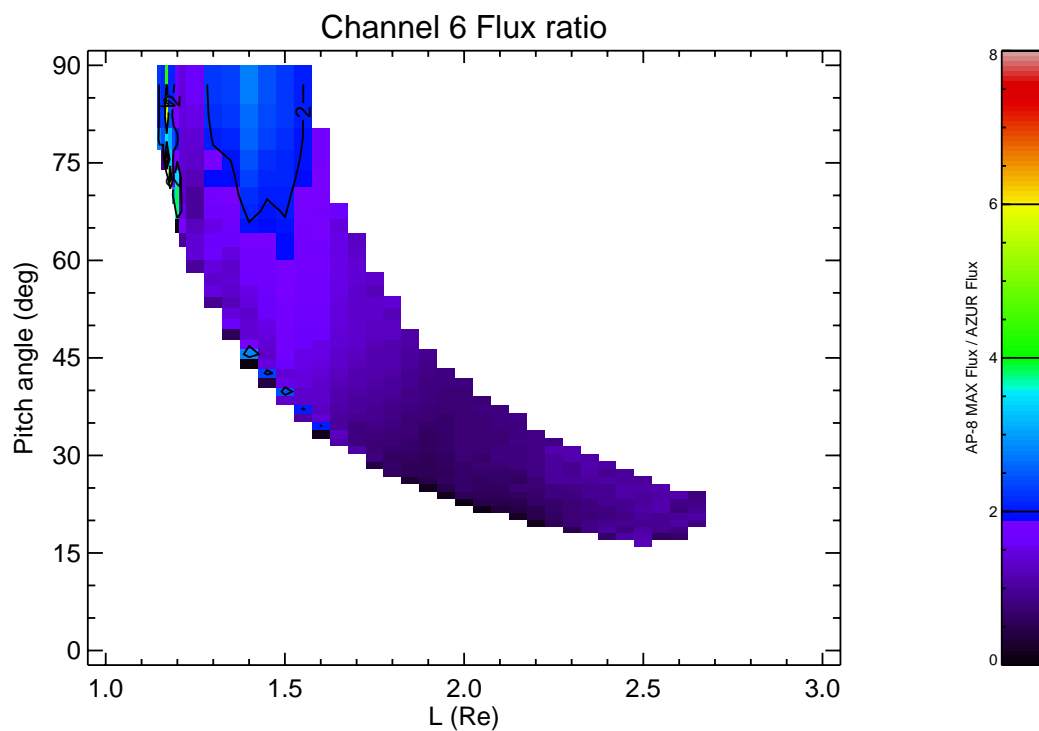


**Figure 4.21.**  $(L, \alpha_0)$  Map of the ratio of AP-8 MAX to the PAB97 model for channel 6

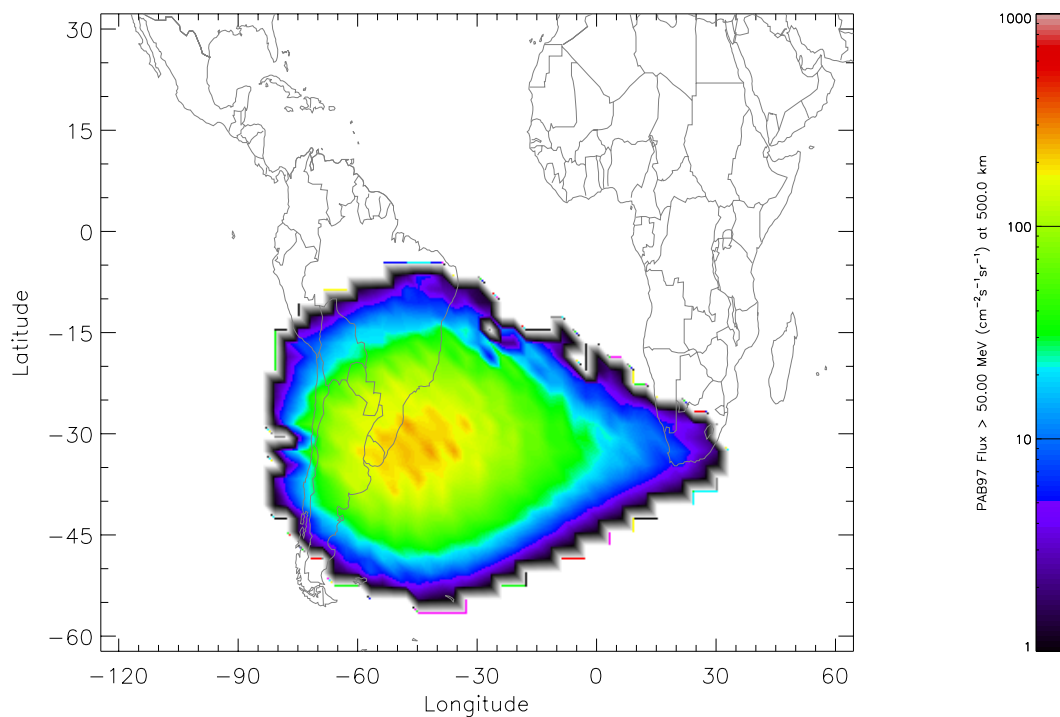


**Figure 4.22.** World map of the PAB97 >50 MeV proton flux at 500 km

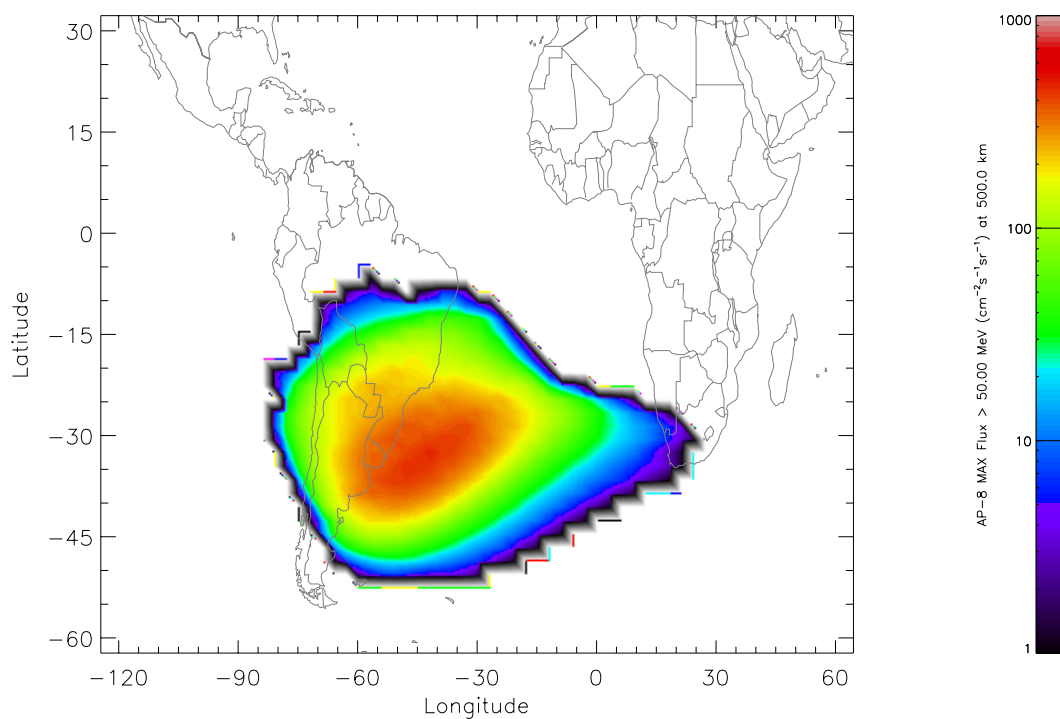


**Figure 4.23.** World map of the AP-8 MAX >50 MeV proton flux at 500 km



# Chapter 5

## The SAMPEX/PET data base and radiation belt model

At the Radiation Belt Workshop held at BIRA/IASB, 17–20 Oct 1995, J.B. Blake of Aerospace Corp. proposed that the observations of energetic proton fluxes made onboard of the SAMPEX satellite with the PET instrument be processed at BIRA/IASB by the TREND team with the aim of building a new trapped proton model. R.A. Mewaldt, PI for the SAMPEX/PET detector, supported this offer and during the spring of 1996, M.D. Looper from Aerospace Corp. visited BIRA/IASB to install the PET data on a DEC/Alpha station. The SAMPEX/PET data base installed at BIRA/IASB spans a time interval of four years during the declining phase of Solar Cycle 22.

This chapter contains a brief description of the SAMPEX mission and the PET instrument, and describes the data processing performed at BIRA/IASB and the new model that resulted.

### 5.1 The SAMPEX mission

The Solar, Anomalous, and Magnetospheric Particle EXplorer (SAMPEX) was the first Small EXplorer (SMEX) mission. SAMPEX measures energetic electrons as well as ion composition of particle populations from  $\sim 0.4$  MeV/nucleon to hundreds of MeV/nucleon from a zenith-oriented satellite in near-polar orbit. SAMPEX was successfully launched from NASA's Western Test Range (Lompoc, CA) at 1419 UT on 3 July 1992. The description of the SAMPEX satellite system and instruments has been taken from a series of papers in IEEE Trans. Geosci. Remote Sensing **31**, Nr. 3, 1993.

#### 5.1.1 Spacecraft configuration

The SAMPEX spacecraft was designed to support a minimum mission duration of 1 year, with a mission goal of 3 or more years (Baker et al. 1993). The SAMPEX mechanical system basically consists of a primary structure, a deployable solar array system, and a yo-yo despin system.

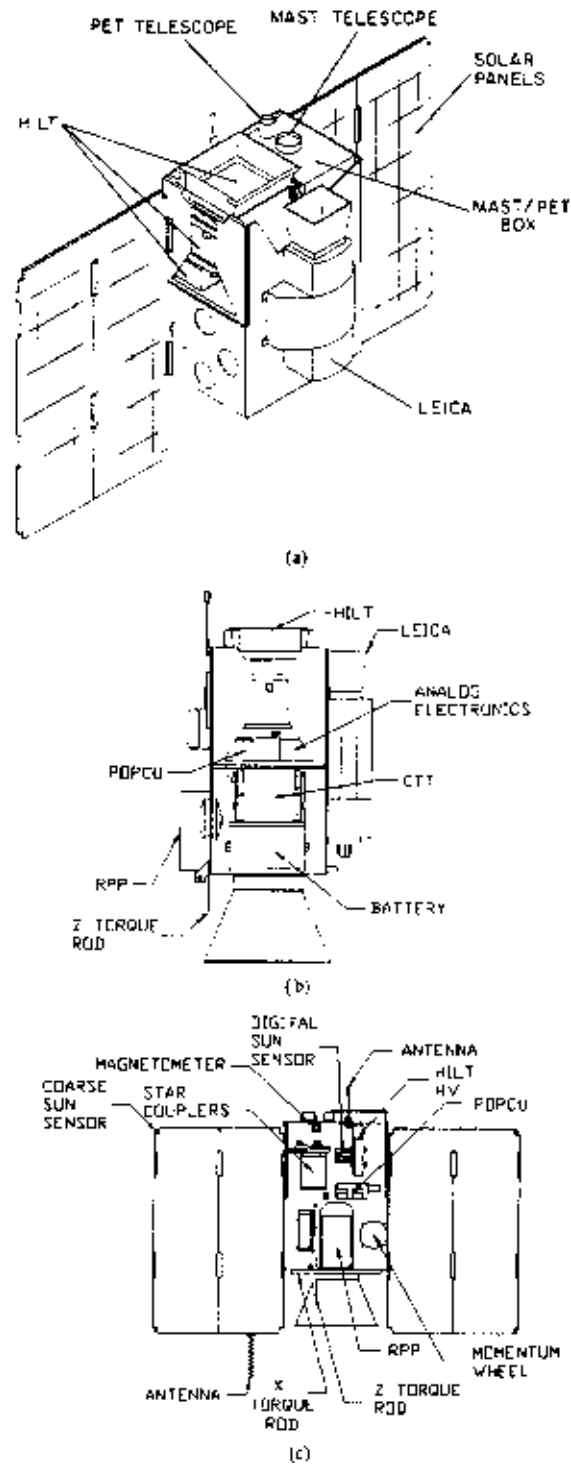


**Figure 5.1.** Mechanical design of the SAMPEX spacecraft and physical layout: (a) scientific instruments; (b) side view of subsystems; (c) back view of subsystem layout [from Baker et al. (1993)].



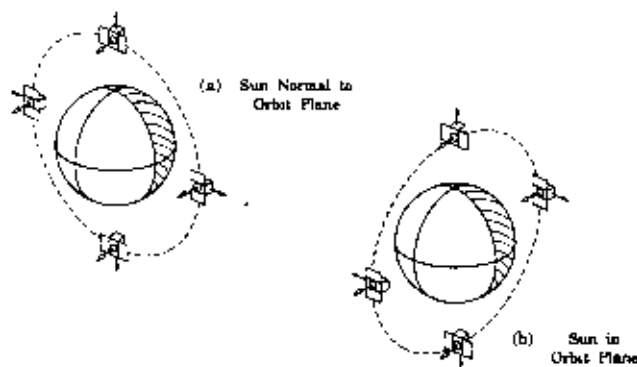


**Figure 5.2.** Pointing strategy for the SAMPEX spacecraft in two illustrative orbit planes [from Baker et al. (1993)].

SAMPEX is built up of machined aluminium plates which form a box-like structure that houses all of the spacecraft components (see Fig. 5.1).

The SAMPEX orbit has an inclination of  $82^\circ$ , apogee of 670 km and perigee of 520 km. The orbit is non-Sunsynchronous and precesses through all local times (noon-midnight to midnight-noon) in about three months.

### 5.1.2 Attitude control

The Attitude Control Subsystem (ACS) is designed as a solar-pointed/momentum bias system. The SAMPEX spacecraft points at the Sun while it rotates about the sunline once per orbit in order to position the instrument lines-of-sight in the zenith direction when overflying the poles. Pointing requirements for the selected experiments are met by choosing sensor, torquers, and system configurations from a standard set of electronics, sensors and actuators. The ACS system utilizes one momentum wheel and three electromagnetic torque rods to orient the experiment viewing axis. Pointing ranges within  $\pm 15^\circ$  of vertical over the poles. The attitude computed onboard the spacecraft is known with an accuracy better than  $2^\circ$  ( $3\sigma$ ). The pointing strategy for SAMPEX is to point the pitch axis (i.e. the normal to the solar panels) directly at the Sun. Then the yaw axis (parallel to the detector bore sights) rotates about the pitch axis once per spacecraft orbit. The spacecraft views north over the north pole, south over the south pole, and parallel to the equator during the equatorial plane crossings (see Fig. 5.2).

An Attitude Control Electronics (ACE) box which contains signal conditioning electronics and an independent analog safhold mode controls the ACS sensor and hardware. The onboard data system performs closed loop real-time attitude determination and control processing. Three-axis attitude determination is provided by comparing the local measured Sun vector and magnetic field vector with an on-board ephemeris model. Digital control of the spacecraft attitude is completed by sending appropriate command signals across the spacecraft data bus to the actuators.

**Table 5.1.** SAMPEX Scientific Instruments

	LEICA	HILT	MAST	PET
<b>Energy range (MeV)</b>				
Electrons	—	—	—	0.4–30
H	0.76–6.1	—	—	18–250
He	0.45–6.1	4.3–38	7–20	18–350 MeV/nuc
C	0.44–11.4	7.2–160	14–210	34–120 MeV/nuc
Si	0.33–5.5	9.6–177	21–330	54–195 MeV/nuc
Fe	0.21–3.1	11.0–90	27–450	70–270 MeV/nuc
<b>Charge range</b>				
Elements	1–25	2–28	2–28	1–2 (1–28*)
Isotopes	2–16	2	2–28	1–2 (1–10*)
<b>Physical characteristics</b>				
Geometric factor (cm <sup>2</sup> sr)	0.8	60	7–14	0.3–1.6
Field of view (deg, full angle)	24 × 20	68 × 68	101	58
Mass (kg)	7.4	22.8	8.8	(incl. with MAST)
Power (W)	4.9	5.6	5.3	(incl. with MAST)
Telemetry (kB/s)	1.3	0.9	1.4	0.5

\*Commandable high-gain mode

The spacecraft determines the directions of the Sun and of the local magnetic field (using the Sun sensors and the magnetometer, respectively) with respect to the spacecraft's body-fixed coordinate frame, then compares these measurements with onboard calculations of the same quantities in the GEI coordinate frame in order to relate the two frames. When the magnetic field is nearly parallel or antiparallel to the Sun line, the roll angle about their nearly common line is poorly determined. Therefore, when the angle between these two lines becomes less than 5° (or greater than 175°) while the spacecraft is out of eclipse, or less than 40° (or greater than 140°) while in eclipse, the spacecraft goes into "coast mode" and stops sending attitude information to the telemetry stream until the two lines diverge far enough to resume normal operations. Thus there is a gap in attitude information available on the ground. The time during which attitude is not being updated can add up to a large fraction of a day. The gaps in the attitude data were filled by interpolation, with a quality flag assigned to the interpolated data.

When the spacecraft enters coast mode, the magnetic torque rods shut off if they are running and the rotation speed about the Sun line is reset to a nominal value, which may be significantly slower than before coast mode began. On 27 May 1994, the spacecraft pointing strategy was changed to the effect that the instrument line of sight is perpendicular to the magnetic field while the spacecraft is in eclipse.

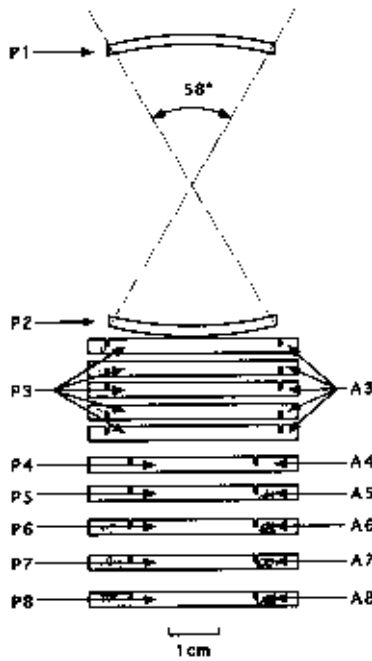


**Figure 5.3.** Schematic of the PET telescope. The primary analysis mode requires P1 and P2 (58° field of view). A wide angle 90° field of view that requires P2 and P4 but not P1 is also available for electrons. The regions labelled A4 through A8 are annular guard regions used to detect particles that enter or leave through the side of the stack [from Cook et al. (1993b)].

## 5.2 The Proton/Electron Telescope (PET)

The instruments on the SAMPEX spacecraft are the Low Energy Ion Composition Analyzer (LEICA), the Heavy Ion Large Telescope (HILT), the MAss Spectrometer Telescope (MAST), and the Proton/Electron Telescope (PET). The four instruments onboard have co-aligned bore-sights. A brief description of these instruments is given in Technical Note 5. The instrument characteristics are summarised in Table 5.1. In this study, only data from the PET are used.

The PET system is designed to complement MAST by measuring the energy spectra and relative composition of protons (18–250 MeV) and helium nuclei (18–350 MeV/nucleon) of solar, interplanetary, and galactic origins, and the energy spectra of solar flare and precipitating electrons from approximately 0.4 to 30 MeV. The instrument measures both trapped and precipitating energetic particles in different parts of the SAMPEX orbit. It also has the capability to look at manmade particle populations such as positrons which are emitted by nuclear reactors that have flown previously in low Earth orbit. The PET system can also duplicate and extend some measurement capabilities of MAST by providing energy spectra and elemental composition of nuclei from Li through Fe using a commandable high gain mode. It provides some isotopic information on nuclei from H to Ne.

**Table 5.2.** PET Detector, ADC, and discriminator characteristics

Detector Name	Nominal Thickness (mm)	Central Active Area (cm <sup>2</sup> )	Guard Active Area (cm <sup>2</sup> )	Nominal ADC Threshold (MeV)	Nominal ADC Full Scale (MeV)	Nominal Discriminator Thresholds (MeV)	Guard Discriminator Thresholds (MeV)
P1	2	8.0	—	0.35	157	P1A=3.1	—
P2	2	8.0	—	0.35	157	—	—
P3	15 (5 × 3) mm	9.2	4.5	0.7	317	P3A=2.8 P3B=12	0.3, 5
P4–P7	3	4.5	8.0	0.36	337	0.23	0.3, 1.2
P8	3	4.5	8.0	—	—	0.3	0.3, 1.2

### 5.2.1 Detailed description of the PET telescope

This section presents the description of PET by Cook et al. (1993b). The PET telescope, shown schematically in Fig. 5.3, consists of a series of eight Li-drifted silicon detectors (P1 to P8) with thicknesses ranging from 2 to 15 mm. The telescope opening aperture is defined by a passive collimator, followed by two curved (spherical) aperture detectors (P1 and P2) designed to minimise pathlength variations over the telescope's 58° opening angle. They are followed by six flat detectors (P3 to P8), where the P3 detector is comprised of five identical devices with a combined thickness of 15 mm. Detectors P3 through P8 are double-grooved devices with a central area for measuring energy loss and an annular guard region (labelled A in Fig. 5.3) used to detect particles that enter or leave through the side of the telescope, a design previously used on Voyager 1, Voyager 2 (Stone et al. 1977), and ISEE-3 (Althouse et al. 1978).

Particles satisfying the P1·P2 coincidence enter through a 1.5 cm long collimator (not shown in Fig. 5.3) that is nominally 0.75 mm thick at its thinnest point, and that preserves the 58° opening angle. The collimator also supports two windows (each 12.5  $\mu$ m thick aluminised Kapton) that provide electrical shielding and protection from sunlight.

Detectors P1, P2, and the centre of P3 are each direct coupled to separate charge-sensitive pre-amplifiers, shaping amplifiers, and 10-bit ADCs. The summed output of the centres of P4 through P7 is fed into a fourth 10-bit ADC. The centre of P8 and the guard regions of P3 to P8 are each connected to pre-amplifiers, shaping amplifiers and discriminators. Each guard signal channel has two discriminators, A1 and A2: A1 is sensitive to minimum ionising particles while the A2 levels are  $\sim 1.2$  MeV for A4–A8 and  $\sim 5$  MeV for A3. Table 5.2 summarises the characteristics of the PET detectors and their analysis chains.

### 5.2.2 Analysis modes

PET Uses the conventional  $dE/dx$ -total energy technique to identify electrons, protons, and heavier nuclei, an approach which is based on the range-energy relations of energetic particles. With this approach a comparison of the rate of energy loss of energetic particles with their total energy loss can be used to identify both the charge and mass of energetic nuclei, as well as

**Table 5.3.** PET Response

Particle	Nominal Energy Interval (MeV or MeV/nuc)	Typical Geometry Factor <sup>1</sup> (cm <sup>2</sup> sr)	Detector <sup>2,3</sup> Combination	Associated counting rates		
				Name	Res. (s)	Duty Cycle
Electrons	> 0.4	10	P1	P1	0.1	0.5
	~ 1–4	1.8	$P1 \cdot \overline{P1A} \cdot P2 \cdot \overline{P3} \cdot \overline{A}$	ELO	6	1
	~ 4–20	1.7–1.1	$P1 \cdot \overline{P1A} \cdot P2 \cdot P3 \cdot \overline{P4} \cdot \overline{A}$	EH1	6	1
	~ 12–30	0.5–0.3	$P1 \cdot P2 \cdot P4 \cdot \overline{P8} \cdot \overline{A}$	RNG	6	1
	~ 12–30	2.8–0.9	$\overline{P1} \cdot P2 \cdot \overline{P3B} \cdot P4 \cdot \overline{P8} \cdot \overline{A}$	EWG	6	1
H, He	> 4	10	P1	P1	0.1	0.5
	19–28	1.8	$P1A \cdot P2 \cdot \overline{P3} \cdot \overline{A}$	PLO	6	1
	28–64	1.7–1.1	$P1A \cdot P2 \cdot P3 \cdot \overline{P4} \cdot \overline{A}$	PHI	6	1
	64–85	0.5–0.3	$P1 \cdot P2 \cdot P4 \cdot \overline{P8} \cdot \overline{A}$	RNG	6	1
	> 85	0.3	$P1 \cdot P2 \cdot P8 \cdot \overline{A}$	PEN	6	1
$Z \geq 3$ Nuclei <sup>4</sup>	60–200	1.7–1.1	$P1 \cdot P2 \cdot \overline{P4} \cdot \overline{A}$	PLO, PHI	6	1

<sup>1</sup>Based on calculation with straight tracks; accelerator calibration data will modify values for electrons.

<sup>2</sup>“A” Represents the logical “OR” of the guard rings on P3 to P8.

<sup>3</sup>P1A, P3A, and P3B are digital discriminators on the P1 and P3 outputs set at 3.1, 2.8, and 12 MeV, respectively.

<sup>4</sup>Commandable mode for  $Z \geq 3$  nuclei; energy range indicated is for Si-28.

measure their kinetic energy. In practice, the rate of energy loss is determined by measuring the energy loss ( $\Delta E$ ) in a detector of known thickness, such as P1 or P2 on PET. In order to minimise the variations in the path length over the telescope’s 58° opening angle, P1 and P2 have been constructed from spherical segments of silicon. As a result, PET should be capable of identifying elements from H to Ni, with isotope identification extending through Ne. Although the range-energy characteristics of electrons are not nearly so precise as those of nuclei, electrons are easily separable from protons because of their much lower rate of energy loss.

PET Includes a number of separate analysis modes that are designed to identify electrons and nuclei over selected energy intervals: the primary Lo-Z mode providing differential energy spectra of electrons and of H and He nuclei, and the commandable Hi-Z mode (in which the gain of P1, P2, and P3 is reduced by a factor of ten) in which energy spectra of the elements from Li to Ni can be measured as well. The data used in this study were obtained in the Lo-Z mode only.

The pulse height of an event is triggered whenever one of the coincidence equations in Table 5.3 is satisfied. The results, along with other information such as the state of various discriminators, are stored in one of five separate event buffers. These event buffers are read out into the telemetry stream by a rotating priority system that ensures that all event types are represented under conditions that range from periods dominated by intense fluxes of solar flare nuclei to periods dominated by trapped protons and electrons.

Because the telemetry rate is insufficient to transmit every event, rate accumulators are used to count events during 6 s intervals. A total of 32 such “counting rates” record instrument live-time, the frequency of electrons and nuclei in several energy intervals defined by the coincidence

**Table 5.4.** SAMPEX/PET Data set file description

File names	File contents
EPHxxxxxx.DAT	Ephemeris data
PTLVxxxxxx.DAT	Livetimes
PKTSxxxxxx.DAT	Count rates

logic, and the triggering frequency of a variety of discriminator levels. Table 5.3 summarizes some of the counting rates of physical interest. In addition, the “singles” counting rate of the front detector (P1) is sampled for 0.05 s out of every 0.10 s to measure the flux of magnetospheric electrons  $> 0.4$  MeV and protons  $> 4$  MeV on a fast time scale. This “high resolution” rate is recorded whenever the count rate exceeds a (commandable) level of  $\sim 50$  counts/s. All of the coincidence equations and some of the discriminator levels can be modified by command to allow for the possibility of noisy or failed detectors, and to optimise the instrument’s response to the various particles of interest.

### 5.2.3 Calibrations

The response of PET to electrons has been calibrated over the energy range from  $\sim 0.3$  MeV to  $\sim 27$  MeV with electron beams incident at a variety of energies and zenith angles. At higher energies the linear electron accelerator at the EG&G Santa Barbara facility was operated in a low intensity mode to provide mono-energetic beams at fourteen separate energies from 1.5 to 27 MeV. Calibrations at somewhat lower energies (0.3 to 3 MeV) were carried out with a  $\beta$  spectrometer. PET Was also calibrated with radioactive sources to determine its positron detection efficiency and its response to  $\gamma$  rays that Compton scatter in the telescope producing a possible background for electron and positron measurements. For accelerator calibrations, where beam time is often limited and expensive, PET has a special port that allows events to be read out at rates of several thousand per second.

PET Has a built-in calibrator that can be initiated either periodically (every 6.8 hours) or by command (Cook et al. 1993a). The calibrator includes an 8-bit DAC that supplies reference voltages to the test pulsers of each of the signal channels. The test pulsers can be stimulated either individually or in groups to perform limited tests of the coincidence logic, measure the thresholds of the various discriminators, and the gain, linearity, and long-term stability of the ADCs. Calibration “events” are flagged and stored in a special buffer for read-out and telemetry along with the regular data.

## 5.3 The SAMPEX/PET data base

The SAMPEX/PET data base was delivered to BIRA/IASB by M.D. Looper on optical disks. The data set consists of ephemeris files, attitude information, count rates and livetimes. The data delivered to BIRA/IASB cover the period from the start of the mission (day 187 of 1992) up to day 121 of 1996.

The PET data base was installed on a DEC Alpha workstation running OpenVMS. The data analysis was performed with a series of IDL programs and the UNILIB library. The analysis is described in detail in Technical Note 5. The data base is stored as a series of files, each containing data for one day, with the date forming the second part of the file name as YYDDD. Table 5.4 list the different file types that make up the data base.

The contents of each file in Table 5.4 correspond to an IDL structure. The structures are defined as:

```
nkts = 14400
eph = replicate({time:0l,alt:0.,lon:0.,lat:0.,pa:0.,b:0.,
                fl:0.,bc:0.,flc:0.,beta:0.,bv:fltarr(3),
                vn:fltarr(3),altm:0.,flag:0b},nkts)
ptlv = replicate({plo:0.,phi:0.,rng:0.,pen:0.},nkts)
pkts = replicate({p21:0b,p22:0b,p23:0b,p24:0b,p31:0b,p32:0b,
                p33:0b,p34:0b,p4:0b,p5:0b,p67:0b,p81:0b,
                p82:0b,p83:0b,p84:0b,d31:0b,d32:0b,d33:0b,
                d34:0b,d4:0b,d5:0b,d67:0b},nkts)
```

**nkts** Is the number of six second intervals per day.

### 5.3.1 PTLVxxxxx.DAT

The PTLV structure contains the livetimes in seconds (maximum 6s) over each six second interval:

**ptlv.plo** livetime (s) for 2-detector (PLO) events;

**ptlv.phi** livetime (s) for 3-detector (PHI) events;

**ptlv.rng** livetime (s) for 4-detector (RNG) events;

**ptlv.pen** livetime (s) for 8-detector (PEN) events.

### 5.3.2 PKTSxxxxx.DAT

The PKTS structure contains the counts of protons and deuterons over each six second interval:

**pkts.p\*** counts of proton events from start to end of interval;

**Table 5.5.** PET Channel characteristics

Channel (PKTS)	Buffer (PTLV)	Energy Range (MeV/nuc)	Nominal Geometric Factor (cm <sup>2</sup> sr)
p21	plo	18.5–20.5	1.792
p22	plo	20.5–22.5	1.792
p23	plo	22.5–24.5	1.792
p24	plo	24.5–27.2	1.792
p31	phi	27.2–37.4	1.714
p32	phi	37.4–45.8	1.527
p33	phi	45.8–53.0	1.356
p34	phi	53.0–65.4	1.146
p4	rng	65.4–71.0	0.477
p5	rng	71.0–76.3	0.420
p67	rng	76.3–86.1	0.341
p81	pen	86.1–120.0	0.277
p82	pen	120.0–200.0	0.277
p83	pen	200.0–300.0	0.277
p84	pen	300.0–500.0	0.277
d31	phi	18.4–25.4	1.714
d32	phi	25.4–31.0	1.527
d33	phi	31.0–36.0	1.356
d34	phi	36.0–44.3	1.146
d4	rng	44.3–48.1	0.477
d5	rng	48.1–51.7	0.420
d67	rng	51.7–58.2	0.341

**pkts.d\*** counts of deuteron events from start to end of interval.

Table 5.5 associates the count rates in PKTS with the livetimes in PTLV, and gives energy ranges and nominal geometry factors for each channel. When a livetime is zero in the PTLV structure, all associated count rates should be discarded.

### 5.3.3 SCEWxxxxx.DAT

For the anisotropy study described in TN 6 Part II, the values of  $L$  and  $B$  calculated at the guiding centre corresponding to each measurement are needed. The SCEW structure contains  $\Delta L \equiv L_{GC} - L$  and  $\Delta B \equiv B_{GC} - B$  at the start of each six second interval: The SCEW data are not used in this study. Instead, we chose to regenerate the values of  $B, L$  with the DGRF or IGRF model for the epoch of Jan 1 of each year of measurements. Using the quaternions in the



**Table 5.6.** Description of the EPH structure

Element	Data Type	Definition
eph.time	Long integer	Universal time (s) of start of six second interval
eph.alt	Single precision	Geodetic altitude (km)
eph.lon	Single precision	Longitude (deg)
eph.lat	Single precision	Geodetic latitude (deg)
eph.pa	Single precision	Pitch angle (deg)
eph.b	Single precision	DGRF Magnetic field intensity (Gauss) at spacecraft location
eph.fl	Single precision	$L$ Value ( $R_E$ ) corresponding to spacecraft location and eph.pa
eph.bc	Single precision	DGRF Magnetic field intensity (Gauss) at the guiding centre of a 100 MeV particle
eph.flc	Single precision	$L$ Value ( $R_E$ ) corresponding to the guiding centre of a 100 MeV particle and eph.pa
eph.beta	Single precision	Azimuthal angle $\beta$ (deg)
eph.bv	Single precision (3)	Geocentric spherical DGRF magnetic field vector components (Gauss)
eph.vn	Single precision (3)	Geocentric spherical components of the local curvature vector of the magnetic field
eph.altm	Single precision	Altitude of the lowest mirror point on the local magnetic field line
eph.flag	Byte	Quality flag

QCORxxxxx.DAT, the look direction of the instrument and the locations of the guiding centres corresponding to each measurement and particle energy  $E$  were determined, and the values of  $B_{GC}$  and the respective  $L_{GC}(E)$  were calculated. Finally, a new value of the pitch angle for each measurement was derived from the look direction and the direction of the local magnetic field vector. The resulting values are stored in the new ephemeris files described in Sect. 5.3.4.

### 5.3.4 Generation of a new ephemeris data set

In order to simplify the data processing, a new set of ephemeris files was generated: the EPHxxxxxx.DAT files. Each of these files combines all the ephemeris, attitude and magnetic field data for one day. The magnetic field vectors and related quantities were recalculated from the ephemeris data using the UNILIB library and DGRF 90 or IGRF 95 updated to Jan 1 of the year of the measurements (see Sect. 5.3.3).

Table 5.6 lists the definitions of the structure elements. eph.beta is the azimuthal angle  $\beta$  defined in TN 6 Part II. The values of  $L_{GC}$  and  $B_{GC}$  correspond to the guiding centre positions

of 103.05 MeV protons (centre of energy channel p81). Storing one value of  $L_{GC}$  and  $B_{GC}$  is sufficient as they depend linearly on the gyroradius.

## 5.4 Model construction

In this section the data binning procedure is outlined, as well as the conversion from counts and livetimes to fluxes. The model construction procedure is analogous to the procedure followed for the AZUR data (see Sect. 4.3). The correction procedure for the field of view, described in general terms in Appendix A, is adapted to the PET telescope and sensors.

### 5.4.1 Data binning

The PET data for the second half of 1994 and the first half of 1995 have been averaged over a rectangular three dimensional bin in  $(E, L, \alpha_0)$  space by means of the IDL programme BINNING.PRO. The  $(E, L, \alpha_0)$  bin limits of the grid are listed in Table 5.7. The limits of the energy bins correspond to the channel limits in Table 5.5. The  $L$  and  $\alpha_0$  bins were selected so as to obtain a uniform distribution of the measurements over the grid. The DGRF magnetic field model for epoch 1995 was used to calculate the magnetic coordinates. No external magnetic field model was used.

Because of the relatively poor statistics of the PET proton counts (only a fraction of the events satisfying detector coincidence conditions are actually processed by the pulse height analysers, and only a few of the twenty analysed events telemetred per second appear in the proton channels; see Technical Note 5), it is not possible to convert individual count rates into fluxes without accumulation. For many measurements, the recorded count rate is zero while the corresponding livetime is not, and is lower than the integration time of 6 s. Therefore, it was decided to average the counts and livetimes separately, so that the average flux in each model bin is the ratio of the sum of the counts in that bin divided by the sum of the livetimes.

### 5.4.2 Correction for telescope field of view

As for the AZUR data, the PET flux averages are corrected for the telescope field of view by means of the program FOVAPP.PRO. Figure 5.4 shows the effective areas for a subset of the PET sensors, which were provided in the form of a table by M.D. Looper.

There are eleven ranges in Fig. 5.4, corresponding to particles stopping in each of the detector wafers from P2 to P8 (counting the P3A, ..., P3E wafers separately) after passing through all the previous detectors starting with P1. With reference to the channels listed in Table 5.5, p21–p24 are P2 range, p31 is P3A, p32 is P3B, p33 is P3C, p34 is the sum of particles with ranges to P3D and P3E (so its response is taken to be the average of the responses for P3D and P3E), p4 is P4, p5 is P5, p67 is P6 and P7 totalled (and again responses averaged), and p81–p84 are all of P8 range.

**Table 5.7.**  $(E, L, \alpha_0)$  Bin limits for the PET model grid

$E$ Limits (MeV)	$L$ Limits ( $R_E$ )	$\alpha_0$ Limits (deg)
18.5	1.005	0.0000
20.5	1.015	21.2018
22.5	1.025	22.7340
24.5	1.035	24.2568
27.2	1.045	25.7705
37.4	1.055	27.2751
45.8	1.065	28.7709
53.0	1.075	30.2579
65.4	1.085	31.7364
71.0	1.095	33.2065
76.3	1.105	34.6683
86.1	1.115	36.1220
120.0	1.125	37.5677
200.0	1.135	39.0055
300.0	1.145	40.4356
500.0	1.155	41.8581
	1.165	43.2730
	1.175	44.6806
	1.185	46.0809
	1.195	47.4741
	1.205	48.8602
	1.225	50.2394
	1.275	51.6118
	1.325	52.9774
	1.375	54.3364
	1.425	55.6888
	1.475	57.0348
	1.525	58.3744
	1.575	59.7078
	1.625	61.0350
	1.675	62.3561
	1.725	63.6712
	1.775	64.9803
	1.825	66.2836
	1.875	67.5812
	1.925	68.8730
	1.975	70.1592
	2.025	71.4399
		72.7150
		73.9848
		75.2492
		76.5084
		77.7624
		79.0112
		80.2549
		81.4936
		82.7273
		83.9562
		85.1802
		86.3994
		90.0000

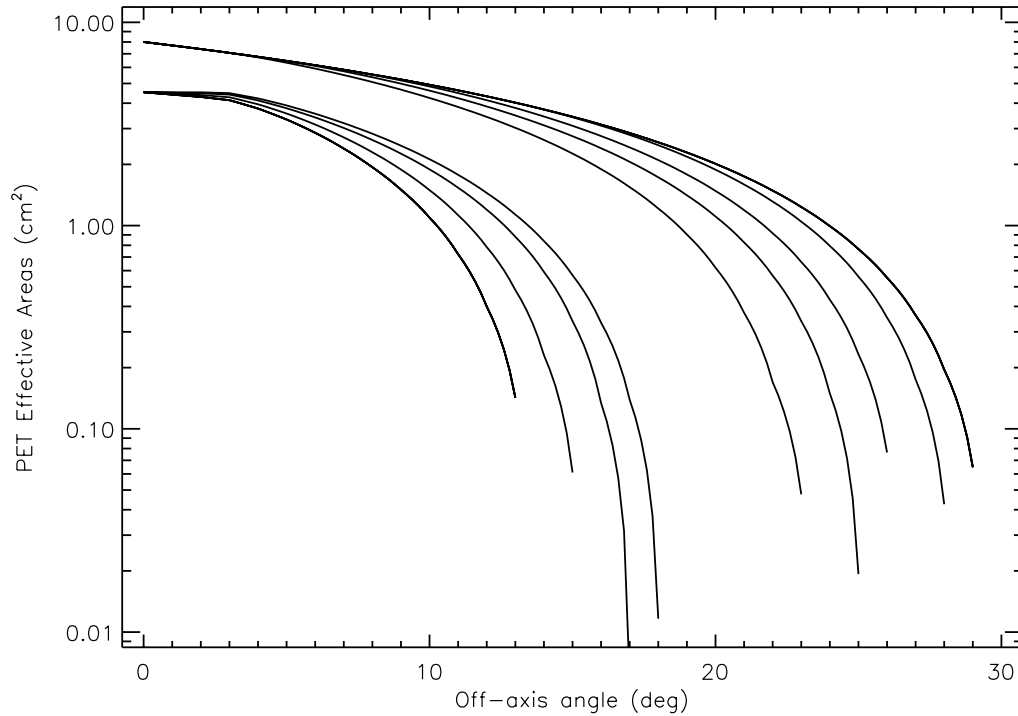


**Figure 5.4.** Effective areas of the SAMPEX/PET sensors

The IDL program `AREAS.PRO` reads the tabulated effective areas and returns the areas for all fifteen proton channels. The field of view correction is carried out by the program `DETCOR.PRO`, which calls `FOVAPP.PRO` and `AREAS.PRO`.

### 5.4.3 Final flux map

The IDL program `MODEL.PRO` reads in the flux averages created by `BINNING.PRO` and writes the final flux map `SAMPEX.DAT`. This program is interactive and allows for the correction of spurious points. For grid points where there are no data, the flux is set to  $-1.0$ .

The final flux map is then transformed into a `BLOCK DATA` file by means of the program `MODTOBD.FOR`. This program also transforms differential into integral fluxes. The implementation of the new SAMPEX model (called PSB97) in UNIRAD is described in Technical Note 10.

### 5.4.4 Comparison to AP-8

Figures 5.5–5.8 show the flux maps of the PSB97 model for channels 1, 5, 9, and 13, respectively, in  $(L, \alpha_0)$  space, together with the directional AP-8 MIN maps for the same grid values.

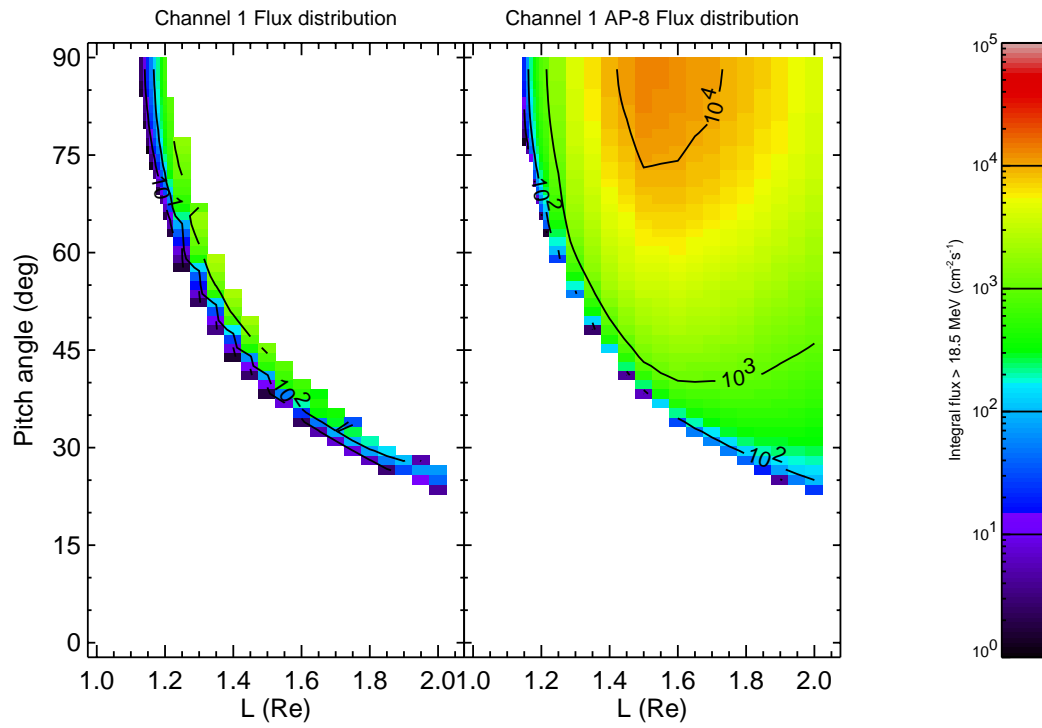


**Figure 5.5.**  $(L, \alpha_0)$  Map of the PSB97 model and AP-8 MIN for channel 1

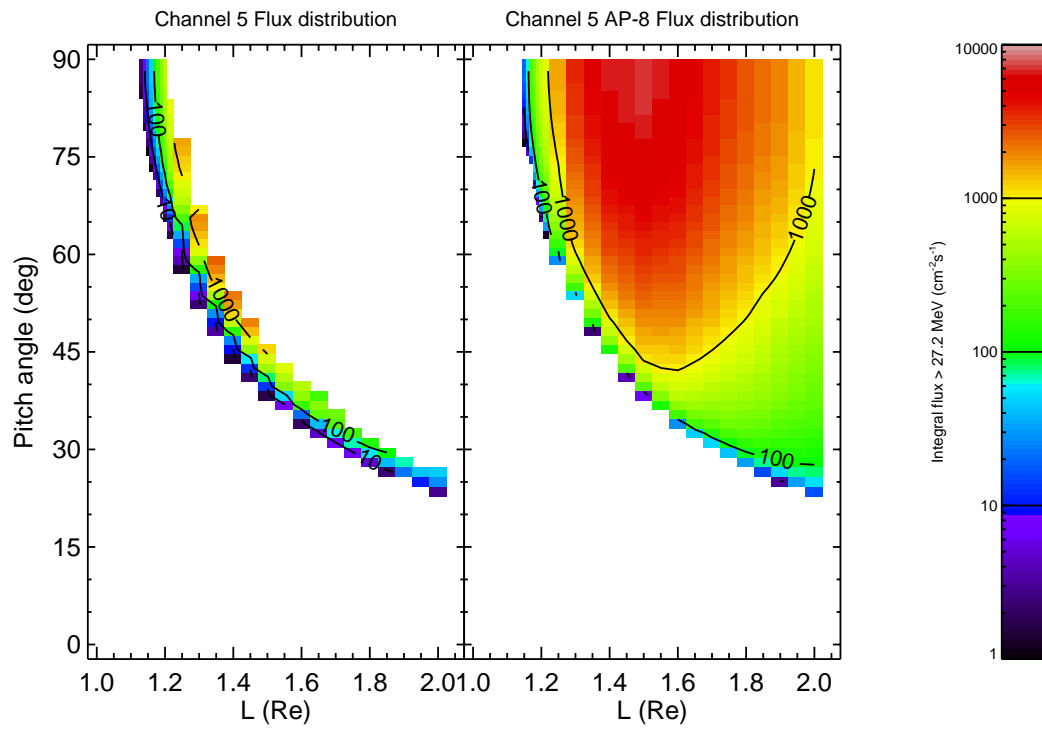


**Figure 5.6.**  $(L, \alpha_0)$  Map of the PSB97 model and AP-8 MIN for channel 5

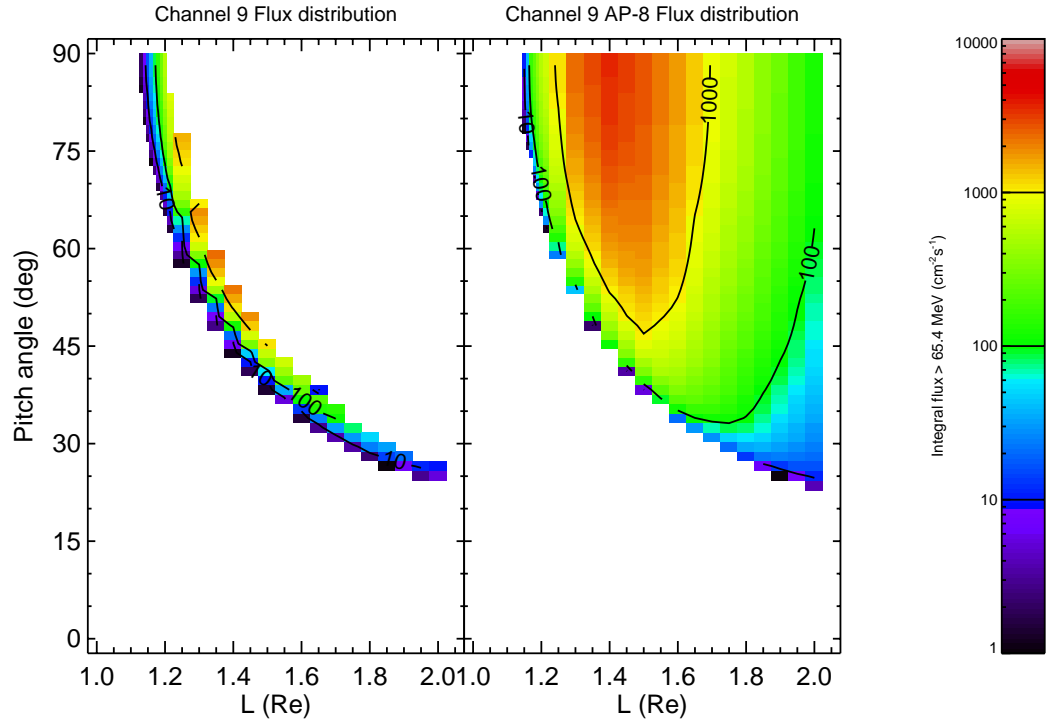


**Figure 5.7.**  $(L, \alpha_0)$  Map of the PSB97 model and AP-8 MIN for channel 9

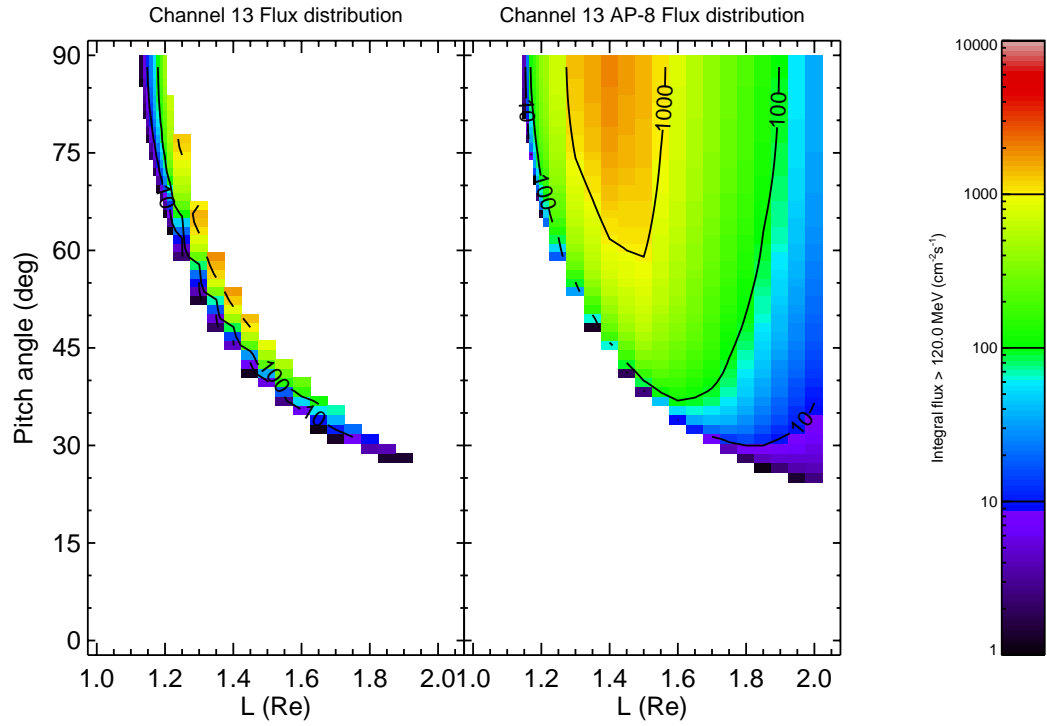


**Figure 5.8.**  $(L, \alpha_0)$  Map of the PSB97 model and AP-8 MIN for channel 13

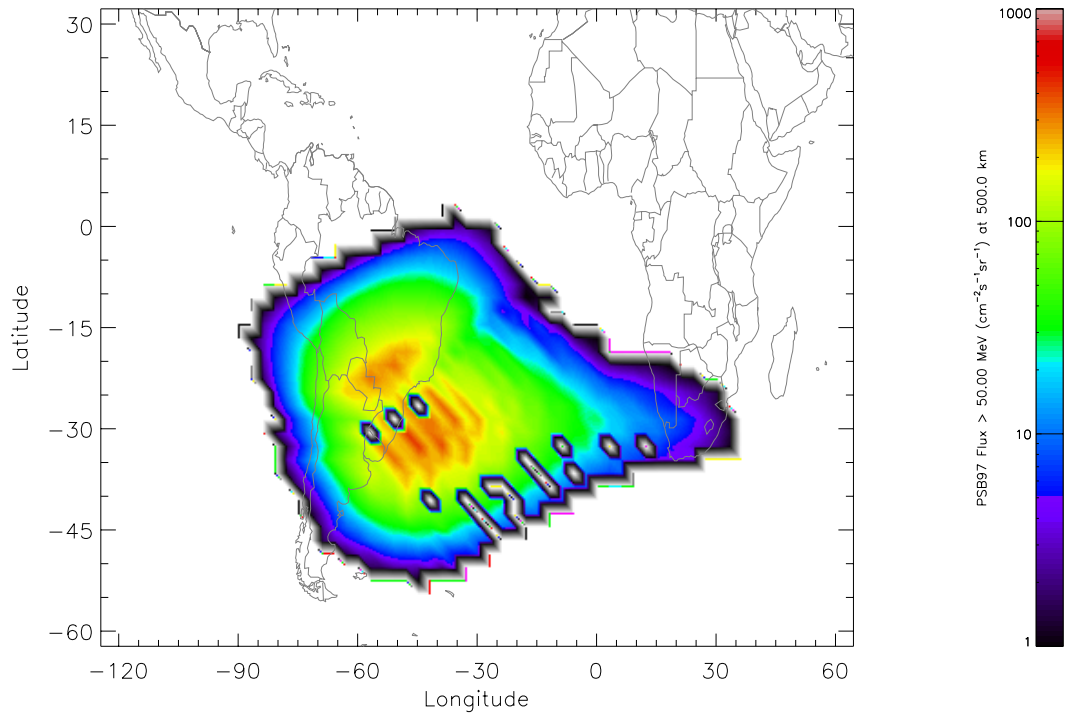


**Figure 5.9.** World map of the PSB97 >50 MeV proton flux at 500 km

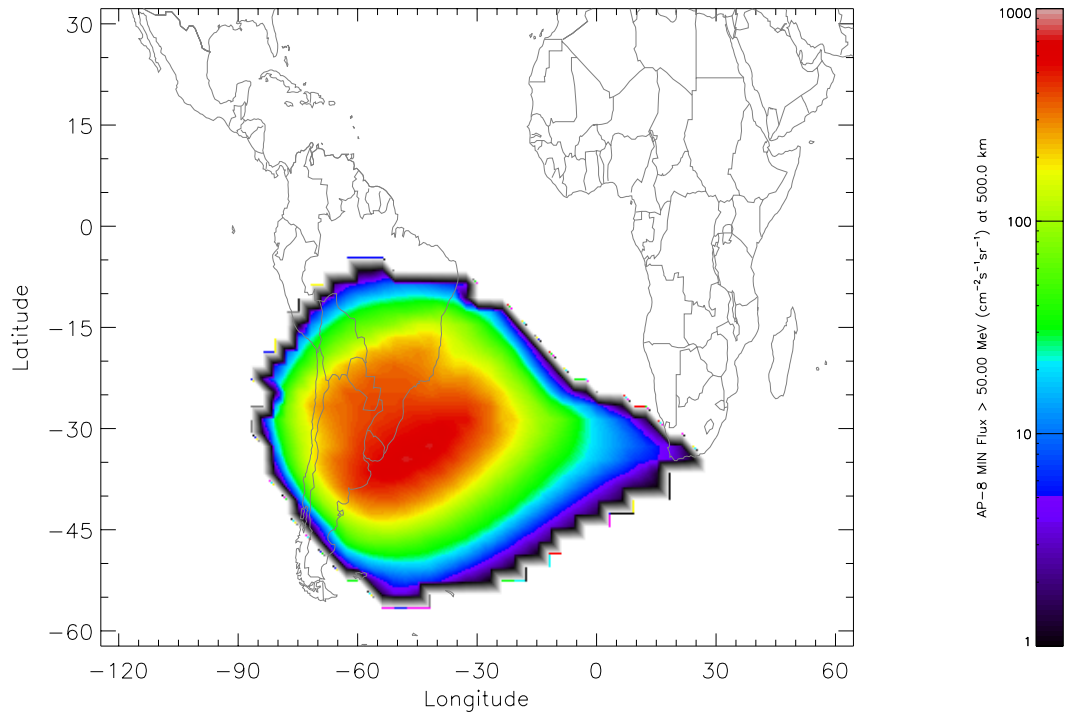


**Figure 5.10.** World map of the AP-8 MIN >50 MeV proton flux at 500 km

It can be seen that for the lowest  $L$  values the PSB97 fluxes are smaller than the corresponding AP-8 MIN fluxes by a factor of about two.

Another way of comparing the PSB97 model to AP-8 consists of drawing world maps of fluxes at fixed altitude. Figures 5.9 and 5.10 show the distributions of the PSB97 and AP-8 MIN proton flux  $>50$  MeV at an altitude of 500 km, respectively. Again, the PSB97 flux is lower than the AP-8 MIN flux.



# Chapter 6

## The UARS/PEM data base and radiation belt model

### 6.1 Mission and detector description

J.D. Winningham, SwRI, Texas, PI for the PEM instrument on the UARS mission, was approached by the TREND project manager, in April 1995. At that time the PEM data had to be recalibrated, and the software to retrieve and process the UARS data had to be reprocessed to run with the VMS operating System installed at BIRA/IASB. Sharber et al. (1996) outline the capabilities as well as the limitations of the PEM-UARS data set for the construction of a new radiation belt models for energetic trapped protons.

In 1996, M. Kruglanski visited SwRI, Texas, to examine the PEM data and to get acquainted with the existing data processing software running there on Sun stations. Thanks to the efficient collaboration of the whole PEM team at SwRI, and especially of R. Frahm, we have been able to transfer two years of PEM data to BIRA/IASB via FTP. Pre-processing of these data had to be done on the SwRI computer facilities due to computer Operating System incompatibility at BIRA/IASB.

Unfortunately, the PEM detectors directional responses (geometric factor) to energetic proton could not be obtained from Lockheed Palo Alto Research Laboratory. Therefore, we had to make an educated guess to determine the sensitivity of the detectors for different incident angles of the energetic protons. This limits to some extent the reliability of the radiation belt model obtained from the UARS data set.

#### 6.1.1 The UARS mission

The Upper Atmosphere Research Satellite (UARS) was launched by the space shuttle Discovery on 12 September 1991 into a near circular orbit at 585 km with  $57^\circ$  inclination. It operated almost continuously until April 1995 after which time the PEM coverage was considerably reduced. The satellite is three-axis stabilized and covers all the local times in approximatively

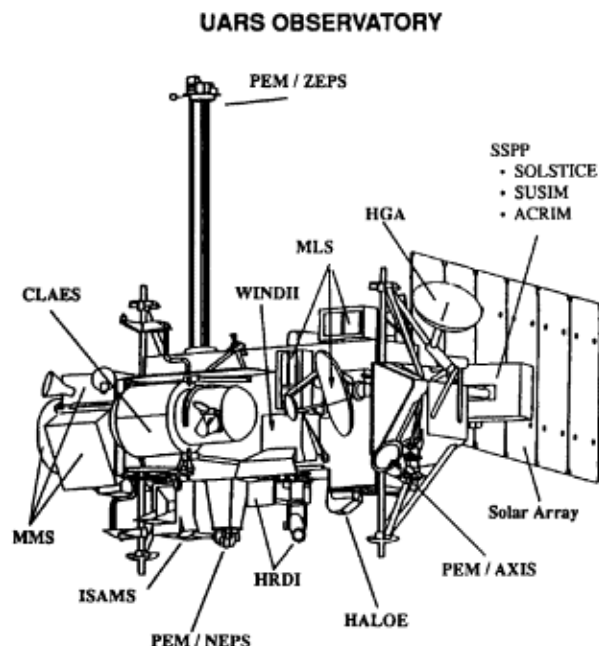


**Figure 6.1.** Line drawing of the UARS observatory showing the placement of the various instruments. The proton and electron sensor are designated by PEM/ZEPS and PEM/NEPS.

36 days. About every 34 days, the spacecraft reverses its attitude by a  $180^\circ$ -rotation around its vertical axis (Reber, 1993; Reber et al., 1993). A line drawing of the UARS spacecraft including the placement of the various experiments is presented in Fig. 6.1. The spacecraft has a length of 10.7 m and a total mass of 6,540 kg.

The goal of the UARS mission was to understand the chemistry, dynamics, and energy balance above the troposphere as well as the coupling between these processes and atmosphere regions. The ten experiments onboard UARS, listed in Table 6.1, meet these objectives. Four experiments (CLAES, ISAMS, MLS and HALOE) are devoted to measure the altitude profiles of chemical species. Two experiments (HRDI and WINDII) are devoted to measure the atmospheric winds. Three experiments (SOLSTICE, SUSIM and ACRIM) are devoted to measure the energy inputs from the Sun. One experiment (PEM) is devoted to measure the energy input to the upper atmosphere contributed by the flux of charged particles penetrating into the Earth's magnetosphere. More extensive information can be found in the dedicated sections of the *Geophysical Research Letters* (Reber, 1993, and following papers in the same issue) and of the *Journal of Geophysical Research* (Reber et al., 1993, and following papers in the same issue).

### 6.1.2 Particle Environment Monitor

The Principal Investigator (PI) of the Particle Environment Monitor (PEM) experiment is J.D. Winningham of the Southwest Research Institute (SwRI) and the collaboration includes more

**Table 6.1.** List of the UARS experiments

CLAES	Cryogenic limb array etalon spectrometer
ISAMS	Improved stratospheric and mesospheric sounder
MLS	Microwave limb sounder
HALOE	Halogen occultation experiment
HRDI	High resolution doppler imager
WINDII	Wind imaging interferometer
SOLSTICE	Solar/stellar intercomparison experiment
SUSIM	Solar ultraviolet spectral irradiance monitor
ACRIM	Active cavity radiometer irradiance monitor
PEM	Particle environment monitor

**Table 6.2.** List of the PEM instruments

AXIS	Atmospheric X-ray imaging spectrometer
HEPS	High-energy particle spectrometer
MEPS	Medium-energy particle spectrometer
VMAG	Vector magnetometer

than thirty scientists from seven institutes. The main objective of the PEM experiment is to provide comprehensive measurements of energy inputs into the Earth's atmosphere by energetic particle precipitations (Winningham et al. 1993, Sharber et al. 1993). The four instruments which are part of the PEM experiment are listed in Table 6.2.

The AXIS instrument consists of an array of cooled silicon detectors. It measures the intensities of bremsstrahlung X-rays that are generated when energetic electrons penetrate the atmosphere.

The HEPS instrument consists of six silicon detector telescopes and two surface barrier detectors. These detectors measure protons in the energy range from 0.1 to 150 MeV and electrons from 0.03 to 5 MeV.

The MEPS instrument is made of eight divergent plate electrostatic analyzers. They measure particles in the energy range from 1 eV to 32 keV.

The VMAG instrument is a boom-mounted three-axis fluxgate magnetometer. Each sensor has a dynamic range of  $\pm 65,000$  nT with a resolution of 2 nT and has the capability to measure disturbances in the field in the frequency range 5–50 Hz.

The HEPS and VMAG instruments of the PEM experiment provide a good opportunity to study the proton radiation belt at low altitude to an energy of 150 MeV. From here on, we will focus on the HEPS instrument of the PEM experiment and especially on the detectors dedicated to the high-energy protons.

**Table 6.3.** Characteristics of the HEPS detectors

Detector name	Angle [degrees]	Electron energy range [MeV]	Proton energy range [MeV]	Geometric factor [cm <sup>2</sup> sr]
HEPS1/T1	+45	0.03 – 5.0	0.5 – 150.0	0.54
HEPS1/T2	+15	0.03 – 5.0	0.5 – 150.0	0.54
HEPS1/LEP	+15	none	0.1 – 0.5	0.07
HEPS2/T1	+90	0.03 – 5.0	0.5 – 150.0	0.54
HEPS2/T2	-15	0.03 – 5.0	0.5 – 150.0	0.54
HEPS2/LEP	-15	none	0.1 – 0.5	0.07
HEPS3/T1	+165	0.03 – 1.5	none	1.53
HEPS3/T2	-165	0.03 – 1.5	none	1.53

### 6.1.3 The HEPS instrument

The technical information on the HEPS telescopes presented in this section is mainly collected from Winningham et al. (1993) and Sharber et al. (1996).

The HEPS sensors were supplied by Lockheed Palo Alto Research Laboratory. They consist of six solid state telescopes and two low-energy proton (LEP) detectors. They are structured into three independent units (HEPS1, HEPS2 and HEPS3) and measure high energy protons and electrons in different viewing directions. They are all situated in the vertical plane that contains the spacecraft velocity vector. Four of the telescopes and the two LEP detectors measure locally downcoming protons and electrons while the two other telescopes measure locally upcoming electrons. The viewing direction, the energy range and the geometric factor of the eight detectors are listed in Table 6.3. The direction of each detector is specified by the angle from zenith to nadir in the local vertical plane. The field of view is 30°. The uncertainties in the geometric factors are 2.5% for the HEPS1 and HEPS2 telescopes, 1.5% for the HEPS3 telescopes and 3.5% for the LEP detectors.

For the study of the proton radiation belt, only the four telescopes HEPS1/T1, HEPS1/T2, HEPS2/T1 and HEPS2/T2 are useful. Except for their orientation, these telescopes are identical. The HEPS instrument operates continuously throughout the orbit.

The cross-sectional view of one of these four telescopes is shown in Fig. 6.2. The silicon detector D has a thickness of 200  $\mu\text{m}$  and measures low-energy protons and electrons. High-energy electrons and medium-energy protons are stopped in detector E which is comprised of two lithium-drifted detectors of a total thickness of 1 cm. Detector E' has a thickness of 0.3 cm and differentiates medium-energy protons from the highest proton energy range. It also rejects particles penetrating from the back direction. Around the stacked E detectors lies a system of annular detectors (A) with a thickness of 0.1 cm. This system rejects high-energy particles entering from the sides.

Signals from the D and E detectors are pulse-height analyzed simultaneously by fast analog-to-digital converters. Logic analysis of the pulses by the coincidence/anticoincidence circuitry

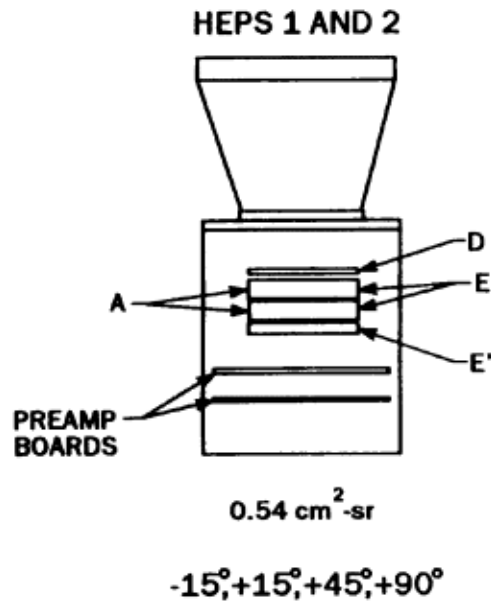


**Figure 6.2.** Diagram of the HEPS1 and HEPS2 telescopes showing the detector arrangements, preamplifier board location, and collimator look angles defined with respect to the zenith direction

distinguishes electrons from protons and accumulates pulse-height distributions in memory. The fast parallel processing allows pulse analysis rates in each telescope of approximately 100,000 events per second. A microcomputer controls the accumulation of signals to form a 32-step logarithmic energy spectrum every four seconds for the electron channels and every 16s for the proton channels. This compression introduces an uncertainty which varies from 3.1% at low count rates to 1.7% at higher count rates, and jumps to 10% at extremely high count rates.

For high-energy protons, a pre-flight calibration of the HEPS instrument was done on the 88-inch cyclotron of the Lawrence Berkeley Laboratories. The energy range was from 6 to 55 MeV. In the South Atlantic Anomaly (SAA) region, it is possible to obtain count rates high enough to be influenced by the processing rate capability of the HEPS counting. Therefore, the livetime as a function of counting rate was also measured during the preflight calibration. This livetime was evaluated with a set of  $^{90}\text{Sr}$  and  $^{204}\text{Tl}$  beta sources.

Two types of in-flight calibration are also executed periodically to monitor the instrument performance. The first type corresponds to an electronic pulser calibration mode where fixed amplitude pulses are applied to the input of the amplifier of each detector. This calibration mode tests the logic functions as well as the gain and resolution in the energy detectors. The second type of in-flight calibration utilizes a weak  $^{241}\text{Am}$  alpha source mounted within the HEPS instrument. The energy of the most intense alpha line (5.48 MeV) is above the range of the normal operating mode, so that the background interference from the sources is minimized. This calibration provides an absolute gain calibration of the D proton detector and the E electron detector during the UARS mission. Based on the two in-flight calibrations, a compensation to

**Table 6.4.** Differential number flux uncertainties for protons from 5 to 150 MeV

Counts/accumulation interval	Measurement uncertainties
2	74.3
10	38.9
31	29.0
32	28.9
$10^2$	24.9
$10^3$	23.1
$10^4$	22.8
$10^5$	24.7

an electronic drift may be initiated by a ground command.

The quality of the HEPS data is influenced by the compression of accumulated data, the adjustments for dead time and the removal of a temperature-dependent background. The uncertainties on the differential number flux for protons from 5 to 150 MeV as a function of the counts per accumulation interval are presented in Table 6.4. At low count rates, the uncertainties are dominated by the Poisson statistical errors. At higher count rates, the uncertainties are dominated by uncertainties on the energy channel widths of the proton detectors. At very high count rates, the uncertainties are also influenced by the errors on the dead time correction.

The flux spectrum measured by each telescope is spread over different sensors. The sensors DP and EP1 contain eight points of the spectrum while the sensor EP2 only contains seven points. Since we are interested in the high energy protons, i.e. above 5 MeV, only the two sensors EP1 and EP2 are taken into account, which provides a 15-point flux spectrum for each of the four proton telescopes. The central energies and the energy widths for the four proton telescopes are listed in Table 6.5.

## 6.2 Data processing

To build a new proton radiation belt model, the processing of the UARS/PEM proton telescope data is realized in two separate steps. During the first step, all the basic data are retrieved from the IDFS database located at SwRI. The basic data include, for each point, the time of measurement, the geographic location of the spacecraft at this time, the telescope orientation and the particle fluxes for different energies. The second step consists of ordering the data in terms of geomagnetic coordinate systems.

During the data processing, the magnetic field vector  $\mathbf{B}_{\text{VMAG}}$  as measured by the VMAG magnetometer is used to validate the data. Records are rejected when  $\mathbf{B}_{\text{VMAG}}$  deviates significantly from the magnetic field vector  $\mathbf{B}_{\text{IGRF}}$  obtained from the magnetic field model IGRF, epoch 1992.

**Table 6.5.** Proton energy (MeV) channels of the EP1 and EP2 sensors of the HEPS detectors

HEPS1/T2		HEPS1/T1		HEPS2/T2		HEPS2/T1	
Centre	Width	Centre	Width	Centre	Width	Centre	Width
6.7	1.5	6.2	1.3	6.6	1.5	6.1	1.3
8.0	1.2	7.4	1.1	7.9	1.2	7.3	1.1
9.9	2.6	9.2	2.5	9.7	2.4	9.1	2.5
12.5	2.7	11.7	2.7	12.4	2.9	11.6	2.7
16.0	4.2	15.1	4.2	15.9	4.2	15.1	4.2
21.7	7.2	20.8	7.2	21.7	7.2	20.8	7.2
29.0	7.3	28.1	7.3	29.0	7.4	28.0	7.3
37.9	10.4	36.9	10.4	38.3	10.4	36.9	10.4
50.9	8.9	49.5	14.6	50.8	8.9	51.8	10.1
61.7	12.9	64.1	14.6	61.7	12.9	64.1	14.5
77.9	19.4	82.7	22.6	77.8	19.4	82.7	22.7
99.3	23.6	108.2	28.5	99.4	23.7	108.4	28.6
120.3	18.3	134.1	23.4	120.0	18.2	134.2	23.1
135.3	11.9	153.4	15.1	135.3	11.9	153.3	15.3
148.4	14.8	168.0	14.0	148.4	14.2	168.0	14.0

### 6.2.1 Geometric factor correction

The HEPS proton flux values included in the IDFS database have been obtained from constant geometric factors that do not take into account the variation of the proton flux over the opening angle of the detector. In other words, the flux values are obtained under the assumption that the detector is perfectly shielded and that the pitch angle distribution of the proton flux over its opening angle is isotropic. Since, at low altitude, the proton flux is strongly anisotropic, corrections have to be applied to the geometric factors. Indeed, the actual counting rates result from the convolution of the proton fluxes by the directional response function  $h(\omega)$  of the detector, as shown by Eq. (A.4).

The available PEM documentation does not include the directional responses of the HEPS detectors (more information has been requested from the builder of the instrument, Lockheed Palo Alto Research Laboratory). The nominal field of view (FOV) of the HEPS detectors is equal to  $30^\circ$  but detailed analysis of the flux measurements shows that the effective FOV is larger and that the HEPS directional response function extends to  $\theta \approx 60^\circ$  for 100 MeV protons. This FOV analysis is reported in Sect. 6.3.2.

Due to the large FOV and the lack of an experimental response function  $h(\omega)$  of the HEPS detectors, only measurements corresponding to a local pitch angle equal to  $90^\circ \pm 10^\circ$  have been used to build the UARS trapped proton model. Indeed, since the pitch angle distribution is peaked at  $90^\circ$ , when the local pitch angle is about  $90^\circ$ , most of the protons penetrate into the detector at an angle within the nominal FOV and Eq. (A.4) is expected to be well approximated by Eq. (A.1), i.e. the geometric factor correction should then be small. Therefore, only a simple

correction algorithm is applied. It should be kept in mind that it is not an ideal procedure to obtain fully reliable trapped proton fluxes from the PEM experiment. This situation jeopardizes the reliability of the radiation belt model determined below.

The correction algorithm is described in Sect. 6.3.3; it is very similar to the algorithm applied to the AZUR and SAMPEX data.

## 6.2.2 Data binning

The proton UARS data are sorted in 15 energy bins, 30 McIlwain  $L$  bins and 45 equatorial pitch angle bins. The bin limits in energy correspond to the limits of the energy channels of each telescope (see Table 6.5). The bin limits in McIlwain  $L$  parameter and in equatorial pitch angle are listed in Table 6.6. The table also includes a reference value for each bin. Note that the reference value of bins generally corresponds to the mid value of the bin limits, except for the outer bins (where the reference value is set to the outer limit). From  $L = 1$  to  $L = 1.2$ , the width of the  $L$  bins is set to  $0.01 R_E$ . From  $L = 1.2$  to  $L = 1.6$ , the value of the  $L$ -bin widths is set alternatively to 0.01 and  $0.04 R_E$ . The alternation between small and large widths above  $L = 1.2$  allows to get narrow bins without a too excessive number of bins. From  $\alpha_0 = 37^\circ$  to  $82^\circ$ , the width of the equatorial pitch angle bins is set to  $1.5^\circ$ . Outside this range the widths are larger.

The limit and reference values, listed in Table 6.6, as well as the bin widths, are stored in the text file `uarspem.lim`. This file is common to all four detectors. Since the energy channels differ slightly from one detector to the other, the values for the energy bins correspond to mean values.

The  $(L, \alpha_0)$  mesh is represented on Fig. 6.3 as well as the data coverage for all four detectors. The data coverage is given for the whole PEM data set corresponding to the year 1991. The solid lines correspond to iso-contours of 35 measurements per month, per degree and per  $L$ -unit for the four different detectors. Equatorial pitch angles near 90 degrees are encountered only by the HEPS1/T2 and HEPS2/T2 detectors for  $1 < L < 1.2$ . The detector HEPS1/T1 offers the largest coverage in  $L$ . The smallest coverage is obtained by the detector HEPS2/T1. The observed difference in coverage between the detector is due to the restriction in local pitch angle and the orbit of the UARS spacecraft (see Sect. 6.3.1).

The UARS proton data are processed separately for different periods of time. Each year is divided in three different periods of about four months. Note, however, that for the year 1991, there is only one single period of about three months. During the binning process, the values of 15 different quantities are calculated in each bin:

- $a_0 = \sum_i F_i$ ;
- $a_1 = \sum_i F_i \Delta L_i$ ;
- $a_2 = \sum_i F_i \Delta \alpha_{0i}$ ;
- $a_3 = \sum_i F_i \Delta t_i$ ;



**Table 6.6.** Bin limits ( $L$ ,  $\alpha_0$ )

	McIlwain $L$ parameter			Equatorial pitch angle		
	Min.	Max.	Ref.	Min.	Max.	Ref.
1	1.00000	1.09500	1.00000	0.0000	7.5000	0.0000
2	1.09500	1.10500	1.10000	7.5000	12.5000	10.0000
3	1.10500	1.11500	1.11000	12.5000	17.5000	15.0000
4	1.11500	1.12500	1.12000	17.5000	22.5000	20.0000
5	1.12500	1.13500	1.13000	22.5000	27.5000	25.0000
6	1.13500	1.14500	1.14000	27.5000	31.0000	30.0000
7	1.14500	1.15500	1.15000	31.0000	33.0000	32.0000
8	1.15500	1.16500	1.16000	33.0000	35.0000	34.0000
9	1.16500	1.17500	1.17000	35.0000	37.0000	36.0000
10	1.17500	1.18500	1.18000	37.0000	38.5000	37.7500
11	1.18500	1.19500	1.19000	38.5000	40.0000	39.2500
12	1.19500	1.20500	1.20000	40.0000	41.5000	40.7500
13	1.20500	1.24500	1.22500	41.5000	43.0000	42.2500
14	1.24500	1.25500	1.25000	43.0000	44.5000	43.7500
15	1.25500	1.29500	1.27500	44.5000	46.0000	45.2500
16	1.29500	1.30500	1.30000	46.0000	47.5000	46.7500
17	1.30500	1.34500	1.32500	47.5000	49.0000	48.2500
18	1.34500	1.35500	1.35000	49.0000	50.5000	49.7500
19	1.35500	1.39500	1.37500	50.5000	52.0000	51.2500
20	1.39500	1.40500	1.40000	52.0000	53.5000	52.7500
21	1.40500	1.44500	1.42500	53.5000	55.0000	54.2500
22	1.44500	1.45500	1.45000	55.0000	56.5000	55.7500
23	1.45500	1.49500	1.47500	56.5000	58.0000	57.2500
24	1.49500	1.50500	1.50000	58.0000	59.5000	58.7500
25	1.50500	1.59500	1.55000	59.5000	61.0000	60.2500
26	1.59500	1.60500	1.60000	61.0000	62.5000	61.7500
27	1.60500	1.69500	1.65000	62.5000	64.0000	63.2500
28	1.69500	1.70500	1.70000	64.0000	65.5000	64.7500
29	1.70500	1.79500	1.75000	65.5000	67.0000	66.2500
30	1.79500	1.80500	1.80000	67.0000	68.5000	67.7500
31				68.5000	70.0000	69.2500
32				70.0000	71.5000	70.7500
33				71.5000	73.0000	72.2500
34				73.0000	74.5000	73.7500
35				74.5000	76.0000	75.2500
36				76.0000	77.5000	76.7500
37				77.5000	79.0000	78.2500
38				79.0000	80.5000	79.7500
39				80.5000	82.0000	81.2500
40				82.0000	84.0000	83.0000
41				84.0000	86.0000	85.0000
42				86.0000	88.0000	87.0000
43				88.0000	90.0000	90.0000

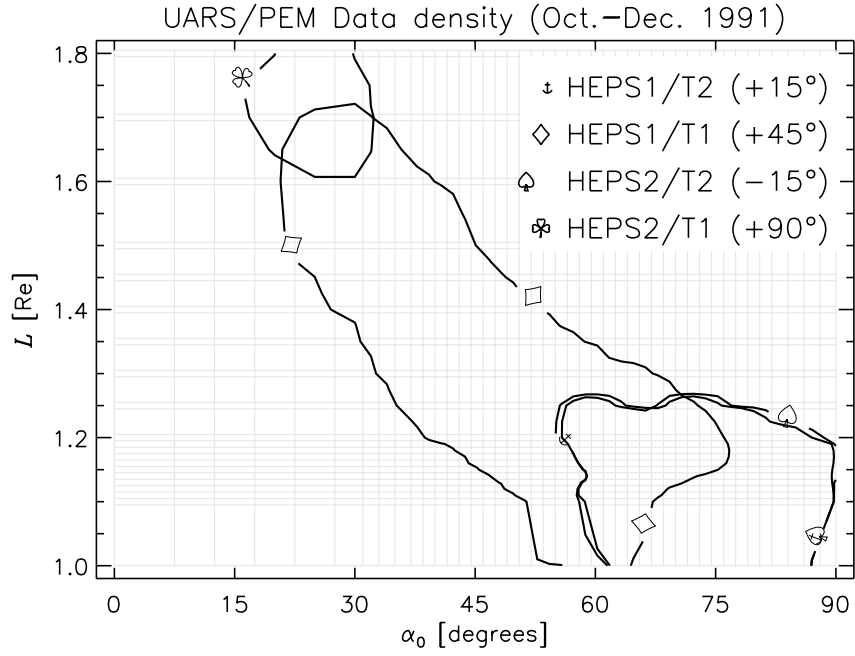


**Figure 6.3.** UARS/PEM data coverage in McIlwain  $L$  parameter and equatorial pitch angle for the four HEPS detectors. The solid lines delimit the area where the bins contain 35 measurements per month, per degree and per  $L$ -unit (year 1991)

- $a_4 = \sum_i 1 = N$ ;
- $a_5 = \sum_i \Delta L_i$ ;
- $a_6 = \sum_i \Delta \alpha_{0i}$ ;
- $a_7 = \sum_i \Delta t_i$ ;
- $a_8 = \sum_i (\Delta L_i)^2$ ;
- $a_9 = \sum_i \Delta L_i \Delta \alpha_{0i}$ ;
- $a_{10} = \sum_i \Delta L_i \Delta t_i$ ;
- $a_{11} = \sum_i (\Delta \alpha_{0i})^2$ ;
- $a_{12} = \sum_i \Delta \alpha_{0i} \Delta t_i$ ;
- $a_{13} = \sum_i (\Delta t_i)^2$ ;
- $a_{14} = \sum_i F_i^2$ .

For each quantity, the summation extends over all the data points inside the bin limits.  $F_i$ ,  $\Delta L_i$ ,  $\Delta \alpha_{0i}$  And  $\Delta t_i$  represent the observed flux, the deviation to the bin-reference of McIlwain's

parameter, the deviation to the bin-reference of the equatorial pitch angle (in radians), and the deviation to a time reference (in day), respectively.

The 15 values evaluated in all the bins are stored for each detector in binary files, the names of which have the form `yyyySddLx.bin` where `yyyy`, `dd` and `x` represent the year, the detector number (2, 5, 9 or 12) and the period label (a, b or c), respectively. The binning of the data is achieved by an IDL program called `binning_data.pro`.

### 6.2.2.1 Flux at the reference points

The 15 calculated quantities allow to evaluate for each bin the mean value ( $\bar{F} = a_0/N$ ) and standard deviation ( $\sigma = \sqrt{(a_{14} - N\bar{F}^2)/(N-1)}$ ) of the proton flux and also to take into account the dependences of the flux on  $L$ ,  $\alpha_0$ , and time. The first order dependence of the flux can be expressed by the linear equation

$$F = \hat{F} + a_L \Delta L + a_\alpha \Delta \alpha_0 + a_t \Delta t \quad (6.1)$$

where  $\hat{F}$  is the flux value for the reference point of the bin. The parameters  $\hat{F}$ ,  $a_L$ ,  $a_\alpha$ , and  $a_t$  can then be obtained by solving the equations:

$$\begin{cases} a_0 &= \hat{F}a_4 + a_L a_5 + a_\alpha a_6 + a_t a_7 \\ a_1 &= \hat{F}a_5 + a_L a_8 + a_\alpha a_9 + a_t a_{10} \\ a_2 &= \hat{F}a_6 + a_L a_9 + a_\alpha a_{11} + a_t a_{12} \\ a_3 &= \hat{F}a_7 + a_L a_{10} + a_\alpha a_{12} + a_t a_{13} \end{cases} \quad (6.2)$$

An evaluation of the error on  $\hat{F}$  is provided by the standard deviation

$$\hat{\sigma} = \sqrt{\frac{a_{14} - \hat{F}^2 N - a_L(\hat{F}a_5 + a_1) - a_\alpha(\hat{F}a_6 + a_2) - a_t(\hat{F}a_7 + a_3)}{N-4}}. \quad (6.3)$$

The flux  $\hat{F}$  differs from the average flux  $\bar{F}$  when

1. the bin-reference point does not lie near the centre of the bin;
2. the bin is not covered homogeneously by the satellite.

The last case occurs especially for bins located at the edge of the  $(L, \alpha_0)$  coverage (see Fig. 6.3).

### 6.2.2.2 Processing algorithm

To build a proton radiation belt model from the UARS data, the geometric factor correction and the data binning has to be combined in an iterative process. The flow chart of this process is displayed in Fig. 6.4.

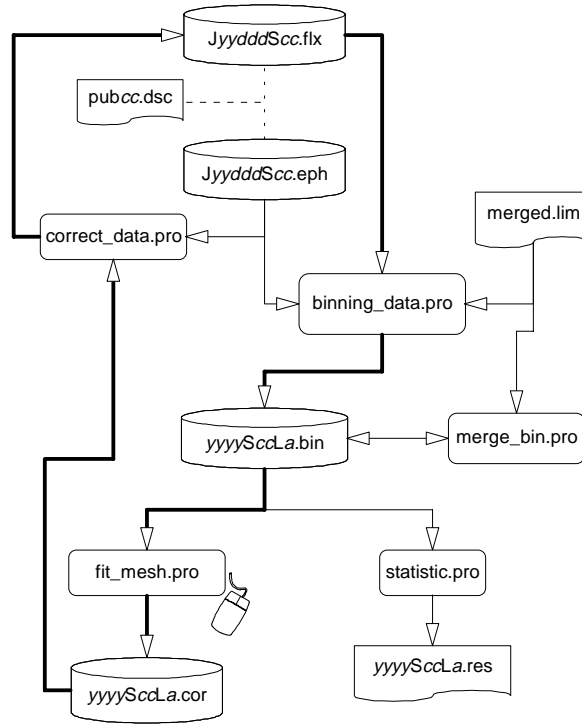


**Figure 6.4.** Flow chart of IDL procedures to produce the ‘.bin’, ‘.cor’ and ‘.res’ files

The proton fluxes and geomagnetic coordinates are stored in the ‘.eph’ and ‘.flx’ files, a catalog of which is stored in the ‘.dsc’ file. The flux data are sorted and binned by the IDL routine `binning_data.pro` according to mesh limits stored in the file `merged.lim`. The binned data are stored in a ‘.bin’ file. The IDL routine `merge_bin.pro` merges different ‘.bin’ files.

For each  $L$  value and energy channel of a ‘.bin’ file, the IDL routine `fit_mesh.pro` fits the proton flux with a 3-parameter function of the equatorial pitch angle. The function is given by

$$j(\alpha_0) = \begin{cases} f01 & \text{when } \alpha_0 < \alpha_{0c} \\ f01 + K\xi(1 + b\xi(1 + b\xi)) & \text{when } \alpha_0 > \alpha_{0c} \end{cases} \quad (6.4)$$

where  $f01$  is a constant fixed at  $10^{-2} \text{ cm}^{-2} \text{ sr}^{-1} \text{ s}^{-1} \text{ MeV}^{-1}$ ,  $\xi$  is defined as

$$\xi \equiv \sin \alpha_0 - \sin \alpha_{0c}, \quad (6.5)$$

and  $\alpha_{0c}$ ,  $K$ , and  $b$  are the three parameters to be fitted. The routine `fit_mesh.pro` allows to modify interactively the different fit parameters and to restore parameters evaluated previously. The whole set of fit parameters is stored in a ‘.cor’ file.

The geometric factor correction is applied by the IDL routine `correct_data.pro`. This routine makes use of the fitted proton fluxes to simulate the detector response and to evaluate a corrected flux. The corrected proton fluxes are stored in the `‘.flx’` files together with the raw data. Afterwards, they can be accessed by the routine `binning_data.pro` to iterate the correction process. The flow path of the iterative process is shown in Fig. 6.4

The IDL routine `statistic.pro` produces a `‘.res’` file from a `‘.bin’` file. The `‘.res’` file includes the values of  $\overline{F}$ ,  $\sigma$ ,  $\hat{F}$  and  $\hat{\sigma}$  for each bin of the mesh. This file has been used to produce the figures of Sect. 6.3.4 as well as FORTRAN a block data for inclusion in the TREP software (see Technical Note 10 and Chapter 2 of this Final Report).

## 6.3 Proton PEM/UARS model

This section is devoted to the proton flux model derived from the HEPS measurements. The model is organized in  $E$ ,  $L$ , and  $\alpha_0$ . The model ranges in energy from 5 to 150 MeV, in  $L$  from 1 to  $1.8 R_E$ , and in  $\alpha_0$  from 0 to  $90^\circ$ . The whole  $(L, \alpha_0)$  space is not covered by the available and validated measurements. The UARS/PEM data coverage in the  $(L, \alpha_0)$  space is displayed in Fig. 6.3. The solid lines delimit for each detector the area where there is more than 35 measurements per month, per degree and per  $L$ -unit. Only the measurements, for which the local pitch angle of the detector is equal to  $90^\circ \pm 10^\circ$  are taken into account. Note that only the HEPS1/T1 data set has been used to model the proton inner belt with the UARS/PEM data. Thus the proton flux model corresponds to protons whose lowest mirror-point altitude is between 500 and 585 km. This limitation results from

1. the circular orbit of UARS which is at an altitude of 585 km;
2. the restriction that the local pitch angle of the detector is equal to  $90^\circ \pm 10^\circ$ , i.e. for nearly locally mirroring particles.

Since, at low altitudes, the proton radiation belt is observed only in the SAA, the HEPS data included into the model corresponds to protons mirroring in the SAA close to the spacecraft altitude. Since the particles whose drift shell is passing through the SAA also have their lowest-altitude mirror point located in the SAA, this new model corresponds to protons with the lowest altitude of their mirror points equal to or slightly smaller than 585 km.

### 6.3.1 Model coverage

This section is focussed on the causes of this rather limited coverage of the proton PEM/UARS model.

In Figs. 6.5 and 6.6, the iso-contours of the McIlwain’s  $L$  parameter and of the magnetic field intensity  $B$  are represented at the altitude of the UARS orbit, respectively. The values of  $B$  and  $L$  are calculated for the IGRF magnetic field model corresponding to epoch 1992. On both figures, the dash-dotted curves indicate the location of the SAA where the NASA AP-8 MIN

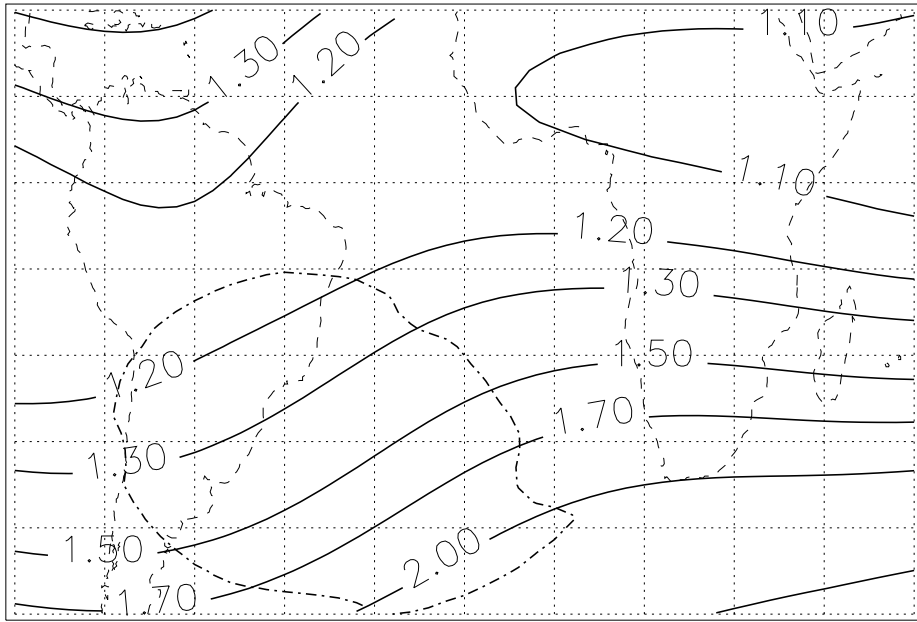


**Figure 6.5.** Iso-contours of  $L$  at 585 km. The dash-dotted line corresponds to an iso-contour where the AP-8 MIN omnidirectional integral proton flux above 10 MeV is equal to  $500 \text{ s}^{-1} \text{ cm}^{-2}$  at 585 km. The figure demonstrates the limitation  $L \leq 2$  of the PEM/UARS model

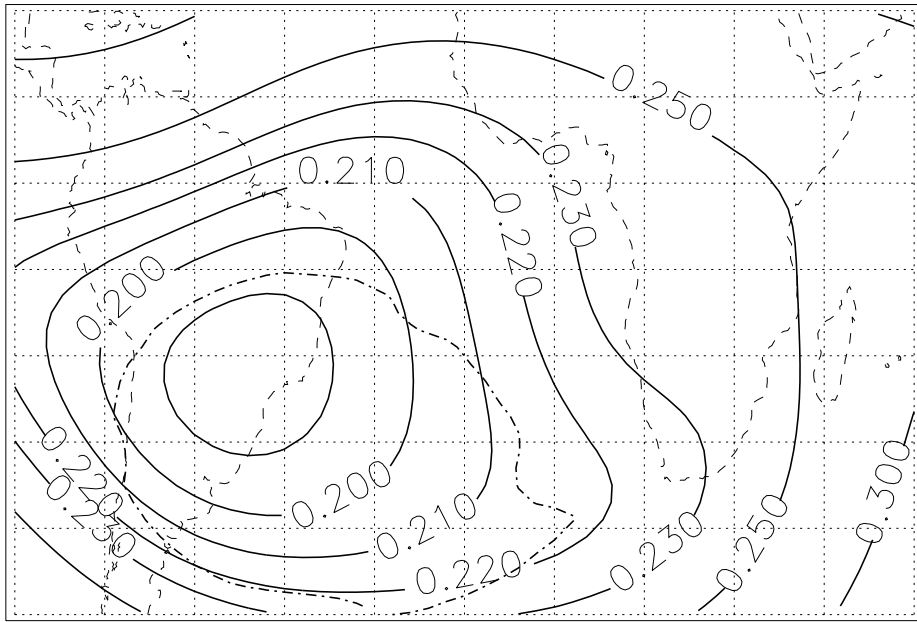


**Figure 6.6.** Iso-contours of the magnetic field intensity at 585 km. The dash-dotted line corresponds to an iso-contour where the AP-8 MIN omnidirectional integral proton flux above 10 MeV is equal to  $500 \text{ s}^{-1} \text{ cm}^{-2}$  at 585 km. The figure demonstrates the limitation  $B_m \geq 0.19$  Gauss of the PEM/UARS model

model predicts at 585 km a proton omnidirectional integral flux of  $500 \text{ s}^{-1} \text{ cm}^{-2}$  for energies above 10 MeV. From Fig. 6.5, it can be seen that the range of  $L$  for the PEM/UARS model will not exceed  $L = 2$ .

Since the observed protons have their mirror points located at the same altitude or below the point of measurement, the magnetic field intensities displayed in Fig. 6.6 correspond to the smallest mirror-point magnetic field intensities  $B_m$  for protons detected at 585 km altitude. The values of  $B_m$  in the PEM/UARS model will never be lower than 0.19 Gauss. Since the equatorial pitch angle  $\alpha_0$  is related to  $B_m$  and  $L$  by the relation

$$\sin \alpha_0 = \sqrt{\frac{0.311653}{B_m L^3}}, \quad (6.6)$$

in the PEM/UARS model, the maximum value of  $\alpha_0$  will not reach  $90^\circ$  for  $L \geq 1.18$ . Note that the data coverage in Fig. 6.3 is compatible with this statement.

Since the UARS spacecraft is three-axis stabilized, the orientations of the four HEPS detectors are only function of the spacecraft latitude  $\ell$ . The field of view of the detectors are oriented at various angles from the spacecraft zenith to nadir in the plane containing the spacecraft velocity vector. The azimuth angle  $\mathcal{A}$  of this vertical plane for the ascending leg of the orbit is given by

$$\sin \mathcal{A} = \frac{\cos 57^\circ}{\cos \ell}, \quad (6.7)$$

where  $\mathcal{A}$  is measured from North to East in the local horizontal plane. For the descending leg of the orbit, the azimuth angle is equal to  $180^\circ - \mathcal{A}$ . The detector angles with respect to the zenith are listed in Table 6.3. Since the spacecraft regularly experienced a  $180^\circ$  rotation around its vertical axis, each HEPS detector may have four different orientations ( $\mathcal{A}$ ,  $\mathcal{A} + 180^\circ$ ,  $180^\circ - \mathcal{A}$ , and  $360^\circ - \mathcal{A}$ ) for every geographic location reached by the spacecraft. Therefore, for every geographic location, each detector may see four different pitch angles.

In the SAA, the detector HEPS2/T2 has a local pitch angle of  $90^\circ \pm 10^\circ$  only when the azimuth angle is equal to  $\mathcal{A}$  or  $360^\circ - \mathcal{A}$ . In these cases, the McIlwain  $L$  parameter does not exceed 1.23. Since the detectors HEPS1/T2 and HEPS2/T2 are positioned symmetrically with respect to the zenith axis, the  $180^\circ$  rotation of the spacecraft switches the field of view of these two detectors. Thus, pitch angles between  $80^\circ$  and  $100^\circ$  are reached in the SAA by the detector HEPS1/T2 when the azimuth angle is equal to  $\mathcal{A} + 180^\circ$  or  $180^\circ - \mathcal{A}$  for the same values of  $L$ .

For detector HEPS1/T1, when the azimuth angle is equal to  $\mathcal{A} + 180^\circ$  (Fig. 6.7) or  $180^\circ - \mathcal{A}$  (Fig. 6.8),  $L$  goes up to 1.7 when the local pitch angle is about  $90^\circ \pm 10^\circ$  in the SAA. This is the reason why the detector HEPS1/T1 provides the larger coverage in Fig. 6.3

Since detector HEPS2/T1 is perpendicular to the vertical axis, the  $180^\circ$  rotation of the spacecraft only reverses the look direction of the detector. Detector HEPS2/T1 crosses the SAA with a pitch angle about  $90^\circ \pm 10^\circ$  only for  $L > 2.0$ . The measurement data of this detector will thus be less useful for the PEM/UARS proton model than the data of the other detectors.

In summary, only half of the HEPS1/T1 measurements can be used to derive our new proton flux model from the PEM instrument.

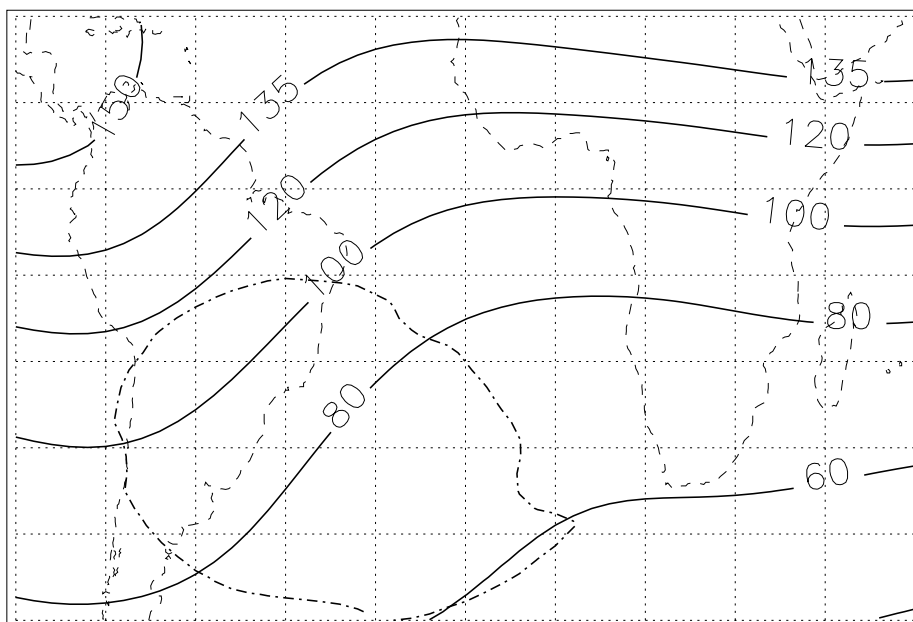


**Figure 6.7.** Local pitch angle of the HEPS1/T1 telescope with azimuth angle  $\mathcal{A} + 180^\circ$  (ascending leg). The central part of the SAA is covered by the  $\alpha$  range  $90^\circ \pm 10^\circ$ .

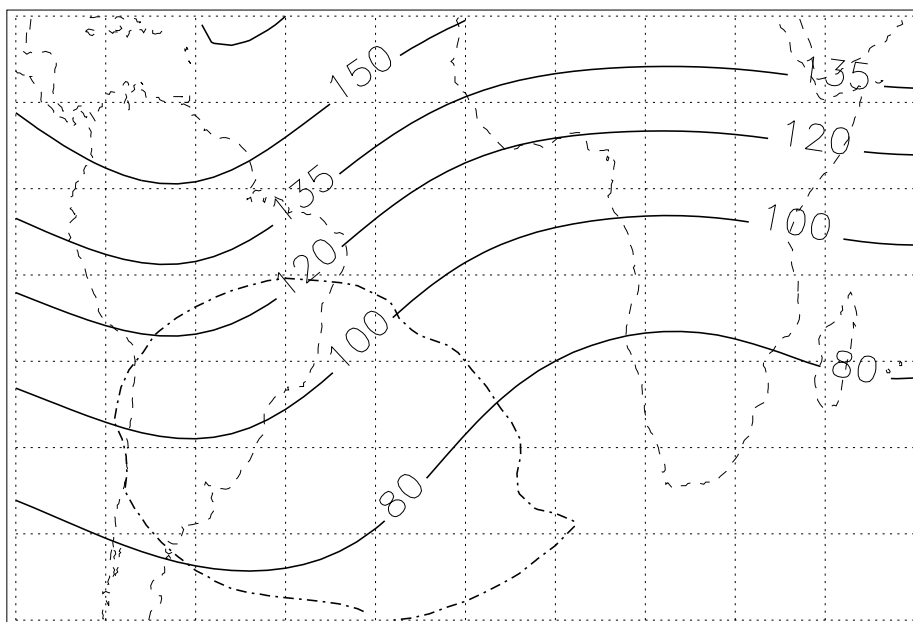


**Figure 6.8.** Local pitch angle of the HEPS1/T1 telescope with azimuth angle  $180^\circ - \mathcal{A}$  (descending leg). A large part of the SAA is covered by the  $\alpha$  range  $90^\circ \pm 10^\circ$ .



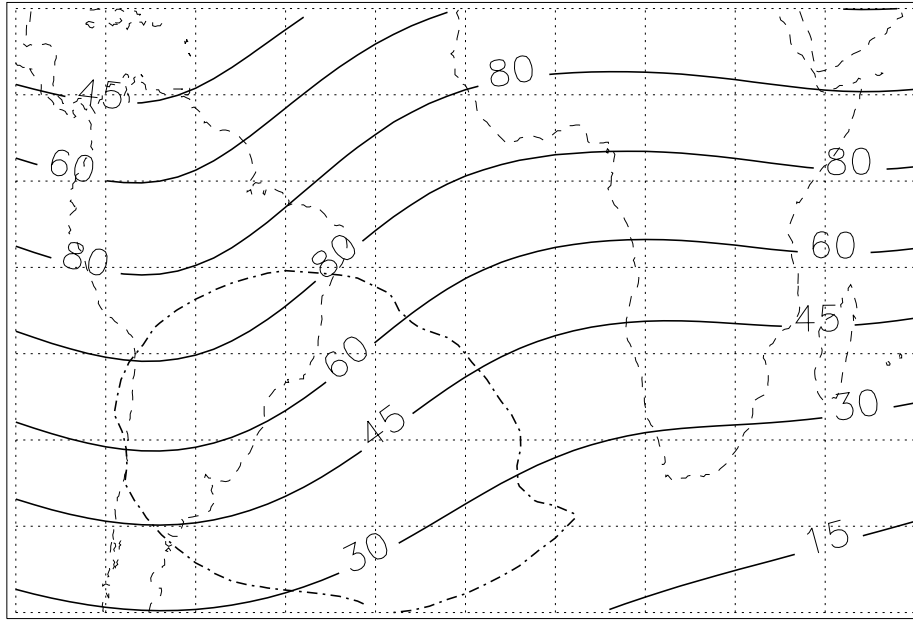


**Figure 6.9.** Iso-contours of the equatorial pitch angle when  $\alpha = 90^\circ$  at 585 km. Equatorially mirroring particles are observable only in the northern part of the SAA.

In Fig. 6.9, the equatorial pitch angle corresponding to a local pitch angle of  $90^\circ$  is shown as a function of the geographic location. The equatorial pitch angle is deduced from Figs. 6.5 and 6.6 with the help of Eq. (6.7). Values of  $\alpha_0$  greater than  $80^\circ$  are reached only when  $L < 1.2$ . Note that a better coverage cannot be obtained even when other local pitch angles are taken into account. The coverage displayed in Fig. 6.3 is mainly a function of the spacecraft attitude. When local pitch angles less than  $80^\circ$  are taken into account, smaller equatorial pitch angles can be reached but they correspond to directions inside the loss cone.

### 6.3.2 Detector field of view

In this section, we illustrate the effect of a finite field of view on the proton flux measurements in the case of the HEPS detectors.

The flux measurements for the time period from 7 Oct to 31 Dec for  $1.295 < L < 1.305$  are displayed on Fig. 6.10 as a function of the equatorial pitch angle for each HEPS detector. In each panel, the proton fluxes have a strange distribution. Moreover, since the coordinates  $L$  and  $\alpha_0$  are related to the adiabatic invariants, the proton flux should have the same distribution for all the detectors. The HEPS1/T1 data at  $\alpha_0 > 38^\circ$  are as expected, whilst fluxes measured for  $\alpha_0 < 38^\circ$  seem to be spurious at first glance. Note that the detectors HEPS1/T2 and HEPS2/T2 provide very similar results. The result of detector HEPS2/T1 is the strangest one. The measurements displayed in Fig. 6.10 indicate clearly that at least one assumption we have made is not satisfied. At this point, different checks have been made:

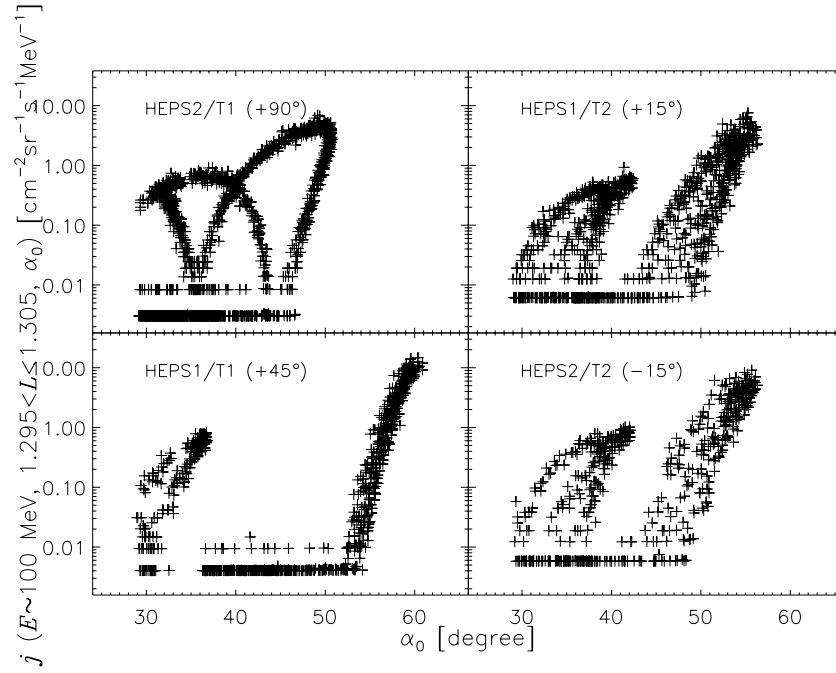


**Figure 6.10.** Raw  $E \approx 100$  MeV proton flux at  $1.295 < L < 1.305$  measured by the HEPS1/T2, HEPS1/T1, HEPS2/T2 and HEPS2/T1 telescopes as a function of the equatorial pitch angle for October to December 1991

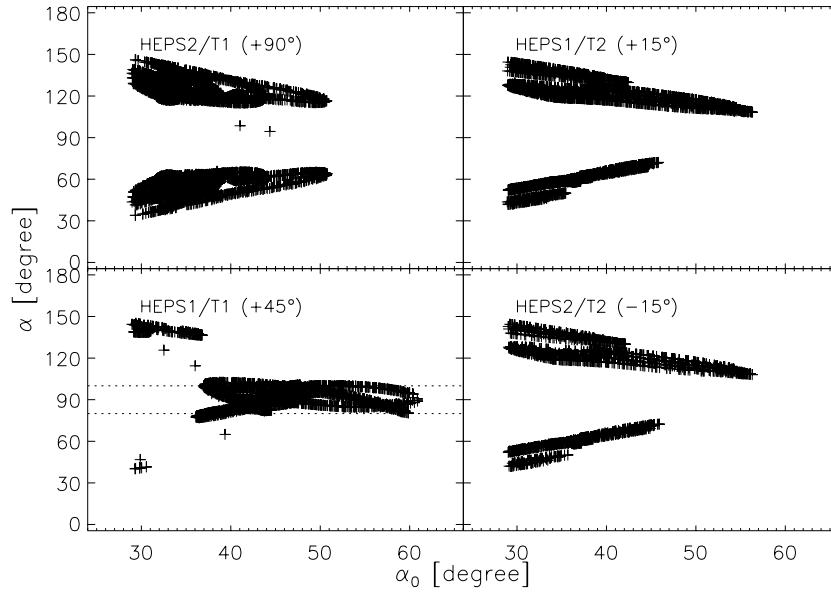


**Figure 6.11.** Distribution of the local pitch angle of the HEPS1/T2, HEPS1/T1, HEPS2/T2 and HEPS2/T1 telescopes as a function of  $\alpha_0$  at  $1.295 < L < 1.305$  for October to December 1991

- each step of the data processing has been checked carefully;
- the validity of the UARS ephemeris stored in the IDFS database has been verified by the comparison between the measured and IGRF magnetic fields;
- the HEPS measurements appeared to be valid according to the quality factors;
- the proton fluxes vanish when the spacecraft is outside the SAA;
- inside the SAA, the time evolution of the proton fluxes is very much like what is expected;
- ...

The only aspect not taken into account for the data in Fig. 6.10 is the opening angle correction, i.e. the geometric factor correction. The raw data of Fig. 6.10 does not include this correction since the correction needs an iterative process and is generally assumed to be sufficiently small to be ignored in a first analysis.

The geometric factor correction is generally supposed to be small for detectors like HEPS where the field of view is equal to  $30^\circ$ . No field of view correction is needed when the particle flux is isotropic but can be very important when the proton flux becomes highly anisotropic. In Fig. 6.11, the local pitch angles of HEPS detectors are displayed for the same conditions as Fig. 6.10. The distribution in  $\alpha$  is different for each detector except for HEPS1/T2 and HEPS2/T2 for which the distributions are similar. The coverage in local pitch angle has been already explained in Sect. 6.3.1. When Figs. 6.10 and 6.11 are compared, a correlation seems to appear between the proton flux behaviour and the local pitch angle distribution. For the detector HEPS1/T1, there are mainly two sets of local/equatorial pitch angles. The separation is near  $\alpha_0 = 38^\circ$  which is also a separation in the HEPS1/T1 proton flux behaviour. At  $\alpha_0 > 38^\circ$ ,  $\alpha \approx 90^\circ$  and the proton flux behaviour is the mostly credible. For the detectors HEPS1/T2 and HEPS2/T2, the two sets of local/equatorial pitch angles overlap for  $\alpha_0 < 47^\circ$ . This angle also seems to be a separation in the proton flux behaviour of these detectors. Finally, for detector HEPS2/T1 which has the strangest proton flux behaviour, the two sets of local/equatorial pitch angles overlap on the whole range of  $\alpha_0$ . So, for all cases, the proton flux has a stranger distribution when the local pitch angle deviates from  $90^\circ$ . Neglecting of the view-angle correction may explain this fact. When the local pitch angle is different from  $90^\circ$ , the detector is looking inside the loss cone where the proton flux is very low. But, due to the finite size of the FOV, locally mirroring protons (for which the flux is much higher) can be seen by the edge of the detector FOV. In that case, the observed flux cannot be associated simply to the look direction of the detector axis.

To test the effect of the view-angle correction on the UARS data, we have simulated the response of the detector HEPS2/T1. The proton flux measurements  $j^*$  are related to the true local flux  $j$  by

$$Gj^* = \int_0^\pi d\theta \int_0^{2\pi} d\phi j(\alpha') h(\theta) \cos \theta \sin \theta \quad (6.8)$$

where  $\alpha'$  corresponds to the local pitch angle of the direction  $(\theta, \phi)$  and is obtained from Eq. (A.20),  $h(\theta)$  is the angular response of the detector and the geometric factor  $G$  is given

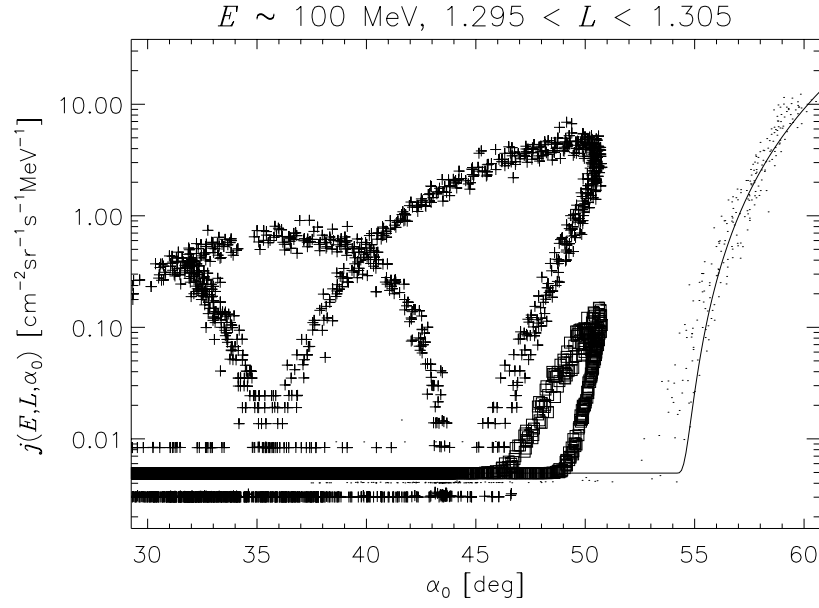


**Figure 6.12.** Simulation of the detector HEPS2/T1 in the same conditions as Fig. 6.10 when its angular response corresponds to a FOV of  $30^\circ$ . The dots correspond to the raw measurements of detector HEPS1/T1 for which  $80^\circ \leq \alpha \leq 100^\circ$  whose have been used to fit the true flux  $j$  represented by the solid line. The plus signs correspond to the raw measurements of detector HEPS2/T1 while the square signs are the result of the simulation based on the flux  $j$  and the angular response  $h_1$ .

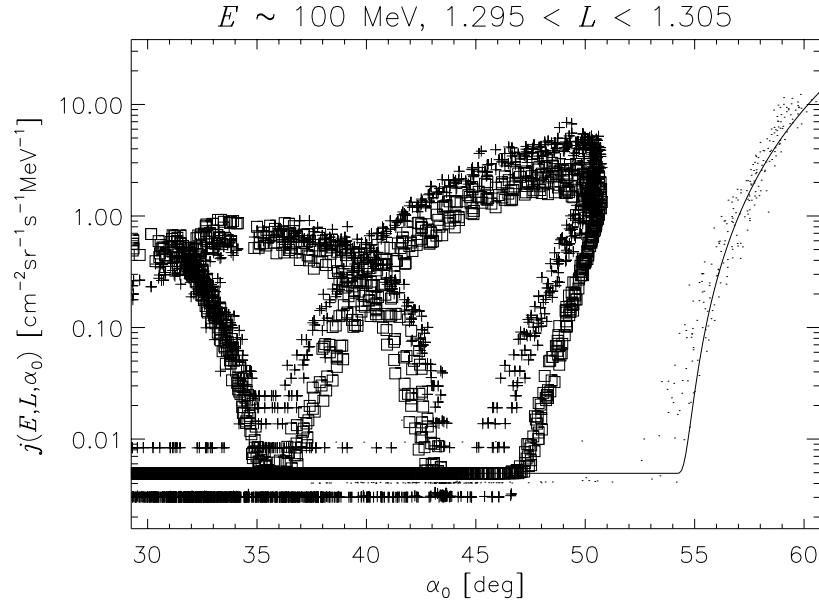


**Figure 6.13.** Simulation of the detector HEPS2/T1 in the same conditions as Fig. 6.10 when the FOV is extended to  $130^\circ$ . The dots, the solid line and the plus signs are the same as Fig. 6.12. But the square signs are the result of the simulation based on the flux  $j$  and the angular response  $h_2$ .

by

$$G = 2\pi \int_0^\pi d\theta h(\theta) \cos \theta \sin \theta. \quad (6.9)$$

The simulation of  $j^*$  for the detector HEPS2/T1 at  $1.295 < L < 1.305$  has been computed for two different response functions  $h(\theta)$ :

1.  $h_1(\theta)$  is equal to 1 when  $\theta < 15^\circ$  and to 0 otherwise;
2.  $h_2(\theta)$  is equal to 1 when  $\theta < 15^\circ$ , decreases linearly from 1 to 0 when  $15^\circ < \theta < 65^\circ$ , and is equal to 0 otherwise.

The first function corresponds to a detector with a FOV of  $30^\circ$  while the second function corresponds to a detector with a larger FOV but where the angular response is weaker on the edge of the FOV, e.g. due to a passive shielding. For the simulation, the true local flux  $j$  is evaluated from a fit to the data of detector HEPS1/T1 for which  $80^\circ \leq \alpha \leq 100^\circ$  (data located between the dotted lines in Fig. 6.11). The results of both simulation are presented in Figs. 6.12 and 6.13.

In Figs. 6.12 and 6.13 the 100 MeV proton measurements of detector HEPS2/T1 are compared to two different simulations as a function of the equatorial pitch angle at  $L = 3$ . In both figures, the dots correspond to the HEPS1/T1 data from which the true flux  $j$  represented by a solid line has been fitted. The plus and square signs correspond to the HEPS2/T1 measurements and simulated measurements, respectively. The simulation of Fig. 6.12 does not reproduce all the detector measurements very well. According to the simulation, when the equatorial pitch angle associated to the detector axis is less than  $45^\circ$  at  $L = 3$ , a telescope with a FOV of  $30^\circ$  should not detect 100 MeV trapped protons. On the contrary, the simulation of Fig. 6.13 with a wider FOV fits better the measurements. Note that when the FOV extends to a value smaller than  $130^\circ$ , the measurements around  $\alpha_0 = 30^\circ$  are not well fitted. The simulations of Figs. 6.12 and 6.13 demonstrate that the effective field of view of the HEPS detectors is probably about  $130^\circ$ . To provide an even better simulation, one would have to know the real angular response of the detector.

The differences between  $j$  (the solid curve in Figs. 6.12 and 6.13) and  $j^*$  (square signs) clearly show that it is difficult to deduce  $j$  from  $j^*$  when the orientation of the detector deviates from an angle of  $90^\circ$  with respect to the local magnetic field direction. This problem is illustrated in Fig. 6.14 where the solid-dashed curve represents the true flux  $j$ , i.e. the flux that should be seen by an ideal detector with an infinitely small FOV. The solid part of the curve corresponds to the fit used in Figs. 6.12 and 6.13 while the dashed part is an extrapolation to  $90^\circ$ . The angular response of the detector is set to  $h_2$ , the same function as in Fig. 6.13. The thin solid lines of Fig. 6.14 are the results of simulations when the orientation of the detector is set to  $\alpha = 45^\circ, 60^\circ, 75^\circ$  and  $90^\circ$ , respectively. One should note that Fig. 6.14 does not depend on  $L$  nor on  $E$  (for different values of  $L$  or  $E$ , the function  $j$  is of course different, of course). When  $\alpha = 90^\circ$ , the proton flux is underestimated. The ratio  $j/j^*$  is equal to 4.7 at its maximum near  $\alpha_0 = 55^\circ$ ; it decreases to 2.6 at  $\alpha_0 = 73\frac{1}{2}^\circ$ , and is equal to 3.9 at  $\alpha_0 = 90^\circ$ . When  $\alpha = 75^\circ, 60^\circ$  or  $45^\circ$ , the proton flux is overestimated and the data does not cover the whole range of  $\alpha_0$ .

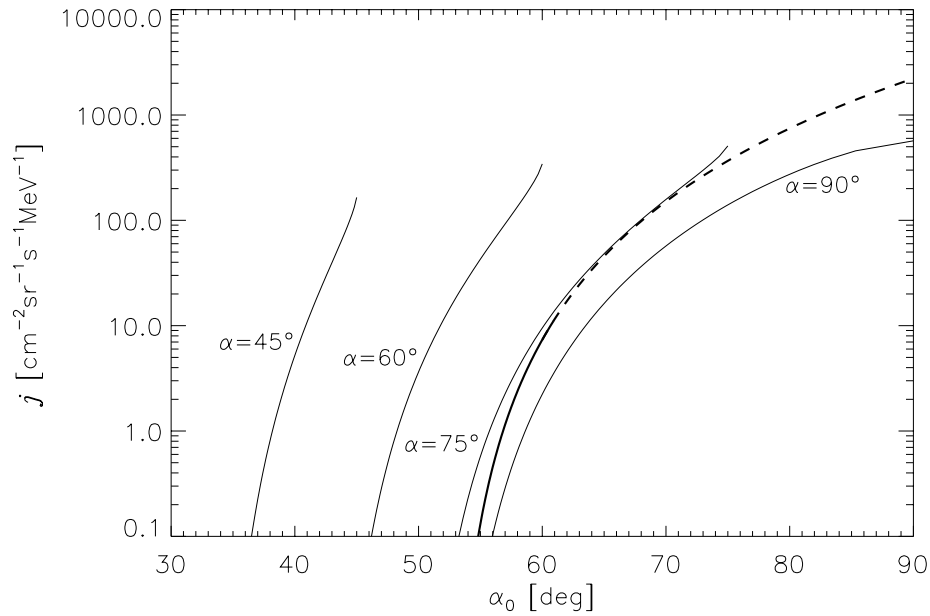


**Figure 6.14.** Simulation of detector measurements as a function of  $\alpha_0$  at different local pitch angles. The solid-dashed line corresponds to the true flux  $j$ . The thin solid lines are the results of simulations.

For  $\alpha = 75^\circ$ , the ratio  $j/j^*$  is minimum at  $\alpha_0 = 53^\circ$ ; it increases to 1 at  $\alpha_0 = 68^\circ$ , and is equal to 0.7 at  $\alpha_0 = 75^\circ$ .

The ratio  $j/j^*$  can be used to correct the measurements a posteriori when the measurements and the simulations cover the same equatorial pitch angle range. This type of correction was applied to the AZUR data (see Sect. 4.3) for which  $\alpha \approx 90^\circ$ . In the case of the UARS data, it appears clearly from Fig. 6.14 that a correction is not possible for local pitch angles less than  $75^\circ$ . Note that since we do not know exactly the angular response of the HEPS detector, such a correction can only be applied approximatively.

One should note also that the flux  $j$  used to produce the simulation of Fig. 6.13 is deduced from raw measurements, i.e. uncorrected data, and can be wrong by a factor of 5. Therefore, the good agreement between the measurement and the simulation does not mean that  $h_2(\theta)$  corresponds exactly to the angular response of the HEPS detectors. Indeed, other angular response function may give similar agreement, if not better.

### 6.3.3 Corrected flux

The flux correction has only been applied to the measurements of the HEPS1/T1 telescope since it is the telescope that covers the largest part of the  $(\alpha_0, L)$  space and that has its local pitch angle near  $90^\circ$  when the spacecraft passes through the SAA. To apply the correction, the proton fluxes have been fitted for each  $L$  value to a 3-parameter function given by Eq. 6.4. Since the correct effective area has not yet been communicated by Lockheed Palo Alto Research Laboratory, a

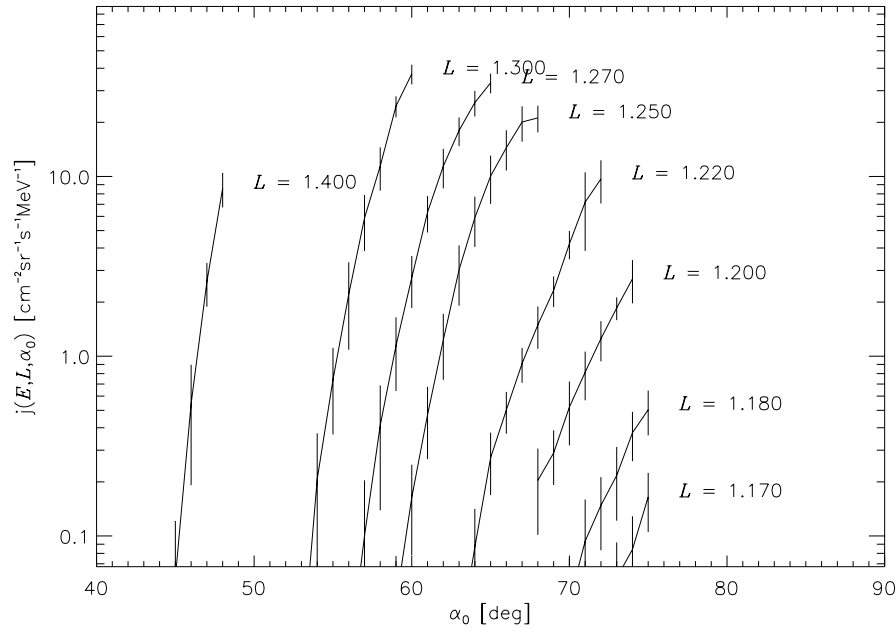


**Figure 6.15.** UARS/HEPS Differential flux as a function of the equatorial pitch angle for 17.2–24.4 MeV protons for different  $L$  values. The error bars correspond to one standard deviation ( $\hat{\sigma}$ ).

simple guess function has been used for the correction. This function is defined by

$$h(\alpha) = \begin{cases} \cos \alpha & \text{when } \alpha < 16^\circ \\ 0 & \text{when } \alpha > 16^\circ \end{cases} \quad (6.10)$$

### 6.3.4 Proton flux model

The trapped proton flux model PUB97<sup>1</sup> obtained from the UARS/HEPS data is illustrated on Figures 6.15–6.22. The PUB97 model is based on the HEPS1/T1 measurements from 12 September 1991 till 1 September 1992 for which the angle between the sensor axis and the local magnetic field vector was near  $90^\circ$ . The PUB97 model is organized in terms of energy, McIlwain's shell parameter and equatorial pitch angle. It includes 15 energy channels from 6 to 168 MeV, 41  $\alpha_0$  bins and 36  $L$  bins. The effective coverage of the model is limited to the space below 600 km where  $40^\circ < \alpha_0 < 75^\circ$  and  $1.12 < L < 1.52$ . The coverage is restricted therefore to the innermost edge of the proton radiation belt. This restriction is due to the fact that the PEM instrument was designed to catch the precipitating flux. Note that PEM data exist at times beyond September 1992.

The dependence of the proton differential flux on the equatorial pitch angle for three energy channels and different  $L$  values is shown on Figs. 6.15 and 6.17. The vertical bars represent the flux value plus/minus one standard deviation [as defined in Eq. (6.3)]. In both figures, the

<sup>1</sup>PUB is the acronym of Proton UARS BIRA

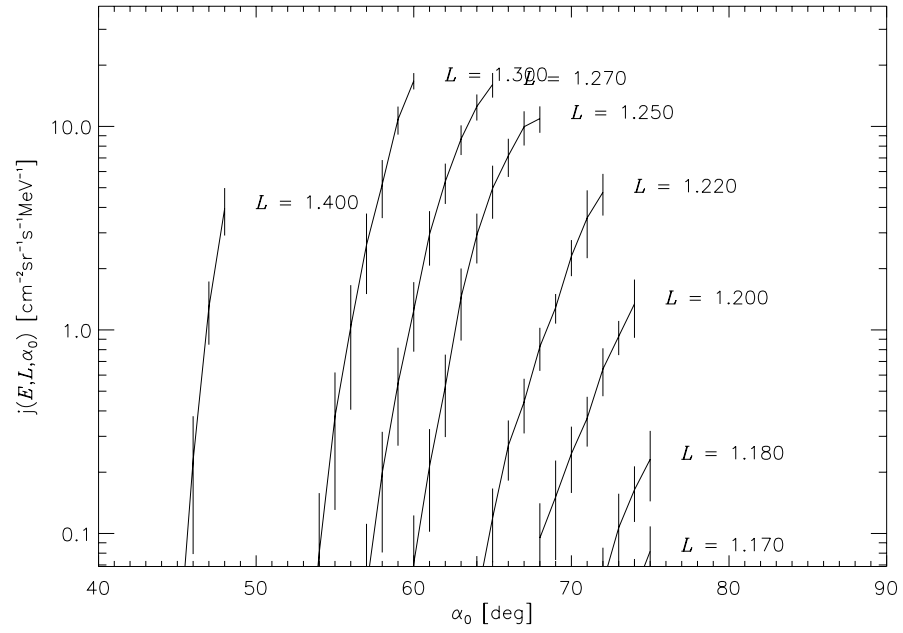


**Figure 6.16.** UARS/HEPS Differential flux as a function of the equatorial pitch angle for 31.7–42.1 MeV protons for different  $L$  values. The error bars correspond to one standard deviation ( $\hat{\sigma}$ ).

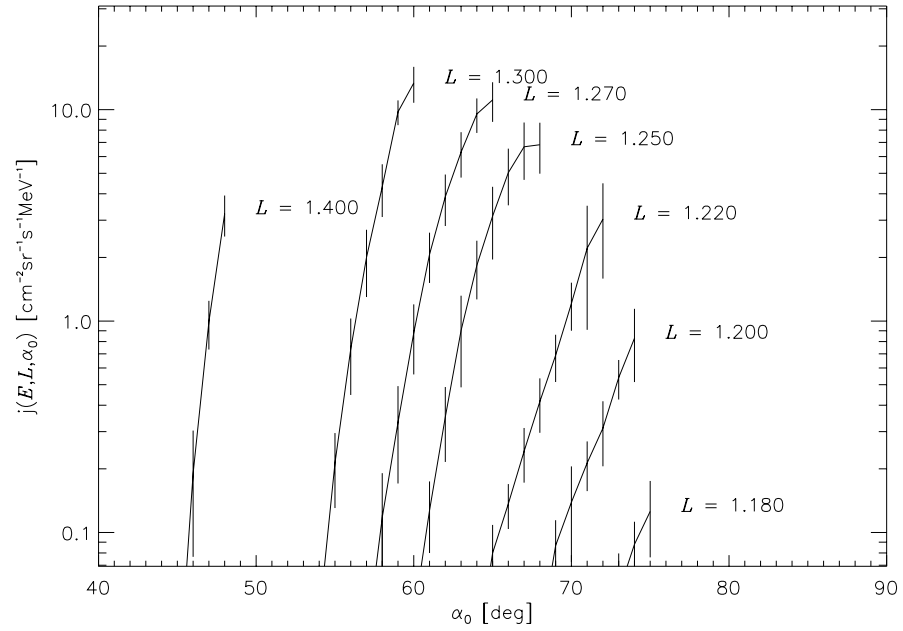


**Figure 6.17.** UARS/HEPS Differential flux as a function of the equatorial pitch angle for 94.0–122.5 MeV protons for different  $L$  values. The error bars correspond to one standard deviation ( $\hat{\sigma}$ ).



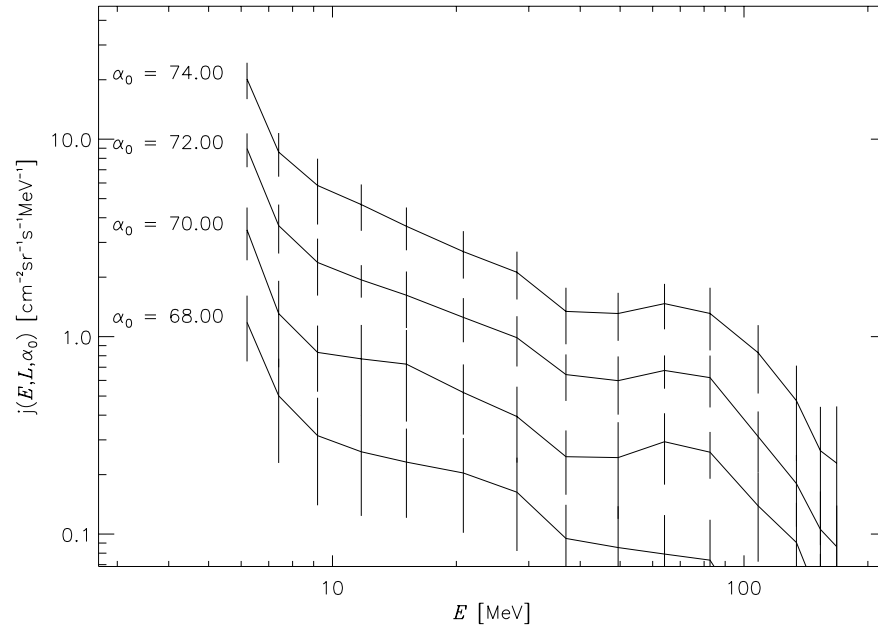


**Figure 6.18.** UARS/HEPS Differential proton flux spectra at  $L = 1.2$  for different values of the equatorial pitch angle. The error bars correspond to one standard deviation ( $\hat{\sigma}$ ).

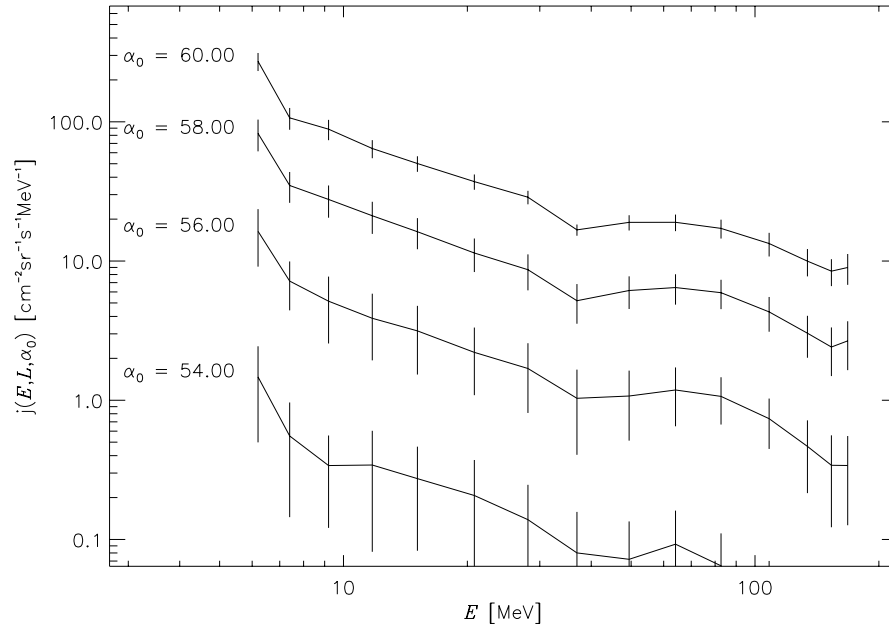


**Figure 6.19.** UARS/HEPS Differential proton flux spectra at  $L = 1.3$  for different values of the equatorial pitch angle. The error bars correspond to one standard deviation ( $\hat{\sigma}$ ).

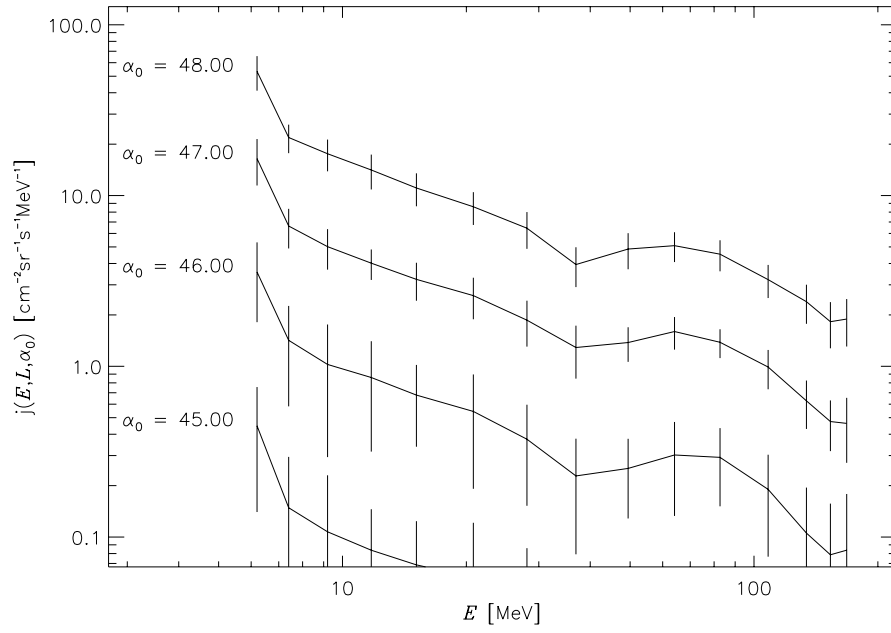


**Figure 6.20.** UARS/HEPS Differential proton flux spectra at  $L = 1.4$  for different values of the equatorial pitch angle. The error bars correspond to one standard deviation ( $\hat{\sigma}$ ).

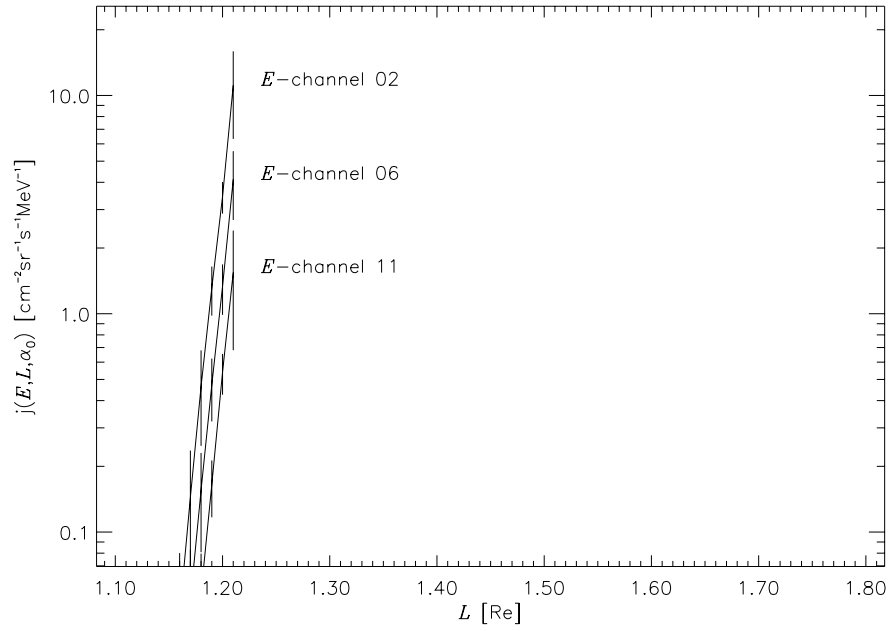


**Figure 6.21.** UARS/HEPS Differential proton flux as a function of  $L$  at  $\alpha_0 = 73^\circ$  for different energy channels. The channels correspond to the energy ranges 8.0–10.5, 24.5–31.8 and 94.0–122.5 MeV, respectively. The error bars correspond to one standard deviation ( $\hat{\sigma}$ ).

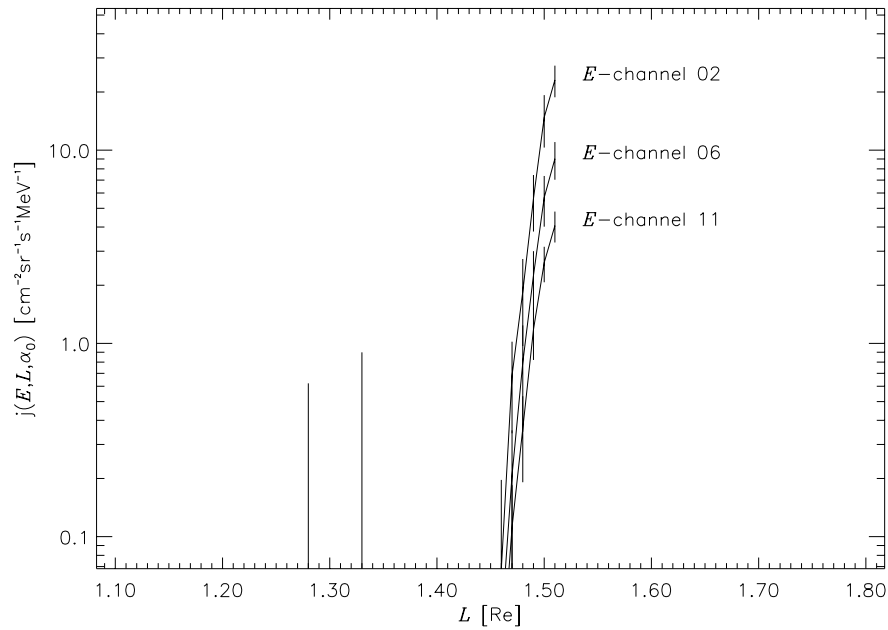


**Figure 6.22.** UARS/HEPS Differential proton flux as a function of  $L$  at  $\alpha_0 = 41^\circ$  for different energy channels. The channels correspond to the energy ranges 8.0–10.5, 24.5–31.8 and 94.0–122.5 MeV, respectively. The error bars correspond to one standard deviation ( $\hat{\sigma}$ ).

PUB97 model never reaches equatorial pitch angle near  $90^\circ$ : only the region in the vicinity of the atmospheric loss cone is properly covered in the model. Both figures show that the flux varies about one order of magnitude on the range of few degrees in equatorial pitch angle. It indicates also a slight dependence in energy of the cut-off location.

The proton energy spectra are displayed for different values of the equatorial pitch angle in Figs. 6.18 to 6.20 for  $L = 1.2, 1.3$  and  $1.4$ , respectively. It can be seen that the different spectra have very similar slopes. Most of the spectra display a hump near 60 MeV, which is not present in AP-8 MAX energy spectra. Note that, due to the coverage of the model, spectra related to different equatorial pitch angles have been displayed for a set of  $L$  value. For  $L = 1.2, 1.3$  and  $1.4$ , the coverage of the PUB97 model is limited to equatorial pitch angles about 74, 60 and 48 degrees, respectively.

The dependence of the differential proton flux on the shell parameter is shown in Figs. 6.21 and 6.22 at  $\alpha_0 = 73^\circ$  and  $41^\circ$ , respectively, for three different energy channels: 8.0–10.5 MeV, 24.5–31.8 MeV and 94.0–122.5 MeV. On each figure, the curves are closed to one another due to the slight dependence in energy of the cut-off location. Both figures show clearly that the coverage of the PUB97 model is restricted to the innermost edge of the proton radiation belt.

To be included in the UNIRAD programme TREP, the differential fluxes of the PUB97 model have been transformed into integral fluxes. The transformation has been applied with the assumption that the proton flux above 175 MeV can be neglected. The integral perpendicular proton fluxes for some of the 15 energy channels are shown on Figs. 6.23 to 6.29. On each fig-

ure, the fluxes of the PUB97 model are compared to the fluxes obtained with the NASA model AP-8 MAX. In order to facilitate the comparison, flux iso-contours and Vette's cutoff have been drawn on each panel. The Vette (1991a) cutoff  $B_c$  does not depend on the energy and is defined by

$$\frac{B_c}{B_0} = 0.65 L^{3.452}. \quad (6.11)$$

Since the PUB97 model and the NASA model do not correspond to the same epoch,  $(\alpha_0, L)$  maps of both models are not directly comparable (Kruglanski 1996). Note also that the PUB97 model has not been extrapolated to higher equatorial pitch angles than available from the data set nor to  $L$  values beyond the region sampled.

On both figures, the cutoff of the PUB97 model appears at higher equatorial pitch angle, i.e. lower  $B$ , than AP-8 MAX for all energies. On the other hand, the PUB97 integral fluxes have a higher gradient than the AP-8 MAX fluxes. The origin of the weak fluxes present inside the loss cone of the PUB97 model has not been clearly identified. These weak fluxes are more prominent at the lower energies.

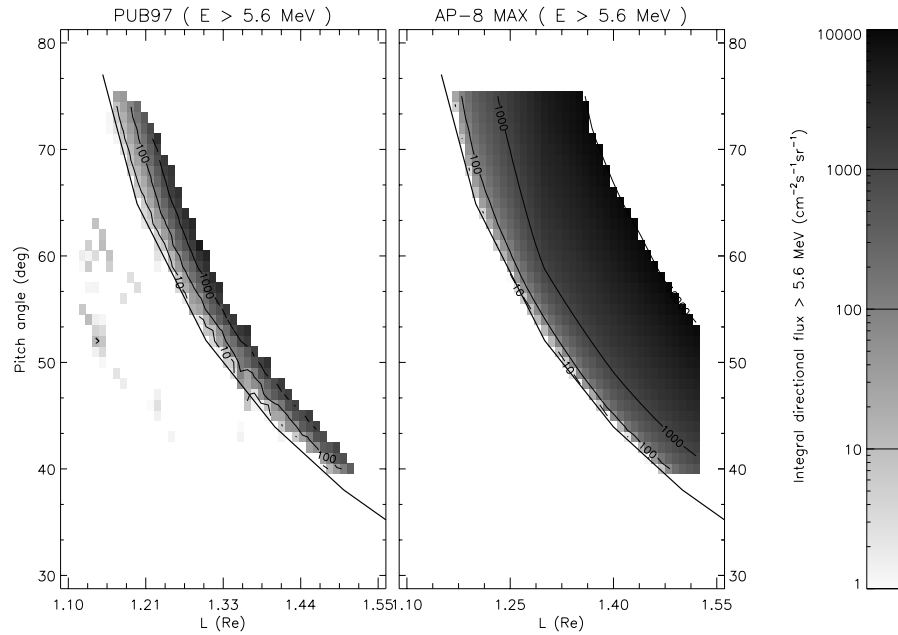


**Figure 6.23.** The integral perpendicular proton flux map of the PUB97 model compared to the NASA model AP-8 MAX at  $E > 5.6$  MeV. The solid curves correspond to Vette's cutoff.

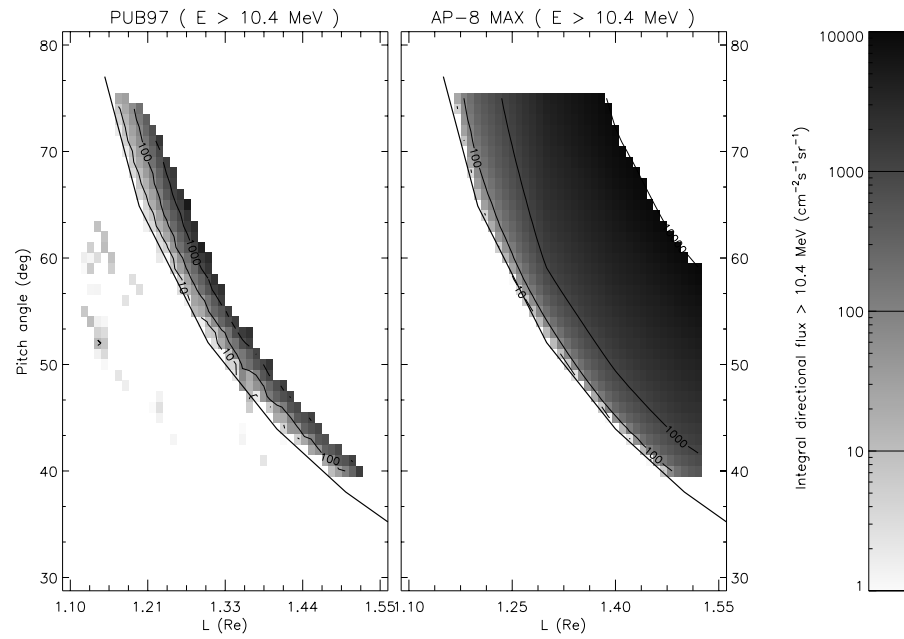


**Figure 6.24.** The integral perpendicular proton flux map of the PUB97 model compared to the NASA model AP-8 MAX at  $E > 10.4$  MeV. The solid curves correspond to Vette's cutoff.

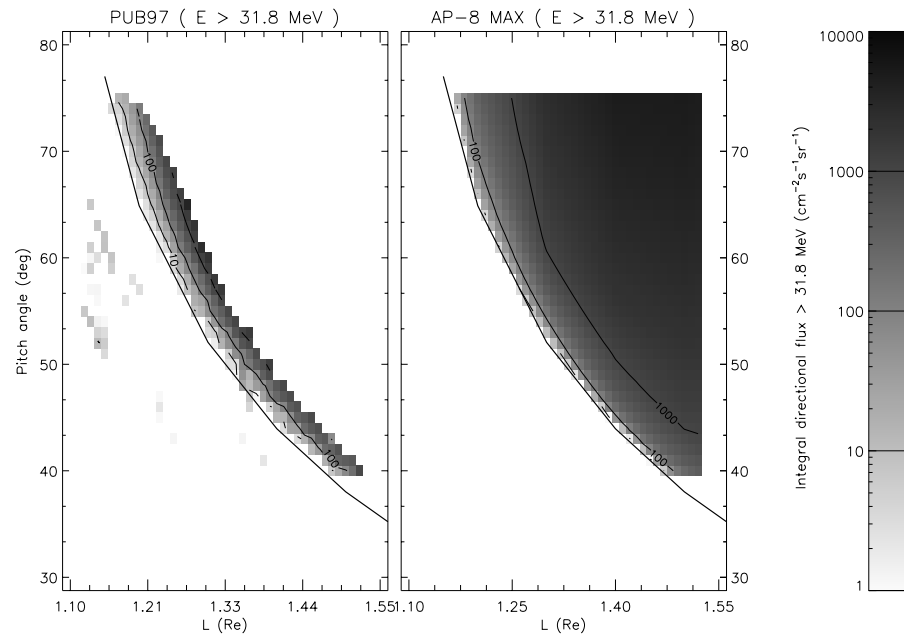


**Figure 6.25.** The integral perpendicular proton flux map of the PUB97 model compared to the NASA model AP-8 MAX at  $E > 31.8$  MeV. The solid curves correspond to Vette's cutoff.

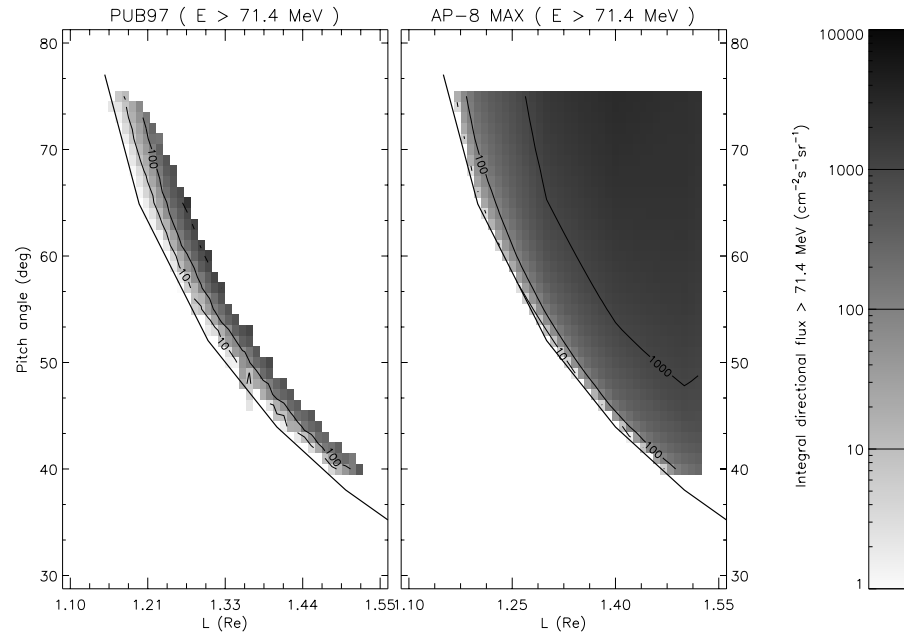


**Figure 6.26.** The integral perpendicular proton flux map of the PUB97 model compared to the NASA model AP-8 MAX at  $E > 71.4$  MeV. The solid curves correspond to Vette's cutoff.

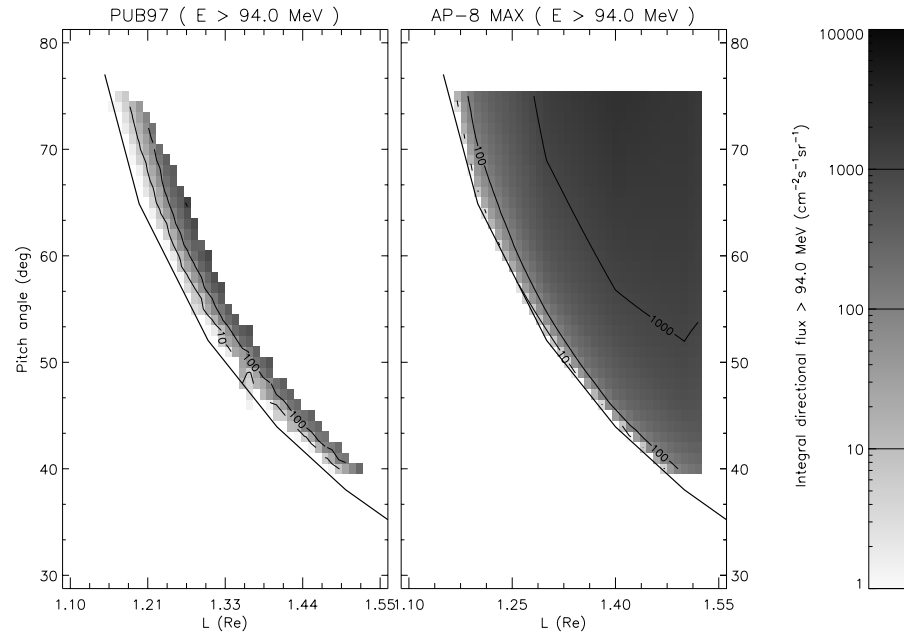


**Figure 6.27.** The integral perpendicular proton flux map of the PUB97 model compared to the NASA model AP-8 MAX at  $E > 94.0$  MeV. The solid curves correspond to Vette's cutoff.

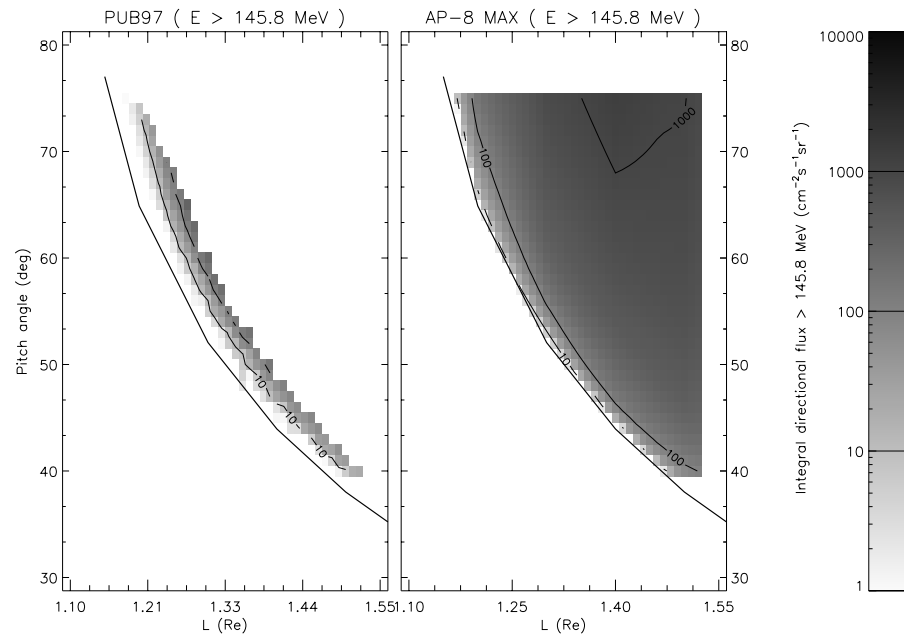


**Figure 6.28.** The integral perpendicular proton flux map of the PUB97 model compared to the NASA model AP-8 MAX at  $E > 145.8$  MeV. The solid curves correspond to Vette's cutoff.

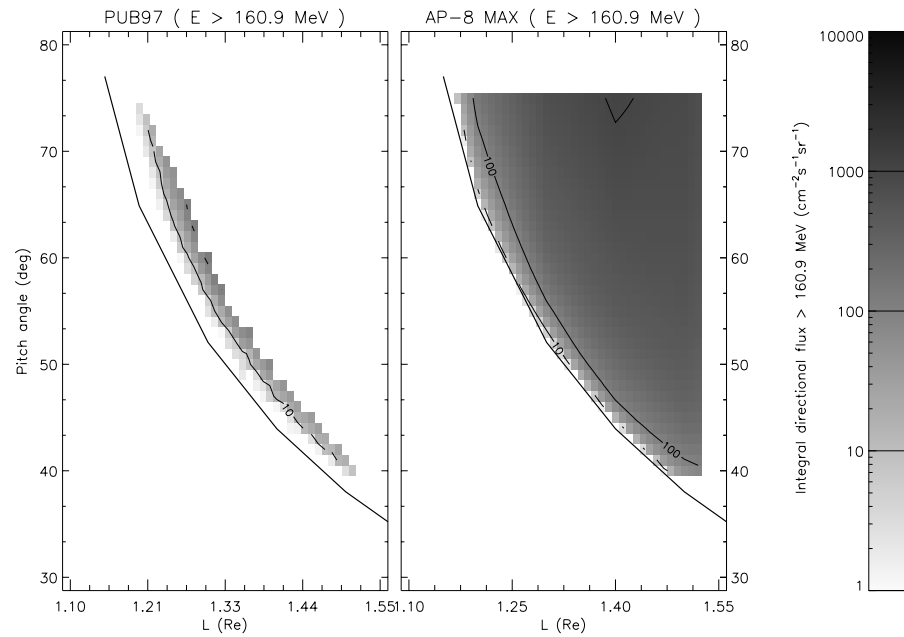


**Figure 6.29.** The integral perpendicular proton flux map of the PUB97 model compared to the NASA model AP-8 MAX at  $E > 160.9$  MeV. The solid curves correspond to Vette's cutoff.





# Chapter 7

## Intercomparisons of the proton models

In this Chapter, we intercompare the flux maps obtained from the AZUR, SAMPEX and UARS data. The AP-8 directional fluxes are added to the comparisons to put into perspective the results. The usage of the models derived from the flux maps, i.e. their implementation in TREP, is described in Technical Note 10 and in Chapter 2 of this Final Report.

As the new trapped proton models are based on data from low altitude satellites, their use is limited to predictions for low altitude missions. In Sect. 7.1, the new models, as well as the AP-8 models, are applied to a typical MIR or Space Station orbit. The model limitations are demonstrated in Sect. 7.2, where the models are applied to a GTO orbit. All model calculations were made with the UNIRAD programme suite.

### 7.1 Comparisons of the models for a LEO mission

The LEO mission selected for the model comparisons is a circular orbit at altitude 400 km and inclination  $50^\circ$ . We generated 14 orbits with SAPRE, and then ran TREP 5 times, once for each new model plus two runs with the directional versions of AP-8 MAX and AP-8 MIN. The resulting positional trapped proton unidirectional integral fluxes above 30 MeV are shown on the world maps in Figs. 7.1–7.5. On these maps, the filled squares represent non-zero fluxes. Orbital points where the flux is zero are not shown. The open squares represent orbital positions which are outside the validity range of the respective models (fluxes outside the model range are given a value  $-1.0$  by TREP). The PAB97 and PUB97 models represent solar maximum conditions (for two different solar cycles), while the PSB97 model represents solar minimum conditions.

The first feature to note when comparing the world maps is the difference in coverage of the models. The nominal range of the AP-8 models extends over the whole region covered by the LEO orbit. This was achieved in the construction of the NASA models by extrapolating the models beyond the actual coverage of the satellite data that were used. For the new models, we decided not to extend their validity range by extrapolation, as this procedure can induce very large uncertainties in the extrapolated fluxes. The model coverage is further influenced by the

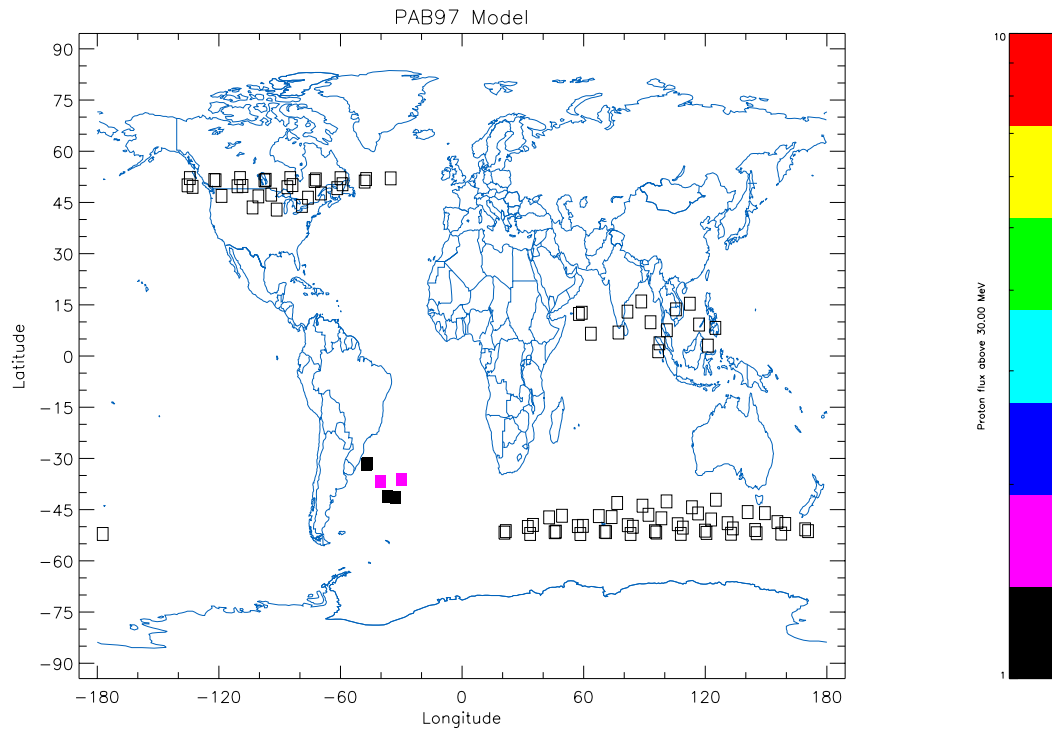


**Figure 7.1.** World map of the PAB97 directional proton flux above 30 MeV for the LEO orbit described in the text. The open squares represent orbital positions which are outside the validity range of the model.

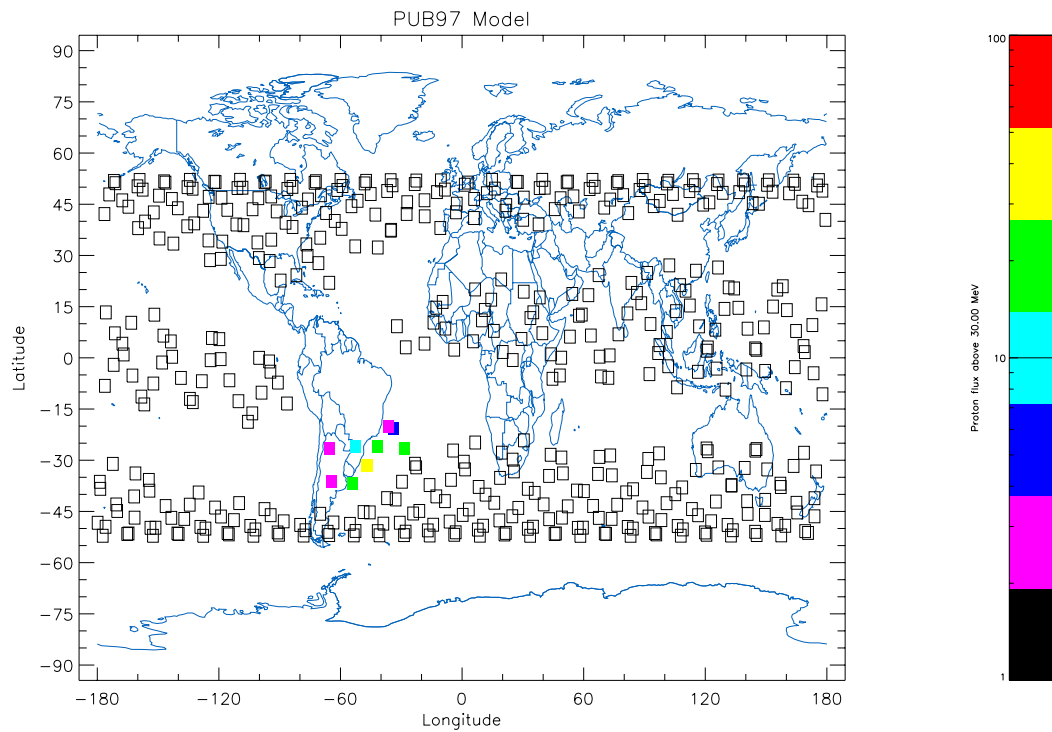


**Figure 7.2.** World map of the PUB97 directional proton flux above 30 MeV for the LEO orbit described in the text. The open squares represent orbital positions which are outside the validity range of the model.

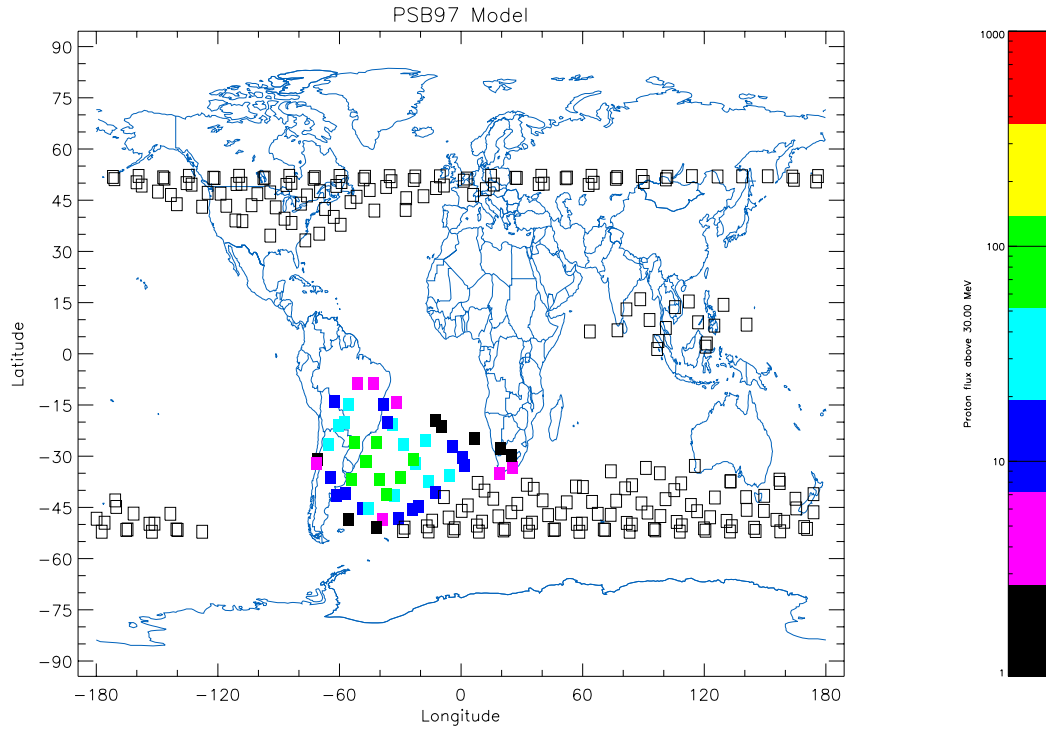


**Figure 7.3.** World map of the PSB97 directional proton flux above 30 MeV for the LEO orbit described in the text. The open squares represent orbital positions which are outside the validity range of the model.

fact that the respective models use different magnetic field models, with different epochs.

Secondly, the non-zero flux values at the orbital points where the models overlap differ significantly between the models. For the new models, this is due to the difference in solar conditions for which they were constructed. The differences between the new models and the AP-8 models have already been discussed in the sections of this document that cover the model descriptions.

Figures 7.6–7.10 show the integral proton flux above 30 MeV obtained with the different models as a function of orbital time. These plots further highlight the differences in model coverage, and provide a more quantitative comparison between the non-zero values. The differential and integral trapped proton spectra integrated over the full trajectory are shown in Figs. 7.11–7.15.

## 7.2 Comparisons of the models for a GTO mission

In order to illustrate the dangers of applying trapped particle models outside their validity range, we repeated the calculations presented in Sect. 7.1 for a GTO orbit with inclination  $18^\circ$ . Figures 7.16–7.20 represent the world maps obtained for this trajectory with the five different models.

As was the case for the LEO trajectory, the AP-8 model covers the whole GTO orbit, while

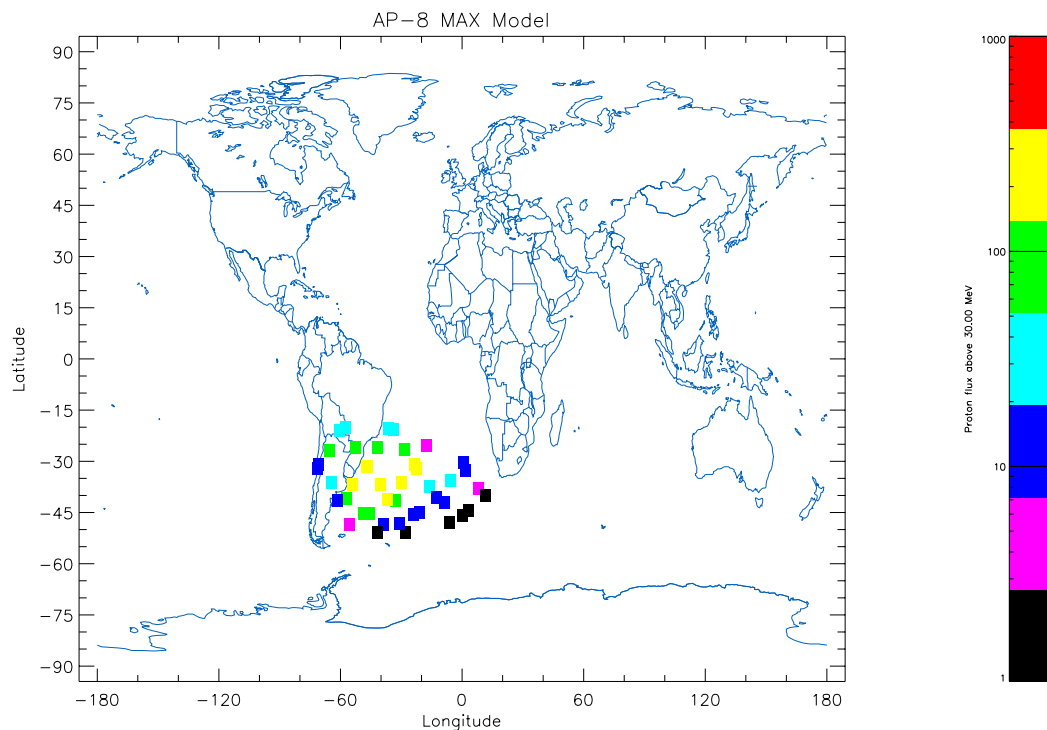


**Figure 7.4.** World map of the AP-8MAX directional proton flux above 30 MeV for the LEO orbit described in the text

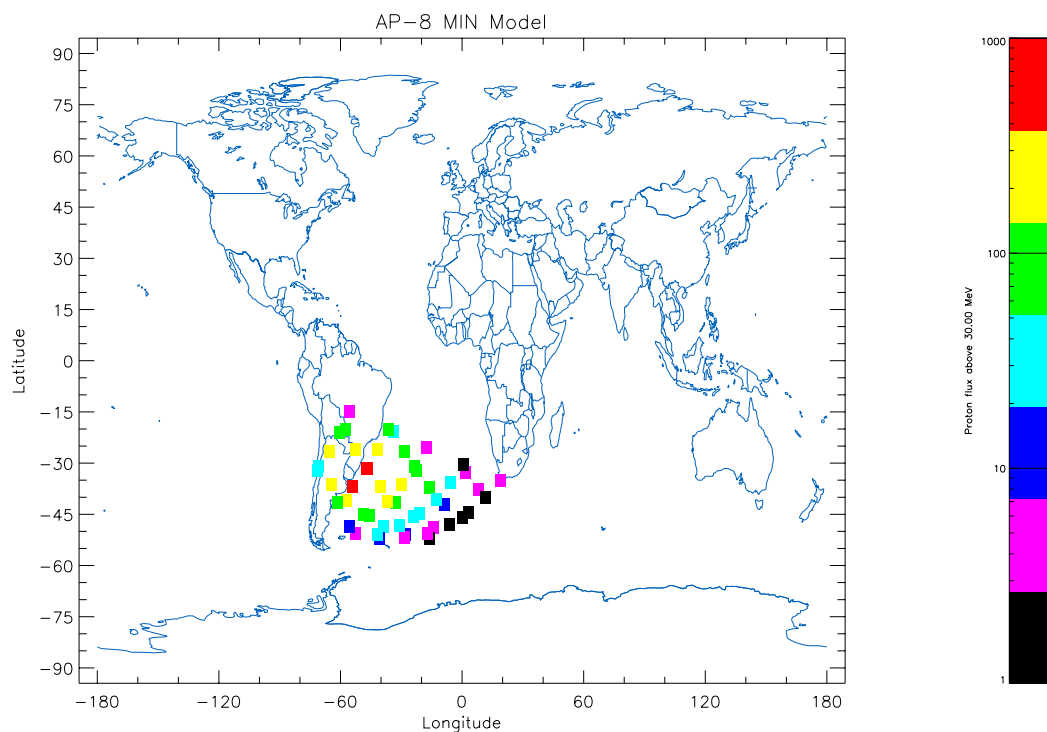


**Figure 7.5.** World map of the AP-8MIN directional proton flux above 30 MeV for the LEO orbit described in the text

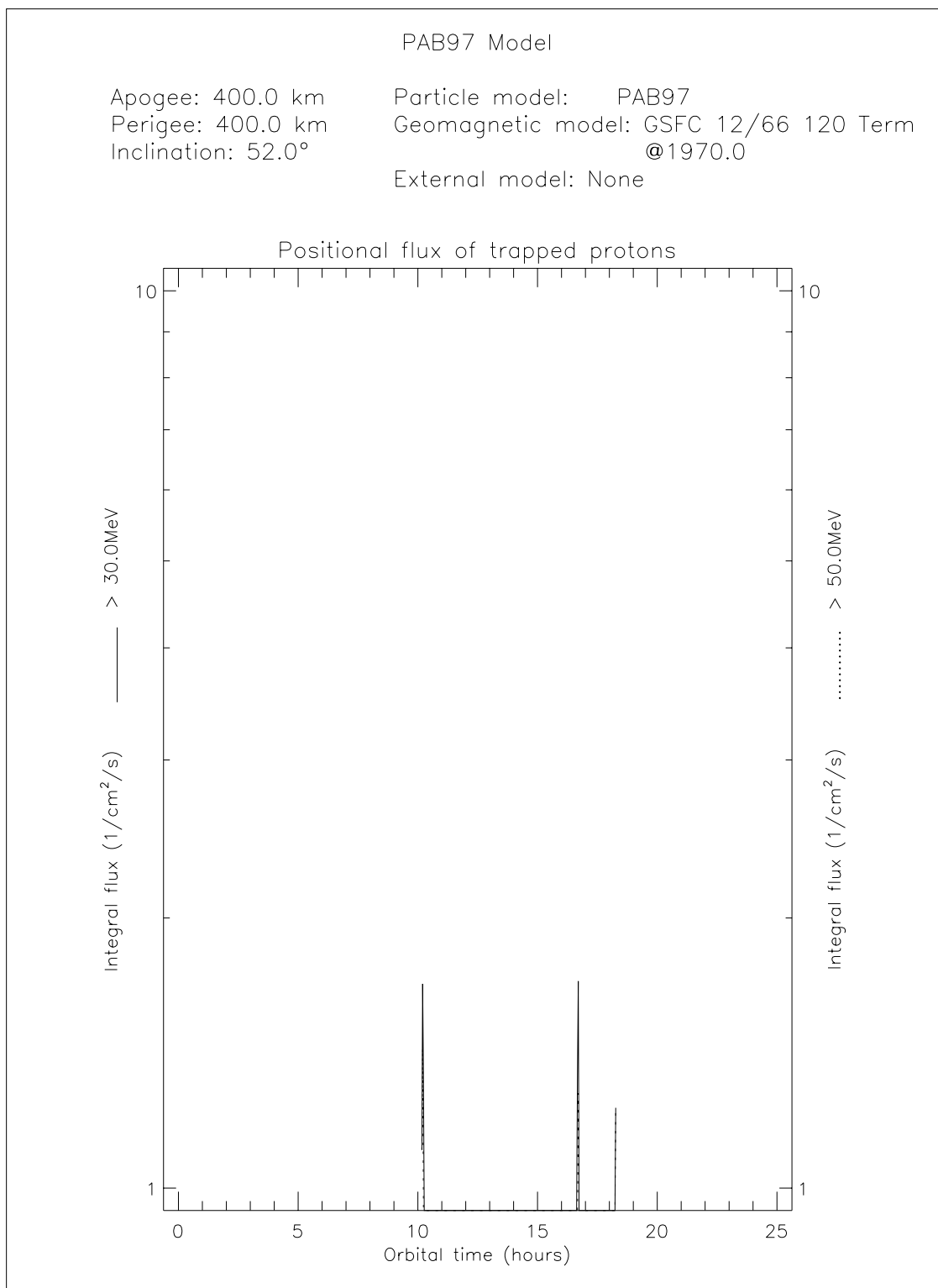


**Figure 7.6.** Integral PAB97 trapped proton fluxes above 30 MeV for the LEO orbit described in the text

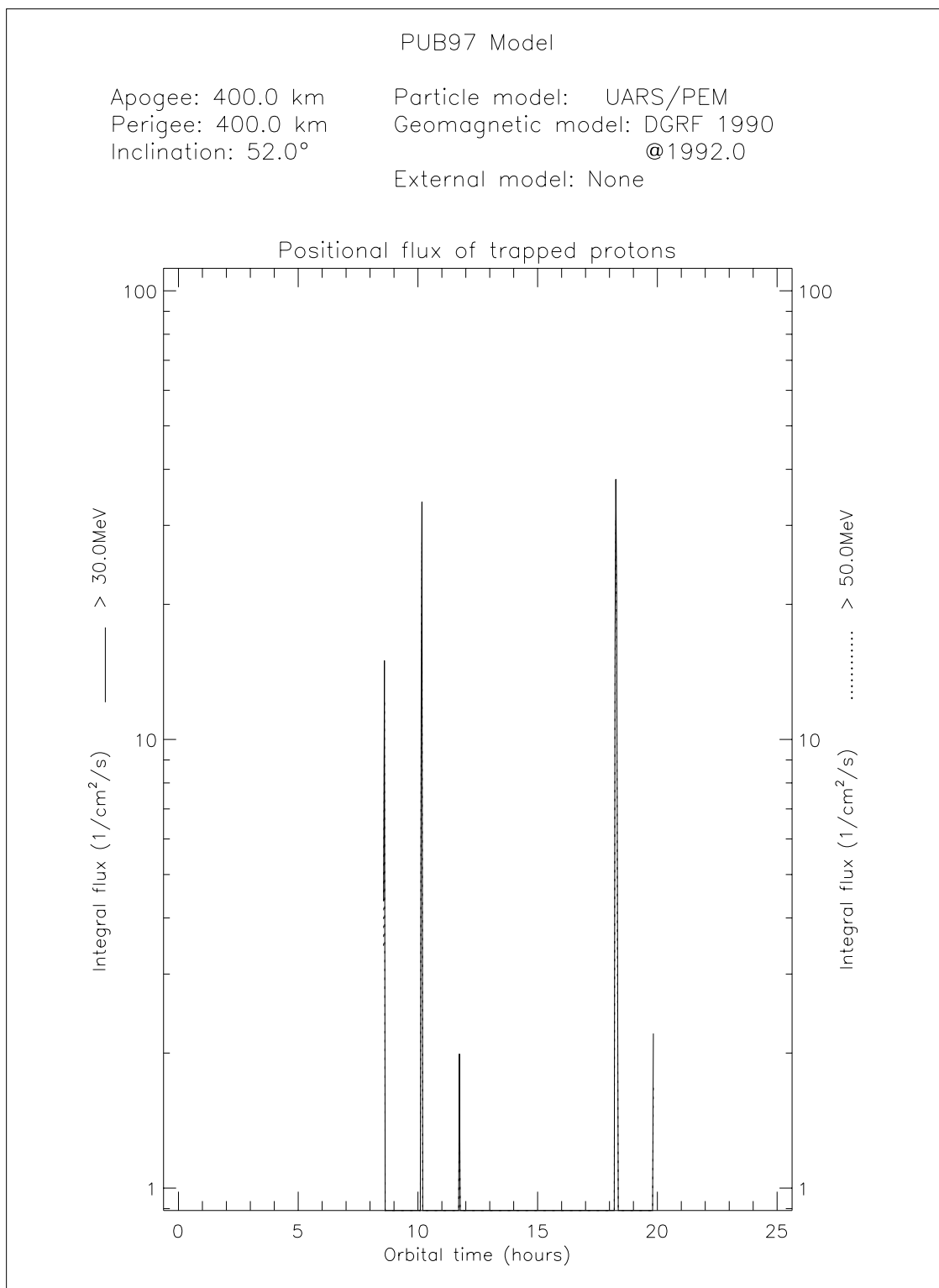


**Figure 7.7.** Integral PUB97 trapped proton fluxes above 30 MeV for the LEO orbit described in the text

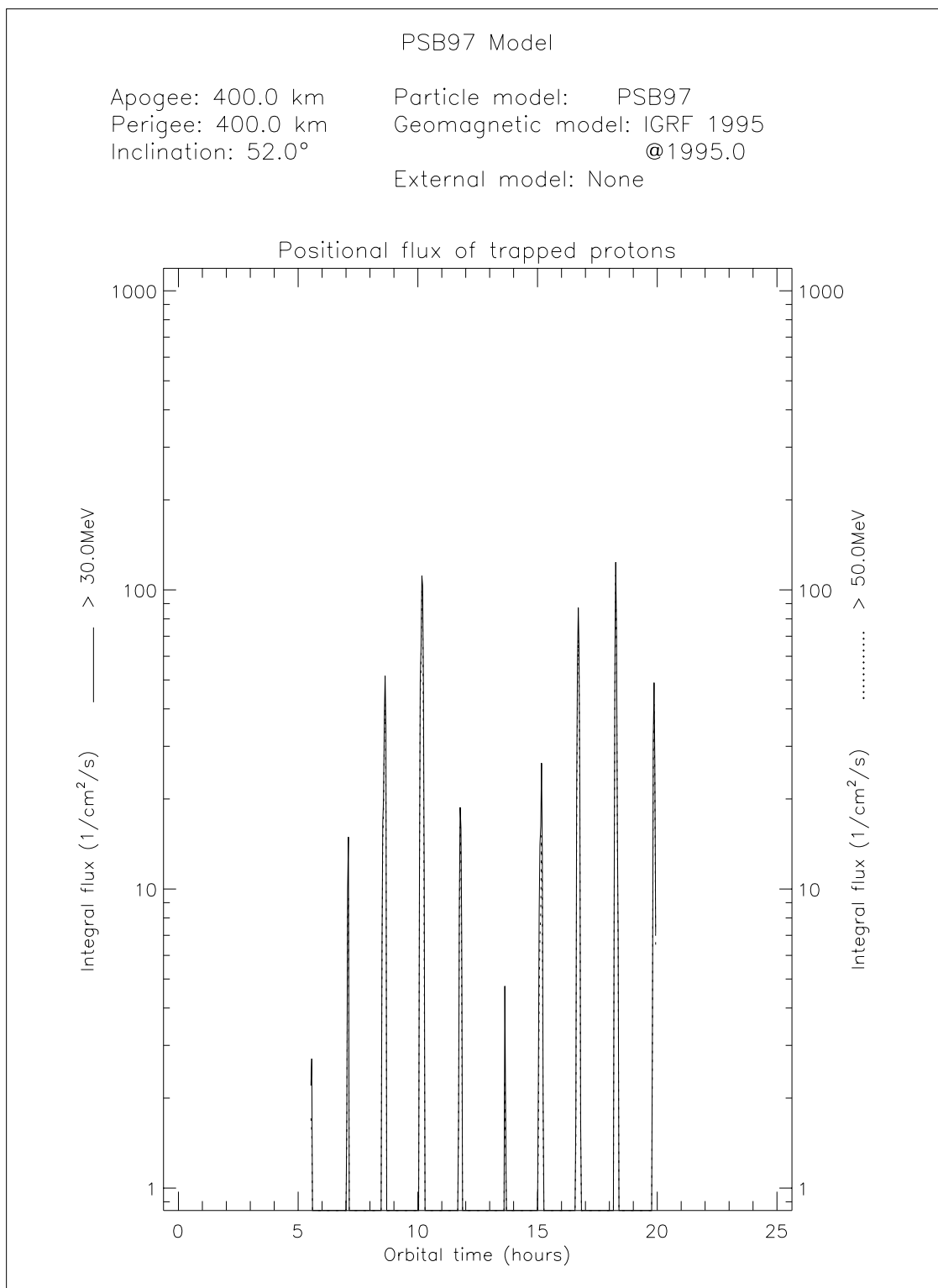


**Figure 7.8.** Integral PSB97 trapped proton fluxes above 30 MeV for the LEO orbit described in the text

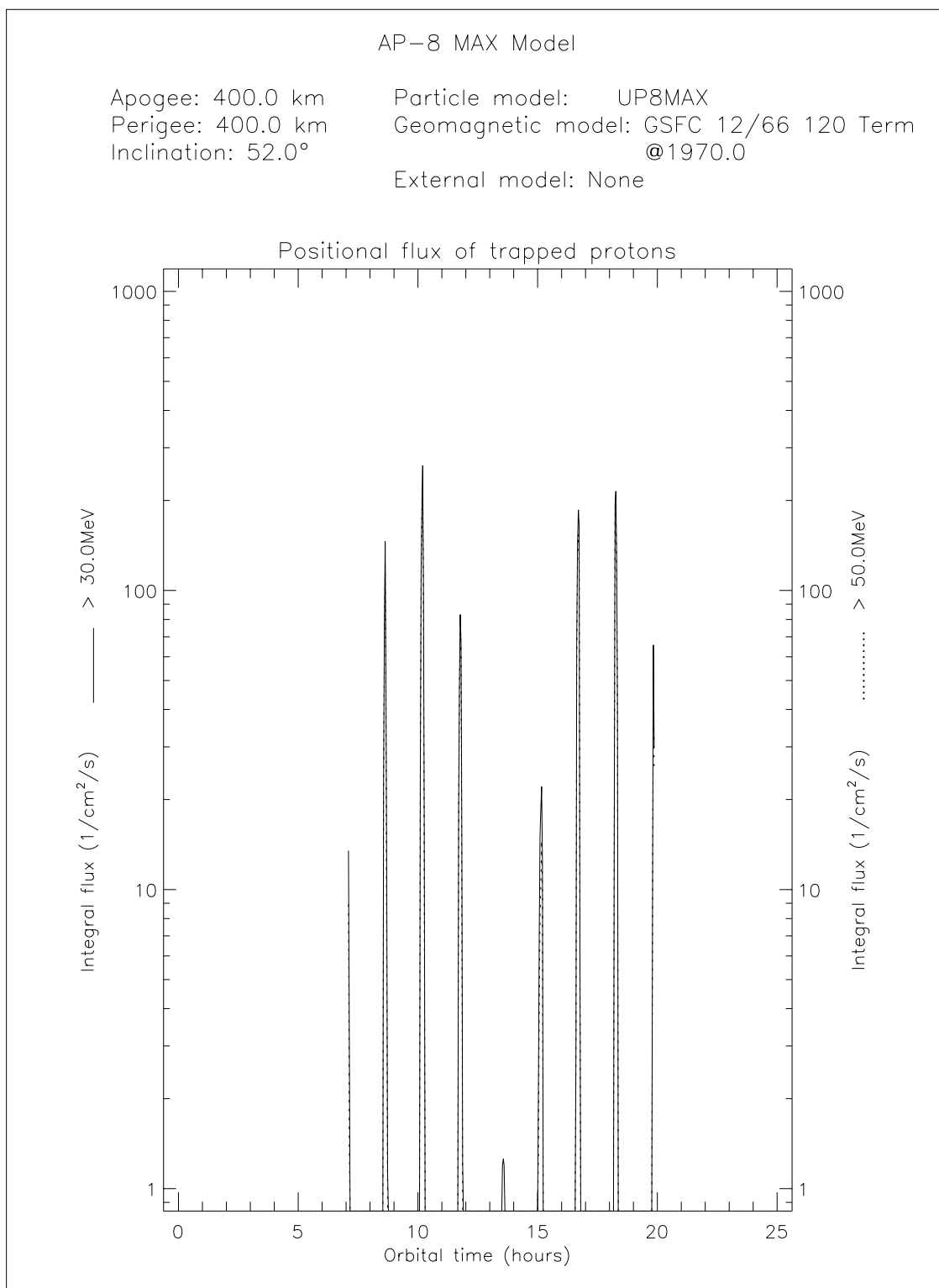


**Figure 7.9.** Integral AP-8 MAX trapped proton fluxes above 30 MeV for the LEO orbit described in the text



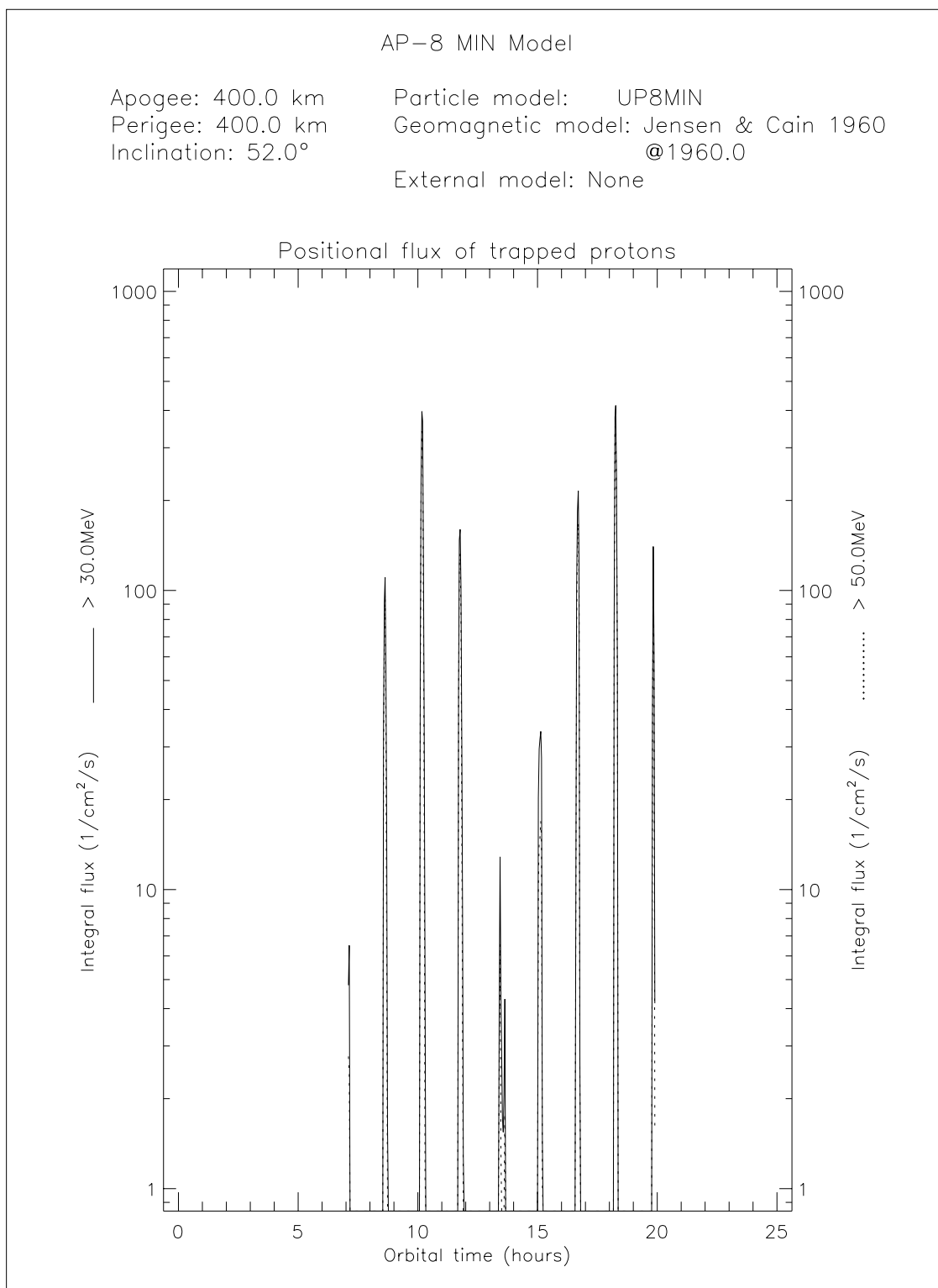


**Figure 7.10.** Integral AP-8 MIN trapped proton fluxes above 30 MeV for the LEO orbit described in the text

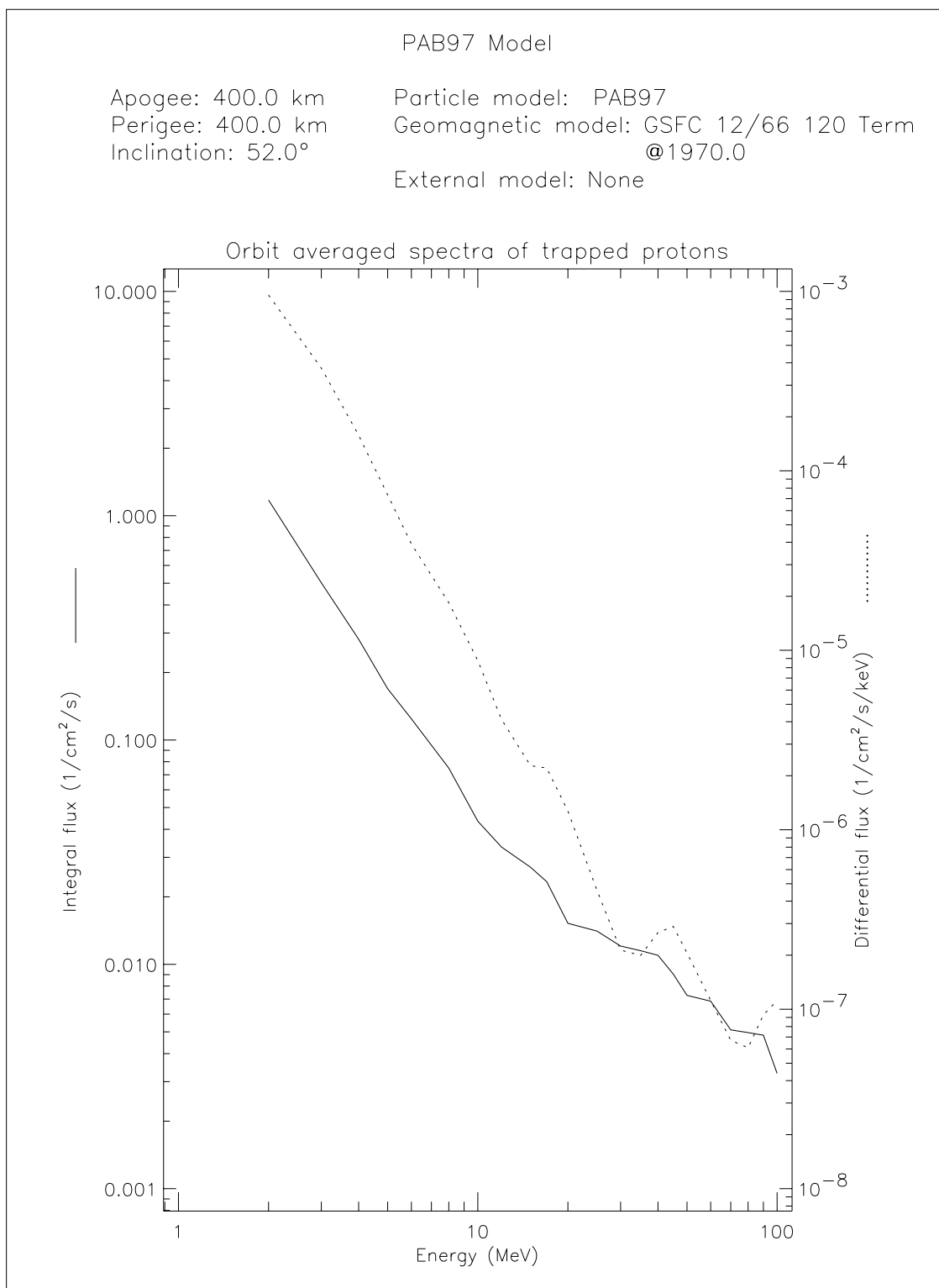


**Figure 7.11.** PAB97 Integral and differential trapped proton spectrum for the LEO orbit described in the text

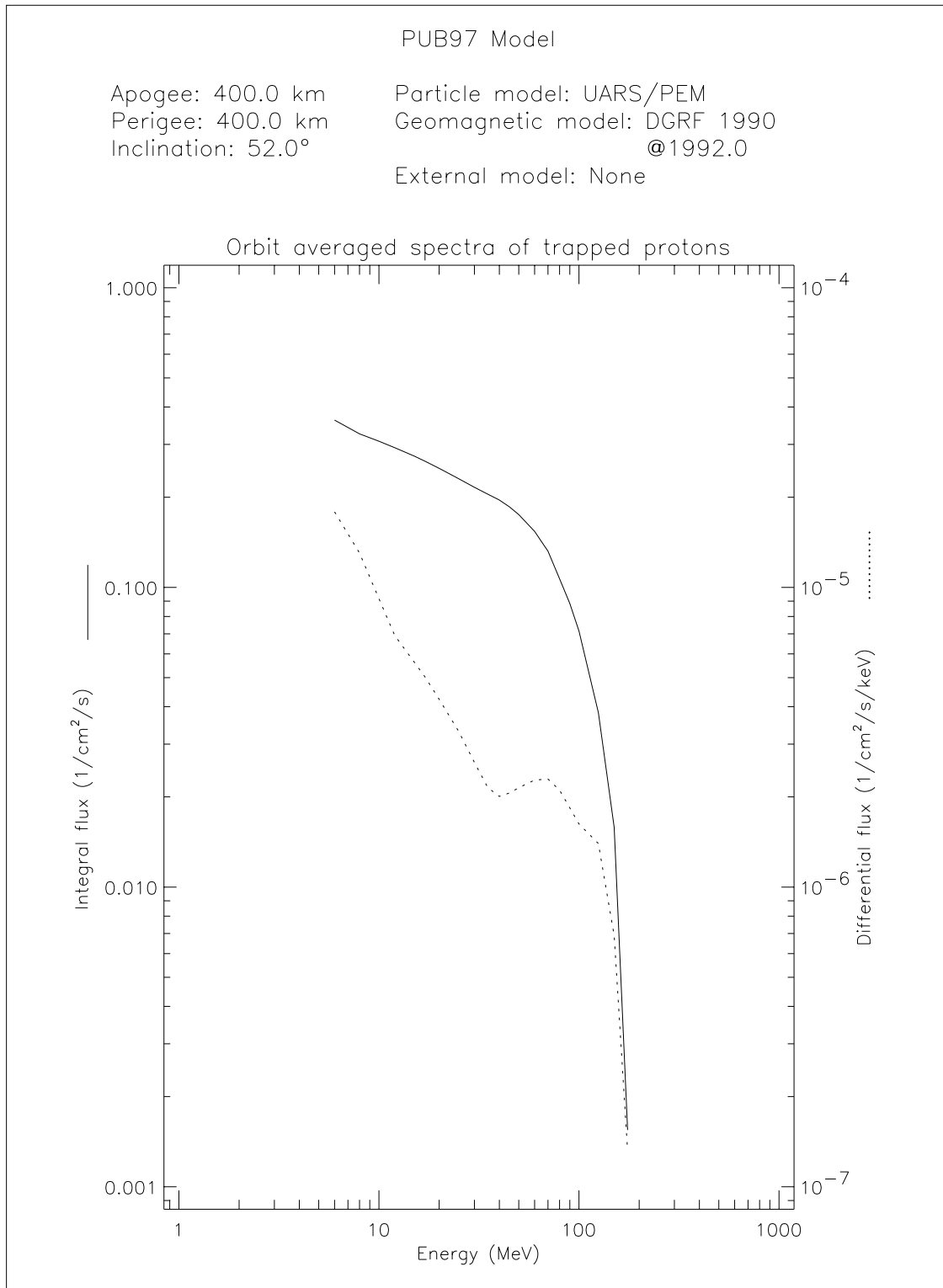


**Figure 7.12.** PUB97 Integral and differential trapped proton spectrum for the LEO orbit described in the text

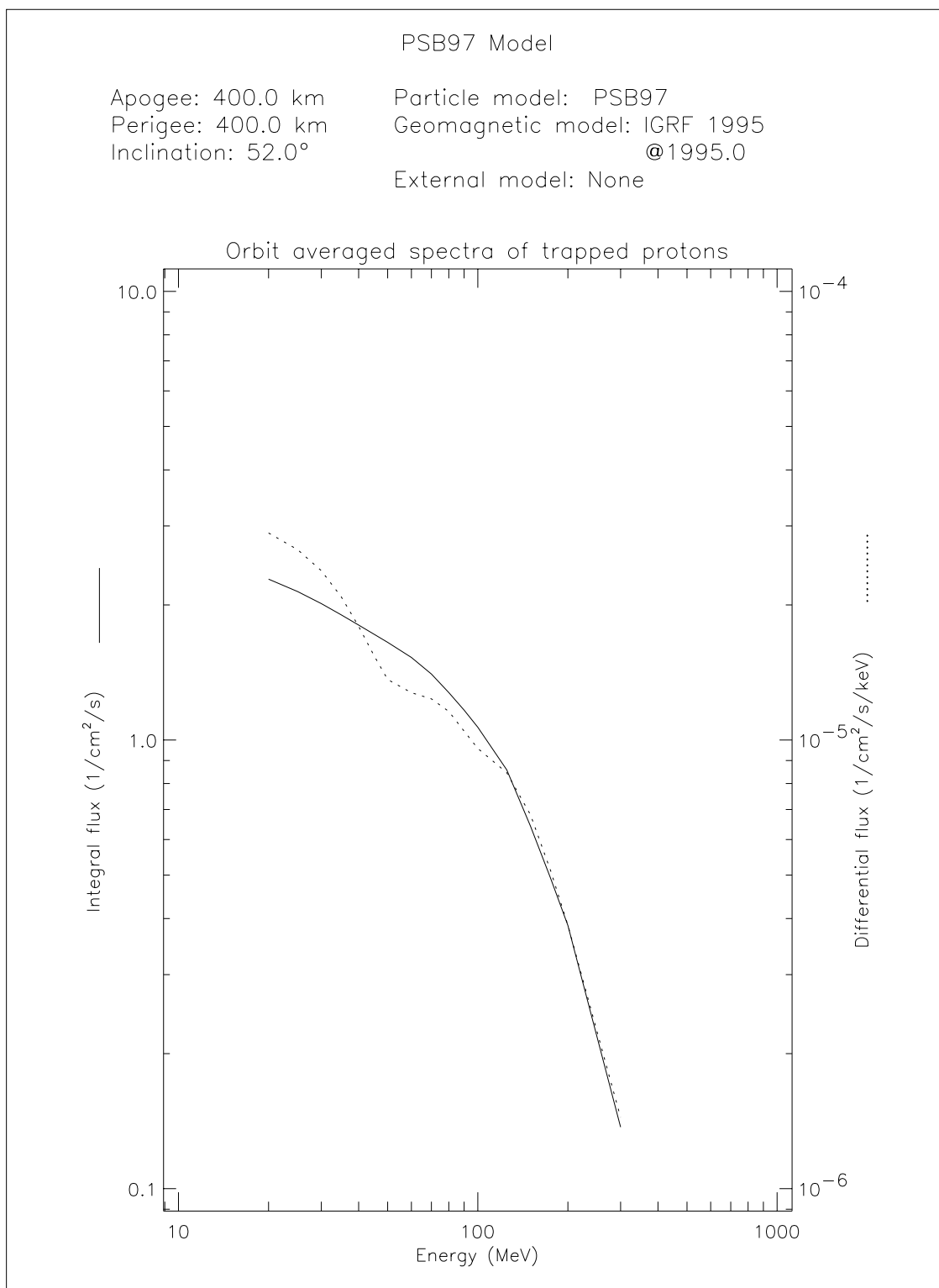


**Figure 7.13.** PSB97 Integral and differential trapped proton spectrum for the LEO orbit described in the text

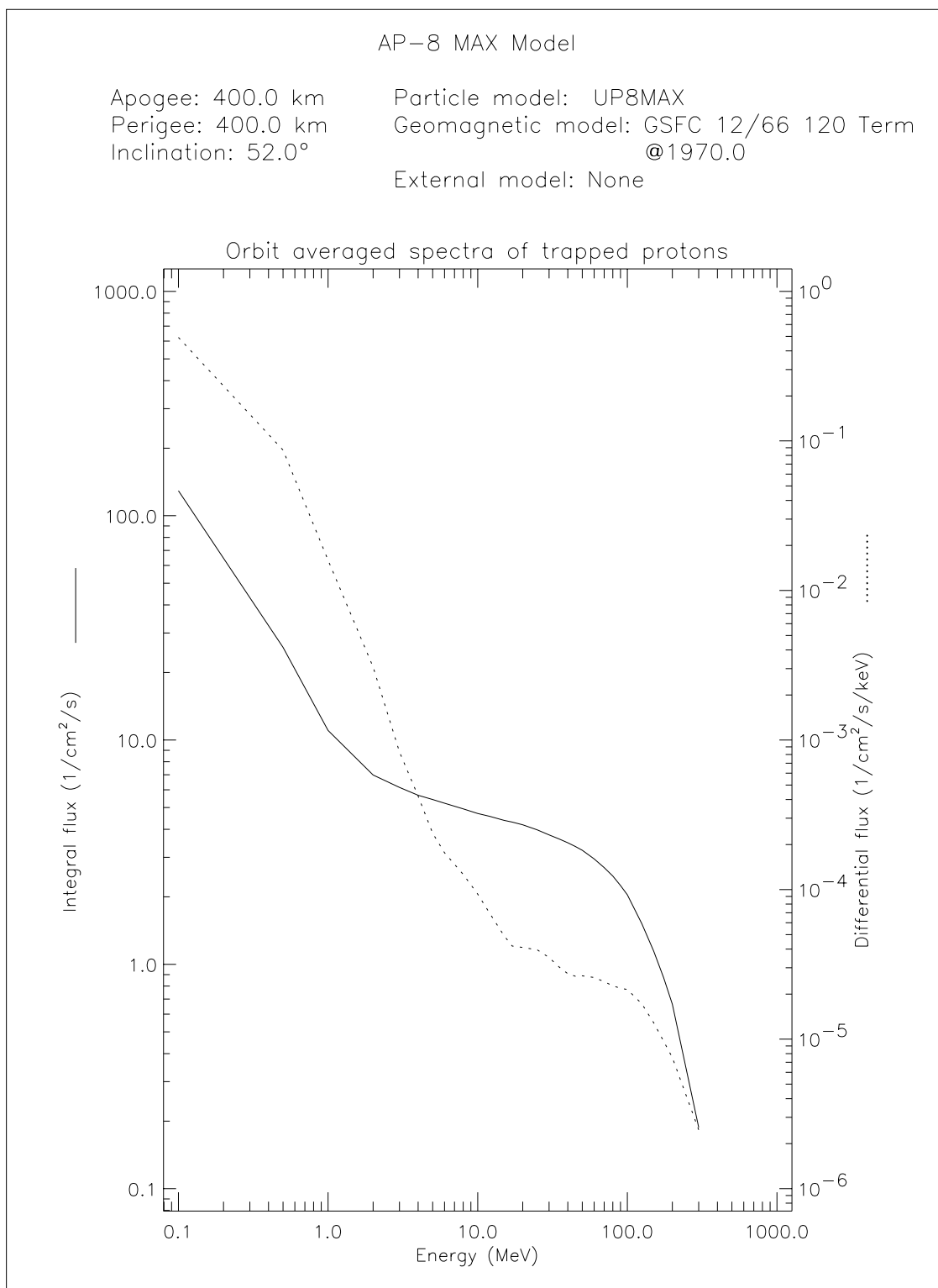


**Figure 7.14.** AP-8 MAX Integral and differential trapped proton spectrum for the LEO orbit described in the text

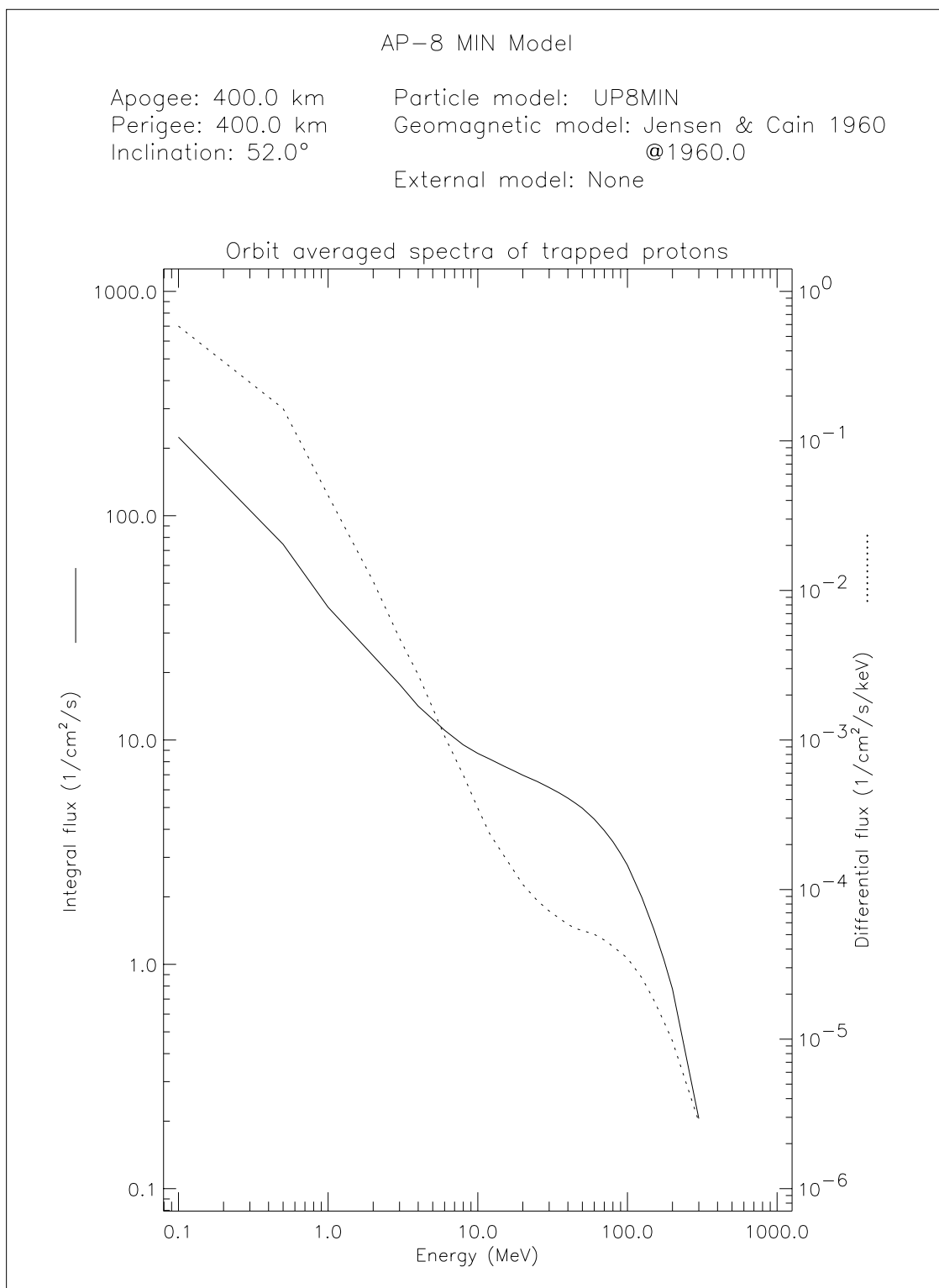


**Figure 7.15.** AP-8 MIN Integral and differential trapped proton spectrum for the LEO orbit described in the text

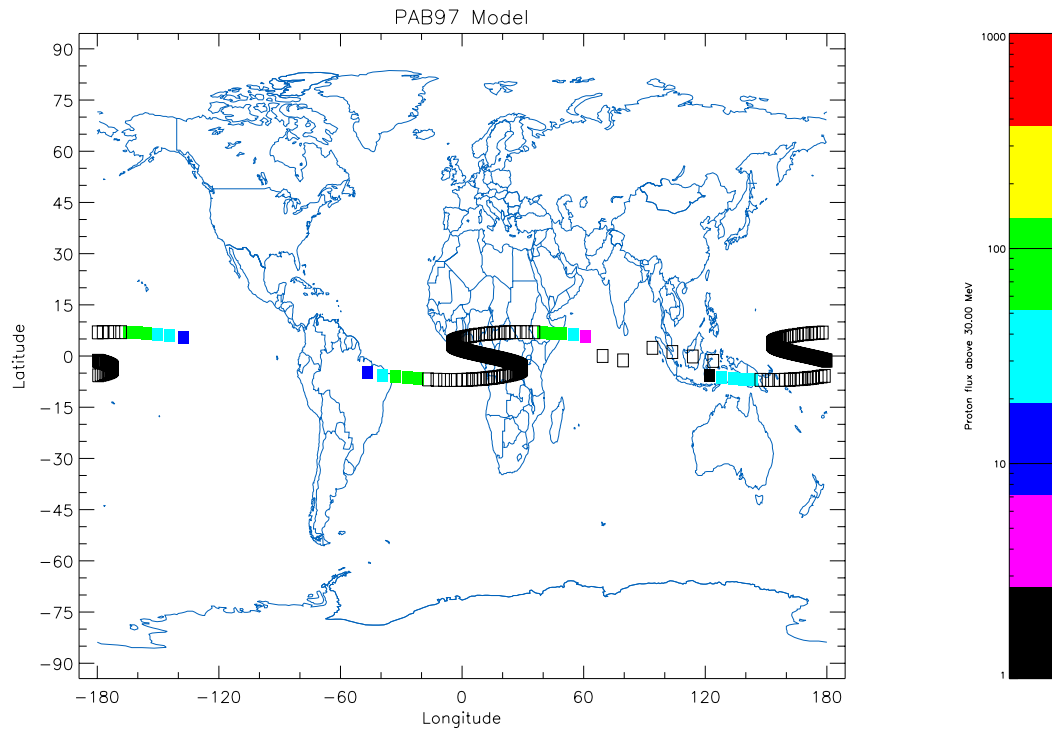


**Figure 7.16.** World map of the PAB97 directional proton flux above 30 MeV for the GTO orbit described in the text. The open squares represent orbital positions which are outside the validity range of the model.

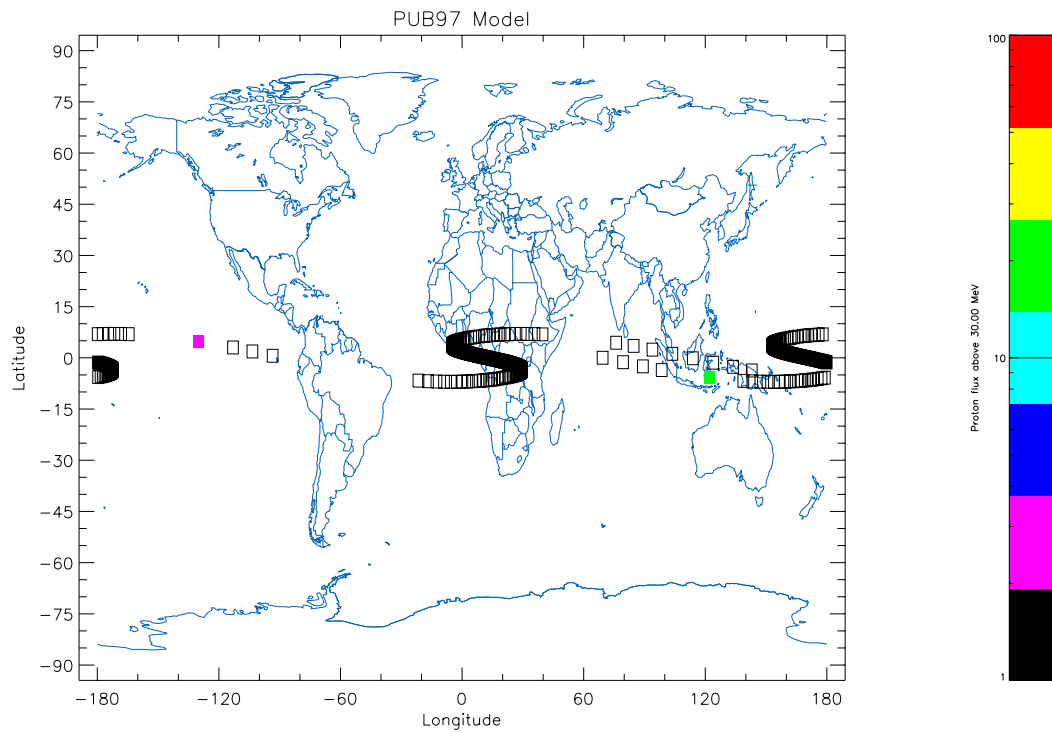


**Figure 7.17.** World map of the PUB97 directional proton flux above 30 MeV for the GTO orbit described in the text. The open squares represent orbital positions which are outside the validity range of the model.

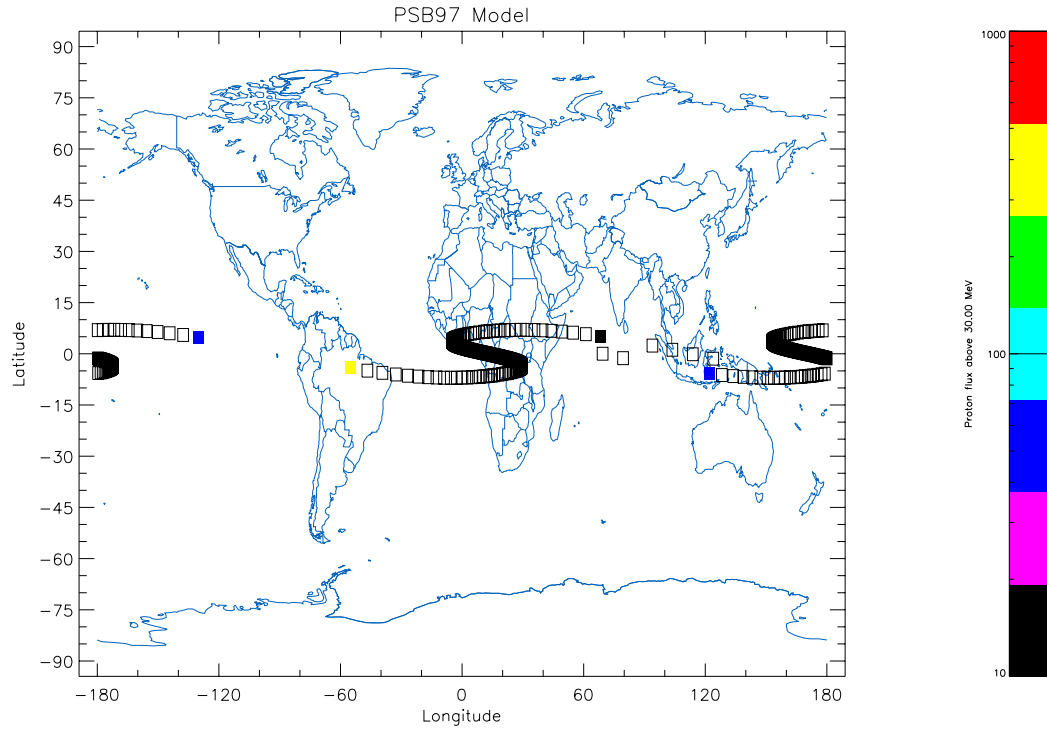


**Figure 7.18.** World map of the PSB97 directional proton flux above 30 MeV for the GTO orbit described in the text. The open squares represent orbital positions which are outside the validity range of the model.

the new proton models only cover the low altitude part. The new models are clearly not suited to evaluate the trapped proton flux over orbits with high apogees (for which, of course, they were not intended).

### 7.3 Conclusions

From the comparisons presented in this chapter, it is clear that the new trapped proton models PAB97, PSB97, and PUB97 should only be used for low altitude regimes. TREP Issues a warning when a trajectory contains geographical points that are outside the trapped particle model ranges, and outputs the number of such points. This helps the user to evaluate the validity of the model calculation. By producing a world map with the UNIRAD IDL programmes, the orbital points outside the model range can be identified.

We believe that the new models represent the low altitude trapped proton environment better than the AP-8 models for several reasons:

1. the models were constructed using only one high quality satellite data base per model, while the AP-8 models are based on data from different satellites;
2. the new models were built with directional data;



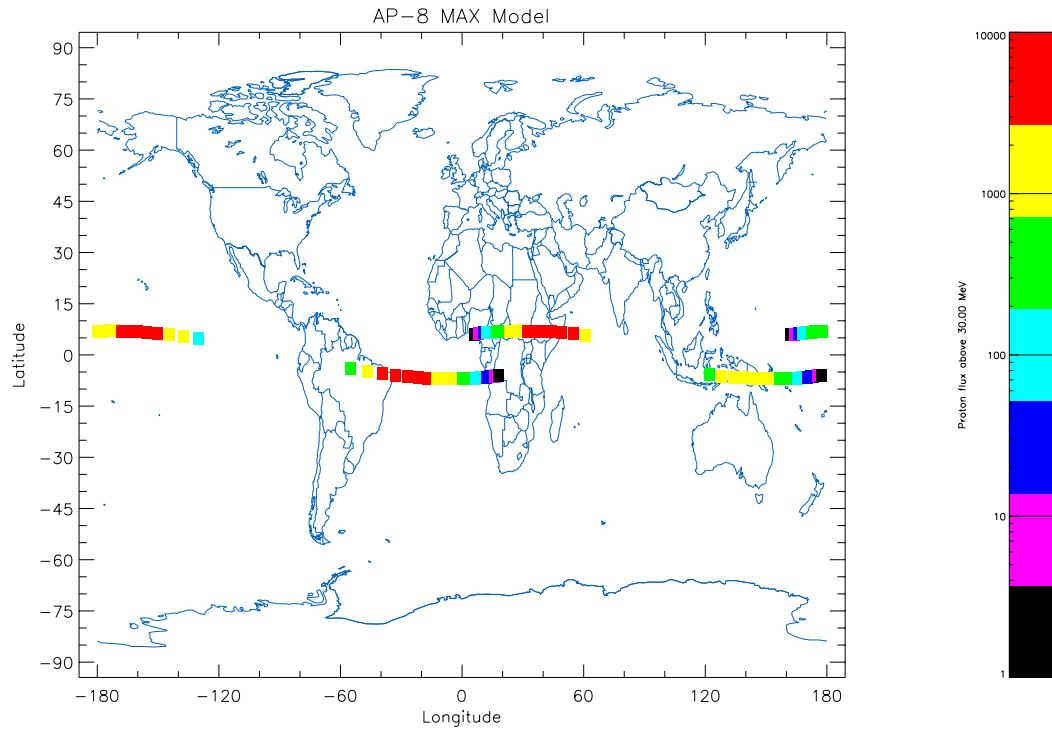


**Figure 7.19.** World map of the AP-8MAX directional proton flux above 30 MeV for the GTO orbit described in the text

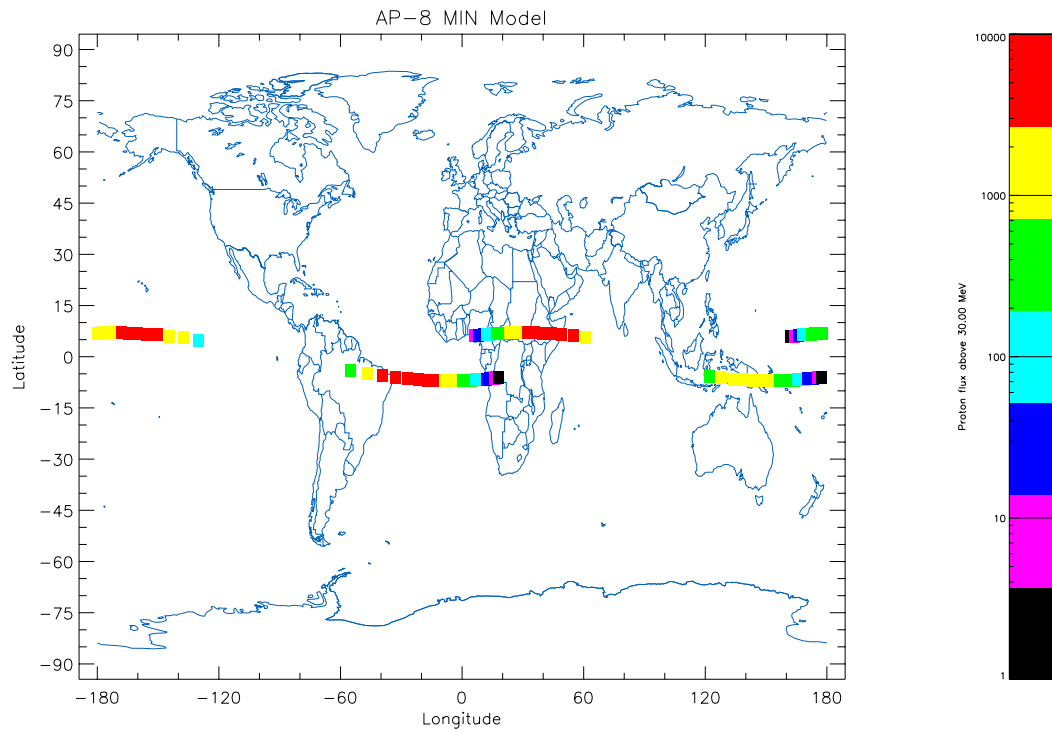


**Figure 7.20.** World map of the AP-8MIN directional proton flux above 30 MeV for the GTO orbit described in the text

3. the three models represent conditions during three different solar cycle phases.

## Chapter 8

# The ISEE data base and radiation belt model

This chapter reviews the results presented in Technical Note 1: it contains a brief overview of the ISEE 1 and ISEE 2 missions, of the KED and WIM instruments which have been used to measure electron fluxes, and a description of the ISEE data base which has been used to produce a new model for the trapped electron radiation belt.

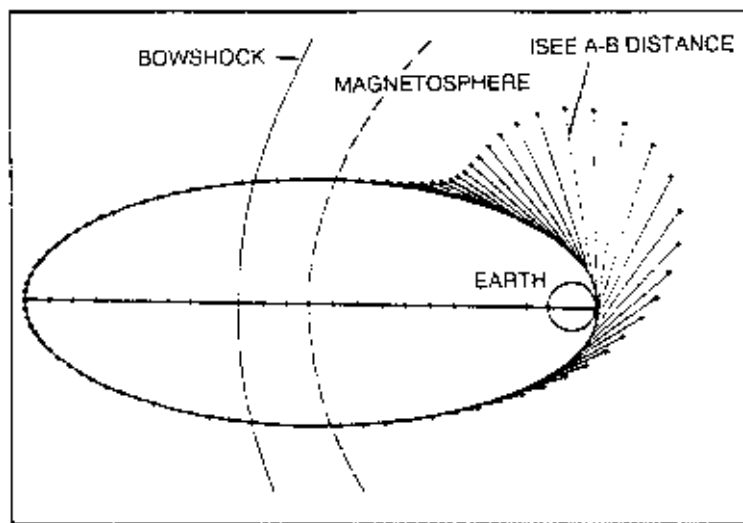


**Figure 8.1.** Plot of the ISEE orbits. Distances between ISEE-A and ISEE-B are represented by straight lines tangential to the leading orbit position of ISEE-A. Distance between both is represented by the length of the tangent.

## 8.1 The ISEE mission and instruments

The ISEE program consisted of three satellites, ISEE 1, ISEE 2, and ISEE 3. ISEE 3 Was anchored at the libration point  $L_1$  in front of the Earth. ISEE 1 and 2 were launched into a highly eccentric orbit with an apogee of  $23 R_E$  and a perigee height of several hundred km. Both were launched into the same orbit, but ISEE 1 had the capability to change its distance along the orbit relative to ISEE 2 from a few hundred km up to several  $R_E$ , as illustrated in Fig. 8.1. During the time span when ISEE 3 was anchored at the libration point, additional information on the solar wind speed and density, and thus on the solar wind ram pressure exerted on the magnetosphere, and the interplanetary magnetic field were available, all of which are important input parameters for the magnetosphere, including particle fluxes in the outer magnetosphere.

The WIM and the KED instruments on ISEE 1 and ISEE 2 were part of a joint proposal between D. Williams, NOAA Boulder, and E. Keppler, MPAE Lindau and their teams. Both instruments rely on the Wide Angle Particle Spectrometer (WAPS), a magnetic spectrometer based on a design already flown on the Helios space probes. On ISEE 1 this sensor was mounted on a sweeping platform, which rotated in a plane including the spacecraft spin axis by  $180^\circ$  in 32 minutes. Due to the spacecraft spin rotation (spin period 3 seconds) sectorisation was possible so that with this instrument a detailed pitch angle distribution could be measured. Energy spectra were measured in 128 channels.

On ISEE 2 the WAPS sensor was mounted in a fixed position almost normal to the spin axis (which was for both spacecraft normal to the ecliptic plane). It was, however, accompanied by four Narrow Angle Particle Spectrometers (NAPSs), which were mounted under different angles relative to the spin axis.

Figure 8.2 shows cross sections of the two sensor types. All sensors were able to measure ion and electron fluxes and to determine their angular distribution and energy spectra by utilizing 16 or 32 sectors, depending on low or high available bit rate, respectively (Williams et al. 1978).

The sensors used inhomogeneous (WAPS) or homogenous (NAPS) magnetic fields in order to separate electrons from ions. Ions and neutral particles could, however, not be distinguished, but neutral particle fluxes were very low as has been shown in a study by Roelof et al. (1976), which was based on ISEE 2 data. All sensors used silicon surface barrier semiconductor detectors. For ions the energy threshold was 25 keV, for electrons 18 keV. The maximum energy for electrons was 1 MeV for WAPS and 300 keV for NAPS. For ions it was 3 MeV in both sensors. Determination of particles of much higher energies was possible by the back detectors, which were shielded by massive tantalum cans up to 35 MeV in the case of protons.

The orbital plane of the ISEE spacecraft rotated about the Earth once per year (see Fig. 8.3) so that the measurements scanned through all parts of the magnetosphere. The active life time for ISEE 2 was almost 10 years from launch in 1977 until 1987, when the spacecraft entered the Earth's atmosphere. The WIM instrument on ISEE 1 ceased operation due to a power failure in 1980. The instruments were designed for measurements in the outer radiation zones. In the presence of energetic particles the interpretation of the data is not straightforward but needs to take into account the energy losses of these penetrating particles. Therefore, the analysis of data should be restricted to those parts of the orbit when the spacecraft was in regions with high  $L$

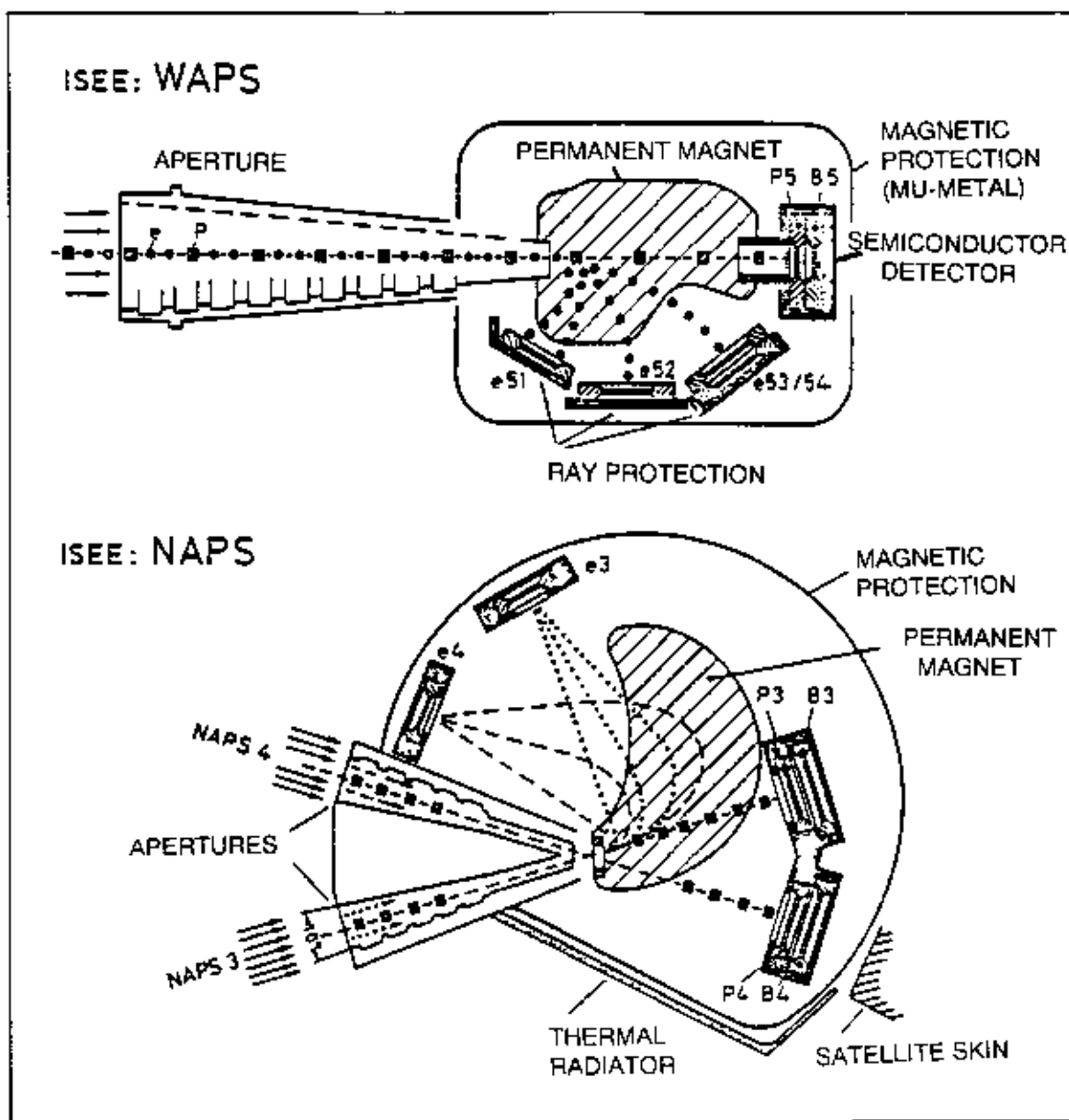


**Figure 8.2.** Cross section through the WAPS and the NAPS magnetic spectrometers. WAPS uses an inhomogeneous magnetic field to deflect electrons, NAPS a homogeneous magnetic field. Ions above the threshold energy of the instruments pass through the fields practically unaffected.

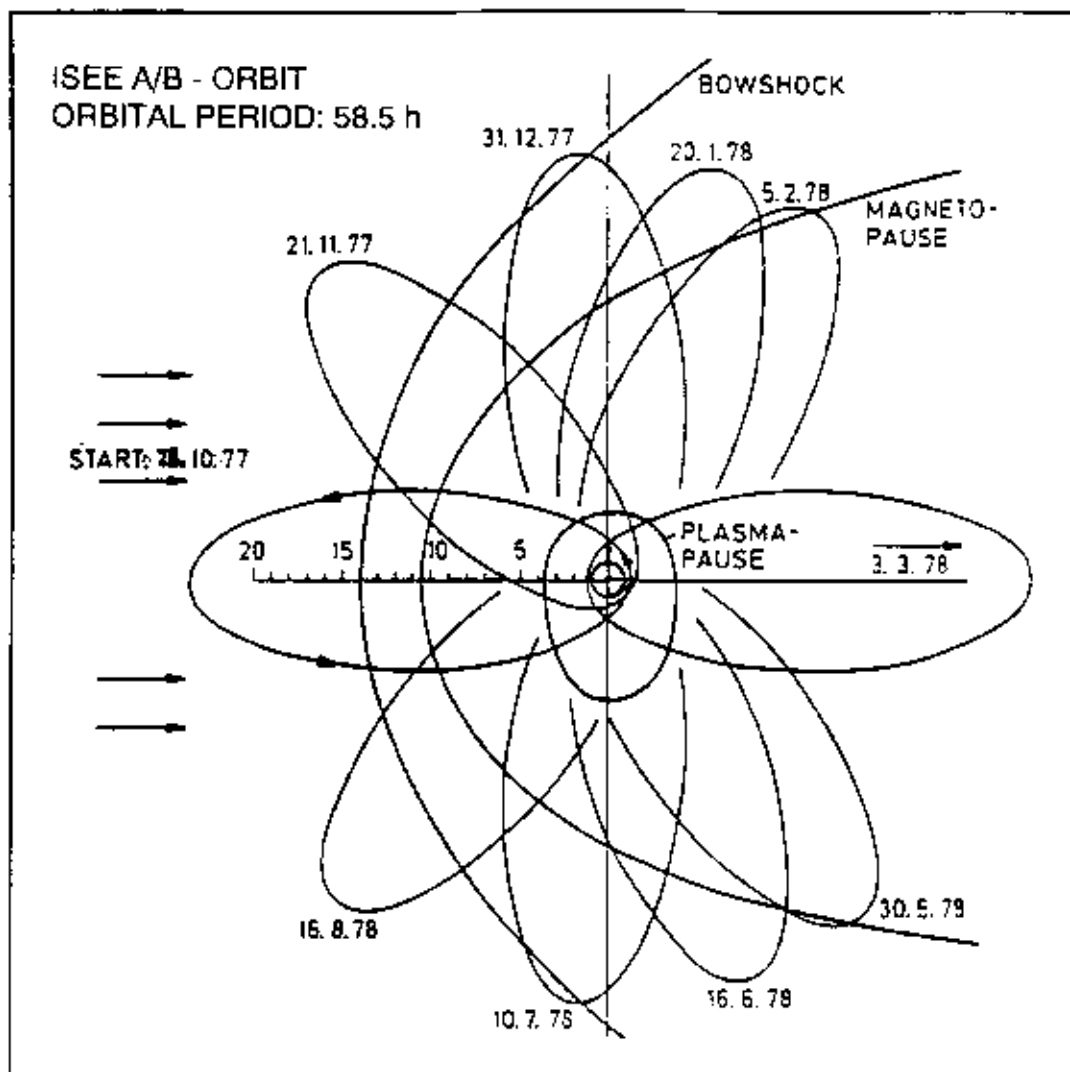


**Figure 8.3.** ISEE orbits during one year. Orbital period was 58.5 h. Apogee was  $21 R_E$ , perigee 400 km.

values ( $L > 4$ ). This can be easily accomplished by inspecting the back detector count rates, which were transmitted along with each data frame.

The data of the WIM instrument and most of the KED instrument data were processed on tapes containing the orbit data, the altitude data, and the magnetic field data (courtesy C.T. Russell). However, after the prime mission was terminated the KED data which were transmitted were no longer processed, but only stored as raw data. In order to make them available for this study, a significant effort had been started in order to convert the raw data (stored on 1000 tapes) to accessible data in the same format as the data which had been processed in the previous period (see Sect. 8.2). Figures 8.4 and 8.5 show examples of time vs. intensity plots of ISEE particle and magnetic field data. The data files contain a set of housekeeping data, sta-

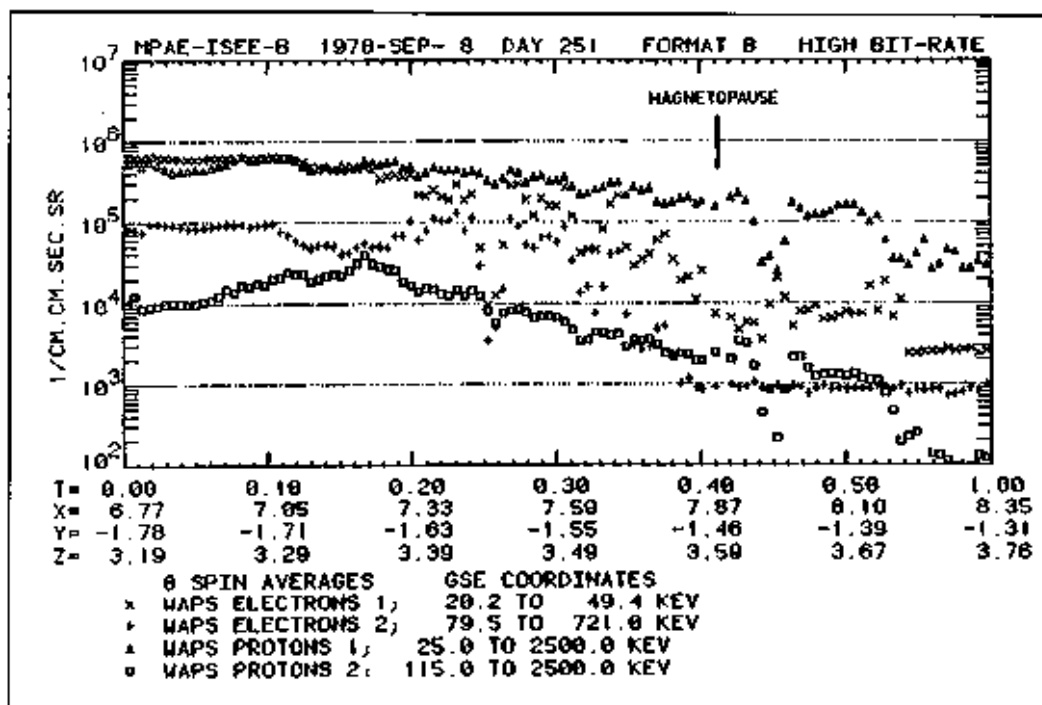


Figure 8.4. ISEE Ion and electron fluxes vs. time on day 251/1978. One hour of data is shown.

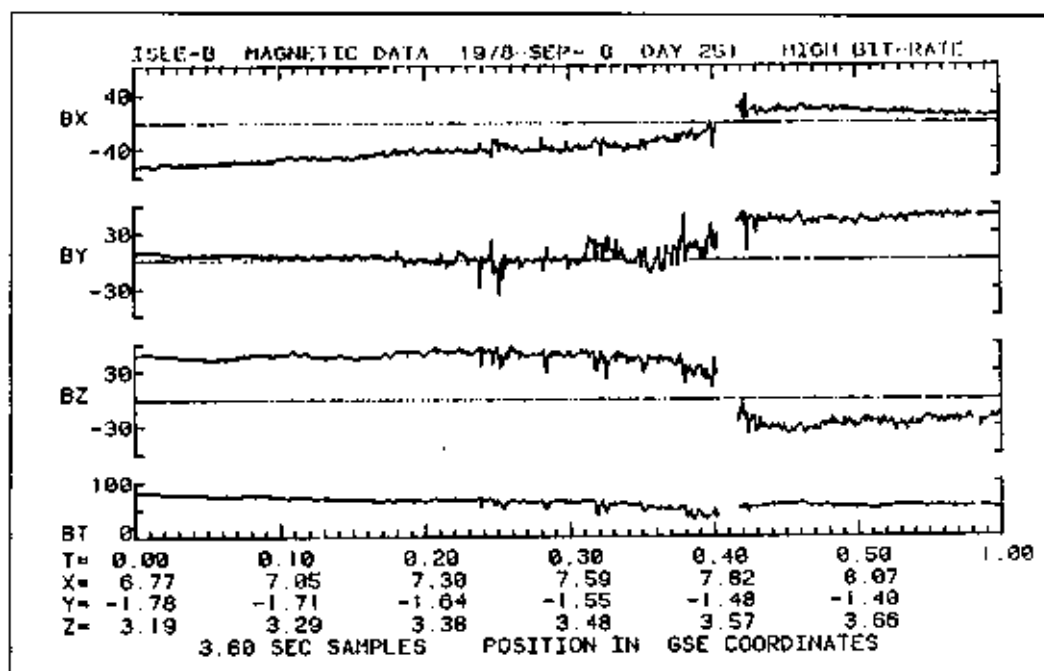


Figure 8.5. Total magnetic field  $B_T$  and components  $B_X$ ,  $B_Y$ ,  $B_Z$  vs. time on day 251/1978. One hour of data is plotted.

tus information and the science data. Orbital data are contained in headers in front of the data blocks. The status data must be inspected in order to recognise the operational mode of the instruments. The science data are generated from 8 bit words which contain the information quasi logarithmically compressed (GSFC 623C counters were used).

The raw data tapes are cleaned for redundancies and errors and contain the fully evaluated magnetometer data, but otherwise contain the original data. Four data analysis programs have been developed that started from these tapes. The programs include all necessary steps to convert the data from technical numbers into physical parameters ( $\text{cm}^{-2}\text{s}^{-1}\text{sr}^{-1}$ ). The programs also contain plotting routines for intensity vs. time plots, angular distribution plots, and energy spectra.

### 8.1.1 The ISEE-1/WIM instrument

The WIM instrument consists of a Wide Angle Particle Spectrometer (WAPS), a Heavy Ion Telescope (HIT), a motor-driven scan platform, and the associated instrument electronics.

#### 8.1.1.1 WAPS

The WAPS has evolved from similar units flown on HELIOS 1 and 2 (Keppler et al. 1978), Explorer 45 (Williams et al. 1968), ATS-6 (Fritz & Cessna 1975), and IMP 7 and IMP 8 (Williams 1977). It consists of an analysing magnet and six surface barrier solid state detectors. The pole pieces produce an inhomogeneous magnetic field having a  $\sim 800$  Gauss peak field generated by permanent SmCoS magnets. The field deflects electrons up to 1.5 MeV onto three electron detector positions E51, E52, and the pair (E53,E54) while protons (ions) proceed undisturbed to the two-element telescope P5/B5. To reduce radiation damage effects, detector P5 is positioned with its  $\sim 15 \mu\text{g cm}^{-2}$  Al contact toward the entrance aperture. All detectors are shielded by material composed of Al, Cu, Au, and Pt positioned to reduce energetic electron and bremsstrahlung background. Electrons with energy  $> 1.5$  MeV may reach the ion telescope, but these will be eliminated from being counted through the coincidence veto signal of detector B5 with almost 100% efficiency.

To reduce system noise, pre-amplifiers are mounted just above the detector mounting bracket. Four pre-amplifiers are used with the responses of the higher energy electron detectors, E52, E53, and E54, being summed into a single pre-amplifier. The entire assembly is surrounded by a magnetic shielding can which reduces the stray field to less than  $26 \gamma$  at 50 cm. The instrument has a geometric factor of  $8.6 \times 10^3 \text{ cm}^2 \text{ sr}$  for ions.

#### 8.1.1.2 Scan platform

The WAPS sensor is mounted on a scanning platform which permits the sensor collimator,  $\hat{f}$ , to scan from a position approximately antiparallel to approximately parallel to the spacecraft spin axis,  $\hat{s}$ , through the radial ( $\hat{f} \times \hat{s} = 0$ ) direction. The platform is rotated by a brushless, direct drive, DC torquing motor which has a history of high reliability. The stall torque of the



motor is 720 g cm. A torque of 145 g cm is required to overcome the centrifugal force of the spinning spacecraft and drive or hold the platform in any location. The controlling electronics are mounted in their own separate housing which interfaces to the spacecraft and command system through the main instrument electronics. The rotation system has two modes of operations: fixed and scanning.

In scanning mode, the platform is driven continuously, completing a  $160^\circ$  rotation cycle from  $\cos^{-1}(\hat{f} \times \hat{s}) = 170^\circ$  to  $\cos^{-1}(\hat{f} \times \hat{s}) = 10^\circ$  in 12 spins ( $\sim 36.5$  s). The platform is driven spin synchronously using the 1024/spin clock line from the spacecraft. Data collection is also synchronized with the scanning cycle. The position of the platform is controlled actively in an analog feedback loop using a Rotary Variable Differential Transformer (RVDT) for position sensing. The RVDT position voltage is monitored routinely once every 8 seconds and on command can be monitored 16 times per second in flight. The scanning mode has been the standard in-flight mode since Oct 31, '77, and operation of the platform has been normal. System linearity is good to within  $\pm 1^\circ$ .

In the manual mode the platform can be commanded into 15 positions by ground command. In the fifteenth position the WAPS "looks" back into the spacecraft and views a radioactive source rod. This rod is rotated by  $90^\circ$  by a mechanical ratchet each time the platform is commanded into position 15. The rod contains radioactive isotopes of Americium (241) and Barium (133) (200 microcuries each) in two positions and blanks in the remaining two positions. These sources can be used to calibrate the WAPS energy channels and pulse height analyzers with  $\alpha$ , electron, and  $\gamma$  ray lines.

A total of fourteen electrical lines are brought across the rotating interface by means of a Poly-twist cable. The Poly-twist feed-through consists of two Kapton film flexible circuits counter-wound on a single axis. 42 Circuit paths are provided and most are used for providing shielding for four pre-amp outputs. Normal life expectancy for these devices is 5 to 20 million cycles, permitting a minimum operational lifetime on ISEE 1 in excess of 6 years.

### 8.1.2 The ISEE-2/KED instrument

The KED instrument consists of five sensor systems mounted at various angular positions with respect to the spacecraft spin axis. All sensor systems are mounted on a common platform and protrude slightly through the spacecraft skin. Two different types of systems are used: the WAPS (described earlier) and the Narrow Angle Particle Spectrometer (NAPS), described below. The whole sensor system is contained within a Mu-metal can to provide for magnetic shielding. In addition to the sensor housing, the instrument consists mechanically of two other boxes housing the analog electronics and the digital electronics. Each of the detectors is connected by a short coaxial cable to the analog box. Signals between the analog and digital boxes are digital. The digital electronics provide all electrical interfaces to the spacecraft.

### 8.1.2.1 WAPS

The ISEE-2 WAPS is identical to that described for ISEE-1 in all operational and scientific aspects. For ISEE-2 the external shape of the collimator is slightly different from that presented in Fig. 8.2 and the pre-amps are located in the analog electronics instead of being colocated with the detectors. The dimensions of all detectors and apertures are identical in the two versions of the WAPS.

### 8.1.2.2 NAPS

A homogeneous magnetic field is used to separate electrons and ions. The ions traverse the field unaffected and are detected with a semiconductor detector telescope arrangement similar to that used in WAPS. All electrons  $< 300$  keV entering the aperture are focused on a semiconductor detector. Two detectors are used in one magnetic system defining two directions ( $4 \times 10^\circ$ ), as shown in Fig. 8.2. A mechanical collimator limits the opening angle. The geometrical factor for each electron detector is  $10^{-5} \text{cm}^2 \text{sr}$ , and  $2.5 \times 10^{-4} \text{cm}^2 \text{sr}$  for ions. Permanent magnets are used to generate the magnetic field. Two such systems are used giving ion ( $E > 25$  keV in case of protons) and electron ( $18 \text{ keV} < E < 300 \text{ keV}$ ) measurements from four different directions.

### 8.1.2.3 Temperature control and detector noise

In order to provide for low operating temperatures, a  $100 \text{ cm}^2$  surface covered with second surface mirrors is mounted in good thermal contact with the detector system. Calculations indicated that by this means the detector temperature should remain below a few degrees centigrade. Actual flight data have shown the temperature to be slightly higher ( $\sim 10^\circ \text{C}$ ).

### 8.1.2.4 Instrument electronics

The electronics can be divided into three sections: the pulse analog section, the digital data processing section, and the command/housekeeping section.

In the pulse analog section each detector is followed by a charge sensitive preamplifier. Preamplifier pulses are differentiated with pole zero cancellation, amplified by linear amplifiers with passive filters and DC restored by an active low level baseline restorer to produce unipolar semi-gaussian-shaped pulses ( $0.9 \mu\text{s}$  width at 10% level) with very rapid recovery even after overload. Amplitude discriminators are differential comparators with DC-hysteresis. In order to save weight and power, low level multiplexers have been introduced between the charge sensitive amplifiers and the pulse shaping amplifier which feed the PHA. However, to provide permanent rate information each detector output is fed into a simple, fast amplifier (integral rates, I data), which is directly connected to it.

Rate channels are digitized by discriminators. For more detailed energy information, a pulse height analyzer, built from 13 discrete discriminators, is used. Whenever a pulse is identified ( $0.6 \mu\text{s}$  after it arrived), its pulse height will be stored in a D-flip-flop for readout. However, the

analyzer is prepared to accept the next pulse for identification. The conversion dead time is less than  $0.2 \mu\text{s}$ , but due to pulse pileup separate pulses are obtained only for  $1.2 \mu\text{s}$  separation which should be considered as the resolution time. It has been shown that the analyzer will provide true spectra without significant pileup deterioration up to statistical pulse rates of  $10^5 \text{s}^{-1}$ .

In the digital data processing section, pulses from 12 rate channels and from the PHA (13 channels) are counted in 27 623C microprocessors, being quasilog compressed to provide 8 bit words (4 bit exponent, 4 bit mantissa, suppression of leading “1”). All data words are sequentially extracted and temporarily stored in a 2 kB buffer memory (two redundant memories are used). Data words are routed from the memory to the telemetry system through two data lines in an alternating sequence. Measurements are performed on a spin synchronous basis using the sun pulse generated by the spacecraft. Four sectors of data per spin ( $\sim 3 \text{ s}$ ) are generated at low bit rate.

The buffer memory has a capacity which is only three quarters of an Experiment Data Frame (EDF). The memories are organized to form a ring and a writing marker identifying the memory cell to be used. This is followed by a read marker. Provision is made to exclude the possibility that both markers meet for nominal spin rates. For non-nominal spin rates an “empty” quarter frame is transmitted (containing “0”).

In the command/housekeeping section, the instrument is controlled via four serial commands of 16 bits each. For safety reasons, 8 bits are used to identify commands, each command being identically repeated in the subsequent 8 bits. Each command has to be identified by the instrument twice, prior to execution. Fifty eight different commands may be executed by the instrument. Four multiplexers (4 positions each) may be commanded to either remain in any given position or to scan continuously, all detectors may be turned on and off, and in-flight calibration may be initiated and stopped. A pulse command is used to turn the instrument on and off. Nine different housekeeping measurements (temperatures, currents, voltages) are transmitted and four data words per EDF are used to transmit command status information.

For in-flight calibration (IFC) a pulse train (30 kHz pulse frequency) of  $2^{10}$  pulses is applied on command to each channel of the test input of charge sensitive pre-amps. The amplitude of the pulse is increased in 128 steps, 1 keV per step. This provides for a determination of discriminator thresholds, channel noise, performance of the counters logic and memory. The data obtained during IFC are organised in the same manner as during measurements. To test one channel, 8 EDFs of data are required, while 88 EDFs are required for a complete instrument test (about 29 minutes). It is planned to have one channel tested per orbit, initiated preferentially while the spacecraft is close to apogee.

#### 8.1.2.5 Operational modes

ISEE-2 may be operated at two bit rates (2 or  $8 \text{ kB s}^{-1}$ ) whilst maintaining the same data format. The KED instrument portion is maintained by accelerating the operational speed by a factor of 4. In addition, in order to properly adapt the information rate to the varying situations along the orbit, the instrument has two basic commandable operational modes (A and B).

**8.1.2.5.1 Mode A** All the sensor systems viewing the five directions relative to the spin axis contribute equal fractions to the data stream. Additional options are to give the full rate to electrons only, or to ions only, or to electrons and ions from one direction only. With decreasing number of detectors thus involved, the time resolution (and spatial resolution) is increased. Identification data for each detector are established and inserted into the appropriate data stream to the spacecraft. Angular resolution is four sectors in LBR and sixteen in HBR.

**8.1.2.5.2 Mode B** Most of the data stream is devoted to the WAPS system, which scans in the ecliptic plane. This mode is of particular interest in situations where the magnetic field subtends large angles with respect to the spin axis and particle fluxes are low (no significant contribution from the NAPS system). The four NAPS systems are monitored and their spin averaged rates transmitted. Again, instead of sharing the data between ions and electrons, either ions only or electrons only may be measured. The NAPS sensors provide spin averaged integral rates in LBR, but these rates are sectorized four per spin in HBR. The WAPS PHA data are obtained for 4 and 16 sectors, respectively, in LBR and HBR, whereas the integral rates above 20 keV and above 100 keV for both electrons and ions are obtained in 8 and 32 sectors for LBR and HBR, respectively. The instrument is described in full detail in Williams et al. (1978).

## 8.2 The ISEE raw data base

The ISEE-B satellite delivered telemetry raw data (experiment data, orbit data, magnetic field data) from 1977 day 307 up to 1987 day 61. The WIM instrument on ISEE-A stopped operation in 1980 after a power supply failure, so only a limited data set is available for ISEE-A. Both sets of electron data will be included in the final data base.

Experiment data tapes have been generated by GSFC. Raw data processing was performed at NOAA, Boulder. Here the experiment data were merged with magnetic field, orbit and attitude data. These data products have been termed Master Sciences Files (MSFs). All programs generated for further data analysis were designed in such a way that they started the calculations from the data contained in these tapes. Data processing in Boulder stopped in 1982. As a result, only the data from 1977 day 305 up to 1982 day 51 existed at the beginning of this study in MSF format. Later data from 1982 day 52 up to 1987 day 61 existed as raw data only, stored on 10" magnetic tapes. To convert this data into a useable format, the MSF production had to be reactivated because all existing analysis programs use the MSF format. At this point, we encountered a major difficulty. The existing raw data programs were written in an old Fortran code for a computer which no longer existed. For this reason, these programs had to be re-established in order to make the data accessible on a modern computer. With the help of still available personnel who had participated in the original ISEE program this was finally achieved. The cooperation and help of L. Matheson and J. Stevenson at NOAA, Boulder, USA have been of great help in resurrecting the original ISEE-B processing chain. After considerable effort, the restoration of the full data set of ISEE-B until its end of life has been accomplished.

### 8.2.1 Telemetry raw data

Original ISEE-2 telemetry raw data tapes have been obtained courtesy of T. Fritz, Boston University, USA. Experiment-Magnetic and Orbit-Attitude data beyond 1982 day 51 existed on old magnetic tapes (9 track, 1600 bytes per inch), but format, word, and record structure of the tapes were unknown. Likewise, there was no information on the interpretation of the obvious words. It was, therefore, first attempted to interpret the bit pattern with conventional formats knowing only a few characteristics of the original processing computer. The production of the MSFs was originally done on a Cyber machine at NOAA in Boulder. With significant effort some of the manuals for the Cyber and some information on the data format descriptions were recovered in Boulder. Some descriptions were wrong because data formats had been changed several times. So all the different formats had to be tested in order to find the correct one. Finally, the right interpretation of the bit pattern was reconstructed, and the program was run on all available data tapes. However, it was then realised that the tapes containing the magnetic field data did not contain the calibration data. As offsets are critical in interpreting these data, C.T. Russell, UCLA, was asked to assist with the calibration factors. These factors had to be inserted from time to time in order to readjust for drifts in the instrument. It turned out that the required calibration data were not easily accessible at UCLA. After many approaches, data files supported to contain the calibration factors were delivered only in April 96, from which the required calibration data were extracted. With these data it was possible to process the remaining raw data and make the full data set accessible.

### 8.2.2 Master Science File production

There were originally two kinds of raw data tapes: DECOM tapes, containing the experiment data, and MCE tapes, containing the orbit and attitude data. The DECOM tapes contain additionally the magnetic field data from C. Russell, UCLA. In order to use this data, some additional offset data and coupling matrices were needed. These data are necessary in order to calculate pitch angles, and were delivered by UCLA. The raw data were then copied from the old 10" magnetic tapes onto DAT. About 1000 old tapes have been copied. They fit on only 7 DATs. Next, the copied raw data were cleaned from bad data and time overlap. Unreadable tapes (the tapes were 10 to 15 years old) caused some minor gaps: approximately 6% of the available data volume could not be recovered and is therefore lost.

The cleaned raw data were used as input to the converted MSF production programs. While the original raw data processing had been performed on a Cyber computer with a word length of 60 bit, the old MSF production programs were written in non ANSI Fortran II and IV for Cyber and some essential subroutines were written in Assembler for Cyber. There were a number of bit operations in these programs based on specific Cyber structure. The programs therefore had to be rewritten in modern Fortran and in C for modern machines. This task turned out to be the bulk of the work and, as such, required several months (it was not expected when this contract started).

The MSF consists of four data blocks, one header data block, one magnetic data block,

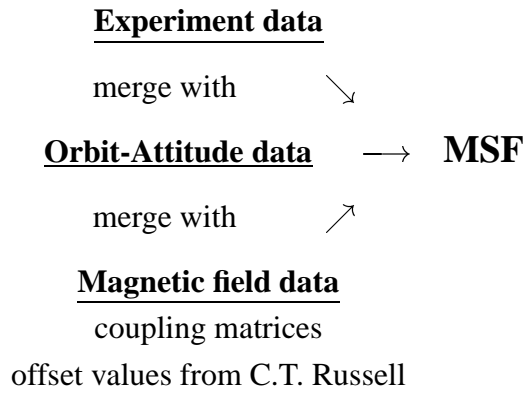


**Figure 8.6.** ISEE Master Science File production scheme

one experiment data block, and one housekeeping data block. For detailed description see the “Description Document for Users of the Master Science File”, delivered with the MSFs. MSFs are delivered on DATs. The production scheme is illustrated in Fig. 8.6.

## 8.3 The ISEE final data base

### 8.3.1 Final data processing

With the existing Fortran programs NAPS pitch angle data, orbit and attitude data, time and measured magnetic field have been extracted from the MSFs.

The pitch angle data do not contain spectral information. The NAPS data contain the spectral information only once per spin. Energy spectra do not vary significantly over one spin period. Therefore, spin averaged spectra may be readily applied. For evaluation of the data the following procedure was applied. Spectral information was derived from the four NAPSs and spin averaged rates were used. Where spectra changed, interpolated spectral slopes have been used (power laws in kinetic energy were always assumed). These normalized spin averaged energy spectra for 12 energy channels have been merged into the final data files. A comparison of original and averaged spectral data is shown in Fig. 8.7.

Mirror point magnetic field intensities for 9 pitch angles and the corresponding  $L$  values have been calculated with BLXTRA and were added to the final data base. The magnetic field was calculated with the Olson & Pfitzer (1977) quiet model, in addition to the IGRF internal field model.

The geomagnetic activity index  $K_p$ , the number density  $n$  and velocity  $V$  of the solar wind, and the geomagnetic activity index  $D_{st}$  have been merged from the OMNI data base.

A quality flag for the magnetic field data and energy spectra, the local time and the invariant

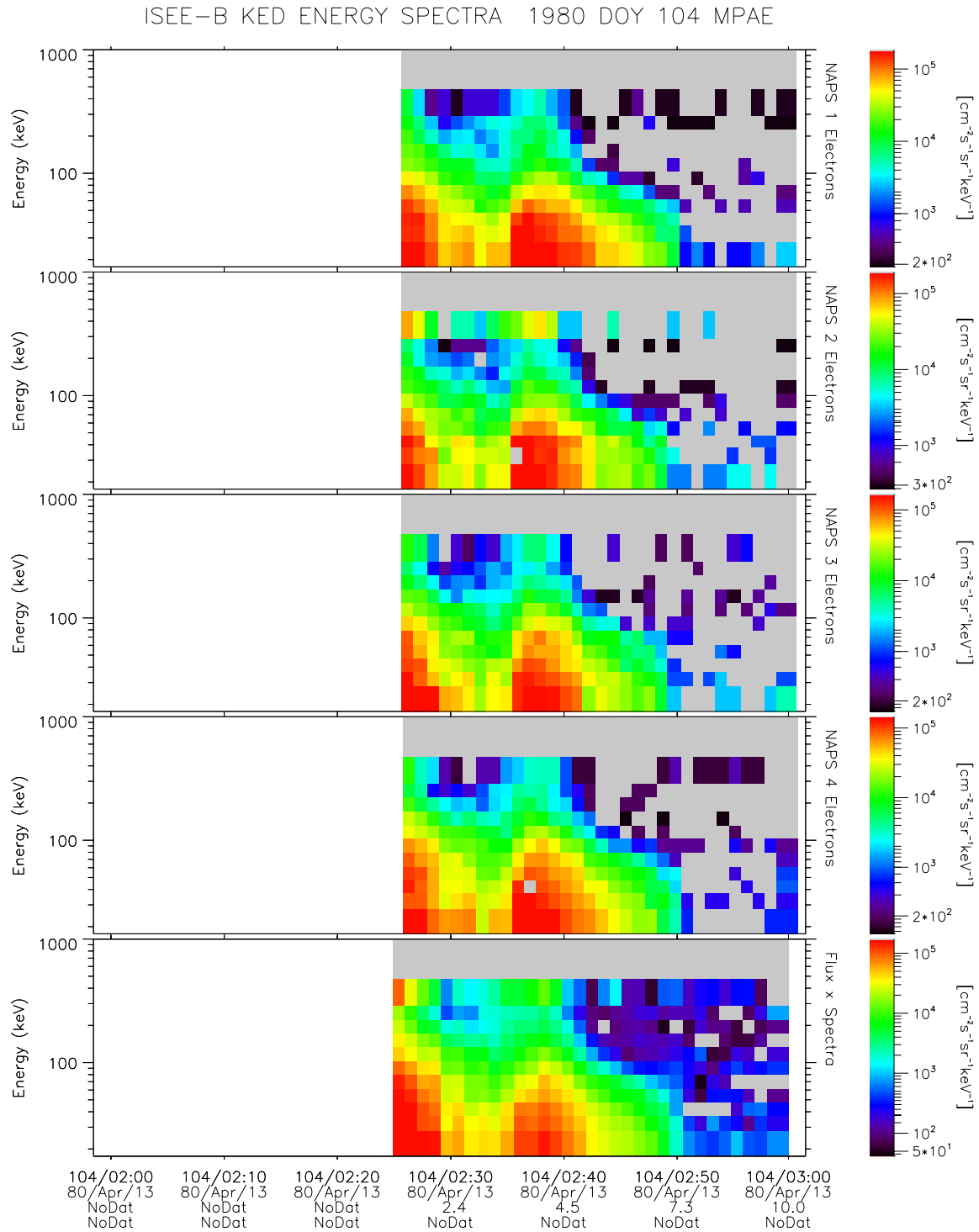


**Figure 8.7.** ISEE Example of four original dynamic energy spectra and the averaged spectrum. The first four plots show the data from the four NAPS sensors, the fifth plot shows the averaged spectrum adjusted to the total flux.

geomagnetic latitude have been calculated and also added.

Only times for which  $L$  values could be calculated are included (i.e. inside the magnetopause). Therefore, there are days without data and the length of the existing files varies. On average, the final daily files (in ASCII format) have a size of about 200 kB. The time resolution of the final data is about one minute.

### 8.3.2 Format of the final data base

#### 8.3.2.1 Data base frame for ISEE-1

The full set of ISEE-1 data files are stored as a set of ASCII files, one file per day. The whole data set is about 21 Gb. The files are named `ISEE1_YEAR_DAY.DAT`, where YEAR is the year expressed as four digits, and DAY is the day of year (three digits).

There are two kinds of files, depending on the bit rate (low or high). On average, a low bit rate file is about 2500 kB, and a high bit rate file is about 7500 kB. Each file contains an integer header, a floating header, magnetic data, pitch angles, and electron flux data. The format of the integer and floating headers is given in Table 8.1, and that of the flux data for low and high bit rates in Table 8.2.

#### 8.3.2.2 Data base frame for ISEE-2

The full set of final ISEE-2 data files are stored as ASCII files, one file per day. The average file size is about 200 kB, the whole data set is about 280 Mb. The files are named `ISEE2_YEAR_DAY.FINAL`, where YEAR is the year expressed as four digits, and DAY is the day of year (four digits). The record structure of the data files is listed in Table 8.3. The values of the one byte quality flag `qf` are given in Table 8.4.

#### 8.3.2.3 Magnetic field model for ISEE-2 data

Since the electron flux data will be ordered by some pre-selected variables such as  $L$  and  $\alpha_0$ , the choice of the magnetic field model used to calculate these data is of paramount importance.

On ISEE-2 we have the magnetic field data available: this can be used to provide some checks on the model calculations. Typically, the only input in a static model is the satellite position and time, for which the model returns model magnetic field values. The  $L$  values can be computed using the model to trace field lines. Some models take input parameters such as  $K_p$  or  $D_{st}$ , and the  $L$  value is a function of particle pitch angle  $\alpha$ .

In the past, a large volume of data was averaged into one single flux map to provide a statistical model as a function of some of these parameters, without any pre-sorting of the data according to quality or applicability. In this way, data can be systematically assigned to the wrong averaging bins if the model used was not applicable or inaccurate for the data point in question. This can frequently happen in the inner magnetosphere which is inherently dynamic, and where, for example, model  $L$  values can be out by several  $R_E$ , or  $L$  values can be assigned



**Table 8.1.** Contents of the ISEE-1 file headers

Header No.	Description
<b>Integer headers</b>	
1	Year
2	Day
3	Hour
4	Minute
5	Second
6	Bit rate (0: low, 1: high)
7	Physical regime (0: trapping region, 1: tail, 2: magnetosheath, 3: inter-planetary)
8	Scan direction (0: up, 1: down)
<b>Floating headers</b>	
1	$L$ Value
2	$B/B_0$
3	Geocentric distance
4	GSE $X$ Coordinate
5	GSE $Y$ Coordinate
6	GSE $Z$ Coordinate
7	Geographic latitude
8	Geographic longitude
9	Magnetic vector, GSE latitude
10	Magnetic vector, GSE longitude
11	GSM Latitude
12	GSM Longitude
13	$\rho$
14	GSM $X$ Coordinate
15	GSM $Y$ Coordinate
16	GSM $Z$ Coordinate
17	Subsolar latitude, GSM
18	Subsolar longitude, GSM
19	Sun-Earth-satellite angle
20	SAO Spin axis, GSE latitude
21	SAO Spin axis, GSE longitude
22	Spin period
23	GSE To GSM transformation
24	GSE To GEI transformation ( $\lambda$ )
25	GSE To GEI transformation ( $E$ )
26	Satellite orbit number

**Table 8.2.** Electron flux channels in the ISEE-1 data frames (in keV)

Channel No.	Channel width
<b>Low bit rate files</b>	
1	22.5–39.0
2	39.0–75.0
3	75.0–120
4	120–189
5	189–302
6	302–477
7	477–756
8	756–1200
<b>High bit rate files</b>	
1 odd	22.5–30.5
1 even	30.5–39.0
2 odd	39.0–60.0
2 even	60.0–75.0
3 odd	75.0–94.5
3 even	94.5–120
4 odd	120–150
4 even	150–189
5 odd	189–238
5 even	238–302
6 odd	302–380
6 even	380–447
7 odd	447–602
7 even	602–756
8 odd	756–952
8 even	952–1200

to data which are obviously already beyond the magnetopause or in the lobes on open field lines (where the concept of an  $L$  value becomes meaningless).

Using the available magnetic field data on ISEE-2 and also checking on the data values to distinguish between open and closed field lines allows us to choose for incorporation into the flux maps only those data for which the used magnetic field models are valid.

Several external models were tested against the ISEE-2 magnetic field data to determine the quality of the model in terms of a long term statistical difference between measured and model field, expressed as a mean offset and a standard deviation. In general, the static models are only good for a certain range of  $L$  values, with around 70% of all data points being reproduced by the

**Table 8.3.** Record structure of the ISEE-2 final data base frames

Variable	Description
<b>Header Records</b>	
iy	Year
id	Day of year
model	Number of internal magnetic field model (from BLXTRA NAMELIST)
mmoflg	Flag for $B$ value at Earth surface (from BLXTRA NAMELIST) 0: $M = 0.311653$ 1: $M = M(\text{epoch})$
outer	Number of external magnetic field model (from BLXTRA NAMELIST)
<b>Data Records</b>	
ih	Hours
im	Minutes
sec	Seconds
dlonm	Longitude (deg)
dlatm	Latitude (deg)
radim	Radius ( $R_E$ )
bm	Measured magnetic field strength (nT)
flux	Flux for 18 pitch angles ( $0^\circ$ – $10^\circ$ , $10^\circ$ – $20^\circ$ , ..., $170^\circ$ – $180^\circ$ )
spec	normalized spin-averaged energy spectra for 12 energy ranges (keV): 17.5–28.0, 28.0–37.6, 47.6–61.5, 61.5–79.5, 79.5–103.5, 103.5–133.1, 133.1–172.5, 172.5–223.3, 223.3–289.5, 289.5–480.5, 480.4–801.0, 801.0–1000.0
iokp	Fitted $K_p$
value_kp	$K_p$ (from OMNI data base)
oni	Density of solar wind (from OMNI data base)
ofs	Velocity of solar wind (from OMNI data base)
iodst	$D_{st}$
b	Model magnetic field strength (from BLXTRA)
ly	Local time, year
ldy	Local time, day of year
lh	Local time, hours
lm	Local time, minutes
ls	Local time, seconds

**Table 8.3.** (Continued)

Variable	Description
bmir	$B_m$ For 9 pitch angles (from BLXTRA): $0^\circ$ – $10^\circ$ , $10^\circ$ – $20^\circ$ , ..., $70^\circ$ – $80^\circ$ , $80^\circ$ – $90^\circ$
lval	$L$ Values for 9 pitch angles (from BLXTRA): $0^\circ$ – $10^\circ$ , $10^\circ$ – $20^\circ$ , ..., $70^\circ$ – $80^\circ$ , $80^\circ$ – $90^\circ$
inlat	Invariant latitude (deg)
qf	Quality flag (see Table 8.4)
wb	WAPS Back detector flux
wk	WAPS Coincidence flux

**Table 8.4.** Values of the one-byte quality flag in the ISEE-2 data files

Bit number	Meaning
no bit set	Valid data point, no problems
bit 0	Local magnetic field measurement differs from model by more than 5%
bit 1	Local magnetic field measurement differs from model by more than 10%
bit 2	Local magnetic field measurement differs from model by more than 20%
bit 3	Local magnetic field measurement differs from model by more than 50%
bit 4	Local magnetic field measurement differs from model by more than 100%
bit 5	Flux below magnetospheric threshold (on open field lines): spin averaged flux $< 1.2 \times 10^5 \text{ cm}^{-2} \text{ s}^{-1} \text{ sr}^{-1} \text{ keV}^{-1}$
bit 6	No spectral data, integral flux only

model to within 5% of the measured data. Using the Tsyganenko 1989 model with the  $K_p$  value adjusted to the published value for the period in question raises the percentage to 76%, while the best results were achieved using the Tsyganenko 1989 with a self-adjusting  $K_p$  (iteratively chosen to minimize the error). This pseudo  $K_p$  has a much more dynamic behaviour than the real  $K_p$ , although the general trend of the real  $K_p$  is followed. This is due to the local nature of the measurement which is scaled using a global parameter.

For the TREND-3 project, the choice of magnetic field model is the Olson & Pfitzer (1977) quiet time model which has no input parameters besides position and time. Using this model, the ISEE-2 data base of energetic electron data was extended by a one byte parameter which serves as a quality flag (see Table 8.4). A comparison of the measured and calculated magnetic

field is given in Technical Note 1.

## 8.4 Flux maps

The flux data have been binned in an  $(E, L, \alpha_0)$  grid with the same grid spacings in  $L$  and  $\alpha_0$  as were used for the CRRES/MEA flux maps. The energy bin limits are (in keV): 17.5–28.0, 28.0–37.6, 47.6–61.5, 61.5–79.5, 79.5–103.5, 103.5–133.1, 133.1–172.5, 172.5–223.3, 223.3–289.5, 289.5–480.5, 480.4–801.0, 801.0–1000.0. The corresponding central energies are (in keV): 22.75, 32.8, 54.55, 70.5, 91.5, 118.3, 152.8, 197.9, 256.4, 385.0, 640.7, 900.5.

The flux maps constitute a new electron belt model, called EIM97. Five versions of the model were created, one each for the  $K_p$  ranges 0 to  $1^+$ , 2 to  $3^+$ , 4 to  $5^+$ , and 6 to  $7^+$ , and one for all  $K_p$  values combined. The corresponding flux maps have been converted to the format described in Sect. 2.1.6 and added to TREP.

Figures 8.8–8.11 show some examples of the final ISEE flux maps. The programs used to produce these plots are described in Technical Note 1. The left hand panel in each plot shows the number of data points in each bin, and the right hand panel shows the average flux in the bins. The plots show the inner and outer radiation belts and some significant fluxes at higher  $L$  values. These plots are only a preliminary result.

Figure 8.8 shows a flux map binned with all available data from 1977 day 307 up to 1987 day 61, over the total energy range. Figure 8.9 is similar to Fig. 8.8, but the flux map only contains data with spectral information and with a good agreement between measured magnetic field data and model magnetic data. Figures 8.10 and 8.11 show the same flux maps for energy bins 1 and 2, respectively.

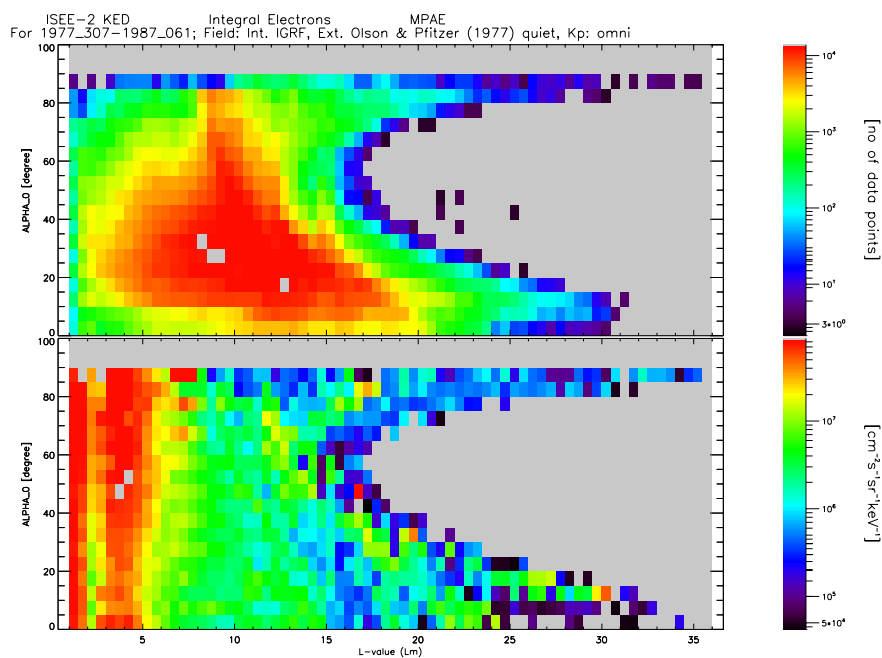


**Figure 8.8.** ISEE Electron flux map for all energies obtained with all data from 1977 day 307 up to 1987 day 61

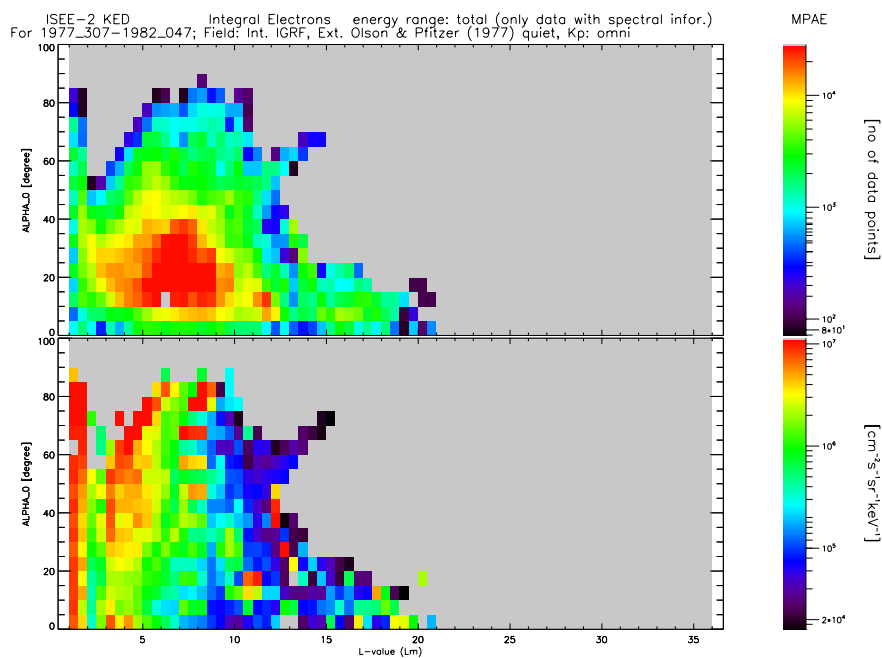


**Figure 8.9.** ISEE Electron flux map for all energies obtained with the data from 1977 day 307 up to 1982 day 47 that contain spectrum information

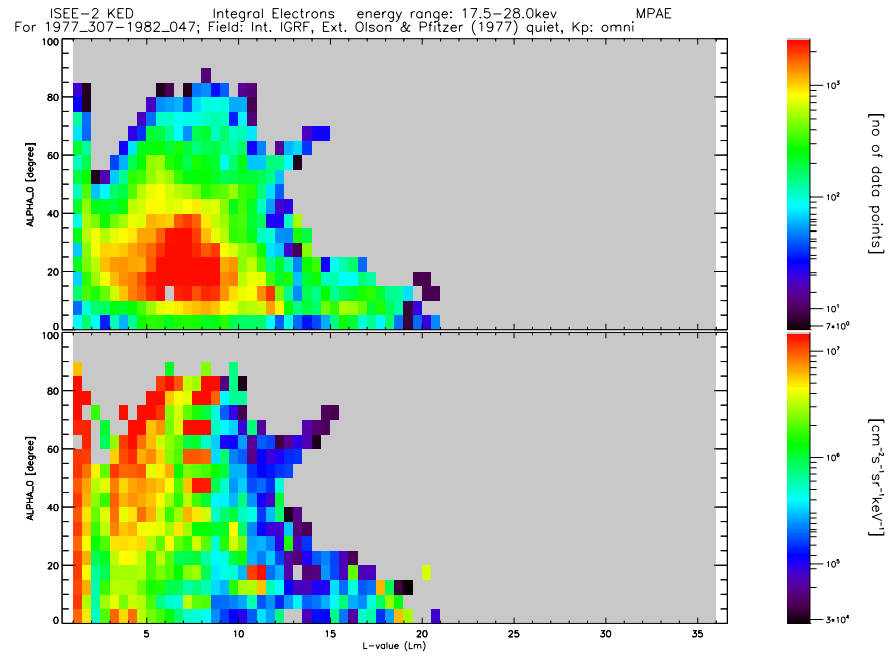


**Figure 8.10.** ISEE Electron flux map for energy range 17.5–28.0 keV obtained with the data from 1977 day 307 up to 1982 day 47 that contain spectrum information

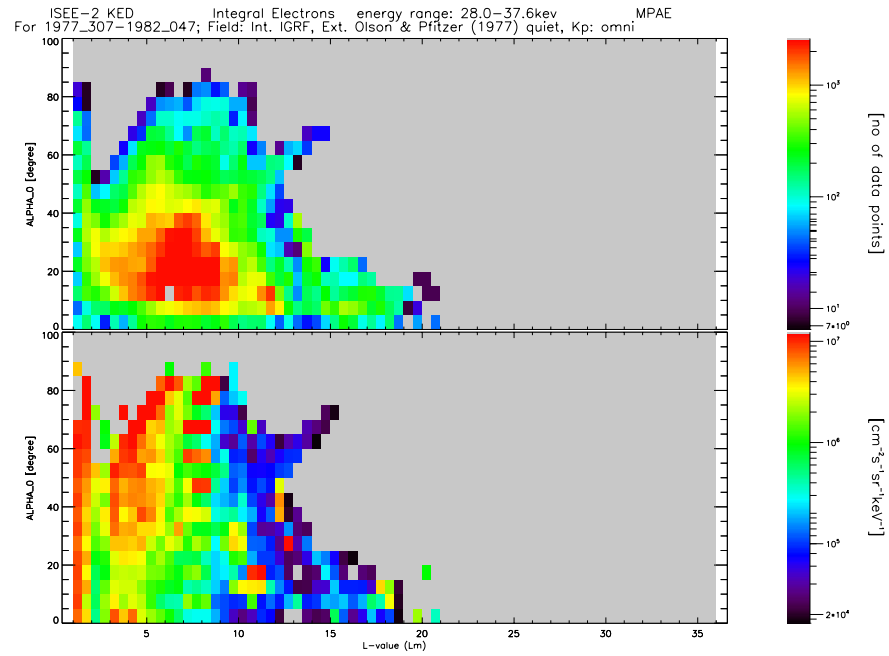


**Figure 8.11.** ISEE Electron flux map for energy range 28.0–37.6 keV obtained with the data from 1977 day 307 up to 1982 day 47 that contain spectrum information





# Chapter 9

## The CRRES/MEA data base and radiation belt model

The CRRES mission and its instrumentation have been described in Technical Note 4 of the TREND-2 study (Heynderickx & Lemaire 1992). A first study of the Medium Energy Analyzer (MEA) data was performed in TREND-2 (Rodgers 1996, Lemaire et al. 1995).

### 9.1 Introduction

The CRRES/MEA data (Vampola et al. 1992) instrument has provided information on energetic electrons throughout the inner and outer belts of the magnetosphere. Its high time resolution, good pitch angle and energy resolution and continuous data coverage has made its data extremely useful for studying the Earth's radiation environment. This chapter describes the use made of the MEA data in the TREND-3 study, i.e. the creation of a new radiation belt model.

### 9.2 Creation of an improved database

In the TREND-2 study (Lemaire et al. 1995), it was found that processing the MEA data from supplied data files was prohibitively time consuming. Frequent passes through the same data have to be made in performing statistical analysis and recalculating derived parameters, such as  $B$  and  $L$ , for each data point in each pass was prohibitively slow. Hence a reduced database of the available data was made with a number of new parameters added. This was very effective and the compact database was used in a study of different coordinate systems for use in radiation belt modelling. The MEA data analysis in the TREND-2 study was principally concerned with the outer belt. However, it was realised in that study, that the data could be used to study the inner belt too.

There were a number of reasons why the database produced in TREND-2 was not good enough for use in the TREND-3 study:

- Foldover: no correction was made for the depressed count rates in the inner belt, caused by excessively high fluxes.
- Time resolution: the 5 minute time resolution was appropriate for the outer belt, when the satellite moves slowly, but led to smearing of the data and consequently high standard deviations in the inner belt.
- Pitch angle resolution: the pitch angle resolution at  $10^\circ$  had been found in TREND-2 to be quite coarse. This proved to be particularly important since one of the ordering parameters selected for the new model depended on the magnetic field at the mirror point and this field is a sensitive function of pitch angle.
- Data coverage: only a third of all the data were in the database.

The new database is a compromise, trying to accurately represent the data while making large reductions in its size and speeding up data processing. The entire database is 0.8 Gb and fits comfortably onto a DAT tape or two magneto-optical disk sides. It is about 10 times larger than the TREND-2 database.

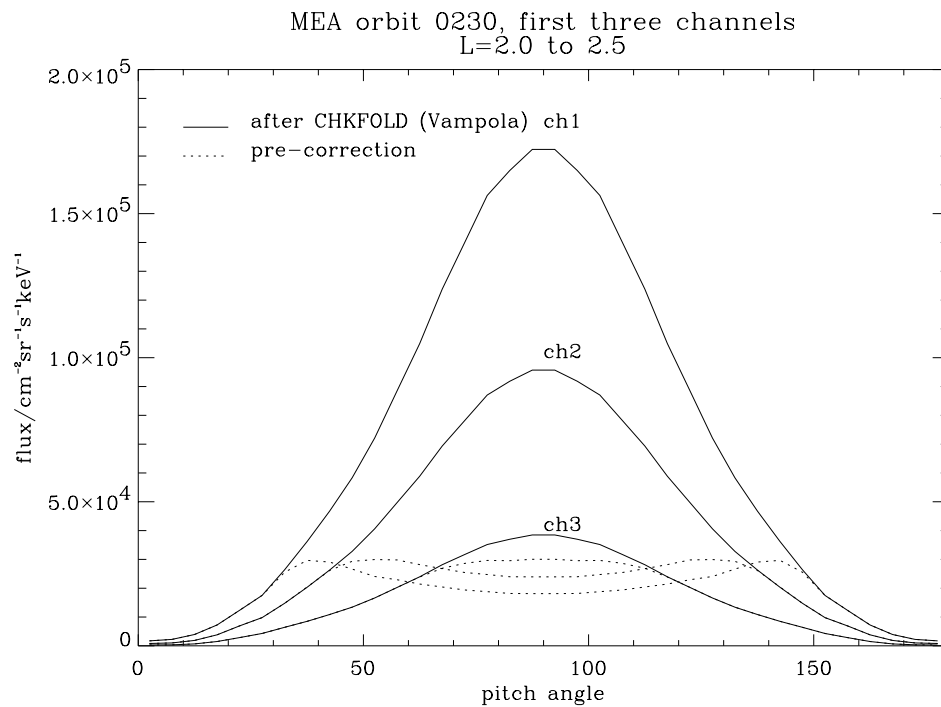


**Figure 9.1.** MEA Fluxes before and after the foldover correction in the three lowest energy channels, plotted against pitch angle

**Table 9.1.** Definitions of the parameters in the new MEA data base

Parameter	Data type	Array length	Content
year	INTEGER*4	1	Year (since 1900)
doy	INTEGER*4	1	Day of year at start of orbit
it	INTEGER*4	1	Minutes of day
agll	REAL*4	1	PLGD Calculation of $L$
aglb	REAL*4	1	PLGD Calculation of $B$
aglb0	REAL*4	1	PLGD Calculation of $B_0$
along	REAL*4	1	Longitude
alat	REAL*4	1	Latitude
aalt	REAL*4	1	Altitude (km)
ablb	REAL*4	1	BLXTRA Calculation of $B$
ablb0	REAL*4	1	BLXTRA Calculation of $B_0$
aloc	REAL*4	1	Local time
aglbm	REAL*4	18	Mirror field based on PLGD calculation
aglalpha0	REAL*4	18	Equatorial pitch angle based on PLGD calculation
ablbm	REAL*4	18	Mirror field based on BLXTRA calculation
ablalpha0	REAL*4	18	Equatorial pitch angle based on BLXTRA calculation
abllm	REAL*4	18	BLXTRA Calculation of $L$
aflux	REAL*4	18,18	Flux as function of pitch angle and energy

### 9.2.1 Vampola's foldover correction

The MEA was fully calibrated on the ground but it appears that count rates in space were higher than expected. As with all counting instruments, dead-time effects become significant when count rates are high. Usually this effect is taken out by the calibration. However, above a critical count rate further counts lead to a decrease in measured counts. This can only be inferred because it causes a dip in pitch angle near  $90^\circ$  when a peak is expected. It is a problem only for the lowest four energy bins because fluxes in the higher energy bins are never too high. In the TREND-2 study, this problem was avoided by considering chiefly the outer radiation belt where fluxes at all energies remain below the critical threshold.

In this study, we have made use of a correction algorithm provided by Vampola. This makes the assumption that the ratio of fluxes at two energies at a certain pitch angle when flux levels are below the threshold for counts saturation is a good approximation of the same ratio when flux levels exceed this threshold.

While the flux is below the critical value (about 45,000 counts per 0.512 s sample period), continuous monitoring takes place of the flux ratio between the bottom 5 energy bins. These ratios are stored as a list. If flux in one of these bins exceeds the critical value, then the data

are assumed suspect in that bin and in the ones of lower energy. Using the lowest energy with flux below the critical flux, the fluxes are propagated down to lower energy, using the latest list of ratios. It is clear that over extended periods of foldover the actual pitch angle fluxes could change but this effect is likely to be small compared to the foldover itself. Figure 9.1 compares corrected and uncorrected fluxes for four energies during a typical inner radiation belt measurement. The foldover correction clearly has a large effect on the data.

### 9.2.2 Changes to resolution and format

The time resolution was set to 1 minute. This makes the maximum change in  $L$  over the binning period, near perigee, about  $0.1 R_E$ . The date was added to each data record. Previously it had to be inferred from the orbit number which formed part of the file name. The pitch angle, which previously had values from  $0^\circ$  to  $180^\circ$  in  $10^\circ$  increments, now takes values from  $0^\circ$  to  $90^\circ$  in  $5^\circ$  increments. Hence, the new pitch angle resolution is higher but we have lost the ability to distinguish whether particles are travelling up or down a field line. The new data format is defined by the following Fortran statement:

```

      write (outunit)
&   year, doy, it, agll, aglb, aglb0, along, alat, aalt,
&   ablb, ablb0, aloct, aglbm, aglalpha0, ablbm, ablalpha0,
&   abllm, aflux

```

The definitions of the parameters are given in Table 9.1.

## 9.3 Data analysis

### 9.3.1 Characteristics of the radiation belts

Because it covers the radiation belts in terms of energy,  $L$  and pitch angle, CRRES/MEA data can provide a comprehensive overview of this region. Figure 9.2 shows equatorially mirroring fluxes as a function of  $L$  for four different  $K_p$  ranges at 153 keV. At these low energies, fluxes are highest in the inner belt. The effect of increasing  $K_p$  is a small decrease in inner radiation belt fluxes and a large increase in outer radiation belt fluxes. At higher energies (as shown in Fig. 9.3), there is an increase in flux in both inner and outer belts. The most striking effect is the filling of the slot region.

### 9.3.2 Time lag correlation analysis

Correlation analysis was used in TREND-2 on Meteosat-3 and GOES-7 data. We have extended this analysis to the CRRES/MEA data. However, because CRRES is not geostationary and has full angular resolution, more comparisons can be made. The interpretation is more difficult,

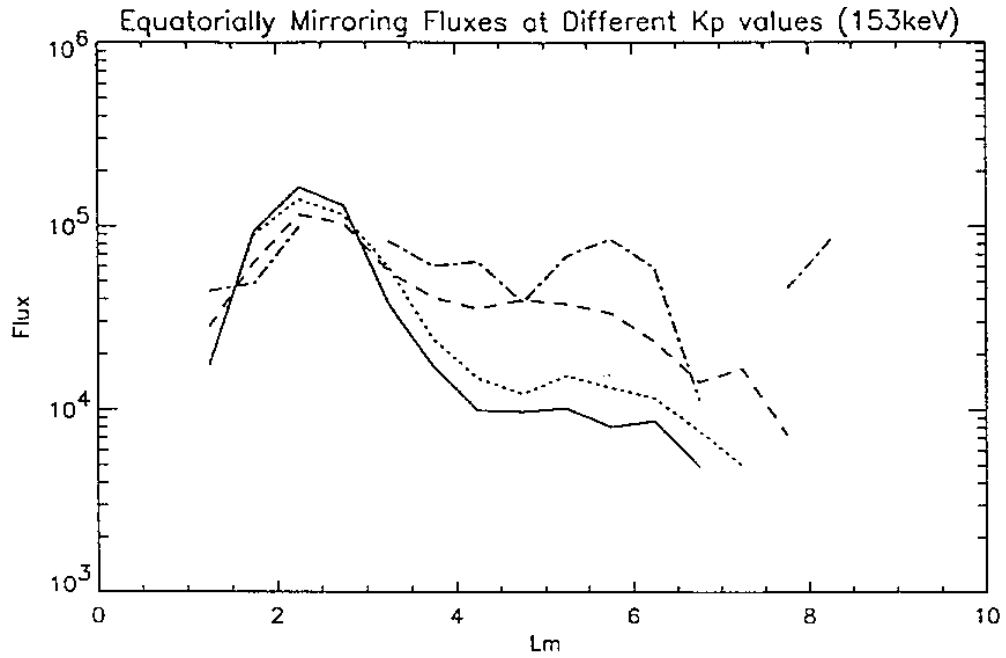


**Figure 9.2.** Equatorially mirroring flux as a function of  $L$  at 153 keV. Solid line:  $K_p \leq 1$ , dotted line:  $1 < K_p \leq 3$ , dashed line:  $3 < K_p \leq 5$ , dash-dotted line:  $5 < K_p \leq 7$ .

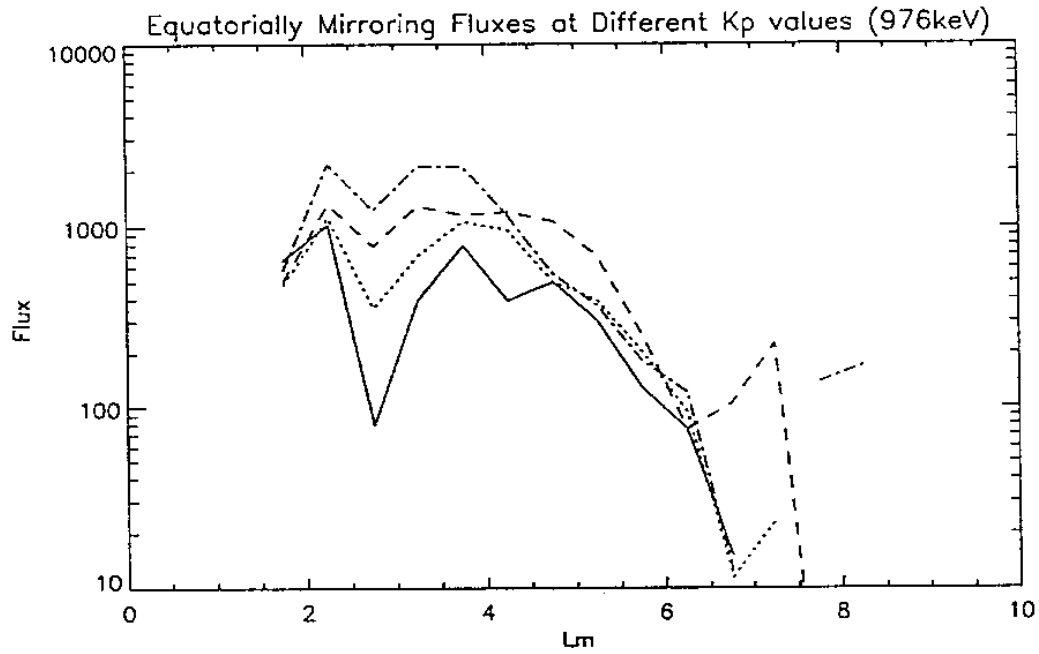


**Figure 9.3.** Equatorially mirroring flux as a function of  $L$  at 976 keV. Solid line:  $K_p \leq 1$ , dotted line:  $1 < K_p \leq 3$ , dashed line:  $3 < K_p \leq 5$ , dash-dotted line:  $5 < K_p \leq 7$ .

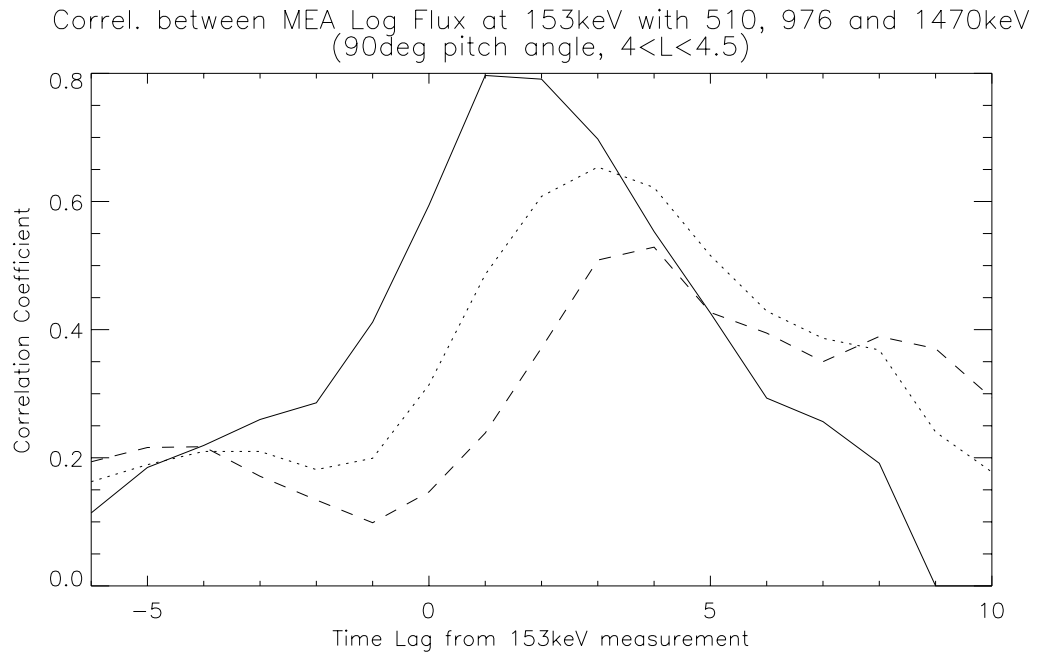


**Figure 9.4.** Time delayed correlation coefficients for fluxes at  $L = 4.0-4.5$  comparing 153 keV and 510 keV (solid line), 153 keV and 976 keV (dotted line), and 153 keV and 1470 keV (dashed line)

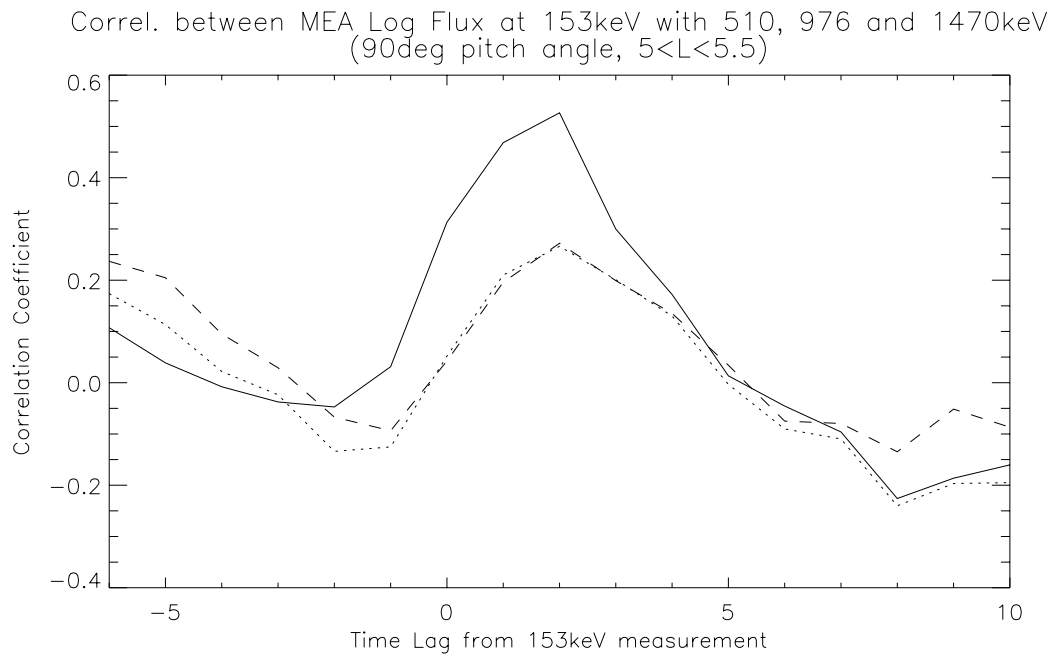


**Figure 9.5.** Time delayed correlation coefficients for fluxes at  $L = 5.0-5.5$  comparing 153 keV and 510 keV (solid line), 153 keV and 976 keV (dotted line), and 153 keV and 1470 keV (dashed line)

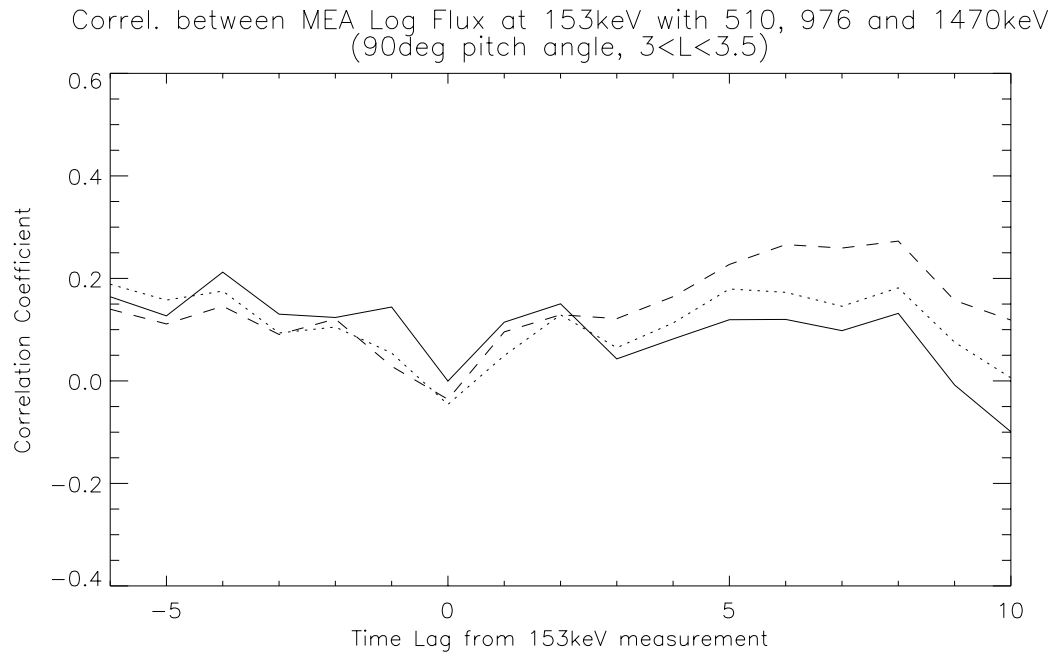


**Figure 9.6.** Time delayed correlation coefficients for fluxes at  $L = 3.0\text{--}3.5$  comparing 153 keV and 510 keV (solid line), 153 keV and 976 keV (dotted line), and 153 keV and 1470 keV (dashed line)

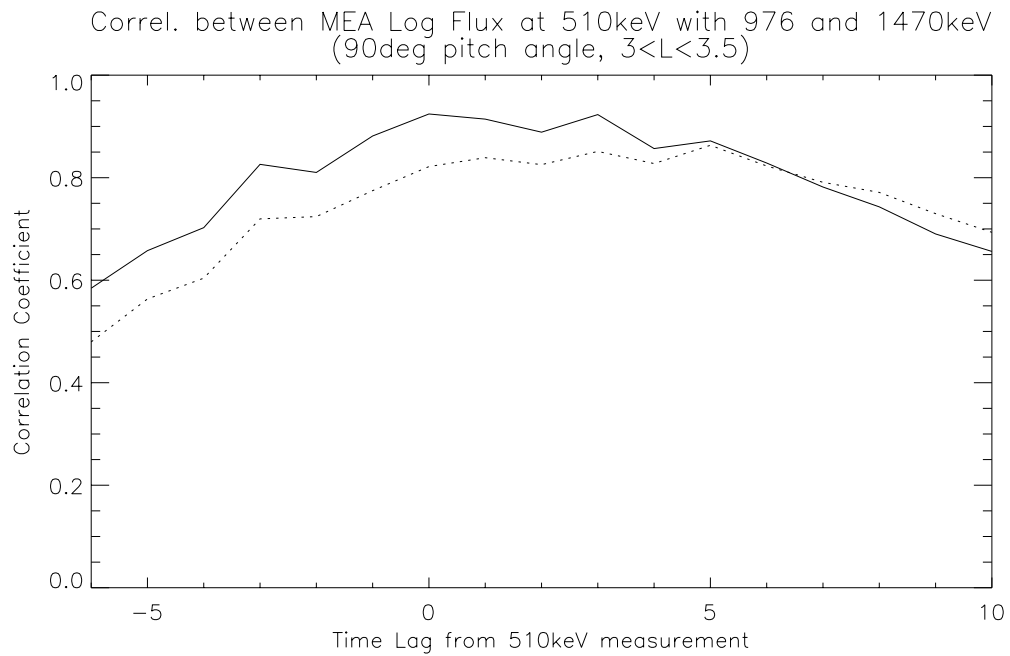


**Figure 9.7.** Time delayed correlation coefficients for fluxes at  $L = 3.0\text{--}3.5$  comparing 510 keV and 976 keV (solid line), and 510 keV and 1470 keV (dotted line)

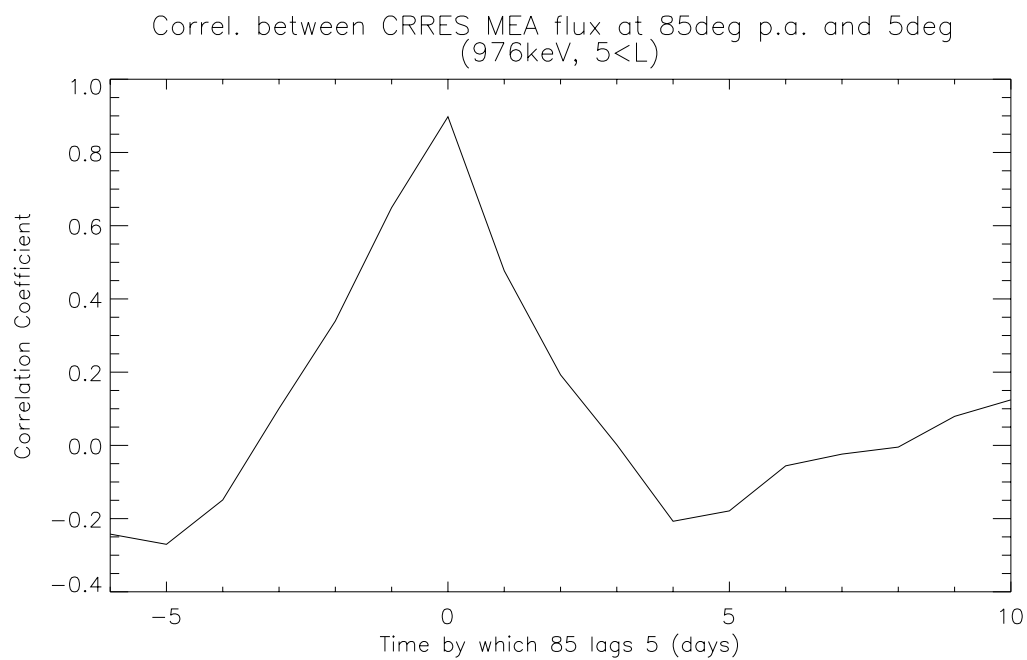


**Figure 9.8.** Correlation coefficient between  $80^{\circ}$ – $90^{\circ}$  fluxes and  $0^{\circ}$ – $10^{\circ}$  fluxes

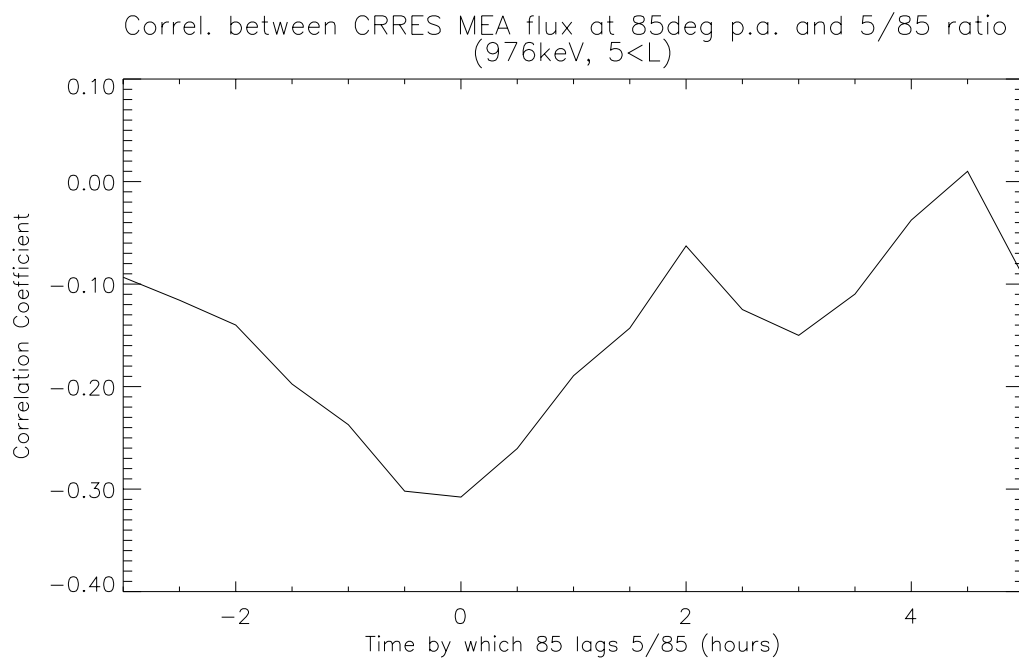


**Figure 9.9.** Correlation coefficient between  $80^{\circ}$ – $90^{\circ}$  fluxes and the ratio of fluxes at  $0^{\circ}$ – $10^{\circ}$  and  $80^{\circ}$ – $90^{\circ}$



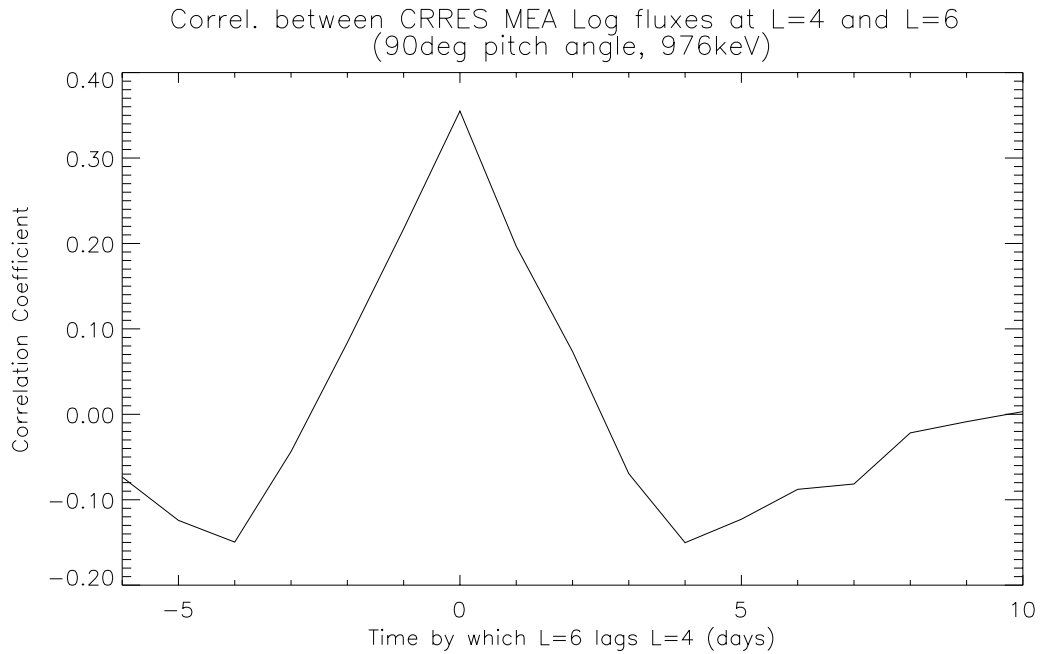


**Figure 9.10.** Correlation coefficient between 976 keV, 80°–90° fluxes at  $L = 4$  and  $L = 6$

however, because the flux observed by CRRES is continuously varying because of its orbital motion. By comparing fluxes at different energies,  $L$  values, and pitch angles, it is possible to tell the sequence of flux rises in the radiation belts. These can be used to support theories of the creation of the radiation belts, but the absence of expected correlations may just mean that other variations are more significant. For instance, it is possible that the magnetosphere undergoes compression and expansion which result in adiabatic heating and cooling as well as  $L$  and pitch angle changes but which return the radiation belts to their original state. Such events may swamp out source events. The use of log fluxes in this analysis prevents the results being dominated by just the highest flux events.

### 9.3.2.1 Energy correlation

Figure 9.4 shows the correlation coefficient achieved by comparing fluxes at 153 keV and 510 keV in the outer radiation belt between  $L = 4.0$  and  $L = 4.5$ . This shows that higher energy fluxes are associated with the lower energy fluxes after a time delay of about 1.5 days. Comparing 976 keV and 153 keV gives a time delay of 3 days. For 1470 keV and 153 keV the delay is almost 5 days. This result confirms observations from Meteosat-3 and GOES at geostationary orbit and is in broad agreement with the predictions of the recirculation process.

The  $L = 4.0$ – $4.5$  band was initially studied because it covered the centre of the outer radiation belt. However, the results obtained in other  $L$  ranges were not the same and were harder to fit into the recirculation picture. Between  $L = 5.0$  and  $5.5$ , there was a 2-day delay between 153 keV and 510 keV fluxes but no further lag between 510 keV and higher energies (see

Fig. 9.5).

Between  $L = 3.0$  and  $3.5$ , comparing 153 keV with energies 510 keV and over produced only low correlation levels (see Fig. 9.6), indicating that there was little correlation between the datasets. In the same  $L$  range there was a high correlation between flux at energies 510 keV to 1470 keV (Fig. 9.7). However, the peak was very broad. This indicates that these energies rise and fall together in a characteristic period which is too long for a short lag to be observed.

### 9.3.2.2 Pitch angle correlation

We have examined the correlation between field-aligned and perpendicular fluxes. Such a study could in principle distinguish between an internal plasma source (such as the recirculation process) and an external source (such as the entry of Jovian electrons from the interplanetary medium). In recirculation, energized particles enter the outer magnetosphere at small pitch angles and then isotropize. In the Jovian process, electrons enter at high  $L$  values and pitch angle diffuse to lower  $L$ . This would result in flux increases occurring first at  $90^\circ$  and then at lower pitch angle.

The cross-correlation analysis, using daily averages is plotted in Fig. 9.8. This shows that the peak correlation coefficient occurred at zero days time lag. This implies that if there is a time delay between pitch angles it is significantly smaller than 1 day. Williams et al. (1968) observed that fluxes at  $> 300$  keV took under 2 hours to isotropize after becoming pancaked. We are looking for diffusion in the opposite direction, nevertheless the same sort of processes are responsible. Williams et al. (1968) inferred, however, that at higher radiation belt energies diffusion should take considerably longer. Going to higher time resolution is very difficult because of the motion of the spacecraft through the magnetosphere. Figure 9.9 shows the correlation coefficient between flux in the  $80^\circ$ – $90^\circ$  bin with the ratio of fluxes at  $0^\circ$ – $10^\circ$  and  $80^\circ$ – $90^\circ$ . Taking this ratio removes the effect on the  $0^\circ$ – $10^\circ$  fluxes of the change due to the spacecraft's progression in its orbit. Data from  $L > 5$  was chosen so that the spacecraft velocity was slower in order to minimize orbital effects on the total flux. The correlation coefficient was negative at zero time lag as one would expect. However, no significant positive correlation was observed at any time lag.

The reason for this result appears to be that the fluxes at  $5^\circ$  and  $85^\circ$  pitch angles are very strongly correlated and the  $5^\circ/85^\circ$  ratio is very nearly constant. The comparison of the varying flux with this constant yields a low correlation. Hence there is no evidence of strong pitch angle differences on this time scale.

### 9.3.2.3 $L$ Correlation

Another prediction of recirculation is that flux increases in a particular energy range should be seen first at low  $L$  values and later at higher ones. Figure 9.10 shows the correlation coefficient between fluxes at  $L = 4$  and  $L = 6$ . It appears that the time delay between flux rises and falls at these different positions is much less than 1 day. In general, it appears that the outer radiation belt fluxes at 1 MeV rise as one. However, when comparing outer radiation belt fluxes

**Table 9.2.**  $A_{p15}$  Ranges used for the new MEA model

Range no.	$A_{p15}$ Range
0	5.0–7.5
1	7.5–10.0
2	10.0–12.5
3	12.5–15.0
4	15.0–20.0
5	20.0–25.0
6	25.0–35.0
7	35.0–55.0

with fluxes in the inner belt or the slot, there is no period with significantly higher correlation coefficient than another.

## 9.4 An $A_{p15}$ dependent electron model based on MEA data

Brautigam et al. (1992) described a quasi-static model of the outer electron belt. In this model, electron fluxes from the HEEF instrument were summed into  $L$  bins and it was assumed that fluxes could be treated as isotropic. The authors justified this assumption by showing that fluxes in the ranges  $45^\circ$ – $65^\circ$  and  $65^\circ$ – $90^\circ$  did not deviate far from equality. It should be noted however, that this test avoided the loss cone by a wide margin. They also paid no apparent regard to  $B/B_0$  or an equivalent parameter to describe the distance of the measurement from the magnetic equator. The satellite spent much of its time near the magnetic equator but there will inevitably be a reduction in the accuracy of the model by ignoring variation along a field line.

The magnetic activity was represented by a 15-day summation of  $A_p$ . It had been found that this average, delayed by 1 day, correlated well with observed fluxes. This averaged, delayed index was named  $A_{p15}$ . Eight different values of  $A_{p15}$  were used to create an activity dependent model. In this study, the  $A_{p15}$  index was recreated using  $A_p$  data obtained from the NSSDC OMNI database. MEA Data from a subset of the new data base were binned in  $L$  and the same 8  $A_{p15}$  ranges (listed in Table 9.2) as the PLGD model.

There were no data in our data subset that fell into the lowest  $A_{p15}$  range. Flux profiles for all 17 energy levels were obtained. Figure 9.11 shows results for the seven occupied  $A_{p15}$  ranges at 510 keV. At low  $A_{p15}$  there is a deep slot region. As activity increases, the slot fills in and flux in the outer belt rises as was observed in Sect. 9.3.1.

The flux at 1470 keV is represented in Fig. 9.12. This plot is comparable with the lowest energy channel of Brautigam et al. (1992), 1.55 MeV, whose data are plotted in Fig. 5 of their

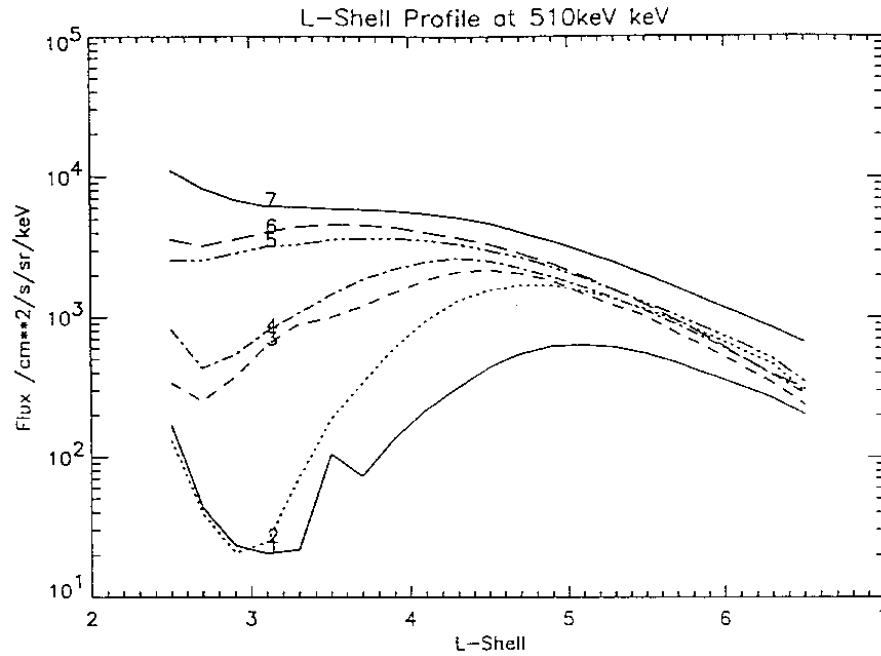


**Figure 9.11.** 510 keV Flux versus  $L$  for 7 ranges of  $A_{p15}$ . The zeroth range had no data and is not plotted; range 1: solid line, 2: line, 3: dashed line, 4: dot-dashed, 5: dash-triple-dotted, 6: long dashed, 8: solid.

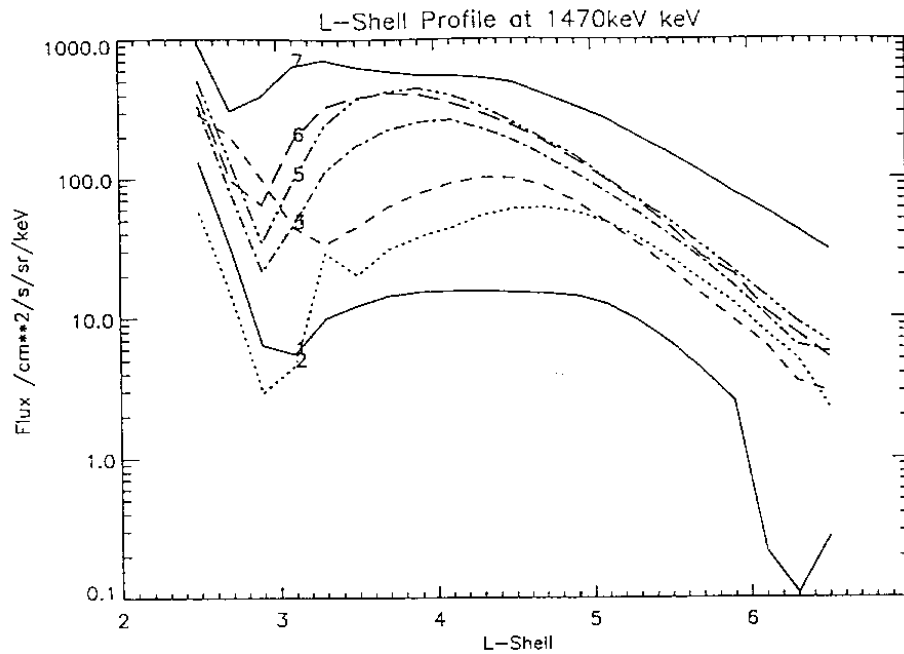


**Figure 9.12.** 1470 keV Flux versus  $L$  for 7 ranges of  $A_{p15}$ . The zeroth range had no data and is not plotted; range 1: solid line, 2: line, 3: dashed line, 4: dot-dashed, 5: dash-triple-dotted, 6: long dashed, 8: solid.

paper. As was noted there, when activity increases, flux increases and peaks at lower  $L$ . There is good agreement between the position and height of the peaks between the MEA data and the PLGD model. Compared to the lower energies, the filling in of the slot is more gradual but the increase in outer belt fluxes is stronger.

## 9.5 The ECM97 model

Based on the results of the TREND-2 study, the  $(L, \alpha_0)$  coordinates were chosen for a new radiation belt model because this:

1. produced a high degree of systematic organization in the fluxes;
2. had reasonably low standard deviation in the outer zone;
3. was easy to visualize;
4. did not exaggerate the pitch angle resolution of the data near the loss cone;
5. and achieved adequate coverage of both inner and outer belts without changing bin sizes between the two zones.

The Tsyganenko (1989)  $K_p$  dependent external magnetic field model was used along with an internal DGRF model field. The BLXTRA software (Heynderickx et al. 1996d) was used to access the field models and calculate  $B$  and  $L$ . Separate flux maps in this coordinate system were created for each energy.

### 9.5.1 Statistical variation

In processing the flux map, the average fluxes were found, along with the standard deviation. Because it was based on the new database, with higher time resolution and corrected fluxes at low altitudes, the new model was expected to be valid in the inner radiation belts. The improved time and pitch angle resolution was expected also to lead to improved performance in the outer belt.

As in TREND-2, we used the standard deviation when  $K_p \leq 1$  as a measure of how well the coordinate system organizes the data because at these times natural flux variations are expected to be low. A lower ratio of standard deviation to mean is evidence that similar flux values are summed in the same  $(L, \alpha_0)$  bins. Figure 9.13 shows the standard deviation ( $K_p \leq 1$ ) for the TREND-2 data at 510 keV and Fig. 9.14 shows the standard deviation at the same energy for the current study. In order to make a comparison possible, the same  $\alpha_0$  and  $L$  bin sizes as the TREND-2 model have been used and the TREND-3 standard deviations have been divided by  $\sqrt{5}$  to account for the 5 times higher time resolution. The new data displays a number of improvements over the TREND-2 data. Unlike the earlier data base, the new one has low standard deviation throughout the outer belt. Low standard deviation has been extended across

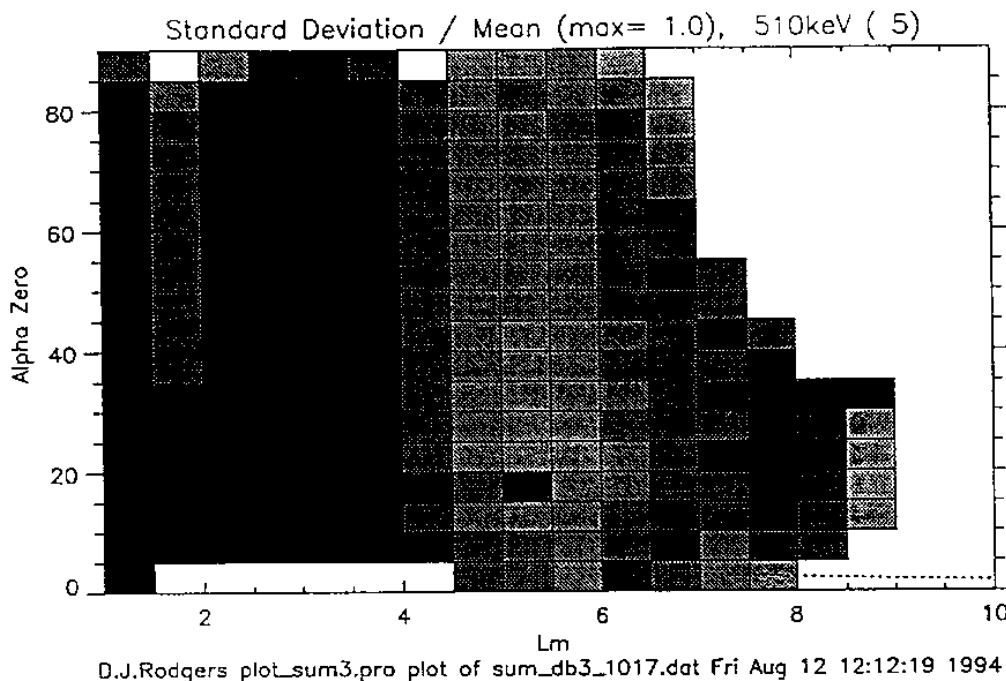


**Figure 9.13.** Greyscale plot of 510 keV standard deviation binned in  $(L, \alpha_0)$  space. The dotted line represents the loss cone. Data from the TREND-2 data base were used.

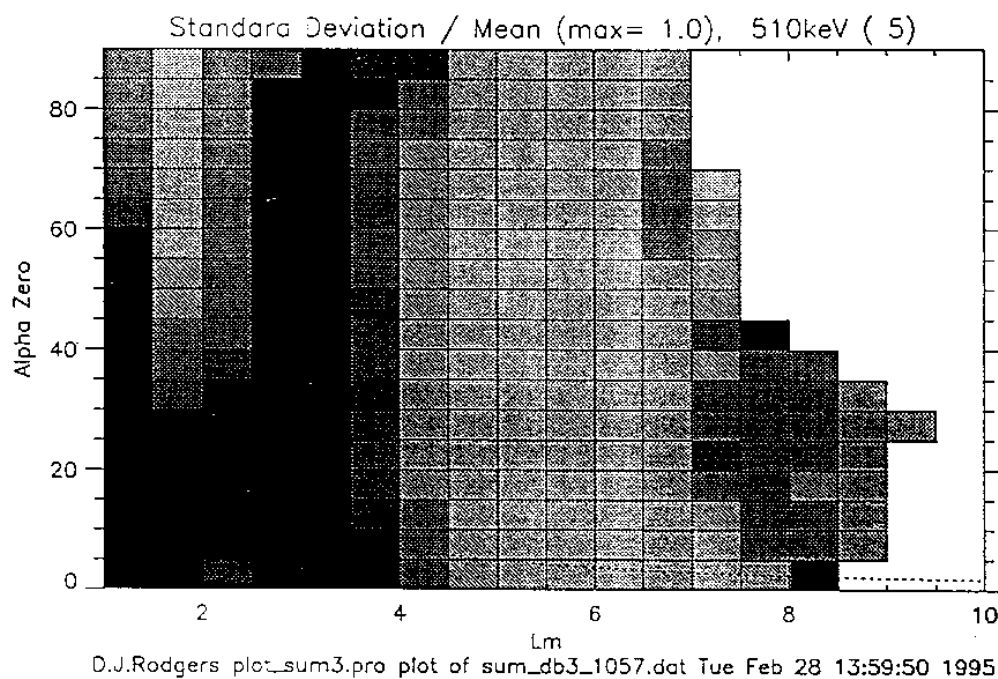


**Figure 9.14.** Greyscale plot of 510 keV standard deviation binned in  $(L, \alpha_0)$  space. The dotted line represents the loss cone. Data from the TREND-3 data base were used.

almost the entire inner belt. However, standard deviations remain high in the slot region and in the loss cone. This is not unexpected since these regions have low fluxes and are highly variable. Hence, the combination of the new data base and the  $(L, \alpha_0)$  coordinate system can create a model that is useful in both the outer and inner belts.

At low energies, in the outer belt, the standard deviation is affected by the efficiency of the binning system and by natural variations in the plasma. At higher energy and in the inner belt, the subtracted background dominates the statistics to varying degrees, depending on energy. Hence a comprehensive energy dependent variance model to complement the model of mean fluxes is not possible.

### 9.5.2 Contamination

Figure 9.20 shows fluxes at 976 keV. There is some flux measured in the loss cone in the inner and outer belts. Since fluxes were expected to be almost non-existent in this region, it was initially thought that this might represent residual noise that was not removed by MEA's on-board noise rejection.

An investigation was carried out into these loss-cone fluxes. Figure 9.15 shows equatorially field aligned flux versus  $L$  in four energy ranges. At all energies there are significant fluxes. If contamination from penetrating radiation were the cause, then the flux in each energy should correspond to the same count rate in the raw data, since the size of the each anode is about the same. Back-calculating the counts from the flux results in the counts shown in Fig. 9.16. Because it is not possible to reverse the effect of the foldover correction, the values in the inner belt are not correct. In the outer belt it is clear that there is not a constant count rate at each energy. This makes contamination unlikely to be the cause.

Further evidence for this is given by a comparison between loss cone fluxes and energetic protons, the most probable source of any contamination. Figure 9.17 shows the time variation of 976 keV flux over a period of 2 months at  $L = 4$ . Figure 9.18 shows the 3 MeV proton flux over the same period, using data taken from the CRRES Science Summary Data Base. There is no similarity. Figure 9.19 shows the 1 MeV electron data from the same database. This shows the behaviour of all electrons, not just those in the loss cone. The similarity to the loss cone flux is very strong, indicating that the loss cone flux rises and falls along with the rest of the electrons. Hence, contamination is not responsible in this case.

The loss cone in the outer belt is only  $6^\circ$  at  $L = 4.5$ , the heart of the outer belt. Inaccuracies in pitch angle measurements could have the effect of moving electrons apparently into the loss cone. However, this explanation does not work for the inner belts, where the loss cone is around  $20^\circ$ .

### 9.5.3 $(L, \alpha_0)$ Binning

To create the new model, flux maps were created by binning data from approximately 900 CRRES orbits with  $L$  resolution 0.2, an improvement in resolution from the model created in

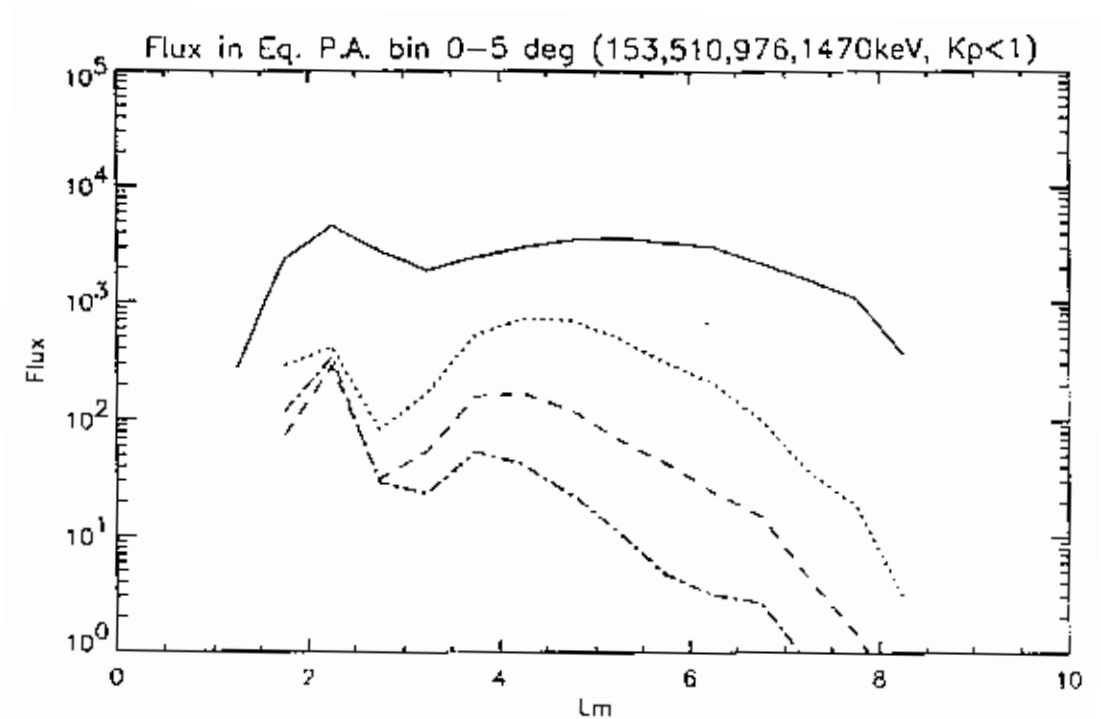


**Figure 9.15.** Fluxes in  $0^{\circ}$ – $10^{\circ}$  equatorial pitch angle bin for energies 153, 510, 976 and 1470 keV

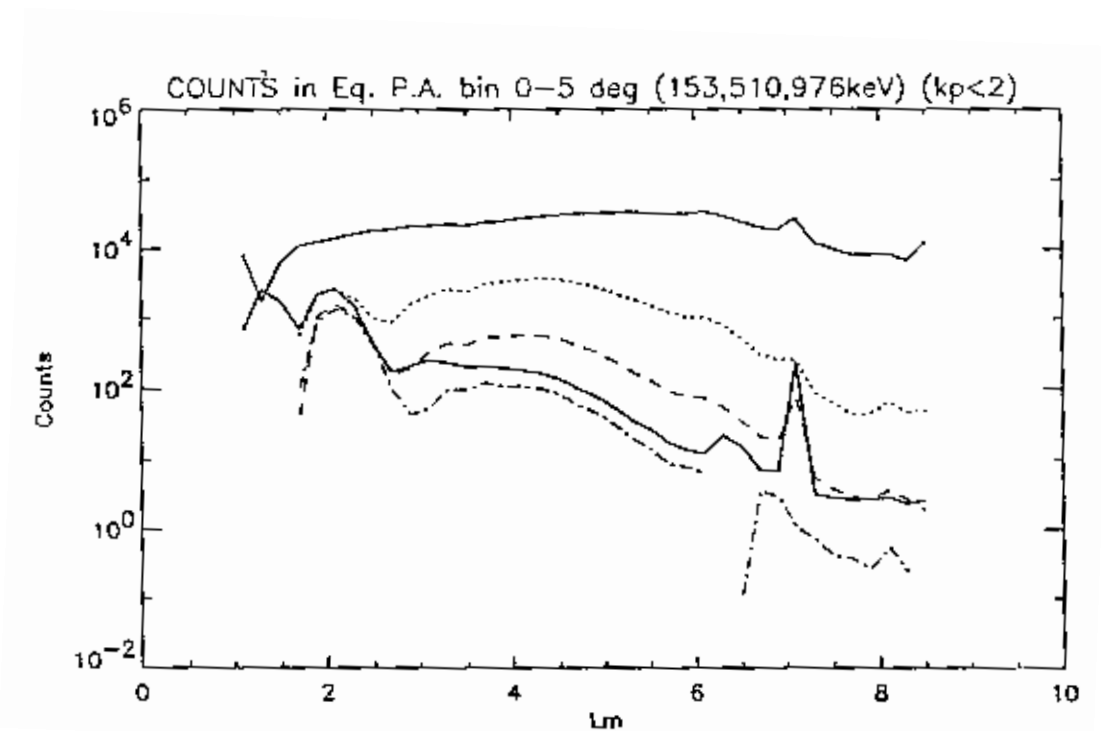


**Figure 9.16.** Back-calculated counts in  $0^{\circ}$ – $10^{\circ}$  equatorial pitch angle bin for energies 153, 510, 976 and 1470 keV. The background channel is shown by a thicker solid line.



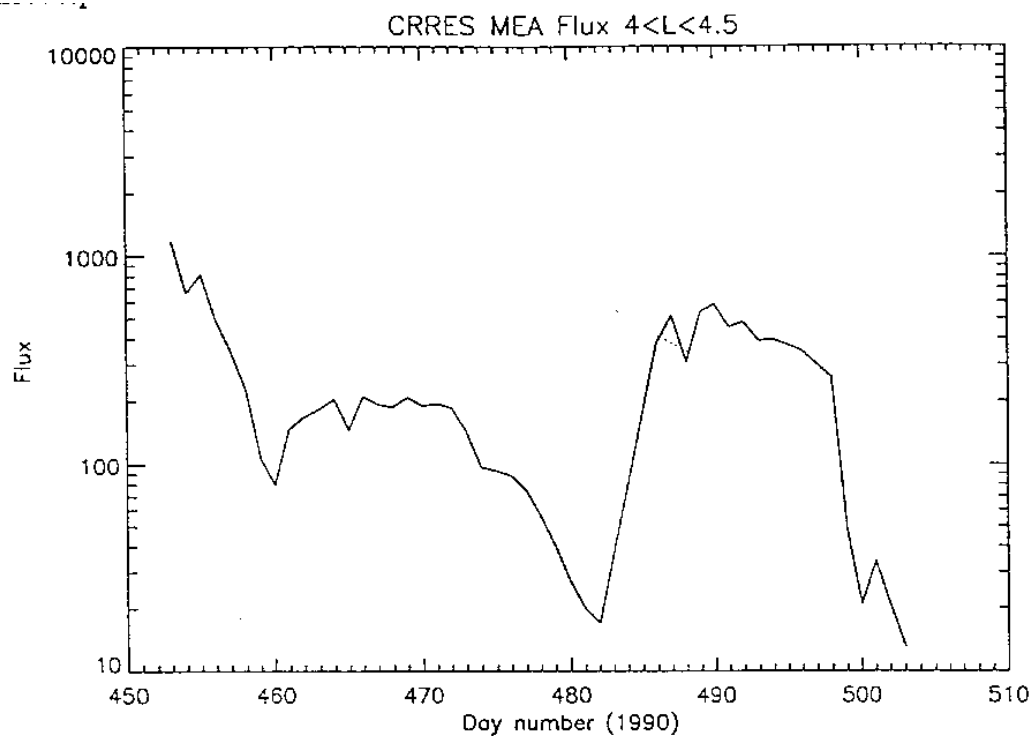


**Figure 9.17.** Loss-cone fluxes at  $L = 4$  over a 2-month period

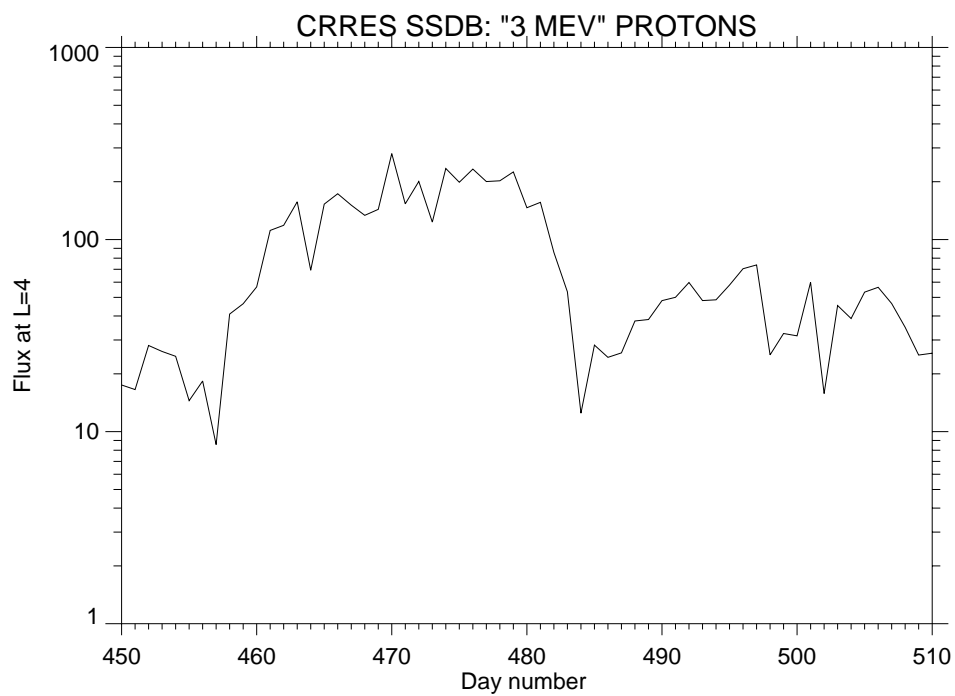


**Figure 9.18.** 3 MeV Proton flux over the same 2-month period as in Fig. 9.17

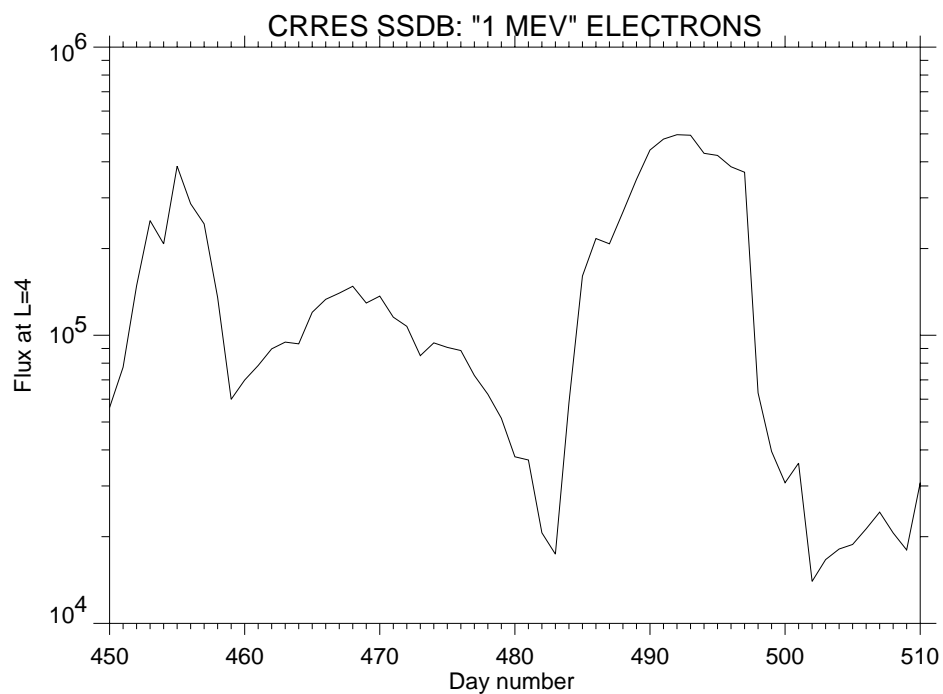


**Figure 9.19.** Total 1 MeV electron flux over the same 2-month period as in Fig. 9.17

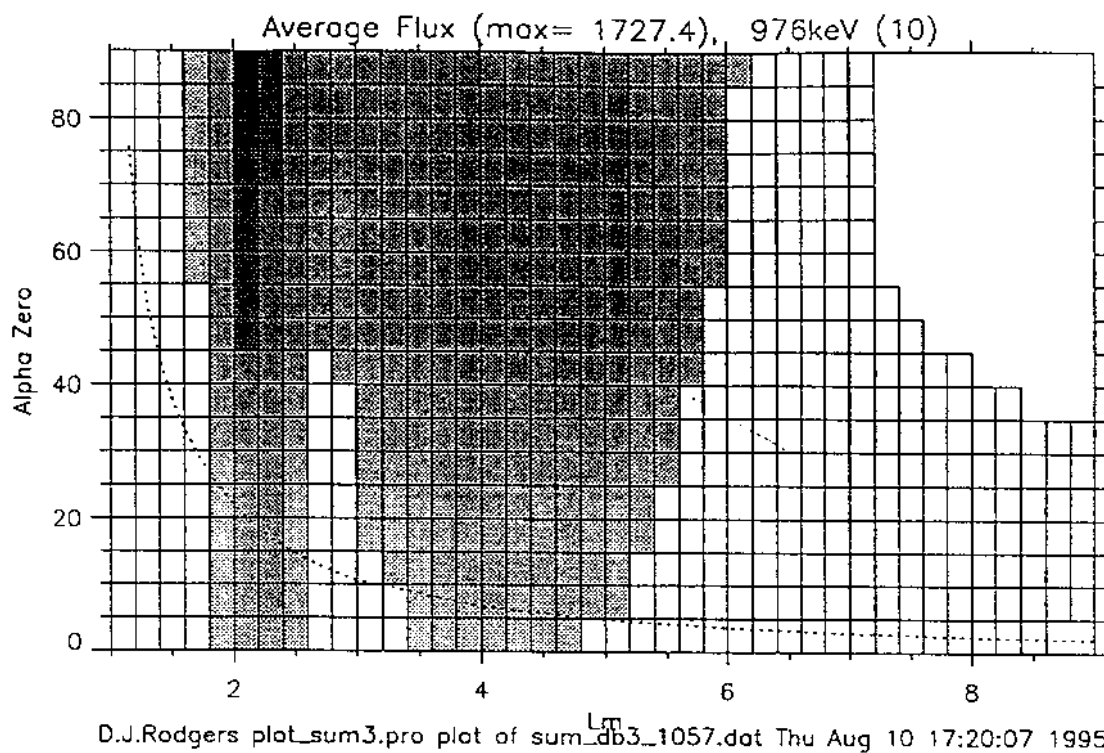


**Figure 9.20.** Greyscale plot of 976 keV mean flux binned in  $(L, \alpha_0)$  space. The dotted line represents the loss cone.

TREND-2. The pitch angle resolution was  $5^\circ$  as in the TREND-2 work but here the raw data were summed to that accuracy, instead of  $10^\circ$  as in TREND-2. Finer binning in pitch angle is not justified because of the limited instrument pitch-angle resolution. The model ranges from  $L = 1$  to  $L = 9$ , from  $\alpha_0 = 0^\circ$  to  $\alpha_0 = 90^\circ$ , and from 153 keV to 1534 keV. An example of the resulting flux map is shown in Fig. 9.20 for 976 keV electrons.

### 9.5.4 Model Format

Five versions of the model were created, one each for the  $K_p$  ranges 0 to  $1^+$ , 2 to  $3^+$ , 4 to  $5^+$ , and 6 to  $7^+$ , and one for all  $K_p$  values combined. The corresponding flux maps have been converted to the format described in Sect. 2.1.6 and added to TREP. The combined model is called ECM97.

### 9.5.5 Comparison with AE-8

Figure 9.21 shows a flux profile at local noon along the sunward equator at 1 MeV for NASA's AE-8 model (Vette 1991a) and the ECM97 model. The peak flux in the two models is similar but the MEA model drops off faster with radius. This difference becomes more pronounced in the tailward direction (Fig. 9.22). The AE-8 model predicts almost no difference from the sunward fluxes but ECM97 drops more rapidly with radius. The difference around geostationary orbit is an order of magnitude. Part of this difference is due to the presence of an external component to the magnetic field model used with the ECM97 model, and part is due to the fact that AE-8 does not take into account pitch angle dependence when constructing omnidirectional fluxes.

### 9.5.6 Model Characteristics

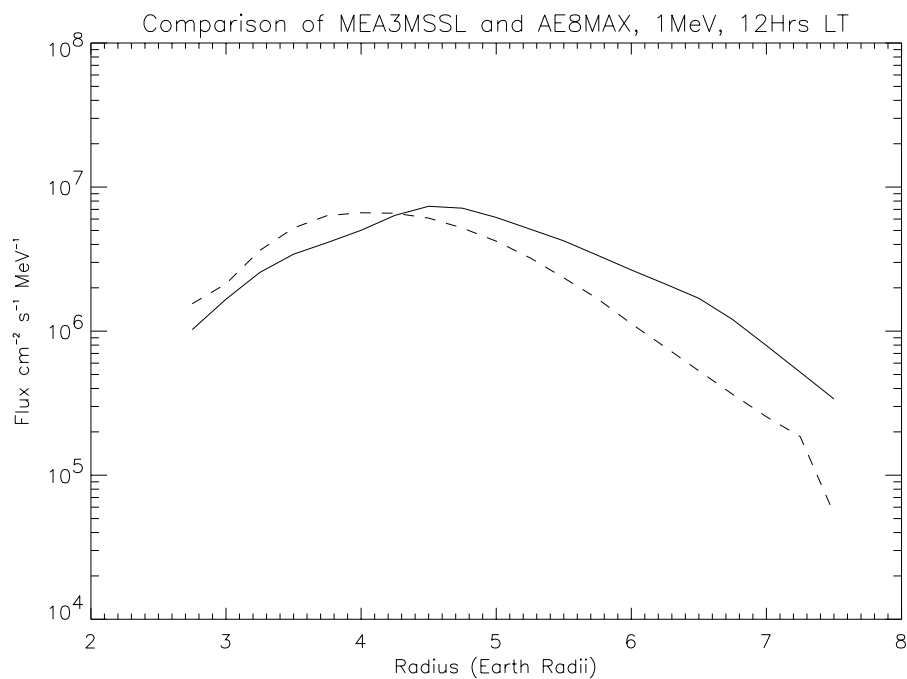
Figure 9.23 shows contours of log flux in a noon-midnight slice through the magnetosphere for  $K_p=0$  at 500 keV. The sampling grid has a resolution of  $0.5 R_E$ . The inner and outer belts are clearly visible. The sunward and tailward sides are fairly symmetric.

Figure 9.24 shows contours of log flux for the same slice as in Fig. 9.23 with  $K_p=7$ . The tailward side of the magnetosphere is now severely compressed, an effect of using a realistic magnetic field model. The peak of the outer belt has moved earthwards and the slot has disappeared. There are some irregularities at the edges of the model due to the poorer statistics for high  $K_p$  values. Overall flux levels in the inner and outer belt are much higher than for low  $K_p$ .

### 9.5.7 Outstanding problems

The model is presently contaminated by high energy protons for energies above 500 keV up to  $L = 3$ . Hence, its use is currently restricted to the outer belt.

In the outer belt the loss cone has a width of only a few degrees, which means that the MEA angular resolution does not characterise it accurately. This has no effect on fluxes near the



**Figure 9.21.** 1 MeV Electron flux along the noon equator. The solid line is AE-8MAX and the dotted line is ECM97.

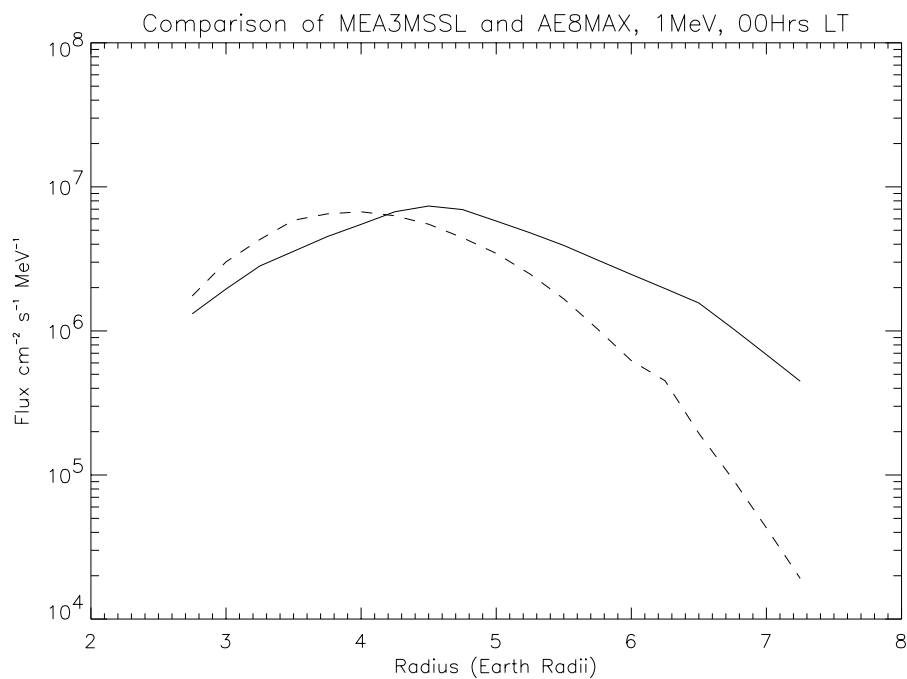


**Figure 9.22.** 1 MeV Electron flux along the midnight equator. The solid line is AE-8MAX and the dotted line is ECM97.

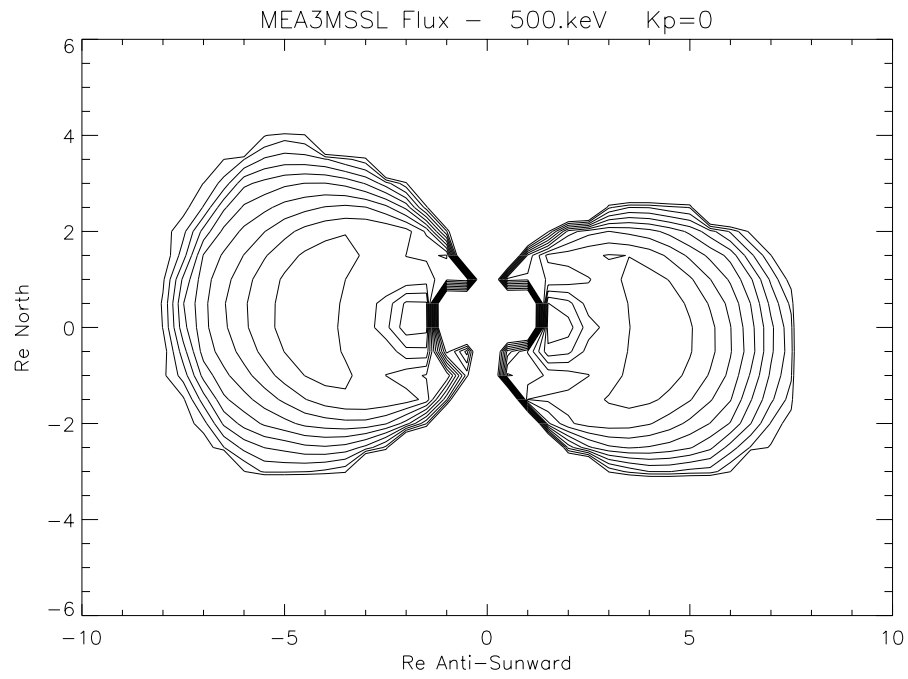


**Figure 9.23.** Contour plot of log flux in a noon-midnight cut through the magnetosphere, for  $K_p = 0$ . The sunward direction is to the left.

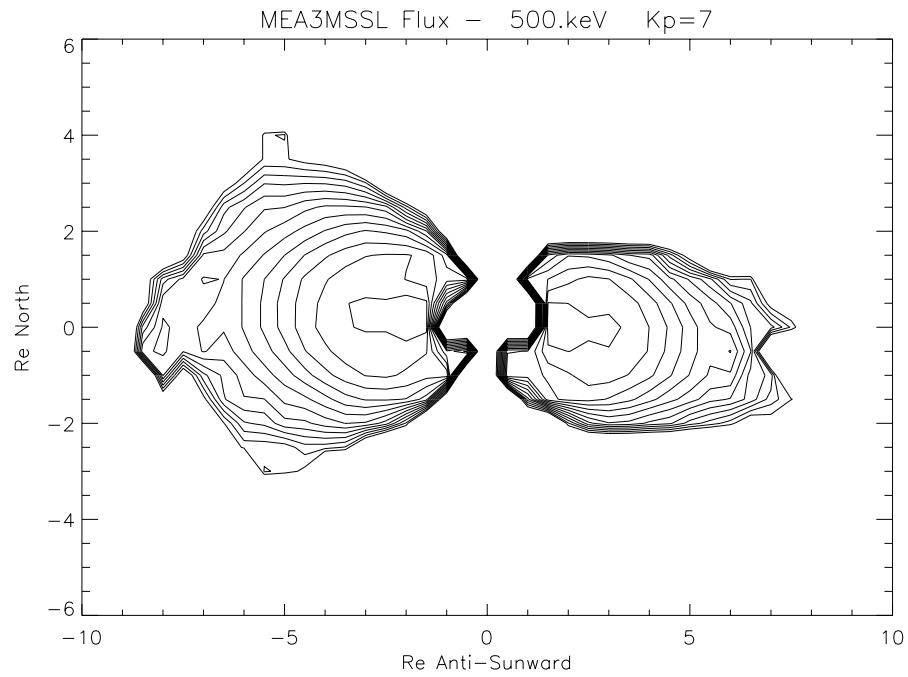


**Figure 9.24.** Contour plot of log flux in a noon-midnight cut through the magnetosphere, for  $K_p = 7$ . The sunward direction is to the left.

equator but results in the model becoming less accurate at low altitudes. This contrasts strongly with AE-8 which mapped the loss cone carefully.

The sudden change in the inner belt fluxes that occurred in March 1991 have shown that the 18 month CRRES mission is not a long enough data base to average out infrequent large events.

## 9.6 Feasibility of a statistical model

One of the most useful aspects of the Meteosat analysis in TREND-2 was the demonstration of how the variation of fluxes was reduced as the time bin over which the measurements were averaged was increased. The result was a model of flux variance as a function of time duration. The Meteosat analysis began with 30 minute averages and progressively increased the time bin up to a year. This worked because Meteosat covered a small  $L$  range and fluxes at the lower energies did not have a steep gradient in  $L$ . For CRRES, this is far more difficult because of its wide coverage in  $L$  and the steep gradient of fluxes at higher energies. Figure 9.25 shows the distribution of fluxes summed over 1 minute, for 976 keV electrons at  $L = 6.6 \pm 0.25$ . The mode of the flux is the lowest flux bin of  $0-1 \text{ cm}^{-2}\text{sr}^{-1}\text{keV}^{-1}$ . When the data were averaged over 2 and 4 minutes, there was no perceptible difference.

However, when the time bin was 8 minutes as shown in Fig. 9.26, the peak at low fluxes has considerably decreased compared with the high flux tail. In this plot, the vertical scale is an eighth of that in Fig. 9.25 to keep the data directly comparable. The total number of data points in Fig. 9.26 is less than 8 times fewer than in Fig. 9.25 because few data periods are available with 8 minutes coverage at this  $L$  value, even though the spacecraft is near apogee. Extending this analysis to longer time bins is not possible. It should also be noted that much of the variation in fluxes in short time bins comes from  $L$  dependent variation. Hence, a model such as was created with Meteosat is not practical until data are summed over multiples of orbits.

Only a third of orbits had any data in the  $L$  range specified. Figure 9.27 shows a histogram of fluxes binned in one complete orbit. From this plot the mean and 10<sup>th</sup>, 50<sup>th</sup> and 90<sup>th</sup> percentiles have been found. These are plotted for successive multiples of the orbital period in Fig. 9.28. As in the Meteosat-3 data all three percentiles start to converge on the mean as the binning period increases. However, poor statistics make some of them diverge again at 16 orbits and above. Hence, only on a time scale of 1–4 minutes or 1–8 orbits can a statistical model be created. This would be of limited use.

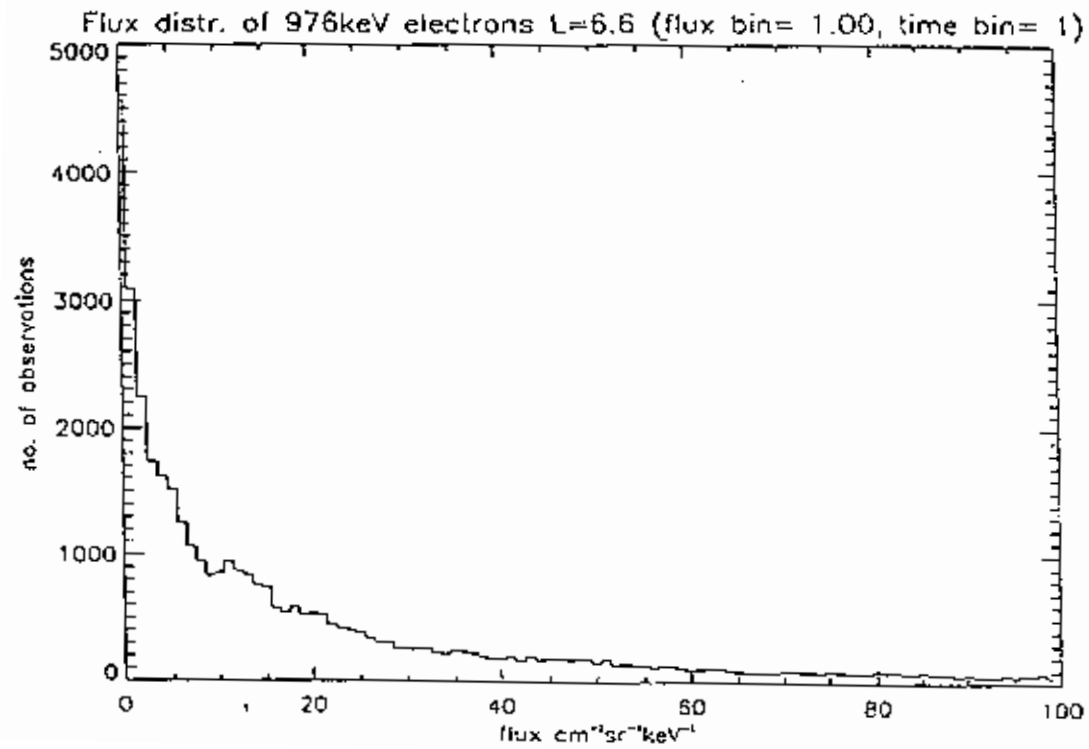


**Figure 9.25.** 976 keV Electron fluxes at  $L = 6.5$ – $6.7$  summed over 1 minute

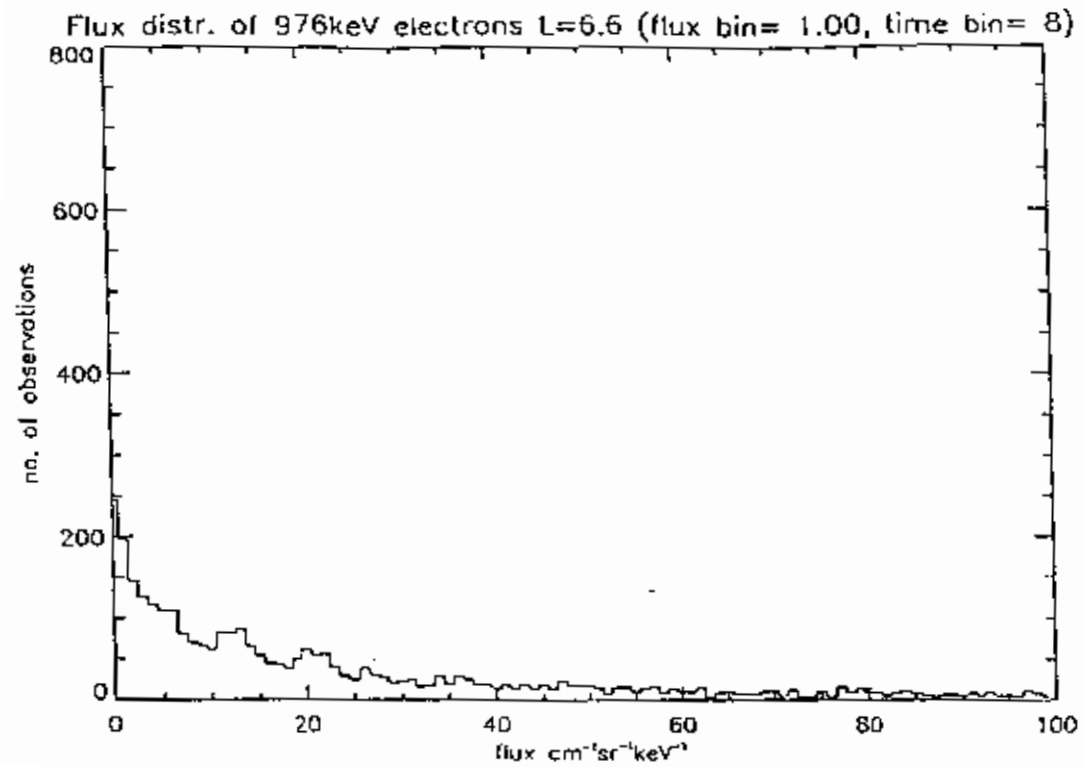


**Figure 9.26.** 976 keV Electron fluxes at  $L = 6.5$ – $6.7$  summed over 8 minutes

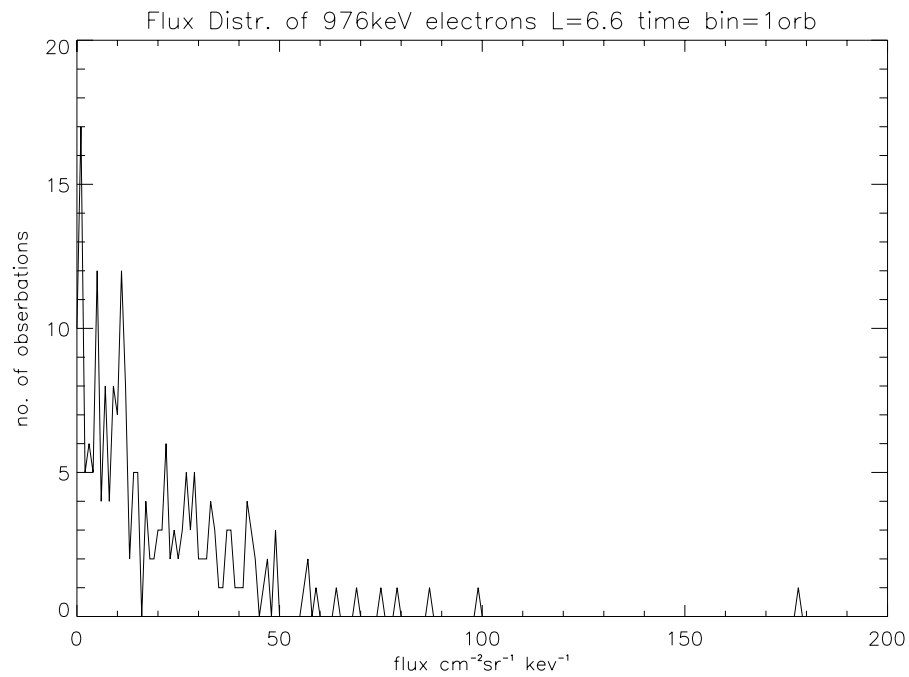


**Figure 9.27.** 976 keV Electron fluxes at  $L = 6.5\text{--}6.7$  summed over 1 orbit

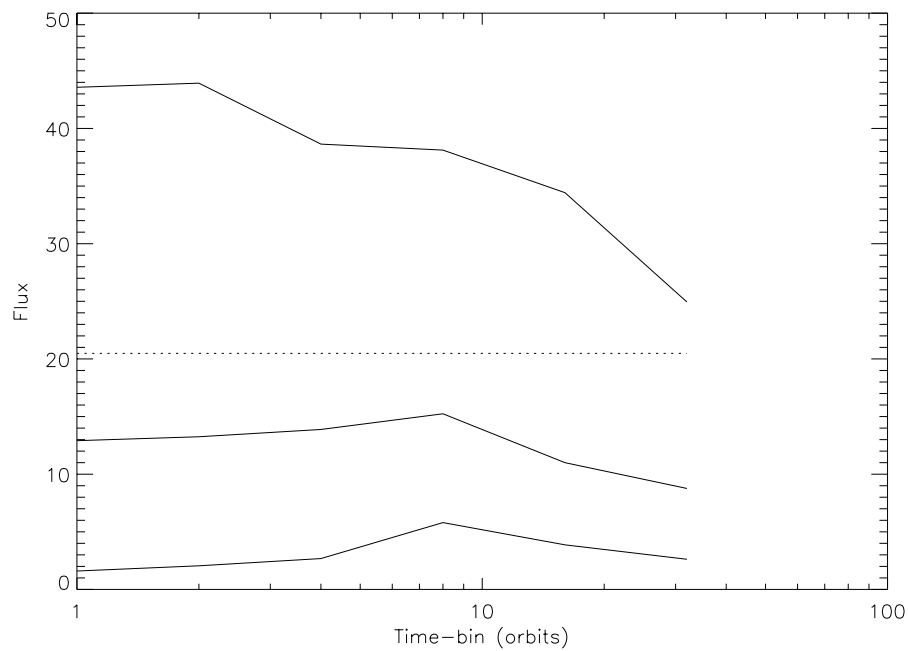


**Figure 9.28.** Dependence of median, and 10<sup>th</sup> and 90<sup>th</sup> percentiles on time bin



# Chapter 10

## Radiation losses and particle injection studies

### 10.1 Introduction

Empirical models of the radiation belts such as the ECM97 model developed in this study (see Chapter 9) are compilations of the data gathered over a period of time collected in bins of finite size. The coverage may not be complete, and the statistical errors in some bins may be greater than in others. There is a need therefore to have some means of smoothing, interpolating and perhaps extrapolating the data to improve the value and coverage of the model. While it is quite possible to use arbitrary functions such as polynomials, it is better to use functions which have an underlying relationship to the physics of the system. In Technical Note 8 we set out to find appropriate functions to fit to the pitch angle distributions measured by the MEA detector on CRRES. We took the averaged values of the flux over the pitch angle range covered by the instrument and relate them to the distributions which would result from the mechanism of pitch angle diffusion. It must be borne in mind that pitch angle diffusion could properly only be related to instantaneous observations of the complete distribution and it is questionable whether diffusion coefficients obtained from averaged distributions have any real significance.

Nevertheless the fitted distributions give a good idea of how the process of pitch angle diffusion varies throughout the outer electron radiation belts and how the loss rates of trapped electrons vary with  $L$ . The analysis has not been successful in deriving the flux within the loss cone and so the final loss rates could not be calculated but the results provide a better means of extrapolating the measurements of CRRES down to low altitudes than the previous technique which was used to extrapolate low altitude measurements to the equatorial region for input to the AE-8 model. In addition the results can be used to adjust the observations of the ISEE electron detectors for input to a directional intensity model of the radiation belts. The data in the current ISEE model were obtained from a set which contained omnidirectional energy spectra, and pitch angle distributions summed over all energies. It then had to be assumed that all energies had the same pitch angle distribution. The results here show that assumption to be inaccurate, and any distribution summed over the energy range will be dominated by the angular

distribution of the lowest energy, which is numerically greatest. The lowest energies are at one extreme of the range of behaviour of pitch angle diffusion encountered in the radiation belts and therefore low energy pitch angle distributions will give a misleading impression at the highest energies. For a complete intercomparison of the MEA and ISEE data sets it will be necessary to take these effects into consideration. A further value of obtaining a parametric fit to the data is that the complete data set can be summarized accurately with a much smaller set of numbers. A model could then be specified with a much smaller set of numbers.

## 10.2 Theoretical background

The main loss mechanism for radiation belt electrons is by precipitation into the atmosphere. Electrons in trapped orbits are scattered randomly in pitch angle by plasma waves and ultimately reach the loss cone by diffusion. The process is most likely to be self-driven; that is, the energy for the waves comes from the particles themselves because as they scatter towards smaller pitch angles they lose energy to wave growth. Alternatively the electrons may be scattered by externally generated waves. Whatever the source of waves the effect is the same; the particles diffuse in pitch angle towards the loss cone and as a result their distribution develops a maximum at  $90^\circ$  and decreases monotonically towards the field-aligned direction. The process has been analysed mathematically by a number of authors (Wentworth 1963, Walt & MacDonald 1964, Kennel & Petschek 1966, Roberts 1969, Schultz & Lanzerotti 1974) by deriving a diffusion equation from the Fokker-Planck equation. We followed the development of Roberts (1969).

If the source function is independent of time the solution of the Fokker-Planck equation can be written in the form:

$$j(\mu_0, t) = j_s(\mu_0) + \sum_{n=1}^{\infty} a_n j_n(\mu_0) e^{-\eta_n t}, \quad (10.1)$$

where  $j_n(\mu_0)$  are the normal modes solutions, which can be defined in terms of Bessel functions of the first kind  $J_n$  (see Technical Note 8), and  $\eta_n$  are the decay constants. We are not interested in the steady state solution  $j_s(\mu_0)$  in which the source is balanced by the loss of particles to the atmosphere and so we ignore it and the source term itself.

If the initial distribution is complex in shape a number of terms in the expansion may be required to fit the profile. However, it can be shown that the higher order terms lead to larger values for the decay constant  $\eta$  and so they rapidly die away leaving the lowest order term to dominate. Thus for our solution we are left with the zero order Bessel function of the first kind in the following form:

$$j_1(\mu_0) = J_0 \left[ \zeta_1 \left( \frac{\mu_0}{\mu_{c0}} \right) \right]. \quad (10.2)$$

It has been assumed so far that the intensity at  $\mu_0 = 0$ , i.e. at a pitch angle of  $90^\circ$ , is normalized so that  $j_1(0) = 1$ . In fact,  $J_0(x) = 1$  at  $x = 0$ . In order to be able to fit to the data we use the following form:

$$j(\mu_0) = j(0) J_0 \left( \frac{\mu_0}{\mu_{sc}} \right). \quad (10.3)$$

Thus we could fit the two parameters  $j(0)$  and  $\mu_{sc}$  by the following procedure.  $j(0)$  can be obtained from the intensity at  $90^\circ$  pitch angle and  $\mu_{sc}$  from the ratio of the flux at the edge of the loss cone to the intensity at  $90^\circ$  by solving the following equation for  $\mu_{sc}$ :

$$\frac{j(\mu_{c0})}{j(0)} = J_0 \left( \frac{\mu_{c0}}{\mu_{sc}} \right). \quad (10.4)$$

In fact, the procedure we shall use is to make a least squares fit to the data involving measurements at a number of pitch angles between  $90^\circ$  and the edge of the loss cone. Note also that our parameter  $\mu_{sc}$  is equivalent to Roberts' (1969) parameters as follows:

$$\mu_{sc} = \frac{\mu_{c0}}{\zeta_{vn}}. \quad (10.5)$$

This solution meets the boundary condition that the slope of the function at  $90^\circ$  is zero and that it is therefore symmetric about  $90^\circ$ . This applies outside the loss cone; inside the loss cone a different solution is required to meet different boundary conditions. There we use the alternate Bessel function  $I_0(x)$  which has the properties that it is equal to 1 at  $x = 0$ , and increases monotonically as  $x$  increases. In this case the function is:

$$j(\alpha_0) = j(\alpha = 0) I_0 \left( \frac{\alpha_0}{\alpha_{sc}} \right). \quad (10.6)$$

We use the intensity at the edge of the loss cone obtained from the Bessel function fit described above and the measured intensity at a pitch angle of  $2.5^\circ$ , which is the minimum pitch angle available. The ratio of the two quantities gives  $\alpha_{sc}$  by solving:

$$\frac{j(\alpha = 2.5^\circ)}{j(\alpha_{c0})} = \frac{I_0 \left( \frac{\alpha = 2.5^\circ}{\alpha_{sc}} \right)}{I_0 \left( \frac{\alpha_{c0}}{\alpha_{sc}} \right)}. \quad (10.7)$$

The value of  $j(\alpha = 0)$  is found by matching the two functions at the edge of the loss cone.

### 10.3 Relation to the work of Vampola (1996)

Vampola (1996) used the CRRES/MEA data and magnetic activity as the input to a neural network which could then be used to estimate the radiation belt intensities over a much wider period of time than the duration of the CRRES mission. He made fits to the pitch angle distribution in order to be able to extrapolate the measurements of CRRES/MEA from a position off the equator to the equatorial plane. The function he used was  $\sin^n \alpha$ , where the exponent  $n$  was obtained from the ratio of the flux at  $90^\circ$  to the flux at  $45^\circ$ . The reason he used the function apart from its simplicity was that the functional form remains the same as one moves along the field line. Figure 10.1 compares the sine function form with the equivalent Bessel function form for a value of  $n$  in the middle of the range of values found by Vampola, i.e.  $n = 2$ . The value of

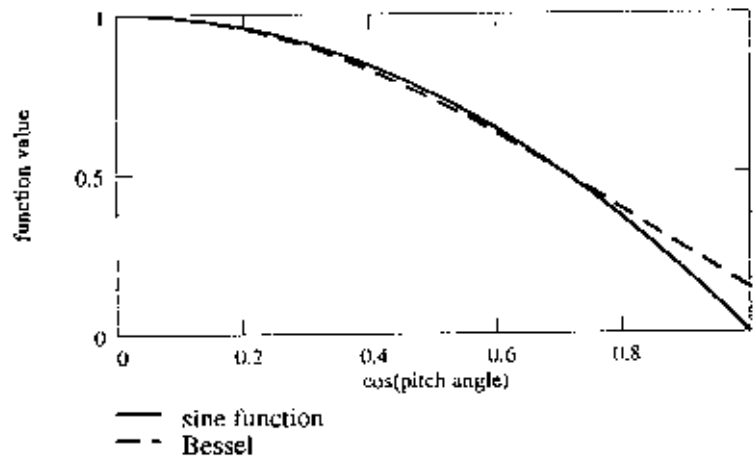


**Figure 10.1.** A comparison between a Bessel function and a sine function fitted between the same two points, at  $90^\circ$  and at  $45^\circ$

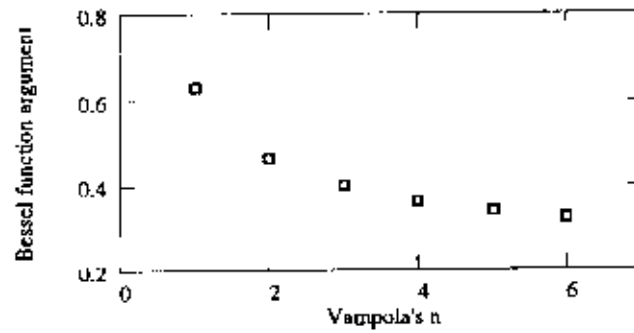


**Figure 10.2.** The relation between the parameter  $n$  from Vampola's (1996) fits and the Bessel function fit from this work

$\mu_{sc} = 0.465$  has been obtained by ensuring that both give the same value at  $45^\circ$ . The diagram shows that the two functions are very similar from  $\mu_0 = \cos \alpha = 0$  to  $\mu_0 = 0.8$  where the pitch angle is  $37^\circ$ . There is a very crucial difference near the loss cone where the sine function goes to zero at a pitch angle of zero. This is not the physical reality since the intensity at zero pitch angle in general has a finite value. Thus the sine function is not useful for studying what happens in or near the loss cone. Figure 10.2 compares the range of values of  $n$  obtained by Vampola with the equivalent values of  $\mu_{sc}$ . These values lie in the range found by the analysis reported here, and the radial variation is approximately equivalent. Thus these results and those of Vampola are consistent with each other.

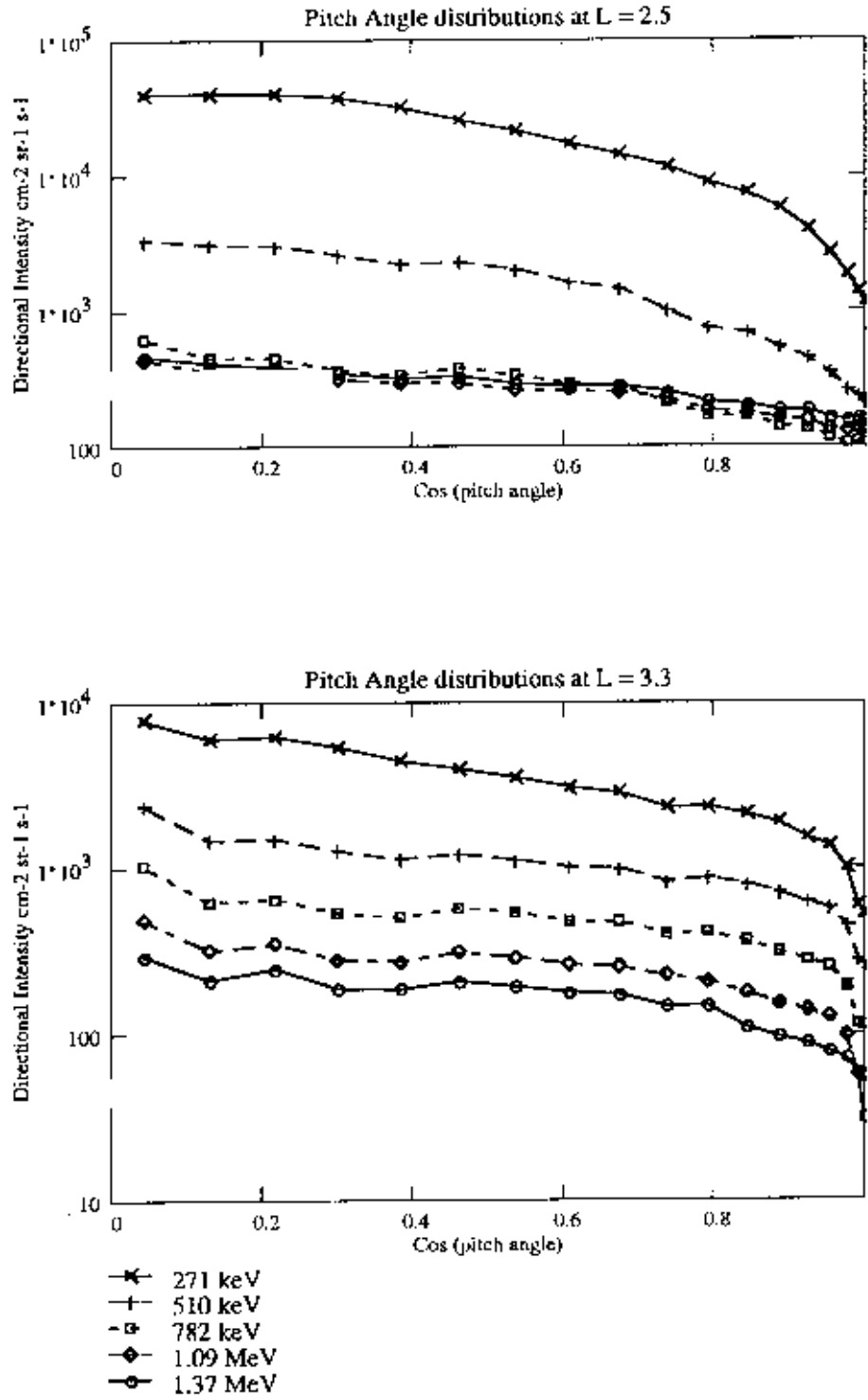


**Figure 10.3.** Pitch angle distributions for  $K_p = 0$  to  $1^+$ , for  $L = 2.5$  and  $L = 3.3$

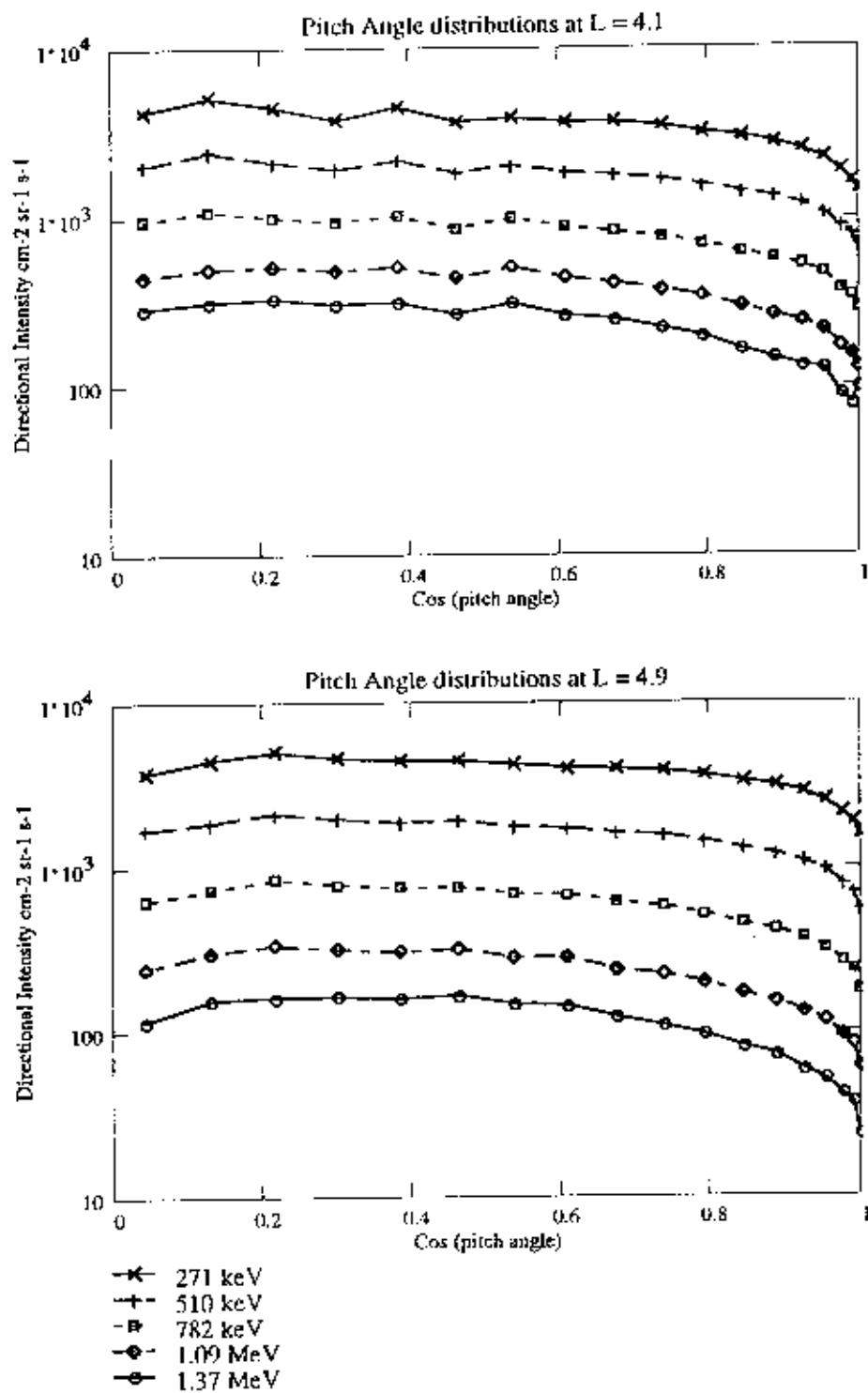


**Figure 10.4.** Pitch angle distributions for  $K_p = 0$  to  $1^+$ , for  $L = 4.1$  and  $L = 4.9$

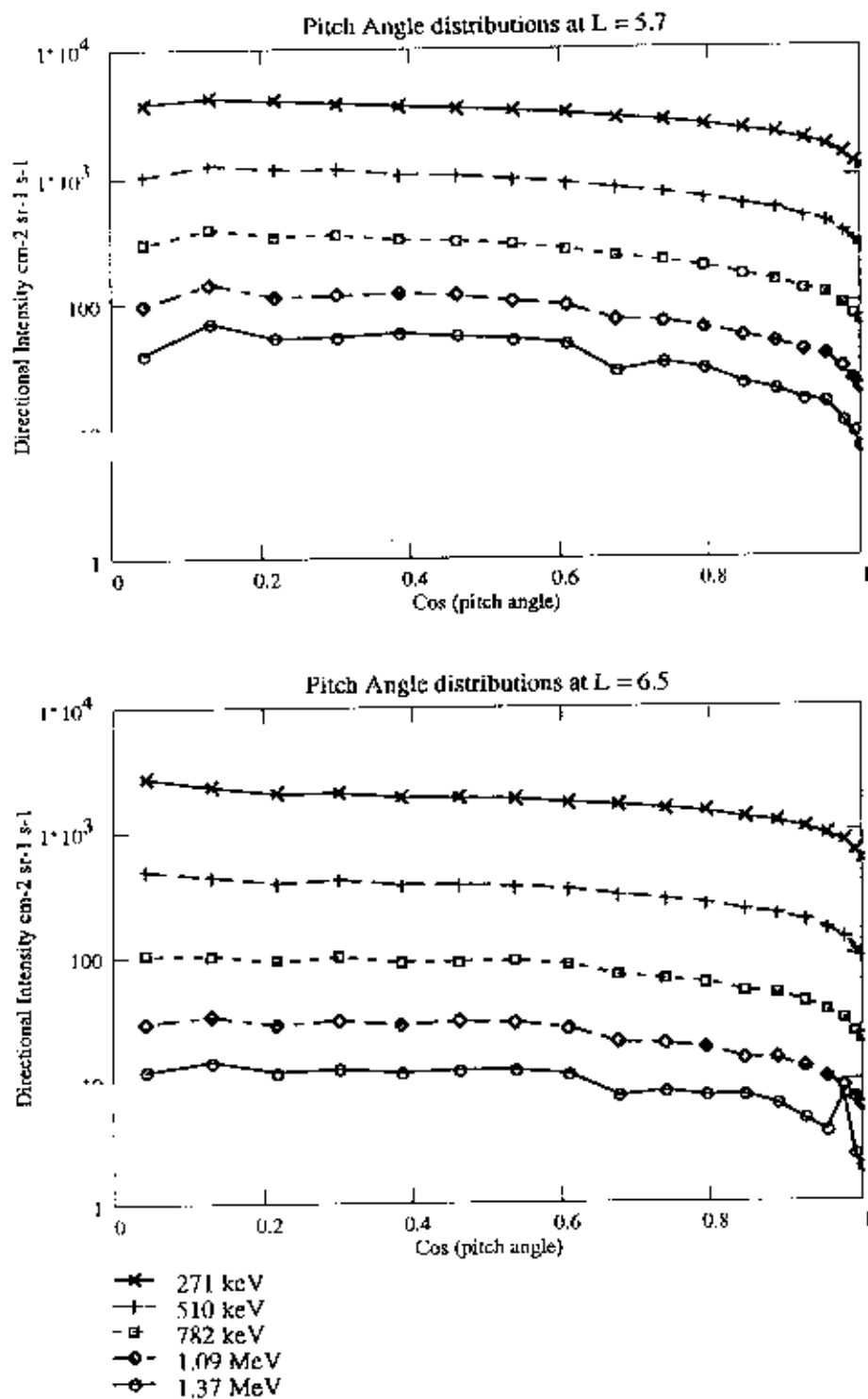


**Figure 10.5.** Pitch angle distributions for  $K_p = 0$  to  $1^+$ , for  $L = 5.7$  and  $L = 6.5$

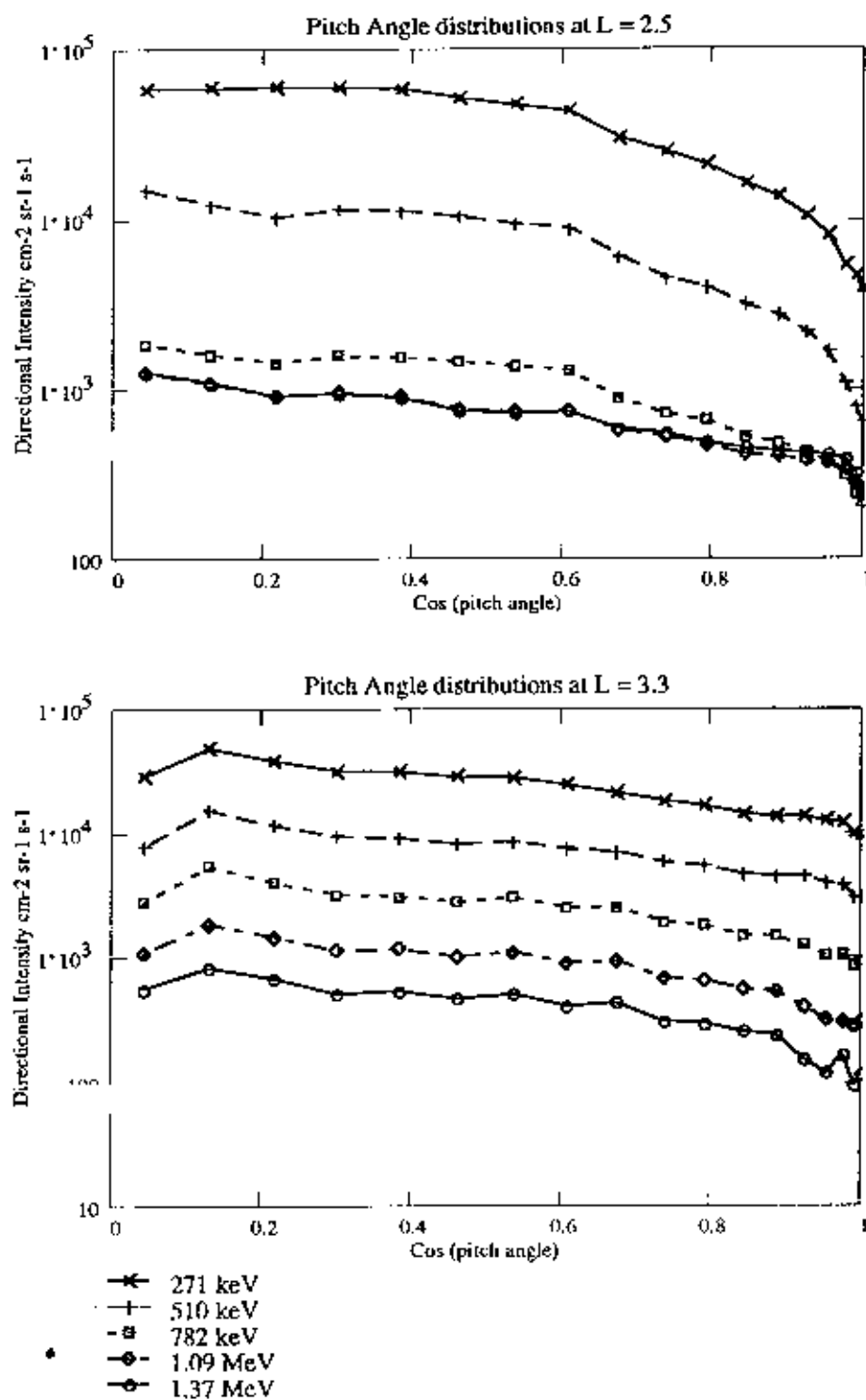


**Figure 10.6.** Pitch angle distributions for  $K_p = 6$  to  $7^+$ , for  $L = 2.5$  and  $L = 3.3$



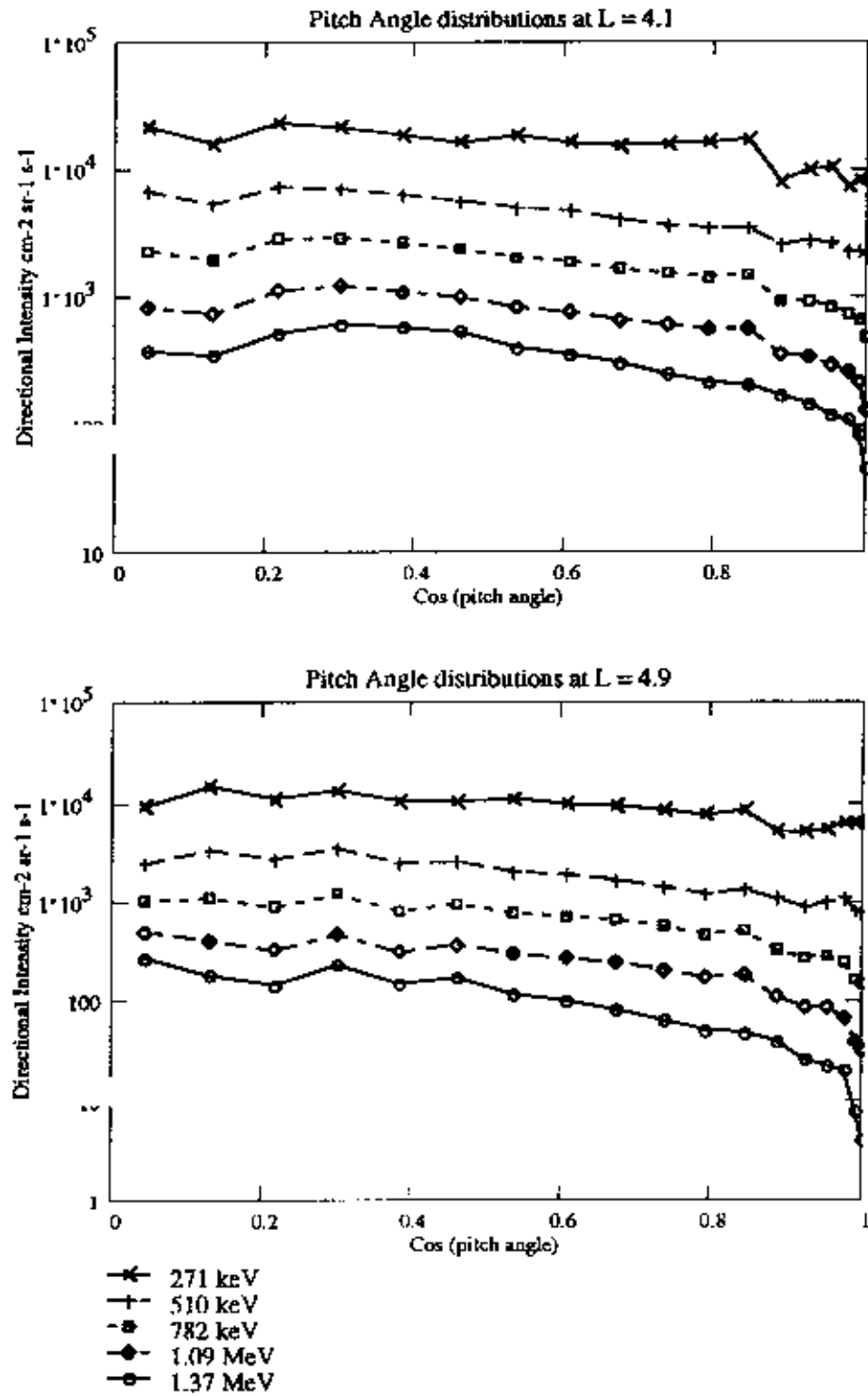


Figure 10.7. Pitch angle distributions for  $K_p = 6$  to  $7^+$ , for  $L = 4.1$  and  $L = 4.9$

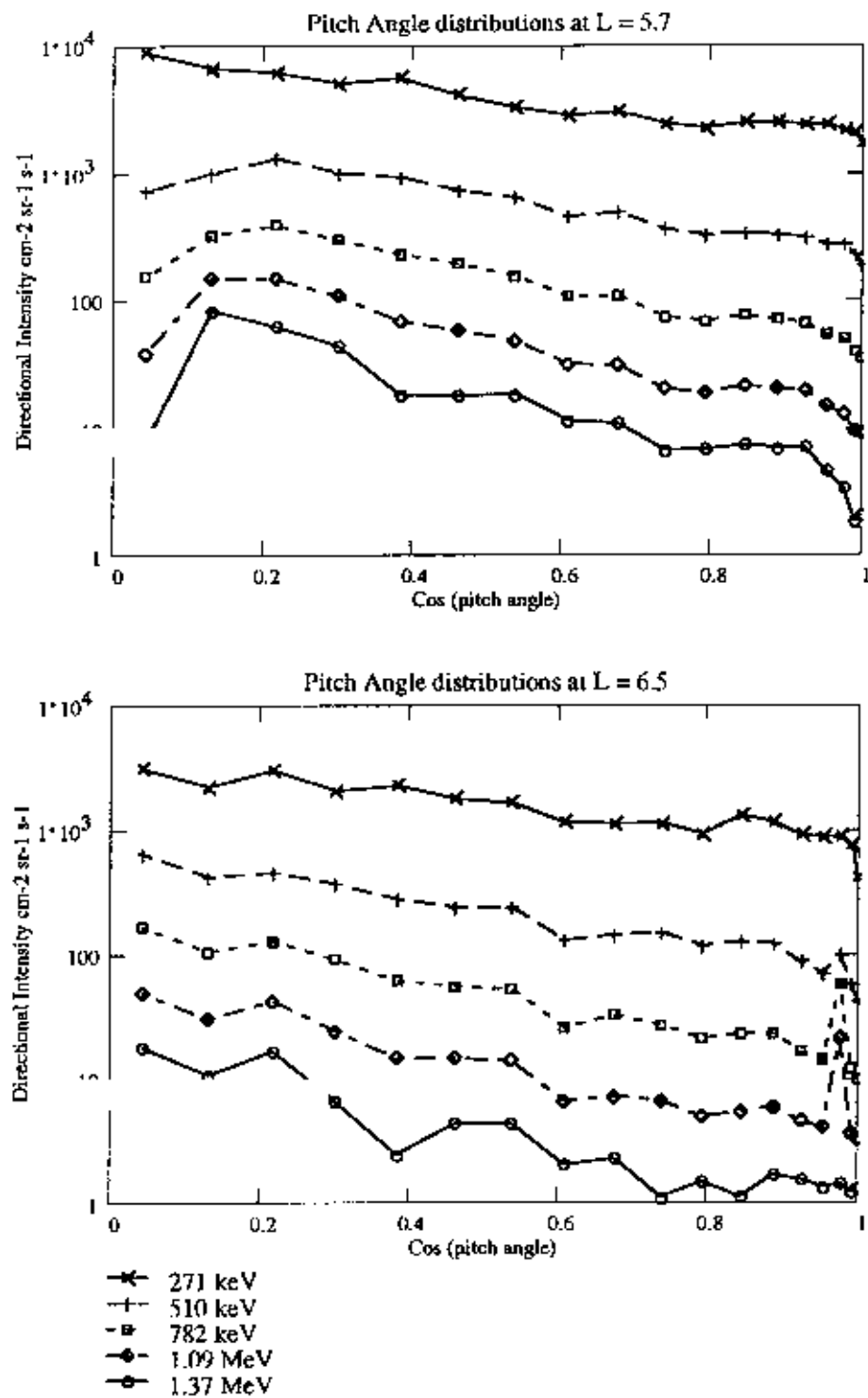
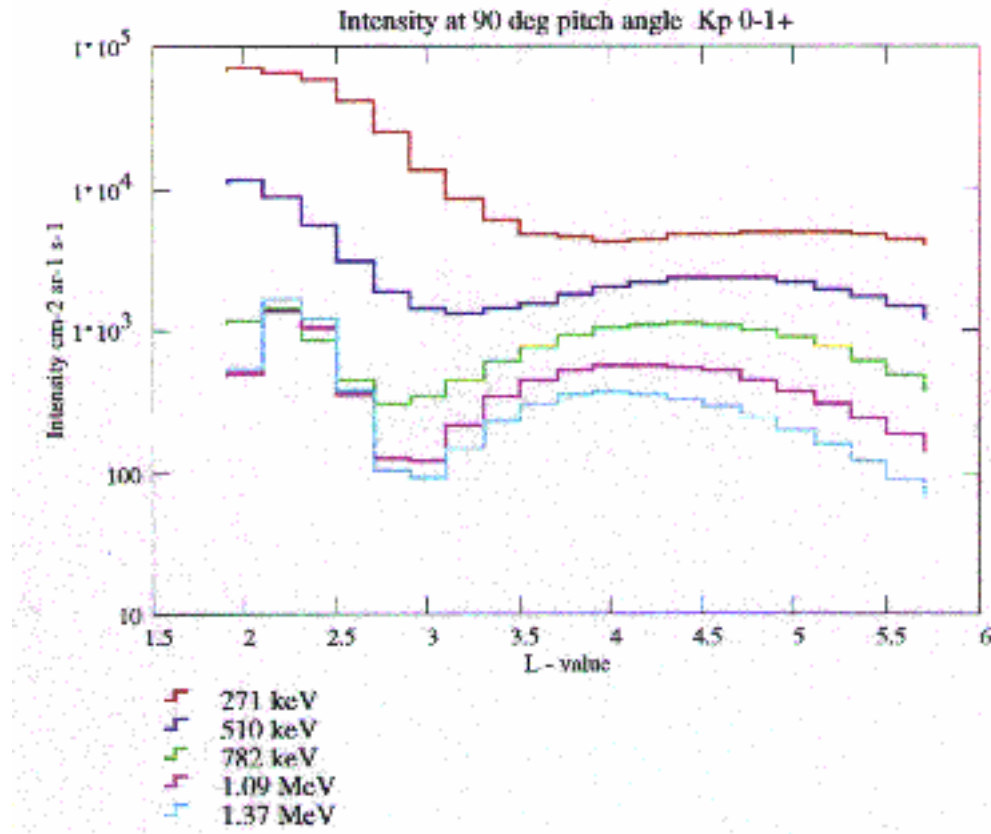


Figure 10.8. Pitch angle distributions for  $K_p = 6$  to  $7^+$ , for  $L = 5.7$  and  $L = 6.5$



**Figure 10.9.** The electron intensity at  $90^\circ$  pitch angle obtained by fitting a Bessel function to the complete distribution as a function of  $L$ , for low  $K_p$  values. Note that at the highest energies and the lowest  $L$  values the overlapping curves indicate that the measurements are contaminated by penetrating protons.

## 10.4 Pitch angle distributions in the outer electron belt

The first step is to examine the shape of the angular distributions in the ECM97 model for a selection of energies at a selection of  $L$  values to establish the normal behaviour. The selected energies are distributed evenly through the range covered by MEA, namely 271 keV, 510 keV, 782 keV, 1.09 MeV, and 1.37 MeV, and the  $L$  values are 2.5, 3.3, 4.1, 4.9, 5.7, and 6.5. The distributions shown in Figs. 10.3–10.5 are for  $K_p$  at the lowest level, of 0 to  $1^+$ . The distributions in Figs. 10.6–10.8 are at the high level of  $K_p = 6$  to  $7^+$ . Some of the points to notice are:

1. the intensity decreases with energy at all distances;
2. the minimum intensity is always at a pitch angle of zero;
3. there are examples of a local minimum at  $90^\circ$ , mainly at high energies and large distances;
4. the distributions tend to be more anisotropic at the higher energies;
5. the distributions tend to be more anisotropic at lower altitudes;

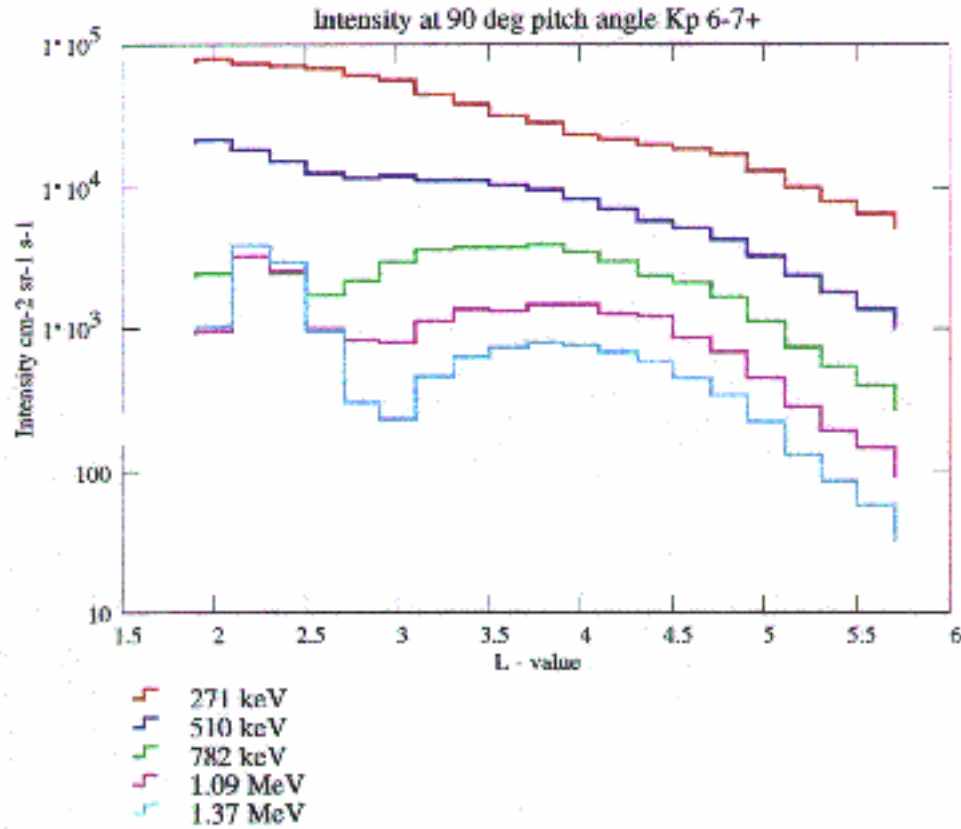


**Figure 10.10.** The electron intensity at  $90^\circ$  pitch angle obtained by fitting a Bessel function to the complete distribution as a function of  $L$ , for high  $K_p$  values

6. the minimum in the loss cone tends to be deeper at higher energies;
7. the variation between energies and/or distance is smooth and apparently continuous;
8. while there is some statistical scatter there is not enough to make fitting difficult;
9. at  $L = 2.5$  there is a detectable background from penetrating protons which render the measurements at the two highest energies, where the intensity is smallest, inaccurate and unusable.

Except for point 1 the similarity to the Bessel function variation is close. The minimum at  $90^\circ$  cannot be generated by pitch angle diffusion and from the magnitude of the scatter over the rest of the pitch angle range and the consistency of the minimum from one distribution to nearby ones it cannot be the result of statistical variation. In fact such pitch angle distributions are well-known, and usually called “butterfly” distributions. The explanation for them is “shell splitting” whereby particles at different pitch angles follow different drift shells. They are most noticeable where there is a steep negative spatial gradient in intensity so that the small difference in drift shell has a large effect on intensity. In deriving the Bessel function fit, pitch angles near  $90^\circ$  have

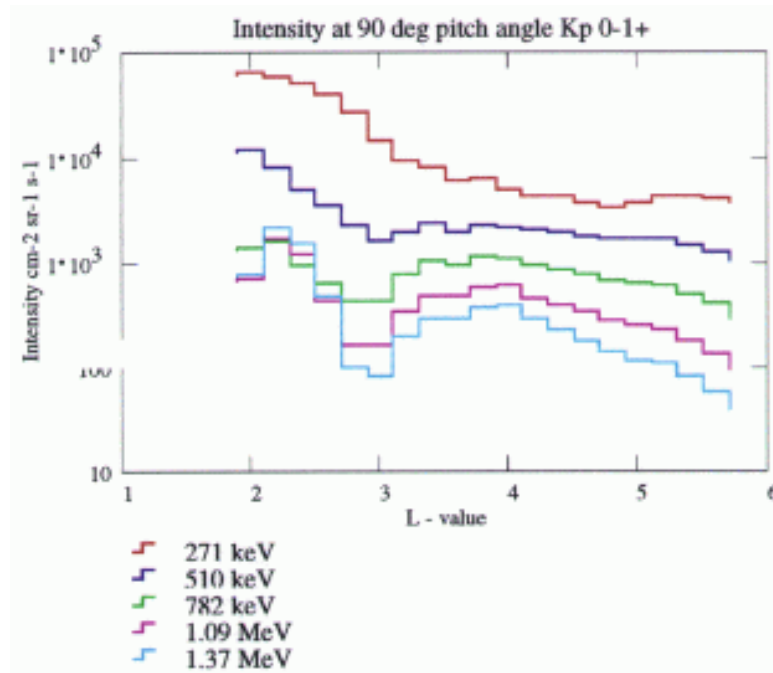


**Figure 10.11.** The electron intensity at  $90^\circ$  pitch angle measured by the CRRES/MEA detector, as a function of  $L$ , for low  $K_p$  values. Note that at the highest energies and the lowest  $L$  values the overlapping curves indicate that the measurements are contaminated by penetrating protons.

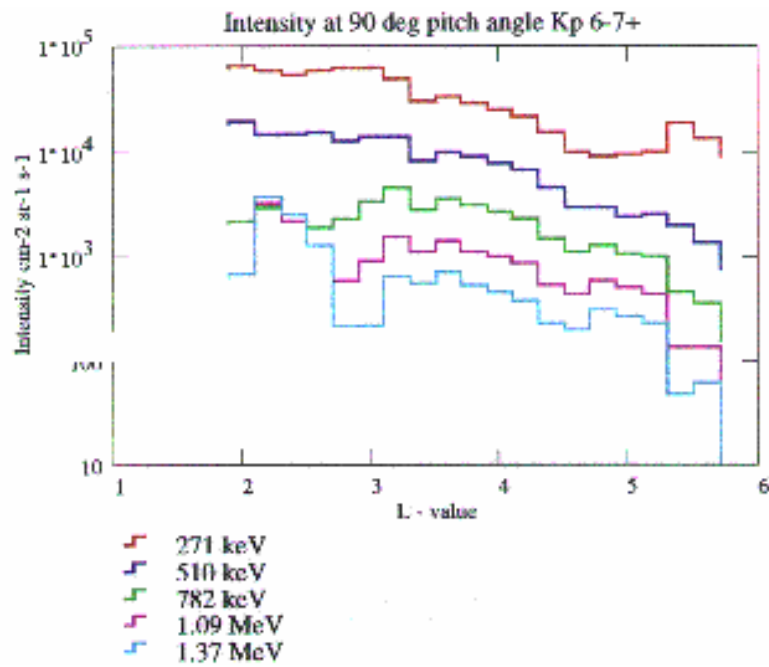


**Figure 10.12.** The electron intensity at  $90^\circ$  pitch angle measured by the CRRES/MEA detector, as a function of  $L$ , for high  $K_p$  values

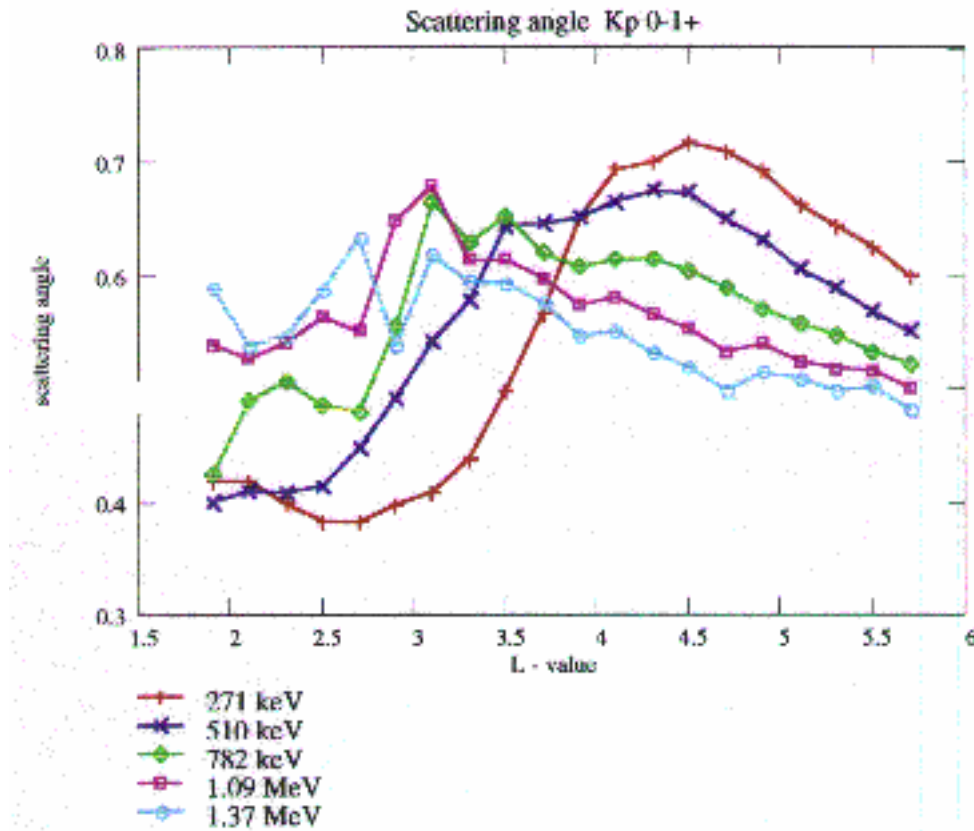


**Figure 10.13.** The scattering angle derived from the Bessel function fit at five energies over the entire  $L$  range for low  $K_p$  values. Note that the measurements inside  $L = 2.7$  and at the three highest energies are contaminated by penetrating protons.

been excluded, as have pitch angles in or close to the loss cone in order to avoid the influence of these effects. The fit is based on the intermediate angles. The shell-splitting minimum did upset Vampola's fit of the sine function since he based it always on the ratio of the intensities at  $90^\circ$  to that at  $45^\circ$ . He records that when the intensity at  $45^\circ$  was the greater he excluded the data.

## 10.5 Fitting a Bessel function to the distribution outside the loss cone

The mathematical basis for the fitting process is described in Sect. 10.2. The software used was the Mathcad Plus package for Macintosh. The nature of the software is such that it is not possible to carry out the fit for more than one energy at a time. It is done at each  $L$  value in the ECM97 model, i.e. at intervals of 0.2 in  $L$ , and for the same two  $K_p$  levels as before. The results from successive runs at the same sequence of energies as used in the pitch angle plots

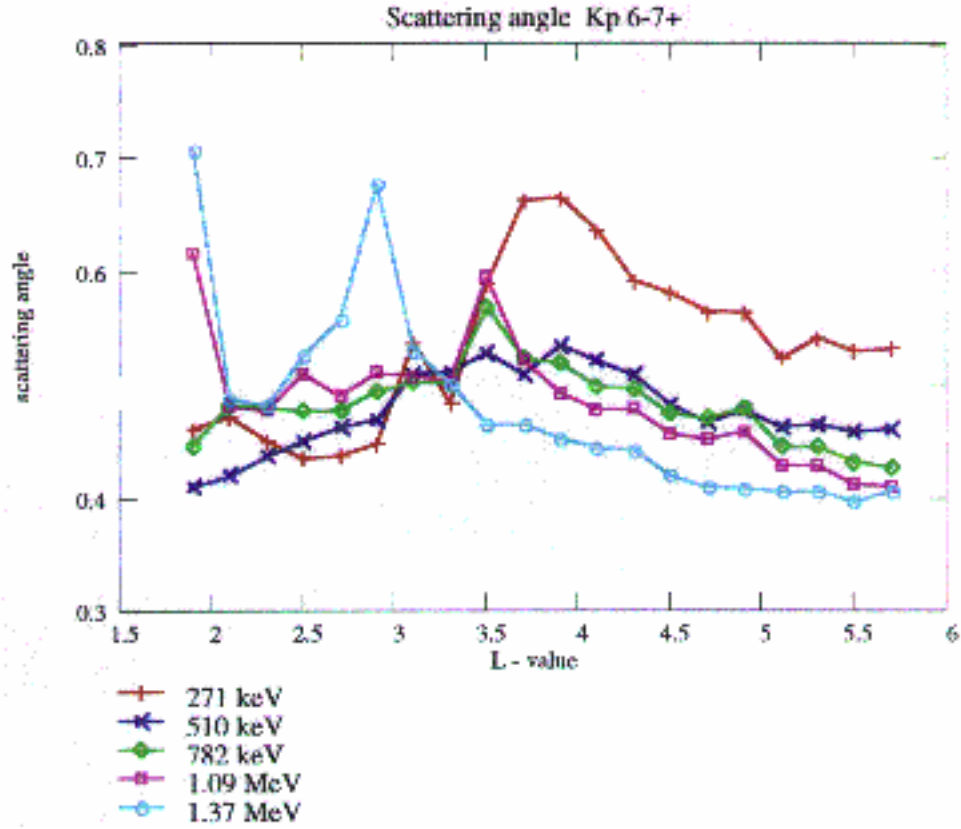


**Figure 10.14.** The scattering angle derived from the Bessel function fit at five energies over the entire  $L$  range for high  $K_p$  values. Note that the measurements inside  $L = 2.7$  and at the three highest energies are contaminated by penetrating protons.

were combined together for plotting and the results are shown in Figs. 10.9–10.14. Figures 10.9 and 10.10 show the radial variation of the equatorial intensity, which is obtained from the parameter  $j(0)$  defined in Eq. (10.3) and which, of course, ignores the minimum arising from the butterfly distributions. Figure 10.9 shows the variation for the weakest  $K_p$  values of 0 to  $1^+$  and Fig. 10.10 for 6 to  $7^+$ . The interesting feature about the comparison is that the intensities at  $L < 3$  and at  $L > 5.5$  are very similar for the two  $K_p$  values. The biggest differences are in the  $L$  range from 3.5 to 4.5 and at the lowest energy. It is also apparent that the fitting process fulfils one of its functions outlined in the introduction—it smooths the data from the model. Figures 10.11 and 10.12 show the corresponding data based on just the intensity at  $90^\circ$  from the ECM97 model where there is clear statistical variation which is removed by the fitting process.

The next figures, Figs. 10.13 and 10.14, show the variation of the parameter  $\mu_{sc}$  from Eq. (10.3). Figure 10.13 is derived from the low  $K_p$  model and shows clear systematic structure. A smaller value for  $\mu_{sc}$  indicates greater anisotropy. We note:

1. all curves show least anisotropy in the  $L$  range where the intensity peaks but the peak for the higher energies is found at smaller  $L$  values;

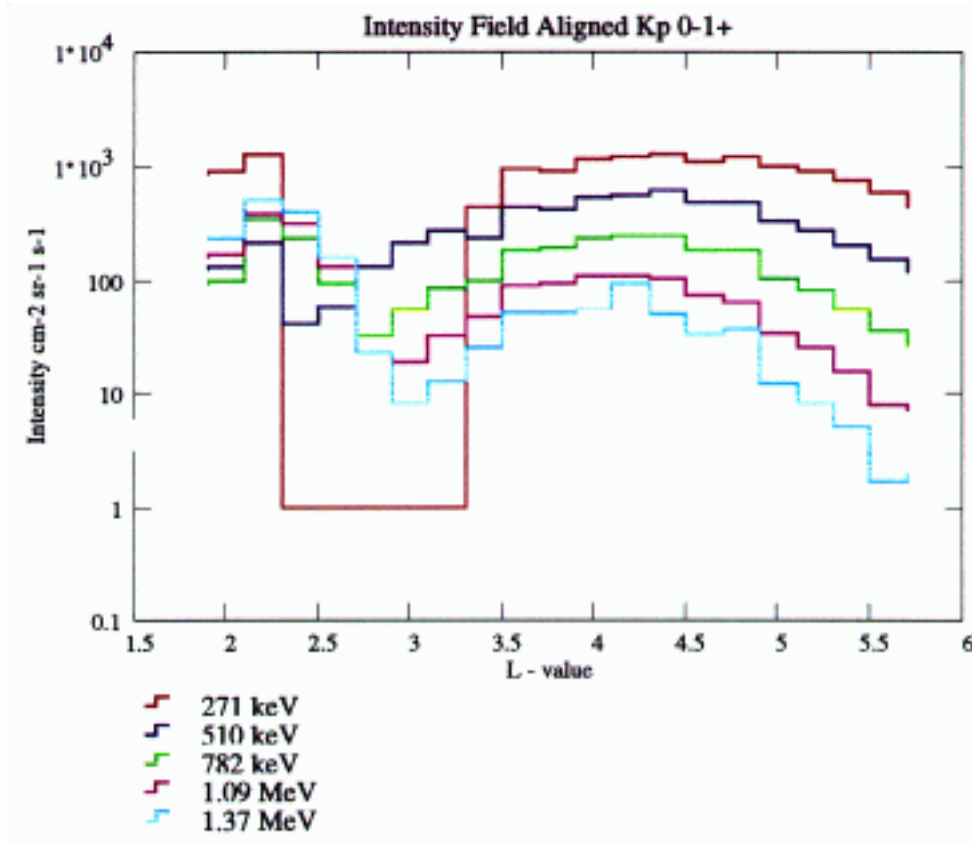


**Figure 10.15.** The intensity in the field aligned direction obtained from the Bessel function fit inside the loss cone at five energies over the entire  $L$  range for low  $K_p$  values. Note that the measurements inside  $L = 2.7$  and at the three highest energies are contaminated by penetrating protons.

2. at large  $L$  values the lower energies have the largest  $\mu_{sc}$  value while at small  $L$  values the reverse is true.

In Fig. 10.14 the same features are visible but less clearly and the radial distance at which the changeover in behaviour occurs has moved closer to the Earth. The peak in  $\mu_{sc}$  is found near the peak intensity at the corresponding energy, and the peak intensities are also found at smaller  $L$  for higher energy but the relationship is not exact. Another relationship which should be explored is with the position of the plasmopause. The average position of the plasmopause is in the range  $4.1 < L < 4.5$  but is further out and less sharp for lower  $K_p$ .

## 10.6 Fitting a Bessel function to the distribution inside the loss cone

Two parameters are derived from the fit inside the loss cone: the intensity at zero pitch angle, or the field aligned intensity, and the second scattering angle  $\alpha_{sc}$ . The field aligned intensity is the



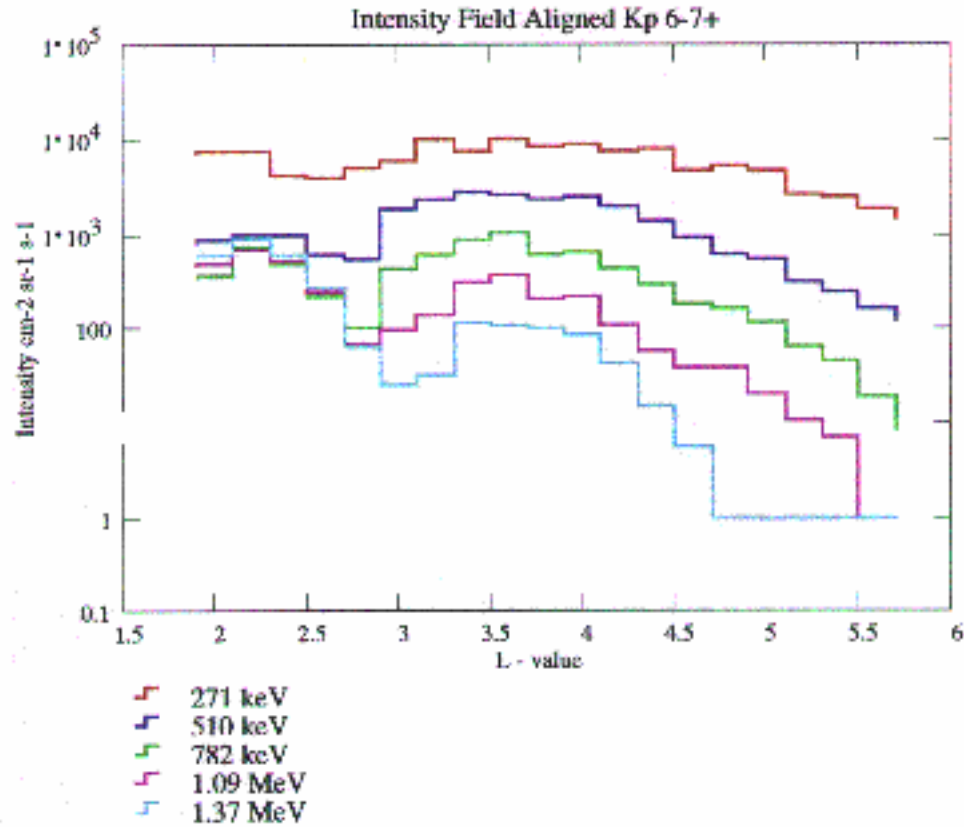


**Figure 10.16.** The intensity in the field aligned direction obtained from the Bessel function fit inside the loss cone at five energies over the entire  $L$  range for high  $K_p$  values. Note that the measurements inside  $L = 2.7$  and at the three highest energies are contaminated by penetrating protons.

best measure of the loss rate as it corresponds directly to the numbers of particles being lost per second. Figures 10.15 and 10.16 show the field aligned intensity for the same set of energies and  $K_p$  values as usual. The features are:

1. there is a peak intensity but it is at the same radial distance for all energies in contrast to the  $90^\circ$  intensity;
2. the peak is in the range  $4.1 < L < 4.5$  for  $K_p$  small and  $3.3 < L < 3.7$  for  $K_p$  large, i.e. it is clearly inside the plasmapause in both cases;
3. the precipitating flux is smaller by a factor of approximately 5 in the low  $K_p$  case over the whole range again in contrast to the  $90^\circ$  intensity, i.e. as would be expected the precipitation rate is smaller for small  $K_p$ .

The values of the scattering angle in the loss cone,  $\alpha_{sc}$ , were the most difficult to obtain because the fitted intensity at the edge of the loss cone was often smaller than the measured value at a pitch angle of  $2.5^\circ$ . Also, outside  $L = 5$ , the edge of the loss cone is inside  $2.5^\circ$ . The results are

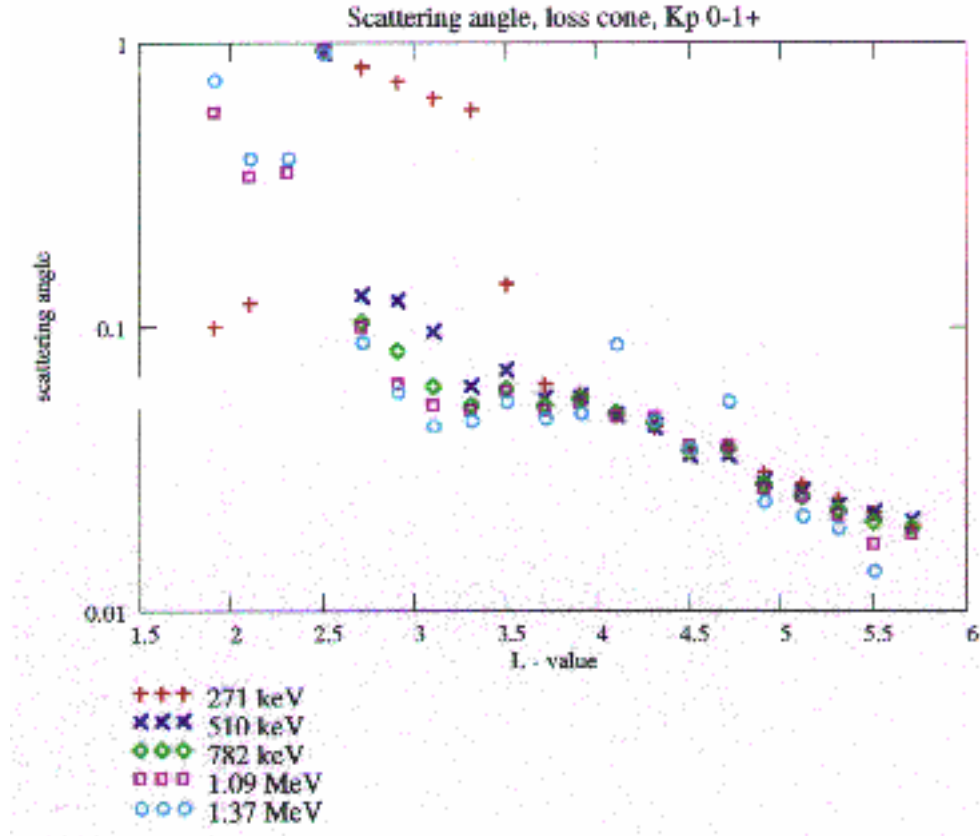


**Figure 10.17.** The scattering angle inside the loss cone obtained from the Bessel function fit at five energies over the entire  $L$  range for low  $K_p$  values. Note that the measurements inside  $L = 2.7$  and at the three highest energies are contaminated by penetrating protons.

shown in Figs. 10.17 and 10.18 for the usual energies and  $K_p$  values. There is a wide scatter on the values in both plots. Referring first to Fig. 10.18 there is a nearly continuous line of points extending from 1 at  $L = 2.5$  down to 0.2 at  $L = 5.5$ . These are the points where no curve could be fitted. A dummy value was put in the results and so these points should be ignored. In Fig. 10.17, there are only a few dummy points for  $L < 3.5$ . There is less scatter in Fig. 10.17 with a solid line of points from 0.1 at  $L = 2.5$  to 0.02 at  $L = 5.5$ , with all energies nearly superimposed on each other. A careful inspection of the distribution of points reveals that in both cases there is a minimum at  $L \sim 3$  and a maximum a little further out. This shape is consistent in all the curves. The magnitude of  $\alpha_{sc}$  is slightly smaller for low  $K_p$  and the minimum and maximum for low  $K_p$  are both slightly further out. In order to use the results for calculations of the loss rate it is necessary to remove the scatter. Since the variation through the maximum and minimum is relatively small a straight line has been fitted to the points on the log scale.

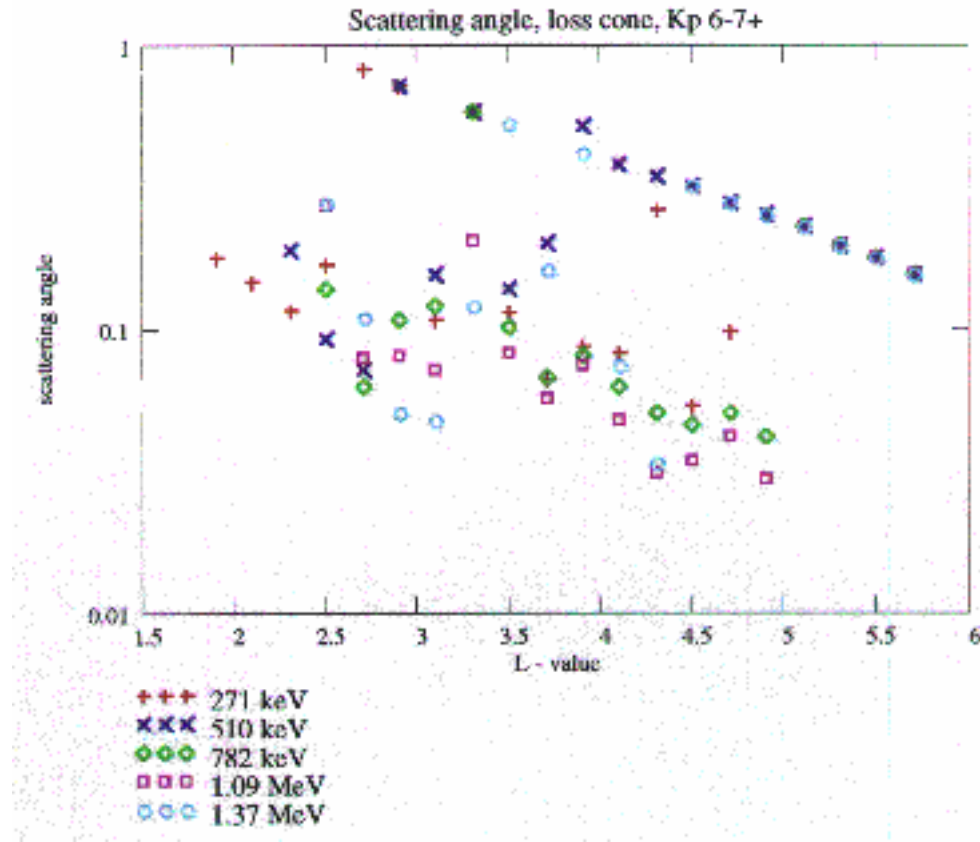


**Figure 10.18.** The scattering angle inside the loss cone obtained from the Bessel function fit at five energies over the entire  $L$  range for high  $K_p$  values. Note that the measurements inside  $L = 2.7$  and at the three highest energies are contaminated by penetrating protons.

## 10.7 Estimated loss rates

If we know the distribution of particles from  $90^\circ$  to the field aligned direction then in principle the loss rate of the particles and the decay time of the radiation can be calculated.

The results of the calculation for the two  $K_p$  ranges are shown in Figs. 10.19 and 10.20. The values range from 10 seconds to 1000 seconds, with the smallest values for the lowest  $K_p$  range and smaller  $L$  values. These values are simply not realistic and do not accord with direct measurements of the decay times, which are normally in the range of 5 to 10 days (McIlwain 1996). Furthermore the times tend to be longer at smaller  $L$  values. The variation in Figs. 10.19 and 10.20 is dominated by the variation in the volume of the flux tube. Why, therefore, are the results clearly in error? The probable reason is that the flux in the loss cone is overestimated by the measurements of the MEA detector because a) the angular resolution is inadequate to resolve the loss cone over most of the  $L$  range, and b) there is probably some background noise which has its greatest effect where the count rates are at a minimum.

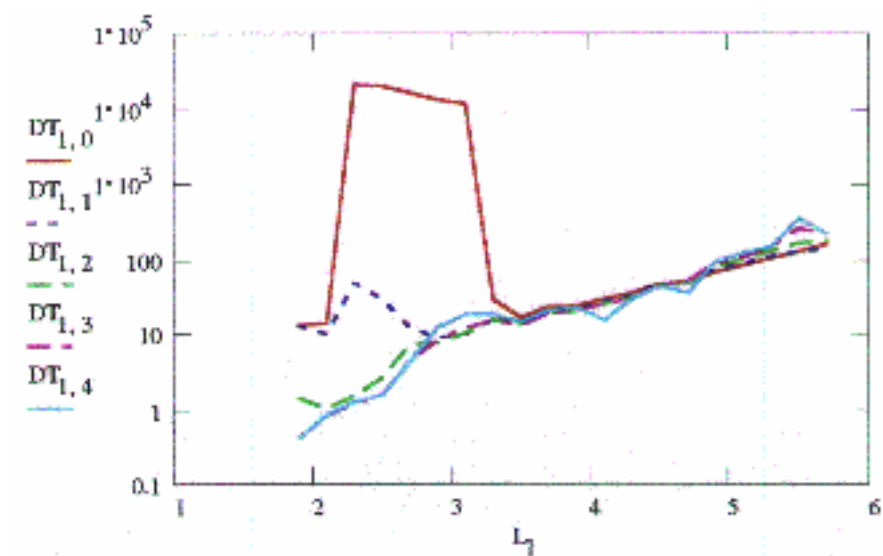


**Figure 10.19.** The decay time calculated for low  $K_p$  values. The peak at low  $L$  for 271 keV is an artifact due to missing data.

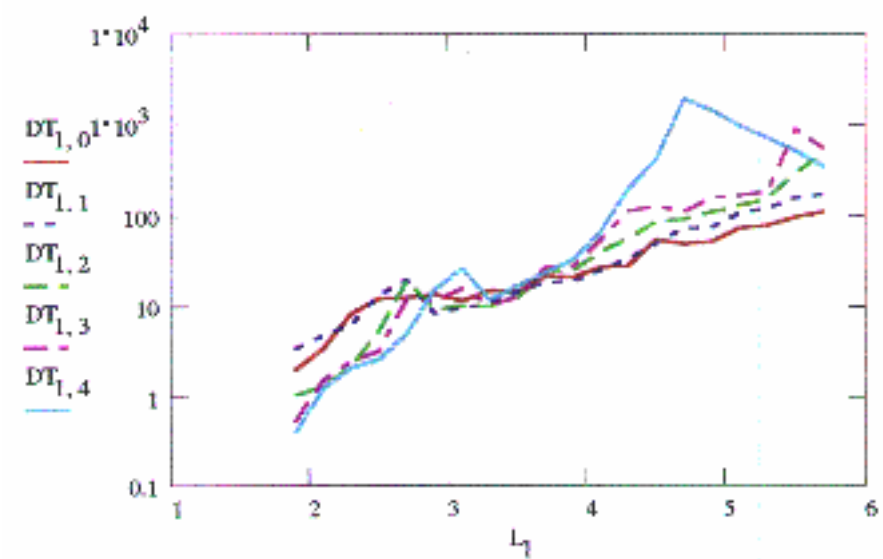


**Figure 10.20.** The decay time calculated for high  $K_p$  values

## 10.8 Conclusions

The use of the Bessel function to parameterise the pitch angle distribution works well in organizing and smoothing the data from the CRRES/MEA detector for pitch angles outside the loss cone. It shows that a model could be based on two parameters for the pitch angle distribution at each energy. One important feature which is not modelled is the existence of butterfly distributions. The effect on the average radiation intensity has not been evaluated but is not likely to be very important.

The two parameters  $\mu_{sc}$  and  $j(0)$  vary systematically, and continuously, with  $L$ , energy and  $K_p$ . Although it has not been done here, the parameters' dependence on these variables could be fitted with simple polynomial functions, thereby reducing the ECM97 model to analytical functions specified by, probably, less than 50 values instead of the current total of 61200 discrete values.

The MEA data is not adequate to specify the flux in the loss cone which is required to determine loss rates and to estimate the omnidirectional radiation levels at low altitudes. As an estimate of the lowest altitude at which the current model is reasonably accurate we take the altitude at which the loss cone is  $20^\circ$ .

The AE-8 model was based on data mainly obtained at low altitudes, and at geosynchronous orbit. Neither gives a good base for a complete model since, as the analysis here shows, only a small fraction of the distribution is actually measured (Vette 1991a).



# Chapter 11

## The Meteosat/SEM-2 data base

This chapter contains the new analysis of the archived data of the Space Environment Monitor SEM-2 onboard Meteosat. This data set provides a record of many aspects of the geosynchronous orbit environment. It is almost continuous from Nov 1988 to Nov 1995. A description of the Meteosat mission and of the SEM-2 instrument can be found in Technical Notes 6 and 7 of the TREND-2 study (the final report of TREND-2 contains a summary of this description).

Since the completion of the TREND-2 study, a number of problems have been found concerning the Meteosat-3/SEM-2 onboard data and postprocessing (see Technical Note 9 for more details). These errors became apparent in the unnatural clustering of the polar-azimuthal data to certain preferred flux values, and in regular spikes seen in some elements of the polar arrays.

During the TREND-3 study the data base has been re-analysed to correct the identified errors. The paper by Rodgers (1991) on Meteosat-3 anomalies has been updated with the corrected data base. The updated text is reproduced in Technical Note 9 of this study.

### 11.1 The new data base

The data base covers the period November 1988 to November 1995, with missing months March 1991, April 1991, and July 1995. The data format is the same as that of the data base used in TREND-2, as described in Table 11.1. The data base files have file names of the types `mmmyy_archive_hr.dat` and `mmmyy_archive_lr.dat`, e.g. `nov88_archive_hr.dat`.

### 11.2 Effect of Data Correction on TREND-2 Results

#### 11.2.1 Overview of the Error Correction

The effect of the numerous errors in the Meteosat SEM-2 data is evaluated here. Overall, the corrected data base does not differ substantially from the old one for most of the time.

**Table 11.1.** Record structure of the Meteosat/SEM-2 archived data set record

Record	Variable
1	Start time of bin in hours UT
2	End time of bin in hours UT
3	Total flux of electrons in energy range 42.9–300 keV, summed over all polar and azimuthal bins
4–8	Flux in each energy bin, summed over all polar and azimuthal bins: 4: energy range 201.8–300 keV 5: energy range 134.9–201.8 keV 6: energy range 90.7–134.9 keV 7: energy range 59.4–90.7 keV 8: energy range 42.9–59.4 keV
9	Spectral index: the slope of the logarithm of the energy spectrum, calculated using a least squares fit
10	Delta spectral index: the error on the above calculation
11–15	Polar flow: flux in one of five polar angle sectors of the analyser (bins are approximately $\pm 5^\circ$ ): 11: $150^\circ$ to spin axis 12: $120^\circ$ to spin axis 13: $90^\circ$ to spin axis 14: $60^\circ$ to spin axis 15: $30^\circ$ to spin axis
16–21	Azimuthal flow: flux in one of six azimuthal angle sectors of the analyser. The angles are (in spacecraft coordinates, where at $0^\circ$ the spacecraft looks towards the Sun): 16: $300^\circ$ – $360^\circ$ 17: $240^\circ$ – $300^\circ$ 18: $180^\circ$ – $240^\circ$ 19: $120^\circ$ – $180^\circ$ 20: $60^\circ$ – $120^\circ$ 21: $0^\circ$ – $60^\circ$
22–51	Polar-azimuthal flux: in 30 bins, for each polar angle sector across the azimuthal angles sector
52–56	Counts in each of the five energy ranges (see record 4–8)



**Table 11.1.** (Continued)

Record	Variable
57–86	Polar-azimuthal counts: again, in 30 bins
87	Anisotropy: the anisotropy index describes the angular shape of the plasma distribution relative to its axis of symmetry
88–89	$\theta$ And $\phi$ : angles describing the angular shape of the plasma distribution relative to its axis of symmetry
90	$K_p$ Index
91	$K_p(\tau)$ : Weighted average of successive $K_p$ (Wrenn 1987)
92	Latch: occurrence of latch-ups in the test RAM (random access memory)
93–96	MUM: Memory upset monitors give number of SEUs in the four memory zones of the test RAM.

- The onboard compression problem is the most common. Although capable of producing errors of 50%, it usually produced errors much lower than that. The effect is always a decrease in the observed flux. Because the output flux arrays are averages of many count values, the effects of this error are generally diluted. No significant changes in the average flux or the dependence on LT are expected.
- The ISCALE error, occurs only for those rare events when an overflow is flagged. The effect is usually a small depression of flux and because of averaging, it is again significantly diluted.
- The overflow error can have a substantial effect when flux is very high, i.e. during sub-storm injection events. This error causes a substantial decrease in flux and, because real overflows may occur one after another, may lead to sections of the flux time sequence being depressed. By affecting the peak height of events, this error may cause a change in variance of 43–60 keV electrons, because the flux of the most significant events will be higher. But whilst the heights of these events will change, there will not be changes in timing so that the dispersion seen by the superposed epoch analysis and the time correlation analysis will be unaffected.

Although the overflow error was potentially very serious, there are believed to be only about 150 genuine overflows out of the 24,000 which were flagged over the seven-year data set. Out of a total data set of over 400,000 data points, this is a very small number of bad points, although statistically it is obviously more important than the number of points implies because the erroneous data points are not randomly distributed throughout the data set, but rather occur during the most energetic injection events.

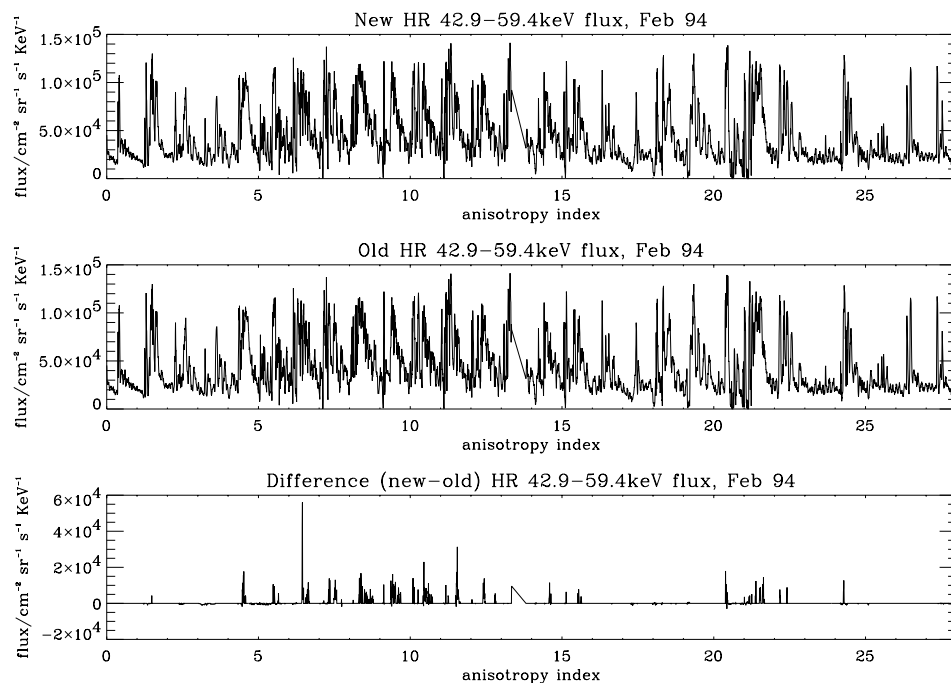


**Figure 11.1.** E5-E4 flux, before and after data set corrections

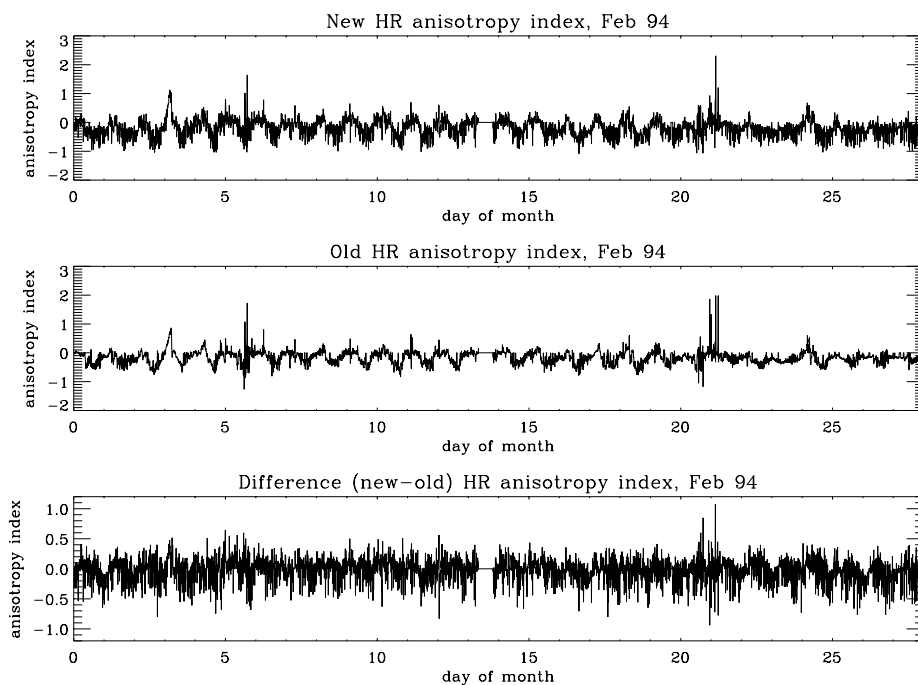


**Figure 11.2.** Anisotropy index, before and after data set corrections

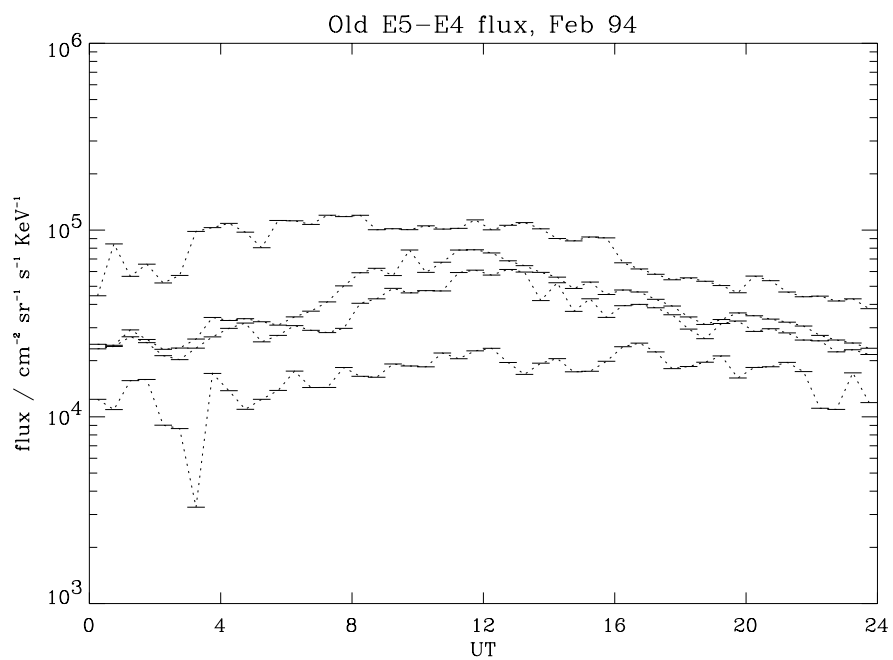


**Figure 11.3.** E5-E4 flux statistical plot, before data set corrections

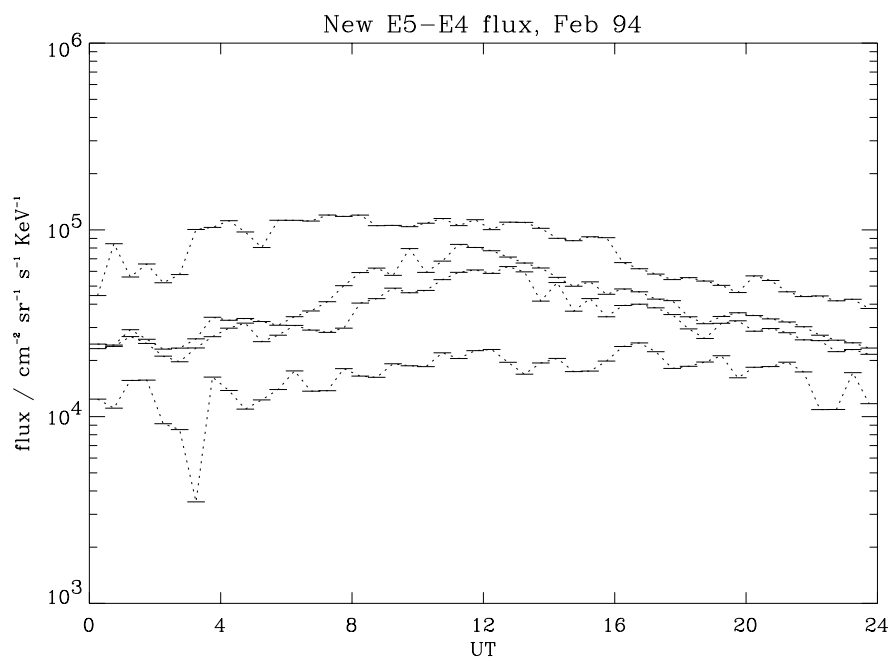


**Figure 11.4.** E5-E4 flux statistical plot, after data set corrections

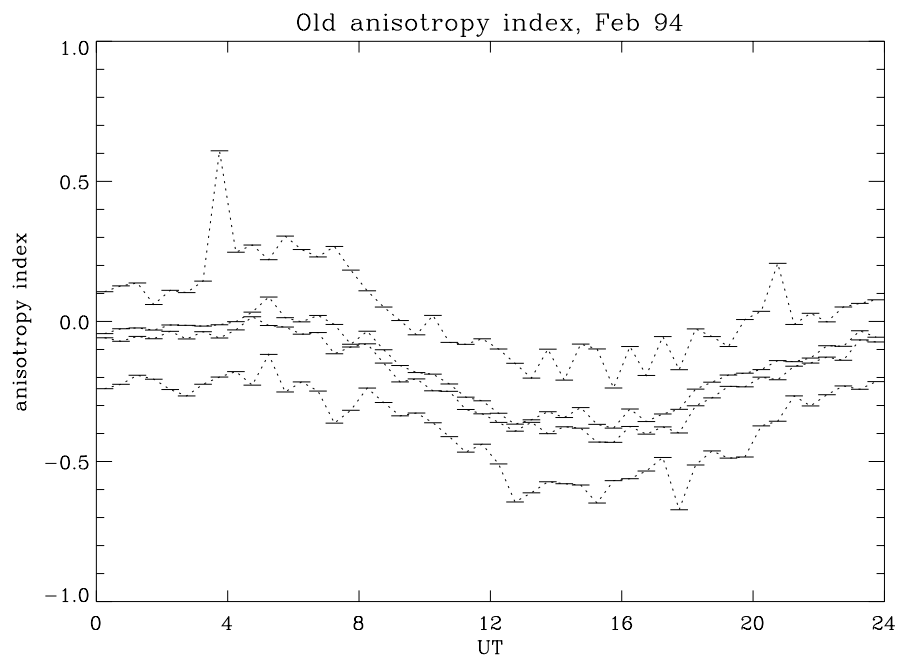


**Figure 11.5.** Anisotropy index statistical plot, before data set corrections

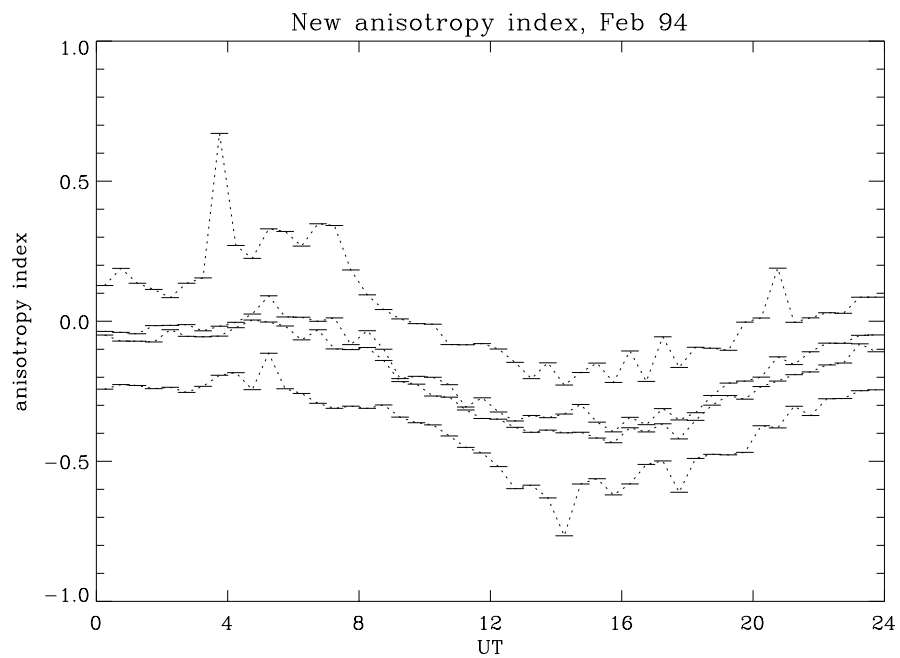


**Figure 11.6.** Anisotropy index statistical plot, after data set corrections

### 11.2.2 Comparison of ‘Before’ and ‘After’ data

Some example plots of data before and after all the errors were corrected are shown in Figs. 11.1 and 11.2. Figure 11.1 shows the high time resolution E5-E4 flux (42.9-59.4keV) for February 1994. This month was chosen because it contained the largest number of genuine overflows: a total of 16. The E5-E4 flux is shown since it is likely to contain the most genuine overflows and therefore the largest errors. Note that all energies include some errors, even the highest energy which does not overflow. Therefore, the differences between the new and old data for this month are likely to be the most severe. The upper two panels of Fig. 11.1 show the new and old data respectively. The diurnal variation can be clearly seen in the flux data, with peak fluxes of the order of  $1.0\text{--}1.4 \times 10^5 \text{cm}^{-2} \text{sr}^{-1} \text{s}^{-1} \text{keV}^{-1}$  occurring daily. The bottom panel of Fig. 11.1 shows the difference between the new and old flux data, as *new minus old*. The maximum difference is less than  $6.0 \times 10^4 \text{cm}^{-2} \text{sr}^{-1} \text{s}^{-1} \text{keV}^{-1}$ . The plot shows that in the old data set, where data points were wrong, their values were generally underestimated. The errors look relatively small, but because of the overflow error the largest errors occur where the flux was severely underestimated: the maximum difference point here corresponds to a flux value which, in the old data set, was 66% too low. However, since most of the erroneous points were not affected by the overflow error but by the less significant errors, most of the errors were much lower. In fact, less than 5% of the 4408 data points that make up February 1994, were out by more than 5%, and only 1.75% of points were out by more than 10%.

The high time resolution anisotropy index is shown in Fig. 11.2. The anisotropy index is affected by the errors because it is calculated from the polar-azimuthal count arrays, which were found to contain strong effects of the decompression and ISCALE errors. These effects are much less obvious in the flux arrays because of the averaging that has been done to produce them. The maximum difference between the new and old values is about 1.0 compared with peak anisotropy index values of about 2.0. Many more anisotropy points are affected than flux points.

In the course of the TREND studies, many statistical models were produced using long-term averaging of the SEM-2 data. Some sample plots have been produced to show how these models may have been affected by the errors.

Figures 11.3 and 11.4 show statistical plots of the E5-E4 flux data for February 1994, before and after error corrections respectively. These plots use the low time resolution data (30 minute averages). Note that the *x*-axis is UT rather than LT (Meteosat was at longitude 74° west at this time, so local midnight is at about 0500 UT on these plots). These plots show four lines: the upper and lower lines are the levels below and above which 95% of the data are observed, and the middle two lines show the median  $\pm 5\%$  of observations. Although the plots use only one month of data and, therefore, can be expected to show a fair amount of scatter, the two plots show hardly any differences.

Similarly, Figs. 11.5 and 11.6 show statistical plots of the anisotropy index before and after error corrections respectively. Again, the plots show very few differences.

### 11.2.3 Conclusions

We conclude that the errors did not affect the results of the previous TREND studies. Although the various errors could have significant effects on individual data points, most of the study results relied on statistical studies where the effect of including a few erroneous points in a large sample of data would have been small.

The example plots of 'before' and 'after' data presented here have shown that the statistical models produced in the TREND reports are unlikely to change significantly with the correction of the errors. The important results are the local time dependence and overall flux range, neither of which should change significantly. This conclusion should hold for all the local time dependence models, for the Fourier and wavelet analysis, for the correlation analyses showing the lag between different energy flux, and the flux probability versus mission duration models. It is our belief that reproducing these models and analyses with the corrected data set would yield very similar results and the same conclusions.

The work most likely to have been affected by the errors would have been the studies of the flux peaks due to substorm injections which used superposed epoch analysis. This work used a sample of 200 flux peaks from the year 1989. This year was found to have 42 genuine overflows, some of which will have been included in the sample. However, generally only the lowest energy bin is affected, and although the flux level will rise, its other attributes such as duration should not change unless, of course, there is a sustained period of high flux.

# References

- Abramowitz, M., Stegun, I.A.: 1964, *Handbook of Mathematical Functions With Formulas, Graphs and Mathematical Tables*, National Bureau of Standards, Applied Mathematics Series **55**
- Achtermann, E., Häusler, B., Hovestadt, D., Paschmann, G.: 1970, *Die Experimente EI 88 und EI 93 zur Messung von energiereichen Elektronen, Protonen und Alphateilchen im Satelliten AZUR. Physikalische Eigenschaften und Testmessungen*, BMBW-FB W 70-67
- Allen, C.W.: 1985, *Astrophysical Quantities*, Third ed., The Athlone Press, London
- Althouse, W.E., Cummings, A.C., Garrard, T.L., Mewaldt, R.A., Stone, E.C.: 1978, *A cosmic ray isotope spectrometer*, Geoscience Electronics **16**, 204–207
- Anderson, A.D., Francis, W.E.: 1964, *A semitheoretical model for atmospheric properties from 90 to 10,000 km*, Lockheed Missiles and Space Company 6-74-64-19
- Appleby, M.H., Griffin B.N., Turner E.R., Pogue, W.R., Golightly M.J.: 1992, *Computer Aided Radiation Analysis for Manned Spacecraft*, Proc. 22nd International Conference on Environmental Systems, Seattle, WA, July 13–16
- Armstrong, T.W., Chandler, K.C.: 1972, *The High-Energy Transport Code HETC*, Nucl. Sci. Engr. **49**, 110
- Armstrong, T.W., Colborn, B.L., Watts, J.W.: 1990, *Characteristics of Trapped Proton Anisotropy at Space Station Freedom Altitudes*, Science Applications International Corporation Report SAIC-90/1474
- Armstrong, T.W., Colborn, B.L., Watts, J.W.: 1992a, *Ionizing Radiation Calculations and Comparisons With LDEF Data*, First LDEF Post-Retrieval Symposium, NASA-CP-3134
- Armstrong, T.W., Colborn, B.L., Harmon, B.A., Parnell, T.A., Watts, J.W., Jr., Benton, E.V.: 1992b, *Comparison of Model Predictions With LDEF Satellite Radiation Measurements*, World Space Congress, 29th Plenary Meeting of COSPAR, Washington D.C., August 29–September 5, Paper F2.7-M.1.06X
- Badhwar, G.D., Konradi, A.: 1990, *Conversion of Omnidirectional Proton Fluxes into a Pitch Angle Distribution*, J. Spacecraft and Rockets **27**, 350–352
- Baker, D.N., Mason, G.M., Figueroa, O., Colon, G., Watzin, J.G., Aleman, R.M.: 1993, *An Overview of the Solar, Anomalous, and Magnetospheric Particle Explorer (SAMPEX) Mission*, IEEE Trans. Geosci. Remote Sensing **31**, 531–541
- Bilitza, D.: 1990, *International Reference Ionosphere 1990*, NSSDC/WDC-AR&S 90-20

- Brautigam, D.H., Bell, J.T.: 1995, *CRRESELE Documentation*, PL-TR-95-2128, Environmental Research Papers, No. 1178, Phillips Laboratory
- Brautigam, D.H., Gussenhoven, M.S., Mullen, E.G.: 1992, *Quasi-static Model of Outer Zone Electrons*, IEEE Trans. Nucl. Sci. **39**, 1797–1803
- Burrell, M.O.: 1964, *The Calculation of Proton Penetration and Dose Rates*, NASA TM X-53063
- Cain, J.C., Hendricks, S.J., Langel, R.A., Hudson, W.V.: 1967, *A Proposed Model for the International Geomagnetic Reference Field-1965*, J. Geomag. Geoelectr. **19**, 335–355
- Carpenter, D.L., Anderson, R.R.: 1992, *An ISEE/Whistler Model of Equatorial Electron Density in the Magnetosphere*, J. Geophys. Res. **97**, 1097–1108
- Chabrillat, S.: 1995, *Optimization and use of Hedin thermospheric empirical model MSIS*, Aeronomica Acta **B 55**
- Colborn, B.L., Watts, J.W., Armstrong, T.W.: 1990 *Data Base Description and Retrieval Program for the Trapped Proton Vector Flux Data Bases VF1MAX and VF1MIN*, Science Applications International Corporation Report SAIC-90/1475
- Cook, W.R., Cummings, A.C., Cummings, J.R., Garrard, T.L., Kecman, B., Mewaldt, R.A., Selesnick, R.S., Stone, E.C., von Rosenvinge, T.T. : 1993a, *MAST: A Mass Spectrometer Telescope for Isotope Studies of Solar, Anomalous, and Galactic Cosmic Rays*, IEEE Trans. Geosci. Remote Sensing **31**, 557–564
- Cook, W.R., Cummings, A.C., Cummings, J.R., Garrard, T.L., Kecman, B., Mewaldt, R.A., Selesnick, R.S., Stone, E.C., Baker, D.N., von Rosenvinge, T.T., Blake, J.B., Callis, L.B.: 1993b, *PET: A Proton/Electron Telescope for Studies of Magnetospheric, Solar and Galactic Particles*, IEEE Trans. Geosci. Remote Sensing **31**, 565–571
- Daly, E.J., Evans, H.D.R.: 1993, *Problems in Radiation Environment Models at Low Altitudes*, Memorandum ESA/ESTEC/WMA/93-067/ED
- Evans, H.D.R., Daly E.J.: 1989, *Anisotropies in the Low Altitude Radiation Environment*, Memorandum ESA/ESTEC/WMA
- Fairfield, D.H., Tsyganenko, N.A., Usmanov, A.V., Malkov, M.V.: 1994, *A large magnetosphere magnetic field database*, J. Geophys. Res. **99**, 11,319–11,326
- Fischer H.M., Auschrat, V.W., Wibberenz, G.: 1977, *Angular Distribution and Energy Spectra of Protons of Energy  $5 < E < 50$  MeV at the Lower Edge of the Radiation Belt in Equatorial Latitudes*, J. Geophys. Res. **82**, 537–547
- Fraser-Smith, A.C.: 1987, *Centered and Eccentric Geomagnetic Dipoles and Their Poles*, 1600–1985, Rev. Geophys. **25**, 1–16
- Fritz, T.A., Cessna, J.R.: 1975, *ATS-6 NOAA low energy proton experiment*, IEEE Trans. Aerosp. Electron. Syst. **11**, 1145
- Gill, S.: 1951, *A process for the step-by-step integration of differential equations in an automatic digital computing machine*, Proceedings of the Cambridge Philosophical Society **47**, 96–108



- Haerendel, G.: 1962, *A Possible Correction to the Spectrum of Geomagnetically Trapped Protons*, J. Geophys. Res. **67**, 1173–1174, and corrigendum, J. Geophys. Res. **67**, 1697
- Hassitt, A.: 1965, *Average Effect of the Atmosphere on Trapped Protons*, J. Geophys. Res. **70**, 5385–5394
- Häusler, B.: 1972, *Untersuchungen des Verhaltens hochenergetischer Protonen und Elektronen in der inneren Magnetosphäre*, MPI-PAE/Extraterr. **66**
- Heckman, H.H., Brady, V.O.: 1966, *Effective Atmospheric Losses for 125-MeV Protons in South Atlantic Anomaly*, J. Geophys. Res. **71**, 2791–2798
- Heckman, H.H., Nakano, G.H.: 1969, *Low-Altitude Trapped Protons during Solar Minimum Period, 1962–1966*, J. Geophys. Res. **74**, 3575–3590
- Hedin, A.E.: 1991, *Extension of the MSIS thermosphere model into the lower atmosphere*, J. Geophys. Res. **96**, 1159–1172
- Hess, W.N.: 1968, *The Radiation Belt and Magnetosphere*, Blaisdell Publishing Company, Waltham (Massachusetts)
- Heynderickx, D., Lemaire, J.: 1992, *Description of the Combined Release and Radiation Effects Satellite Experiments and Data Sets*, Technical Note 4 of the TREND-2 Project, ESA/ESTEC/WMA TRP Contract No. 9828/92/NL/FM
- Heynderickx, D., Lemaire, J.: 1993, *Improvements to Trapped Radiation Software*, Technical Note 1 of the TREND-2 Project, ESA/ESTEC/WMA TRP Contract No. 9828/92/NL/FM
- Heynderickx, D., Lemaire, J., Pierrard, V.: 1995, *Atmospheric Cut-Off*, Technical Note 2 of the TREND-2 Project, ESA/ESTEC/WMA TRP Contract No. 9828/92/NL/FM
- Heynderickx, D., Lemaire, J., Daly, E.J.: 1996a, *Historical Review of the Different Procedures Used to Compute the L-Parameter*, Radiat. Meas. **26**, 325–331
- Heynderickx, D., Lemaire, J., Daly, E.J., Evans, H.D.R.: 1996b, *Calculating Low-Altitude Trapped Particle Fluxes With the NASA Models AP-8 and AE-8*, Radiat. Meas. **26**, 947–952
- Heynderickx, D., Kruglanski, M., Lemaire, J.F., Daly, E.J.: 1996c, *A New Tool for Calculating Drift Shell Averaged Atmospheric Density*, Proc. Workshop on Radiation Belts: Models & Standards, Brussels, October 17–20, 1995 (eds. J.F. Lemaire, D. Heynderickx, D.N. Baker), Geophysical Monograph 97, 173–178
- Heynderickx, D., Kruglanski, M., Lemaire, J.F.: 1996d, *UNIRAD User Manual*
- Hunerwadel, J.L., Sellers, B., Hanser, F.A.: 1987, *Design, Fabricate, Calibrate, and Deliver Two Satellite Electron Flux Detectors*, AFGL-TR-87-0205, Air Force Geophysics Laboratory, Hanscom AFB, MA, ADA 190799
- Jensen, D.C., Cain, J.C.: 1962, *An Interim Geomagnetic Field*, J. Geophys. Res. **67**, 3568
- Kennel, C.F., Petschek, H.E.: 1966, *Limit on Stably Trapped Particle Fluxes*, J. Geophys. Res. **71**, 1–28
- Keppeler E., Wilken B., Umlauf G., Fischer H., Williams D.J., Richter K., Bubla E., Fischer K.: 1978, *Ein Spectrometer für geladene Teilchen mittlerer Energien—Experiment KED-ISEE*, Forschungsber. des Bundesmin. f. Forschung und Technologie, BMFT-FB W 78-19

- Kern, J.W.: 1989, *A Note on Vector Flux Models for Radiation Dose Calculations*, preprint
- Kruglanski, M.: 1996, *Use of (B, L) Coordinates in Radiation Dose Models*, Proc. of Workshop on Radiation Belts: Models & Standards, Brussels, October 17–20, 1995, Geophysical Monograph **97**, 195–199
- Lemaire, J., Johnstone, A.D., Heynderickx, D., Rodgers, D.J., Szita, S., Pierrard, V.: 1995, Final Report of the TREND-2 Project, ESA/ESTEC/WMA TRP Contract No. 9828/92/NL/FM
- Lenchek, A.M., Singer, S.F.: 1962, *Effects of the Finite Gyroradii of Geomagnetically Trapped Protons*, J. Geophys. Res. **67**, 4073–4075
- Looper, M.D., Blake, J.B., Mewaldt, R.A.: 1998, *Maps of Hydrogen Isotopes at Low-Altitude in the Inner Zone from SAMPEX Observations*, Adv. Sp. Res., in press
- Lynch, K., Boughan, E., Fisch, D., Hardy, D., Riehl, K.: 1989, *PROTEL: Design, Fabrication, Calibration, Testing, and Satellite Integration of a Proton Telescope*, AFGL-TR-89-0045, Air Force Geophysics Laboratory, Hanscom AFB, MA, ADA 214564
- McIlwain, C.E.: 1961, *Coordinates for Mapping the Distribution of Magnetically Trapped Particles*, J. Geophys. Res. **66**, 3681–3691
- McIlwain, C.E.: 1996, *Processes Acting Upon Outer Zone Electrons*, Proc. Workshop on Radiation Belts: Models and Standards, Brussels, October 17–20, 1995 (eds. J.F. Lemaire, D. Heynderickx, D.N. Baker), Geophysical Monograph 97, 15–26
- Mead, G.D., Fairfield, D.H.: 1975, *A quantitative magnetospheric model derived from spacecraft magnetometer data*, J. Geophys. Res. **80**, 523–534
- Meffert, J.D., Gussenhoven, M.S.: 1994, *CRRESPRO Documentation*, PL-TR-94-2218, Environmental Research Papers, No. 1158, Phillips Laboratory
- Olson, W.P., Pfizter, K.A.: 1977, *Magnetospheric magnetic field modeling*, Annual Scientific Report, AFOSR Contract No. F44620-75-C-0033
- Olson, W.P., Pfizter, K.A., Mogstad, T.: 1988, *A time dependent source driven magnetospheric magnetic field model*, EOS **69**, 426
- Ostapenko, A.A., Maltsev, Y.P.: 1997, *Relation of the magnetic field in the magnetosphere to the geomagnetic and solar wind activity*, J. Geophys. Res. **102**, 17,467–17,473
- Pfizer, K.A.: 1990, *Radiation Dose to Man and Hardware as a Function of Atmospheric Density in the 28.5 Degree Space Station Orbit*, MDSSC Report No. H5387 Rev A
- Pfizer, K.A.: 1991, *Improved Models of the Inner and Outer Radiation Belts*, Phillips Laboratory Scientific Report PL-TR-91-2187
- Pierrard, V.: 1994, *Cross sections for collisions between electrons or protons and the main atmospheric components*, Aeronomica Acta **B 54**
- Reber, C.A.: 1993, *The Upper Atmosphere Research Satellite (UARS)*, Geophys. Res. Let. **20**, 1215–1218
- Reber, C.A., Trevathan, C.E., McNeal, R.J., Luther, M.R.: 1993, *The Upper Atmosphere Research Satellite (UARS) Mission*, J. Geophys. Res. **98**, 10643–10647

- Roberts, C.S.: 1969, *Pitch-Angle Diffusion of Electrons in the Magnetosphere*, Rev. Geophys. **7**, 305–337
- Rodgers, D.J.: 1991, *Correlation of Meteosat-3 Anomalies with Data from the Spacecraft Environment Monitor*, ESTEC Working Paper **1620**
- Rodgers D.J.: 1996, *A New Empirical Electron Model*, Proc. Workshop on Radiation Belts: Models & Standards, Brussels, October 17–20, 1995 (eds. J.F. Lemaire, D. Heynderickx, D.N. Baker), Geophysical Monograph 97, 103–107
- Roederer, J.G.: 1970, *Dynamics of Geomagnetically Trapped Radiation*, Springer-Verlag
- Roelof, E.C., Keath, E.P., Bostrom, C.O., Williams, D.J.: 1976, *Fluxes of  $\geq 50$  keV protons and  $\geq 30$  keV electrons at  $35 R_E$ . 1. Velocity anisotropy and plasma flow in the magnetotail*, J. Geophys. Res. **81**, 2304
- Russell, C.T.: 1987, *The Magnetosphere*, in The Solar Wind and the Earth, Akasofu, S.I. and Kamide, Y. (eds.), Terra Scientific Publishing Co., Tokyo, 71–100
- Sawyer, D.M., Vette, J.I.: 1976, *AP-8 Trapped Proton Environment for Solar Maximum and Solar Minimum*, NSSDC/WDC-A-R&S 76-06
- Schultz, M., Lanzerotti, L.J.: 1974, *Particle Diffusion in the Radiation Belts*, Springer-Verlag
- Sharber, J.R., Frahm, R.A., Winningham, J.D., Biard, J.C., Lummerzheim, D., et al.: 1993, *Observations of the UARS Particle Environment Monitor and Computation of Ionization Rates in the Middle and Upper Atmosphere During a Geomagnetic Storm*, Geophys. Res. Lett. **20**, 1319–1322
- Sharber, J.R., Link, R., Frahm, R.A., Winningham, J.D., Lummerzheim, D., et al.: 1996, *Validation of UARS particle environment monitor electron energy deposition*, J. Geophys. Res. **101**, 9571–9582
- Stone, E.C., Vogt, R.E., McDonald, F.B., Teegarden, B.J., Trainor, J.H., Jokipii, J.R., Webber, W.R.: 1977, *Cosmic ray investigation for the Voyager missions; Energetic particle studies in the outer heliosphere—and beyond*, Space Sci. Rev. **21**, 355–376
- Sullivan, J.D.: 1971, *Geometrical factor and directional response of single and multi-element particle telescopes*, Nucl. Instr. Meth. **95**, 5–11
- Tsyganenko, N.A.: 1987, *Global quantitative models of the geomagnetic field in the cislunar magnetosphere for different disturbance levels*, Planet. Space Sci. **35**, 1347–1358
- Tsyganenko, N.A.: 1989, *A magnetospheric magnetic field model with a wrapped tail current sheet*, Planet. Space Sci. **37**, 5–20
- Tsyganenko, N.A., Stern, D.P.: 1996, *Modeling the global magnetic field the large-scale Birke-land current systems*, J. Geophys. Res. **101**, 27187–27198
- Valot, P., Engelmann, J.: 1973, *Pitch-angle Distribution of Geomagnetically Trapped Protons for  $1.2 < L < 2.1$* , Space Research XIII, Akademie Verlag, Berlin, 675–681
- Vampola, A.L., Osborn, J.V., Johnson, B.M.: 1992, *CRRES Magnetic Electron Spectrometer AFGL-701-5A (MEA)*, J. Spacecr. Rockets **29**, 592–595
- Vampola, A.L.: 1996, *Outer Zone Energetic Electron Environment Update*, Final Report of ESA/ESTEC/WMA/P.O.151351

- Vette, J.I.: 1991a, *The AE-8 Trapped Electron Model Environment*, NSSDC/WDC-A-R&S 91-24
- Vette, J.I.: 1991b, *The NASA/National Space Science Data Center Trapped Radiation Environment Model Program (1964–1991)*, NSSDC/WDC-A-R&S 91-29
- Violet, M.D., Lynch, K., Redus, R., Riehl, K., Boughan, E., Hein, C.: 1993, *Proton Telescope (PROTEL) on the CRRES Spacecraft*, IEEE Trans. Nucl. Sci. **40**, 242
- Walt, M.: 1994, *Introduction to Geomagnetically Trapped Radiation*, University Press, Cambridge
- Walt, M., MacDonald, W.M.: 1964, *The Influence of the Earth's Atmosphere on Geomagnetically Trapped Particles*, Rev. Geophys. **2**, 543–577
- Watts, J.W., Parnell, T.A., Heckman, H.H.: 1989, *Approximate Angular Distribution and Spectra for Geomagnetically Trapped Protons in Low-Earth Orbit*, Conf. on High-Energy Radiation in Background Space, A.C. Rester Jr. and J.I. Trombka (Eds.), Santibel Island, FL 1987, Am. Inst. Phys. Conf. Proc., New York, 75–85
- Wentworth, R.C.: 1963, *Pitch Angle Diffusion in a Magnetic Mirror Geometry*, Phys. Fluids **6**, 431–437
- Williams, D.J.: 1977, *The magnetic ion-electron separation and solid state detector detection system flown on IMP 7 and 8:  $E_p > 50$  keV,  $E_e > 30$  keV*, MPAE Research Report MPAE-W-100-77-51
- Williams, D.J., Arens, J.F., Lanzerotti, L.J.: 1968, *Observations of Trapped Electrons at Low and High Altitudes*, J. Geophys. Res. **73**, 5673
- Williams, D.J., Keppler, E., Fritz, T.A., Wilken, B., Wibberenz, H.: 1978, *The ISEE-1 and -2 medium energy particles experiment*, NOAA Technical Memorandum ERL SEL-51, Space Environment Laboratory, Boulder, Colorado, USA, April 1978; IEEE Transact. Geosci. Electronics **16**, 270
- Winningham, J.D., Sharber, J.R., Frahm, R.A., Burch, J.L., Eaker, N., et al.: 1993, *The UARS Particle Environment Monitor*, J. Geophys. Res. **98**, 10,649–10,666
- Wrenn, 1987
- Yoshida, S., Ludwig, G.H., Van Allen, J.A.: 1960, *Distribution of Trapped Radiation in the Geomagnetic Field*, J. Geophys. Res. **65**, 807–813

# Appendix A

## Correction procedure for finite telescope opening angles

In order to construct flux maps, count rates have to be converted to physical units (fluxes) and averaged over two dimensional coordinate grids. The conversion to fluxes is an iterative process because of the finite aperture of the detectors, i.e. the true unidirectional flux has to be derived from the measured count rate in successive approximations.

### A.1 Conversion to fluxes

The description of geometric factor and directional response in this section is based on a paper by Sullivan (1971).

#### A.1.1 General formulation

The coincidence counting rate of any particle telescope depends upon the effective dimensions and positions of the telescope sensors as well as on the sensor efficiencies. For an ideal telescope—whose efficiency for detecting particles of a given type is one in a given energy interval and zero otherwise and whose sensors are mathematical surfaces with no thickness—the factor of proportionality relating the counting rate  $C$  to the integral directional particle flux  $J$  is defined as the gathering power  $\Gamma$  of the telescope. When the flux is isotropic, i.e.  $J = J_0$ , the factor of proportionality is called the geometric factor  $G$ :

$$C = G J_0 . \quad (\text{A.1})$$

Exact expressions can be obtained for the geometric factor and directional response of cylindrically symmetric telescopes.

The coincidence counting rate of a particle telescope can be expressed as:

$$C(\mathbf{x}, t_0) = \frac{1}{T} \int_{t_0}^{t_0+T} dt \int_S \mathbf{r} \cdot d\sigma \int_{\Omega} d\omega \int_0^{\infty} dE \sum_i \varepsilon_i(E, \sigma, \omega, t) j_i(E, \omega, t) , \quad (\text{A.2})$$

where

$C$	=	coincidence counting rate ( $\text{s}^{-1}$ ),
$\mathbf{x}$	=	position vector of the telescope
$i$	=	label for type of particle,
$j_i$	=	differential directional flux of particle type $i$ ( $\text{s}^{-1}\text{cm}^{-2}\text{sr}^{-1}\text{MeV}^{-1}$ ),
$\varepsilon_i$	=	detection efficiency for particle type $i$ ,
$t$	=	time,
$t_0$	=	time at start of observation,
$T$	=	total observation time,
$d\sigma$	=	element of surface area of the last sensor to be penetrated,
$S$	=	total area of the last telescope sensor,
$\mathbf{r}$	=	unit vector specified by spherical coordinates $(\theta, \phi)$ ,
$d\omega = -d\phi d\cos\theta$	=	element of solid angle around $\mathbf{r}$ ,
$\Omega$	=	domain of $\Omega$ defined by the other telescope sensors,
$\mathbf{r} \cdot d\sigma$	=	effective element of area looking into $\omega$ .

Equation (A.2) expresses the requirements for the detection of a particle. Although it is quite general, the following implicit assumptions have been made:

1.  $d\sigma$ ,  $\omega$ , and  $\mathbf{x}$  are time independent;
2. no transformation of particle type occurs other than that included in  $\varepsilon_i$ ;
3. the particle trajectory is a straight line.

Dropping these assumptions severely complicates the treatment of the problem and renders an analytic solution difficult. The first assumption may not be valid for a rapidly spinning satellite and/or long accumulation times.

To simplify the problem further, we consider only ideal telescopes where the efficiency is independent of  $\omega$ ,  $\sigma$  and  $t$ , and consider only one particle type (henceforth, we will drop the subscript denoting particle type).

With the assumption that  $j$  is independent of  $t$  and separates into

$$j(E, \omega) = j_0(E) F(\omega), \quad (\text{A.3})$$

where  $F(\omega)$  is normalised so that  $\int F(\omega) d\omega = 1$ , Eq. (A.2) becomes

$$C = \left[ \int_{\Omega} d\omega \int_S F(\omega) \mathbf{r} \cdot d\sigma \right] J \equiv \Gamma_F J, \quad (\text{A.4})$$

where

$$J = \int_0^{\infty} j_0(E) \varepsilon(E) dE. \quad (\text{A.5})$$

In the case of a detector with well defined energy channels with uniform response

$$\varepsilon_1 = \begin{cases} 1, & E_1 \leq E \leq E_u, \\ 0, & E < E_1, E > E_u, \end{cases} \quad (\text{A.6})$$

$J$  is given by

$$J = \int_{E_l}^{E_u} j_0(E) dE, \quad (\text{A.7})$$

which, for small energy ranges, can be approximated by

$$J = j_0[(E_l + E_u)/2] (E_u - E_l). \quad (\text{A.8})$$

The expression in square brackets in Eq. (A.4) is the gathering power  $\Gamma_F$  of the telescope when the intensity has an angular dependence given by  $F(\omega)$ , i.e.

$$\Gamma_F = \int_{\Omega} d\omega \int_S F(\omega) \mathbf{r} \cdot d\sigma = \int_{\Omega} F(\omega) d\omega \int_S \mathbf{r} \cdot d\sigma. \quad (\text{A.9})$$

The directional response function  $R(\omega)$  of a telescope can be defined as:

$$R(\omega) = \int_S \mathbf{r} \cdot d\sigma. \quad (\text{A.10})$$

For a telescope with cylindrical symmetry the effective area  $h$  is related to  $R$  as:

$$h(\theta) \cos \theta = \int_S \mathbf{r} \cdot d\sigma. \quad (\text{A.11})$$

With this definition Eq. (A.9) can be rewritten as

$$\Gamma_F = \int_0^{2\pi} \int_0^{\theta_1} F(\theta, \phi) h(\theta) \cos \theta \sin \theta d\theta d\phi, \quad (\text{A.12})$$

where  $\theta_1$  is the telescope opening half angle. If the flux is isotropic then  $F$  is unity and the geometric factor (the gathering power for isotropic flux) depends only on the geometry of the telescope, i.e.:

$$G = \Gamma_1 = 2\pi \int_0^{\theta_1} h(\theta) \cos \theta \sin \theta d\theta. \quad (\text{A.13})$$

### A.1.2 Single element telescope

For an ideal telescope consisting of a single planar detector without shielding,  $h(\theta) = A$  with  $A$  the surface area of the detector, so that the geometric factor is given by

$$G = 2\pi A \int_0^1 (-\cos \theta) d(\cos \theta) = \pi A. \quad (\text{A.14})$$

If particles are incident from both sides then the detector area is doubled, and

$$G = 2\pi A. \quad (\text{A.15})$$

The gathering power and effective area are also easily evaluated from Eqs. (A.9) and (A.11). A single detector embedded in a viewing cone with opening angle smaller than  $\pi$  can be treated as the lower detector of a two-element telescope in which the respective surfaces of both detectors and their separation define the same solid angle as the viewing cone of the single detector.

### A.1.3 Multi-element telescope

For a multi-element telescope with cylindrical symmetry, the effective area can be written in analytical form, although the derivation becomes tedious for more than two detectors. The gathering power and geometric factor can be determined by integration, which may involve elliptical integrals depending on the form of the angular dependence  $F$  of the intensity.

For complex geometries a numerical approximation usually is easier than the analytical approach. This technique involves numerical integration of the effective area taking into account the path of an incoming particle through a mathematical description of the detector plates.

## A.2 Geometric factor correction

The quantity typically measured by a particle telescope is the number of incoming particles  $N$  over the accumulation period  $T$ , in the solid angle  $\Omega$  defined by the telescope configuration and centered around a direction  $\mathbf{r}$ , in the energy interval  $[E_l, E_u]$  defined by the detector response. The physical quantity that the telescope aims to measure is the differential directional particle flux  $j$ .

In general, the trapped particle flux measured by a telescope differs from the true flux because of the finite opening angles of these instruments. A zero-order approximation of the true flux is given by:

$$j^{(0)}(E) = \frac{1}{G} \frac{N}{T} \frac{1}{E_u - E_l}, \quad (\text{A.16})$$

where  $G$  is the nominal geometric factor of the detector element and  $E$  represents the reference value of the energy interval  $[E_l, E_u]$ .

The measured flux can be corrected by an iterative procedure:

1. The first step consists of averaging the zero-order fluxes given by Eq. (A.16) over an  $(E, L, \alpha_0)$  grid, using the averages of the uncorrected measured flux as the zero-order approximation  $j^{(0)}$ . This is equivalent to assuming that the ambient flux is isotropic.
2. For step  $i$ , evaluate the gathering power  $\Gamma_F$  [Eq. (A.12)] for each measurement (and for each energy channel), using the pitch angle dependence of the last iteration  $j^{(i-1)}$ .
3. For each measurement (and energy), integrate the zero-order flux (using the bin averaged  $j^{(0)}$ ) over the telescope opening angle using Eqs. (A.12) and (A.4); compute the ratio of this integrated flux defined to  $j^{(0)}$  corresponding to the  $(E, L, \alpha_0)$  value for each measurement, and multiply the measured flux by this ratio.
4. Re-bin the measured fluxes, applying the correction factor from step 3. The new bin averages constitute the  $i^{\text{th}}$  order approximation  $j^{(i)}$  of the true flux.
5. Repeat from step 2 until convergence is reached. One step should be sufficient.



This procedure ignores the dependence of the flux on azimuth. This approximation is reasonable when the measurements used for the flux averages were taken over the full azimuth range  $[0^\circ, 360^\circ]$ . Taking into account both pitch angle and azimuth dependence would significantly increase the complexity of the procedure, which is already very demanding in calculation time.

The gathering power [Eq. (A.12)] is determined by integrating the effective area function  $h$  over the telescope opening, whereby the flux dependence on  $\alpha_0$  of the previous iteration is used for  $F(\theta)$  (we have ignored the dependence of the flux on  $\phi$ ). The integration is carried out in the variable  $\theta$ , the off-axis angle, and the azimuthal angle  $\phi$  measured in the plane perpendicular to the telescope axis. For a measurement point  $P$  and a local pitch angle  $\alpha$  (corresponding to the pitch angle of the detector axis), the drift shell coordinates  $(B_m, L)$  can be evaluated with BLXTRA. The corresponding equatorial pitch angle  $\alpha_0$  is given by

$$\alpha_0 = \arcsin \left( \sqrt{\frac{B_0}{B_m}} \right), \quad (\text{A.17})$$

with

$$B_0 \equiv \frac{0.311653}{L^3}. \quad (\text{A.18})$$

The flux seen by the detector then is

$$j(E, L, \alpha_0) = \int_0^{2\pi} d\phi \int_0^{\theta_1} j^{(0)}[E, L, \alpha'(\theta, \phi)] h(\theta) \cos \theta \sin \theta d\theta, \quad (\text{A.19})$$

where  $\alpha'$  is the local pitch angle corresponding to the off-axis angle  $\theta$  and the azimuthal angle  $\phi$ .  $\alpha'(\theta, \phi)$  is given by:

$$\cos \alpha' = \cos \alpha \cos \theta - \sin \alpha \sin \theta \cos \phi. \quad (\text{A.20})$$

